# Mechanisms and Optimisations of 3D Shock Control Bumps


Wai Sam Wong

Department of Mechanical Engineering

The University of Sheffield

Supervisor: Professor Ning Qin

A thesis submitted for the degree of

*Doctor of Philosophy*

October 2006

I would like to dedicate this thesis to my loving parents, sister and brother, my cute little dog, Fifi and my lovely girlfriend Pau Ling.

# Acknowledgements

I would like to thank my parents, sister, brother and Fifi for their unselfish support for these long years of studying abroad and spending less time at home. I would also like to thank Prof. Qin for giving me this opportunity regardless of my lack of experiences and his invaluable suggestions and guidance throughout the course of this study. Many thanks to the our CFD group in Sheffield, Alan, Xia Hao, Greg, Naveed and Jahanzeb for their help and also to the CFD group in Cranfield (although I have only been there for five months). I would also like to acknowledge the support of BAE Systems, Airbus and the ORS award from Universities UK that have made this study possible in the sense of both financially and intellectually. I am also grateful of the help and support from Pau Ling that has made my final study year a memorable one. Last but not the least, I would like to thank all my friends in Sheffield for all the fun and help.

# Abstract

By using an efficient adjoint-based aerodynamic optimisation method, both the 2D and 3D bumps are optimised on an unswept wing with either a natural laminar flow aerofoil or a turbulent aerofoil. The mechanisms of the shock control bumps are analysed through pressure drag analysis, as well as wave drag analysis that uses a far-field method. It is shown that the bumps reduce both the wave drag and the form drag. Comparisons of the performance of these two types of bumps indicate that the 3D bump has an advantage over the 2D bump at lower-lift off-design conditions. A low-order geometrical model for the 3D bump is derived based on the correlations of the design parameters with respect to the strength and position of the original normal shock wave on the datum wing. A finite number of 3D shock control bumps are placed on a full 3D transonic swept wing. The designs of the 3D bumps have been optimised in advance on an infinite swept wing with a constant aerofoil section that is extracted from the mid-span of a chosen 3D transonic wing. Further drag analysis exhibits the effects of the 3D bumps on the various drag components. The combined wing shape with 2D bump optimisations demonstrates the potential of designing a wing with low sweep angle. The feasibility of carrying out a large aerodynamic optimisation is demonstrated in the combined optimisation study of a BWB aircraft with 3D bumps.

# Contents

# List of Figures

# List of Tables

# Nomenclature

### Roman Symbols

| | |
|---|---|
| $\mathbf{A}$ | generic LHS matrix in a linear system |
| $A^+$ | van Driest constant in the Baldwin-Lomax model |
| $A_{area}$ | reference area |
| $a$ | speed of sound |
| $B_{k,N}$ | Bernstein polynomials |
| $\mathbf{b}$ | generic RHS vector in a linear system |
| $C_{cp}$ | additional closure coefficient for the Baldwin-Lomax model |
| $D$ | drag |
| $E$ | total energy |
| $e$ | specific internal energy |
| $\mathbf{F}$ | flux vector |
| $\mathbf{F}$ | flux vector in the $x$-direction |
| $\mathbf{G}$ | flux vector in the $y$-direction |
| $\mathbf{H}$ | flux vector in the $z$-direction |
| $F_{kleb}$ | the Klebanoff function for the Baldwin-Lomax model |
| $F$ | objective function |
| $F_{wake}$ | wake function for the Baldwin-Lomax model |

| | |
|---|---|
| $g$ | gravitational acceleration constant |
| $\mathbf{H}$ | Hessian matrix |
| $i$ | index |
| $in$ | maximum number of grid points in the $i$-direction |
| $j$ | index |
| $jn$ | maximum number of grid points in the $j$-direction |
| $k$ | index |
| $k$ | turbulence kinetic energy |
| $kn$ | maximum number of grid points in the $k$-direction |
| $L$ | lift |
| $l$ | mixing length in the Baldwin-Lomax model |
| $\mathbf{L}$ | lower triangular matrix in a BILU decomposition |
| $l$ | turbulence length scale |
| $m$ | mass |
| $\mathbf{n}$ | normal unit vector |
| $n$ | time level |
| $N$ | index number for the number of parallel processors |
| $\mathbf{P}$ | primitive variables $= (\rho \quad u \quad v \quad w \quad p)^t$ |
| $p$ | static pressure |
| $P_{yk}$ | Bézier control point |
| $\mathbf{Q}$ | vector of conservative variables $= (\rho \quad \rho u \quad \rho v \quad \rho w \quad \rho E)^t$ |
| $q$ | heat flux vector |
| $q$ | iteration number for optimisation |
| $R$ | perfect gas constant, for air = 287 J/kgK |

| | |
|---|---|
| $r$ | aircraft cruising range |
| $\mathbf{R}$ | residual vector |
| $\mathbf{S}$ | source term vector |
| $S$ | area |
| $\mathbf{S}$ | vector of search direction |
| $s$ | entropy |
| $S_{ij}$ | strain-rate |
| $S_k$ | kinetic energy source term for the k-$\omega$ turbulence model |
| $S_i$ | slope limiter in the MUSCL scheme |
| $S_{speedup,N}$ | the speed-up index for $N$ of processors over 32 processors |
| $S_\omega$ | specific dissipation rate source term for the k-$\omega$ turbulence model |
| $T$ | static temperature |
| $t$ | time |
| $u$ | velocity component in the $x$-direction |
| $U^+$ | Non-dimensional velocity |
| $\mathbf{U}$ | upper triangular matrix in a BILU decomposition |
| $U_{diff}$ | maximum difference of the velocity magnitude across the boundary layer |
| $\overline{U}$ | velocity component normal to the boundary |
| $v$ | velocity component in the $y$-direction |
| $V_\infty$ | resultant freestream velocity |
| $\overline{V}$ | velocity component parallel to the boundary |
| $V$ | volume |
| $w$ | velocity component in the $z$-direction |
| $w$ | weight of the aircraft |

| | |
|---|---|
| $\overline{W}$ | velocity component parallel to the boundary |
| $\mathbf{x}$ | generic LHS vector of unknown in a linear system |
| $\mathbf{X}$ | vector of grid points |
| $y^+$ | Non-dimensional normal distance from the wall |
| $\delta y$ | distance of the first cell from the wall |
| $y_n$ | normal distance from the body surface in the Baldwin-Lomax model |

**Greek Symbols**

| | |
|---|---|
| $\alpha$ | Clauser constant in the Baldwin-Lomax model |
| $\alpha$ | step-size taken in the search direction |
| $\boldsymbol{\beta}$ | vector of design variables |
| $\delta_{ij}$ | Kronecker symbol |
| $\Delta$ | increment |
| $\gamma$ | ratio of specific heats |
| $\kappa$ | coefficient of thermal conductivity |
| $\kappa$ | von Karmann constant in the Baldwin-Lomax model |
| $\kappa_{curve}$ | curvature function for the curvature-based algebraic turbulence model |
| $\lambda$ | second coefficient of viscosity |
| $\boldsymbol{\lambda}$ | adjoint vector = $(\lambda_1 \quad \lambda_2 \quad \lambda_3 \quad \lambda_4 \quad \lambda_5)^t$ in 3D |
| $\mu$ | molecular viscosity |
| $\mu_t$ | turbulent viscosity |
| $\Omega$ | bounded domain |
| $\omega$ | specific dissipation rate |
| $\omega$ | vorticity |
| $\rho$ | density |

$\sigma$ constant for the k-$\omega$ turbulence model

$\tau$ shear tensor

$\varepsilon$ ratio of the new $(L/D)$ to the old $(L/D)$

$\varepsilon$ small number

$\xi$ ratio of the aircraft mass at the end of the cruise to the start of the cruise

$\boldsymbol{\eta}$ metric vector/cell face normal vector in $j$-direction

$\boldsymbol{\xi}$ metric vector/cell face normal vector in $i$-direction

$\boldsymbol{\zeta}$ metric vector/cell face normal vector in $k$-direction

**Superscripts**

$i$ convective or inviscid

$t$ transpose operator

$\sim$ approximate Jacobian

$v$ diffusive or viscous

**Subscripts**

$b$ on the boundary

$far$ farfield

$\infty$ freestream condition

$L$ relative to the left hand side of the interface in the Riemann solver

$R$ relative to the right hand side of the interface in the Riemann solver

$w$ at the wall

**Other Symbols**

$\nabla$ gradient operator

**Acronyms**

$CFD$ Computational Fluid Dynamics

$CFL$ Courant-Friedrichs-Lewy

$DOC$ Direct Operating Cost

$EC$ European Committee

$HLF$ Hybrid Laminar Flow

$LE$ Leading Edge

$LFC$ Laminar Flow Control

$LHS$ Left hand side

$M-DAW$ Modelling and Design of Advanced Wing Tip devices

$MEMS$ Micro-Electro-Mechanical Systems

$MPI$ Message-Passing-Interface

$NDV$ number of design variables

$NLF$ Natural Laminar Flow

$RHS$ Right Hand Side

$sfc$ specific fuel consumption

$SQP$ Sequential Quadratic Programming

$TDR$ Turbulent Drag Reduction

$TE$ Trailing Edge

$TS$ Tollmien-Schlichting

$UKAAC$ UK Applied Aerodynamics Consortium

# Chapter 1

# Introduction

## 1.1 Review in Aircraft Drag Reduction

With the prospect of substantial growth in future passenger demand, and a gaining awareness of climate change issues particularly global warming, the European Commission has issued the VISION 2020 document in 2001 [1]. In this document, by the year 2020, it is envisioned to achieve a reduction of the $CO_2$ emissions by 50% and of the $NO_x$ emissions by 80%. Part of the reduction will be achieved by improved engine design with higher bypass ratio, by increased use of advanced materials, i.e. carbon fibre, and by better multidisciplinary optimisation. However, the expected benefits from these technologies is limited and might be insufficient to meet the stated target. Thus, drag reduction technologies are essential in meeting the VISION 2020 targets.

Recent surging fuel prices have also motivated the investigations and implementation of drag reduction technologies in the aerospace industry. The average price for one gallon of kerosene in Rotterdam over the period from mid 1986 to the end of 2001 was 59 US-Cents. However, between 2002 and 2005, the price of kerosene surged above 180 US-Cents. When it was 60 US Cents per gallon, the fuel for a typical 6000 nautical miles mission of a long-range aircraft cost about 17% of the DOC. With all the other parameters kept constant, the fuel share rises to 38% of the DOC when the fuel price hits 180 US-Cents per gallon [2]. Consequently, a small drag reduction implies substantial fuel economy benefits. For example, a drag reduction of 1% can lead to a DOC decrease of about 0.2% for a large transport aircraft [3].

A typical drag breakdown of a civil transport aircraft in Figure 1.1 shows that the skin friction drag and the lift-induced drag or vortex drag constitute about 45% and 40% of the total drag respectively [2]. Even though from this figure, the wave drag contribution to the total drag is not that high compared to friction drag (around 3%) , there is still room for significant improvements in this area on the off-design performance of the aircraft. These presented data is averaged from difference sources, the amount of each component may vary by a few percent. For example, the percentage of wave drag can go as high as 10% on an executive jet. In the following sections, various drag reduction technologies and recent progress in these areas will be briefly presented to provide a context for this project. The focus will be on wave drag reduction technologies particularly shock control methods.

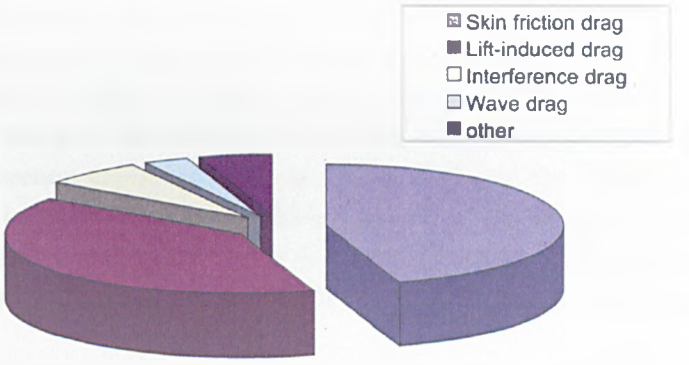


Figure 1.1: A typical drag breakdown of an aircraft.

## 1.2 Skin Friction Drag Reduction

Since the late 1930s, researchers have looked into innovative ways to reduce skin friction drag. In the 1970, the Arab oil embargo triggered further research in this area. Skin friction drag reduction technology is generally categorised into two major methods: 1) Delaying transition to maintain large extent of laminar flow and 2) Reducing turbulent skin friction drag.

### 1.2.1 Laminar Flow Control

In order to delay transition efficiently, it is essential to identify the mechanisms responsible for transition in the particular application, especially whether linear instability mechanisms dominate or whether non-linear/bypass mechanisms are the primary concerns. Non-linear/bypass transition refers to any transition process not dominated by a single linear instability mechanism, i.e. early transition induced by the development of crossflow and Tollmien-Schlichting instabilities. These instabilities can be weakened to delay transition by choosing an appropriate pressure gradient, by removing the slowest part of the boundary layer via suction through slots or small holes, or by cooling the surface.

For small aircraft with a low-sweep wing, laminar flow can be maintained by shaping the aerofoil to provide a favourable pressure gradient up to an extent. This is regarded as the Natural Laminar Flow (NLF) concept. However, at a higher Reynolds number, larger civil transport aircraft with a highly swept wing need other ways to achieve transition delays, such as suction near the leading edge. Suction has been proved to be an efficient LFC tool. For minimal fabrication and inspection problems, researchers have developed the Hybrid Laminar Flow concept. In the HLF concept, suction is applied at the region of the leading edge with favourable pressure gradients in the spar box region. Since both active control (suction) and shaping (NLF) have been employed, the concept is regarded as "hybrid".

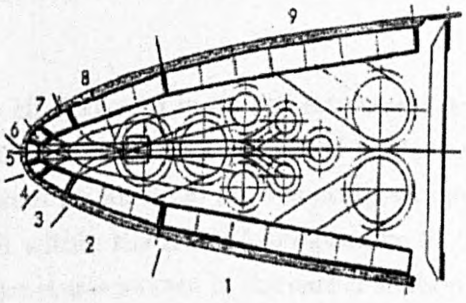


Figure 1.2: Classical suction system design.

Although using suction to control boundary layer transition has long been understood, the technologies to produce very small holes with acceptable surface

finish and accuracies were not available until about fifteen years ago in the early 1990s. Small holes may now be drilled using laser or electron beams. An early typical suction system (Figure 1.2) was then designed in order to control accurately the suction distributions for flight test demonstrations. Early test flights [4, 5] utilising the earlier suction system design have demonstrated the potential and feasibility of the HLF concept in modern civil transport aircraft. Critical issues in the certification, design and manufacture of a HLF aircraft have been investigated in the flight tests. The demonstrations were also aimed at analysing the behaviour of the HLF devices during operation. Although the experimental suction system on the A320 [4] was much too heavy to obtain a net benefit, the flight tests have nevertheless shown that for high sweep and Reynolds number conditions, a large extent of laminar flow can be achieved at cruise.

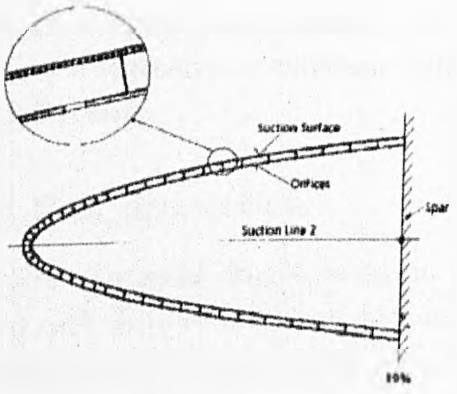


Figure 1.3: New revised suction system design.

In order to make the HLF system more attractive and economically viable, the suction system design has to become simpler and lighter. A new approach with a simplified suction system for an A320 fin was designed and developed by Airbus Deutschland and DLR within the ALTTA programme [6, 7]. As shown in Figure 1.3, the complex substructures as seen in the earlier suction system design (Figure 1.2) are removed and the whole leading edge box is used as a single suction duct. The revised design has much less complexity and hence reduced the maintenance costs and weight. Furthermore, the new system is also self-adapting, for example, it is automatically switched on when a predefined altitude has been reached. Hence, it works without controlling the internal flow with the help of valves and

flow meters.

Surface imperfections such as isolated roughness, gaps, steps, waviness due to manufacturing, i.e. holes drilling for the suction system, can provoke premature transition. It is then necessary to study their effects on transition and to develop calculation methods and criteria in order to estimate these effects [8, 9]. However, recent studies have shown that modern manufacturing techniques can provide smooth surfaces, compatible with laminar flow requirements.

With all the promising results shown above, there are still some unresolved issues with the HLF system. Laminar surfaces might easily be contaminated by insect debris or other types of dirt when it is in operation. The HLF system will also need to have an integrated anti/de-icing system. Potential solutions were proposed to tackle these issues [2]. For example, cleaning/de-icing by pressing liquid or foam out through suction holes. Although these systems were demonstrated to work, the additional weight and maintenance requirements might again outweigh the benefits gained from HLF control.

### 1.2.2 Turbulent Drag Reduction

Although LFC can achieve substantial drag reduction in many applications and flow conditions, it is very difficult to establish and maintain laminar flow. Therefore, turbulent drag reduction is also a key issue in aeronautics even though the possible drag reduction that can be achieved is lower than that of LFC. Turbulent skin friction drag can be defined as the area integral of the local skin friction coefficient multiplied by the dynamic pressure. Thus, from this definition, a general way of reducing turbulent drag is cutting down the total wetted area, skin friction coefficient and local dynamic pressure. Reduction of wetted area can be achieved by various means such as introducing innovative technologies, i.e. thrust vectoring, to the aircraft design to reduce the control surface area, and by novel aircraft configurations such as the blended wing body that obviate much of the fuselage wetted area [10].

For a given wetted area, TDR can be achieved by active or passive boundary layer manipulations. One of the active control methods of the turbulence boundary

layer structure is surface air mass injection that is tangential or normal distributed blowing. Other methods include interactive wall-turbulence control as can be achieved by zero-mass air jets (synthetic jets) or MEMS actuator arrangements [11]. The latter approach is similar to that of controlling TS-waves. Since it is known that high skin friction regions in turbulent boundary layers are closely related to the near-wall streamwise structures, Refs. [12, 13] have investigated effective ways to control the near-wall turbulent structures through proper interactive manipulation. The studies address the design concept of an adaptive TDR control and it is shown that the streamwise mean velocity is reduced and hence the turbulent skin friction drag.

Passive boundary layer manipulators for TDR include surface modifiers, such as riblets and outer boundary layer devices to break up the large structures within the boundary layer. The mechanisms of such devices is aimed to reduce the spanwise strong exchange of high speed and low speed flow in the turbulent boundary layer, where such exchange of fluid normal to the surface generates the enhanced shear stress of a turbulent flow. Thus, obstructing this motion may significantly reduce momentum transfer and skin friction [11].

Of all the various investigated devices, V-groove riblets have demonstrated up to 8% reductions of the local skin friction. However, there is also some indication that the riblets perform well only within a particular velocity range [14]. Thus, the spacing between the riblets have to be optimised for a given flight condition. Nevertheless, experiments have been conducted to verify the performance of the V-groove riblets in a large wind tunnel on a 1/11 scale complete model of the Airbus A320 [15]. In this experiment, two-thirds of the model is covered with the selected riblets and total drag reductions up to 1.6% have been obtained at simulated cruise conditions. Based on the results gathered from the wind tunnel tests, a flight test with the riblet film installed covering 75% of the wetted surface of an Airbus A320 has taken place. Comparisons between the performance of the aircraft with and without riblets have confirmed the drag reduction predictions based on the wind tunnel tests.

Ref. [16] has then investigated the operational aspect and maintenance problems of these types of devices. Based on that, Cathay Pacific Airways airline has

already implemented this device on an in-service Airbus A340. Although significant fuel consumption benefits have been obtained, it is indicated that the riblet film has a service lifespan of around two to three years. In order to obtain a net benefit from the application of this technology, the quality of the riblet film needs to be improved to sustain a longer service lifespan of at least 5 years.

## 1.3 Lift-Induced or Vortex Drag Reduction

As shown earlier from the drag breakdown in Figure 1.1, drag due to lift or vortex drag comprises about a third of the total drag, hence it is a second major drag component. Classical linearised theories [17] indicates that elliptical loading and increased aspect ratio are the primary approaches to vortex drag reduction. However, the wing aspect ratio requires structural feasibility. In fact, modern civil transport aircraft such as the Airbus A340 wing design already has a reasonably high aspect ratio of 9.3. Therefore, alternative approaches to this problem were considered. For example, various wing tip devices were developed to weaken the tip vortex, which is the origin of vortex drag.

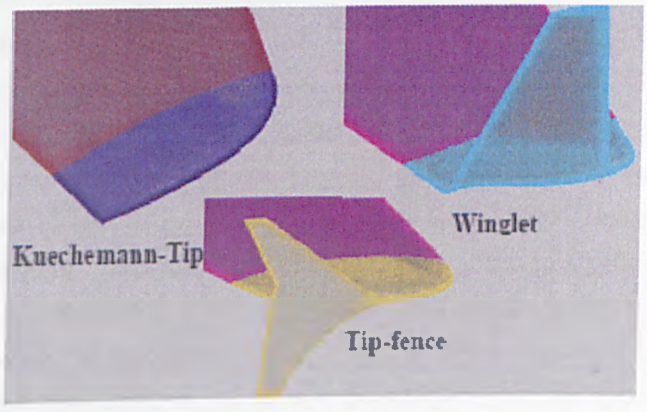


Figure 1.4: Conventional wing tip devices.

In recent years, there have been extensive research into many types of wing tip devices in Europe. Besides wind tunnel testing, advanced CFD has also emerged as an important tool in designing and optimising these devices. Improved far-field drag extraction techniques have allowed drag predictions with greater accuracy [18]. Some examples of conventional wing tip devices investigated are shown

above in Figure 1.4. Unconventional novel wing tip designs have also been designed and investigated, such as blended winglet and spiroid (Figure 1.5). Ref. [19] studies these two unconventional wing tip devices using an Euler solver and a numerical optimisation approach. The study found that compared to a wing without any devices, vortex drag is reduced by 4% and 3.3% with the blended winglet and spiroid respectively.

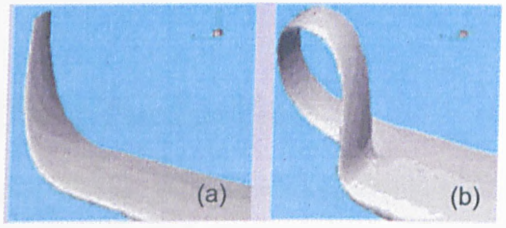


Figure 1.5: Unconventional wing tip devices. (a) blended winglet and (b) spiroid

The M-DAW Project, which aims to deliver to the European aerospace industry a novel wing tip device, was launched in the year 2002 [20]. Recent progress from the project have been reported in Refs. [21, 22]. In order to take into account various other multi-disciplinary trades, for example, additional weight from the device and bending moment of the wing, an "Equivalent Drag" function has been defined. Although assumptions have been made, this function enables a quick assessment of the overall design issues, not just aerodynamic performance but also implications of the design impact on the whole aircraft system. As part of the M-DAW project objectives, which is to assess the capabilities of advanced CFD to predict the effects of these devices, Ref. [22] investigates the effects of aeroelastic wing deformations and half model considerations on the previous CFD results analysing various wing tip devices. It is found that by introducing wing twist data from the wind tunnel into the CFD calculations, the results from the simulation is greatly improved. Additionally, the studies also realise that the discrepancies of the results at the inboard wing between the simulation and experiment are due to the experiment using a half-model mounted on the wind tunnel wall, whereas in CFD, a half-model with a symmetry boundary condition is adopted. Therefore, comparisons of the results can be improved by simulating the wind tunnel with the half-model.

From the M-DAW project, the detailed data of the performance and characteristics of two conventional wing tip devices (a large canted winglet and an Airbus tip fence) has confirmed much of the understanding of the aerodynamics of the devices and has been used for extensive CFD validation. A design exercise from this project has achieved advances in the capability to manage wing tip loads to provide drag improvements with reduced structural weight penalties. Future project stages have then been planned to explore the most promising wing tip device design.

## 1.4 Wave Drag Reduction

A typical Mach number region defined as transonic is between 0.7 to 1.2. From there and with speeds up to Mach 3, it is considered as supersonic. Beyond that, it is then hypersonic. For years, the SR-71 "Blackbird" has been officially the fastest jet-powered aircraft, which has reached a record speed of Mach 3.3. In the year 2004, this record has been broken by NASA's X-43 Hyper-X experimental aircraft. It uses an advanced scramjet engine and reached Mach 9.68. It was during these pursuit of ever higher speed that engineers and designers realised that another form of drag is imposed on transonic, supersonic and hypersonic aircraft, which was later found to be caused by shock waves. Shock waves are strong mechanical waves due to rapid compression of the air. Across the shock wave, there is a large entropy increase, which is paid for in terms of a large drag acting on the aircraft. This drag is then known as "wave drag".

During transonic flight, even when the aircraft is travelling slightly below the speed of sound or just below Mach 1, there are "patches" of local supersonic flow on the wing. The supersonic flow is then terminated as a normal shock wave. When this shock wave gains strength, not only will the wave drag increase substantially, there could be eventual boundary layer separation due to the severe adverse pressure jump across the shock. Therefore, shock-boundary layer interaction basically ascertain the flight performance of a transonic aircraft. Shock control methods are the main focus here and the various methods will be reviewed in the next subsection. In the meantime, let us look at some other technologies with basically the same aim of reducing wave drag for transonic flight.

A widely spread concept for wave drag reduction for transonic flight, is the introduction of supercritical wing, in which the lift vector is moved rearward overall with considerable lift carried by the aft portion of the aerofoil. The aerofoil has little curvature over the forward portion downstream of the nose and is highly cambered in the aft region to produce a reasonable amount of lift whilst the strength of the shock wave formed on the upper-wing-surface is greatly reduced at a given speed [23]. Thus, a thicker wing (structural benefits) can be designed without reducing the design Mach number. Most modern civil transport aircraft such as the Airbus A3XX series, have well-designed supercritical aerofoil sections for their wings.

For transonic aircraft wings, another widely adopted method for reducing wave drag is to sweep the wing back. This concept is originally dated back to the time of the second world war. With a sweep angle, only the velocity component at right angles to the leading edge of the wing contributes to the aerodynamic performance. Consequently, aircraft can be designed to operate at a high transonic Mach number while reducing the effective Mach number seen by the wing section to a value just below the transonic drag rise. However, swept wings perform worse at low speed [24].

Research by Whitcomb *et al.* (Ref. [17]) has shown that smooth variations in the axial cross-sectional area of the whole aircraft can substantially delay the divergence Mach number, which is known as the "area rule". This finding has then given rise to the famous "coke-bottle" design in some of the fighters.

With the design concepts introduced above, new materials, improved jet engines and modern manufacturing technologies, global civil air travel, particularly long haul intercontinental flights are then started to emerge to be more a feasible and economical way of travelling. Although supersonic transport seems to be next logical step. However, due to the combination of economic reality and environmental concerns, modern transport aircrafts are still limited in the transonic regime. An early version of supersonic transport aircraft, Concorde, has not proven to be economically viable. Even though most military aircraft were designed to fly supersonically, but these fighters are only capable of supersonic cruise over a limited distance due to the wave drag. During most of the flight distance and in combat,

they still cruise in transonic speeds [23]. Thus, the preceding discussions have mainly focused on the transonic flight regime.

### 1.4.1 Shock Wave/Boundary-Layer Control Methods

In theory, shock-boundary layer control methods can greatly enhance transonic flight performance in terms of cruise drag, hence speed and/or fuel consumption, and with respect to the drag-rise and buffet boundaries. Shock-boundary layer control can also be utilised to design wings of simpler geometry, e.g., thicker wings, without the penalty of performance degradation, allowing a reduction in weight and increase in payload [25]. In addition to that, control of shock strength and buffet also provides scope for noise reduction on rotorcraft and improved agility for military aircraft [26].

The potential benefits of shock and boundary layer control has motivated the investigation of a wide range of devices and strategies. These can be broadly categorised into two main types, passive and active shock control. The basic principles underlying the development of such control methods are to raise the energy of the boundary layer flow immediately ahead of the interaction region and to achieve compression of the flow immediately ahead of the shock wave via local modification of the aerofoil or streamline contours [26].

#### 1.4.1.1 Passive Shock Control

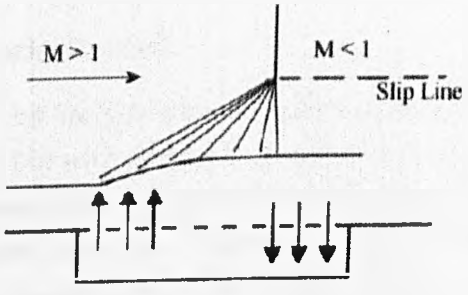


Figure 1.6: Illustration of a typical passive control with underlying cavity.

Passive control, which means here control via a perforated surface with underlying cavity in areas of strong shocks without applying suction (Figure 1.6). Promising results from the preliminary investigations of such devices have initiated extensive research activities. In Europe, the EC Project EUROSHOCK(I) was launched [27, 28]. Investigations conducted in the EUROSHOCK (I) Project were concentrated on laminar-type aerofoils. Laminar-type aerofoils were considered to be more suitable for shock control, hence of higher potential for control, because the inherent acceleration of the flow on the aerofoil/wing upper surface leads to strong shock waves even at design conditions [11].

The investigations by Fulker *et al.* [27] have shown that the passive control surface has the effect of replacing the single straight shock of the datum case with a multi-shock system, and thus the wave drag is significantly reduced due to the multi-shock system. However, it is also observed that there is a viscous drag penalty is due to the aerodynamic roughness of the porous surface and/or the flow through the surface causing excess thickening of the boundary layer. Therefore, the reduced wave drag is overcompensated by this viscous drag penalty. Consequently, the total drag increases. Further numerical and experimental results from the thorough investigations of these devices in the EUROSHOCK (I) Project [28] have confirmed that an increase in total drag is consistently observed due to the dominating increase in viscous drag as discussed above. It is then concluded that passive shock control is ruled out as an effective means of reducing drag of laminar wings. Nevertheless, it still remains as a potential for other applications where aspects such as shock induced boundary layer separation is of primary concern instead of drag reduction, e.g. to delay buffet on-set.

#### 1.4.1.2 Active Shock Control

Active shock control may include several control mechanisms: perforated plates with underlying cavity but with part-suction from the cavity, discrete slot suction, local contour modification (i.e. bumps) and even using spoilers. A hybrid control concept, which combines a passive ventilation cavity in the shock region with a discrete slot suction downstream of the passive cavity has also been proposed and investigated. Although applying suction downstream of the device reduces the viscous drag penalty due to the thickened boundary layer after the control device, but the datum total drag level is difficult to obtain, at least not for a feasible suction rate [25]. Bur *et al.* [29] also studied active and hybrid control

experimentally and numerically. They concluded that a possible way to reduce the viscous drag penalty when employing hybrid control is to reduce the distance between the interaction region and the suction slot placed downstream of it.

In other investigations, Zhu suggests that when discrete slot suction is employed ahead of the interaction region, the solution tends towards the inviscid solution, resulting in the occurrence of a strong shock normal to the wall. Thus reduction in viscous drag is achieved through re-energisation of the boundary layer are offset by an increase in wave drag [30, 31].

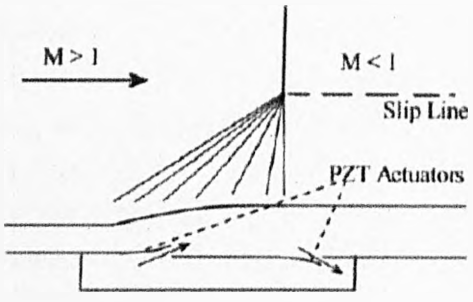


Figure 1.7: Illustration of an active control using "smart" flap piezoelectric actuators.

There are other innovative concepts, such as active control using "smart" flap actuators reported in Refs. [32, 33]. An illustration of the concept is shown in Figure 1.7. The control is similar to a typical passive control with a perforated plate covering a plenum chamber. The amount of bending of the piezoelectric flap can be controlled and hence the rate of mass transfer going in and out of the plenum chamber, hence it is considered as an active control device. The experimental results of this control concept indicate that due to limited achievable deflection of the piezoelectric material, the level of shock control is limited though favorable. However, the position of the flaps relatively to the shock wave can be improved to provide a better performance.

Due to the fact that spoilers are already widely used within the aircraft industry, there is potential for solving many of the system integration issues that troubled other shock control strategies. Thus, Shaw *et al.* investigated the potential of

using spoilers for shock control purpose [26]. It is found that there are no drag reduction benefits identified for the spoiler in comparison with the contour bumps, due to a base drag penalty associated with the spoiler. However, the study is far from complete since there are still a large number of parameters that can be altered.

As part of the EC Project EUROSHOCK(II), Dima *et al.* [34] compared the performances of a contour bump and a novel suction/blowing plenum chamber arrangement or a "multi-box" device in the shock region. It is then concluded that both contour bump and the "multi-box" device are very effective in reducing wave drag and alleviating buffet. However, both devices will need to be adaptive for optimum performance. The EUROSHOCK (II) Project has also involved thorough investigations on various shock control devices as mentioned and concluded that local contour modification is the most effective shock control methods when drag reduction is the main driver and with additional potential benefits related to buffet and without significant viscous drag penalty [25]. The following subsections will then present a more detailed review of the research on reducing wave drag and hence shock wave-boundary layer control utilising local contour modifications or shock control bumps, which include both two-dimensional and three-dimensional shock control bumps.

#### 1.4.1.3 Two-Dimensional Shock Control Bumps

Shock control by local contour modifications or bumps was proposed by Fulker *et al.* [35]. A simple illustration of the basic principle of a shock control bump is shown in Figure 1.8.

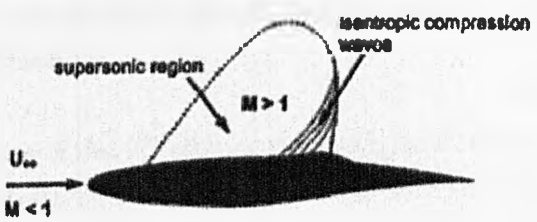


Figure 1.8: Mechanisms of shock control bump.

The upstream concave part of the bump induces an isentropic compression wave leading to a pre-shock compression and thus decreases the Mach number ahead of the shock. Note that the design of the shock control bump is two dimensional in the sense where the shape of the bump is the same along the span, thus it is referred as "2D bump" for the rest of the thesis. Encouraging preliminary results from Fulker *et al.* [35, 27] were then extended to further investigations of the effect of 2D bumps on drag and high-speed performance boundaries of transonic aerofoils and wings in the EUROSHOCK (II) Project [25].

Zhu [30] has also conducted some investigations on 2D shock control bumps. His findings suggest that its effectiveness is strongly dependent on the shock position, which therefore implies that this type of device is very suitable for a laminar flow aerofoil, for which the shock wave position is relatively steady. In addition, the height of the bump also imposes significant impact on its performance and is largely dependent on the original shock strength. The beneficial effects of the bump is directly proportional to the shock strength.

Investigations from Ref. [36], which is part of the EUROSHOCK(II) Project, studied the influence of sweep on the 2D bump effectiveness. The influence has been found to be rather small. This is consistent with the findings from Kutzbach *et al.* [37], who have also investigated the effects of sweep of a 2D bump on infinite swept wings numerically using various turbulence models. Effectiveness of the 2D bump placed in the shock region in reducing wave drag has been further confirmed and that the parameters of the 2D bump, i.e. height and position have to be optimised, in terms of drag, with respect to the shock strength, which agrees with the findings by Zhu [30]. It has also been found that a 2D bump positioned at the downstream of the shock reduces viscous drag and postpone buffet onset to higher lift coefficients.

Since the effectiveness of the 2D bump relies strongly on the bump height with respect to the shock strength and on the relative location of the bump with respect to the shock location, the 2D bump has to be adaptive. A bump optimisation study carried out by EADS-Airbus for the laminar-type aerofoil DA LVA-1A suggested the following geometric characteristics of the 2D bump. Effects of the bump shape are found to be insignificant in terms of drag. At a structurally feasible optimum of 20% chord bump length, the crest location at 70% of the

bump length to achieve a reduced sensitivity to shock movement, bump crest located about 2-5% downstream of the inviscid-outer-flow shock position, and bump height to be adjusted according to the lift coefficient or shock strength [11].

A research group at Stuttgart University has also carried out extensive research on 2D bumps [38, 39, 40, 37]. Sommerer *et al.* [38] have employed a direct numerical optimisation strategy using a commercial optimisation package (The Pointer Code of Synaps Inc. [41]) on several different bump shapes, including a shape based on a loaded beam on two ends, a triangular shape, a concave polynomial and a polynomial of 11th order. The optimisation results obtained indicate that the shape of the 2D bumps has a minor effect on the performance of the bumps with the best being the triangular and high-order polynomial bumps. The 2D bumps have also been optimised at multiple design-points to obtain a more compromised performance over a larger range of operating conditions.

For further improvements, the team has also looked at the possibility of employing both variable camber and shock control bumps on an aerofoil. Research by Coustols *et al.* [42] has shown that a thick cambered trailing edge, which increases the rear loading whilst reduces the upper surface pressure recovery, can reduce wave drag significantly. Thus, with this wave drag reduction capability from the cambered trailing edge, an additional 2D bump promises a further increase in aerodynamic efficiency. The optimisation of this combination produces substantial gains in terms of lift-drag ratio. It is also noticed that the height of the optimised 2D bump in this combination with variable camber is lower than that without variable camber.

Some structural design concepts have been proposed to implement an adaptive 2D bump structure into the aircraft design [40, 43]. In order to retain the principal design of the aircraft and to avoid too much additional complexity and weight penalties, the adaptive shock control bump system can be integrated in the wing spoilers. An illustration of the system is shown in Figure 1.9. The wing adaptive system also includes a variable camber and a feedback control system to control the shape of the 2D bump on the spoiler. Both studies utilise "smart structure" shape memory alloys as the micro-actuators in the bump shape control mechanism. Shape memory alloys have the advantage of extremely high power to volume ratio and good mechanical properties [44]. It is then demonstrated that

impediments from the adaptable structural side can be solved and implementing an adaptive 2D bump into the aircraft system is feasible.

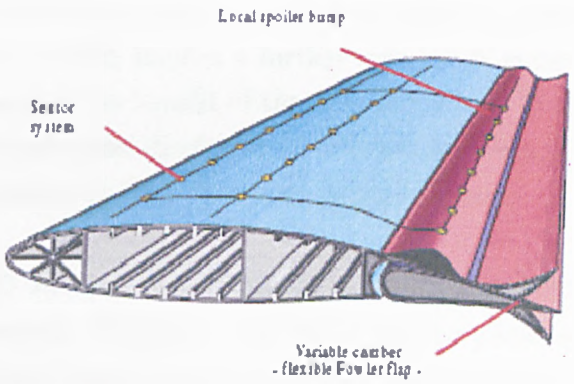


Figure 1.9: Adaptive wing system.

In the EUROSHOCK(II) Project, the benefits and penalties of implementing 2D bump on wings have also been evaluated via introducing bump control into a hybrid-laminar-flow (HLF) wing of a long-range A340-type aircraft [25]. The wing is designed to have fairly strong shocks but limited shock movements with changing Mach number and lift coefficients, hence, chordwise bump adaptation was not considered in this demonstration. The bump designs were based on the optimised geometric characteristics mentioned earlier for an off-design Mach number. The results indicate that the bump is not as effective as expected at the design point of the wing section due to the bump crest being located too far downstream. Furthermore, it is also indicated that at off-design Mach number and at off-design lift coefficients, a variable-height bump is still required to achieve optimum drag reduction.

With all the information obtained on shock control on the HLF wing, the long-range mission benefits of such implementation are estimated to give a reduction in fuel consumption per year of about 353 tons or 1.23%. However, a final assessment of the bump control benefits and penalties can only be made after a much more detailed device-integration study.

#### 1.4.1.4 Three-Dimensional Shock Control Bumps

As discussed in the previous section, although the wave drag reduction capability of a 2D bump is confirmed, it is also realised that 2D bump is only effective over a narrow operating range. This setback could be tackled by introducing an adaptive device, which implies a further increase of system weight load that might overcompensate the benefit of the drag reduction. Thus, other alternative potential three-dimensional shock control devices have been proposed for possible wider operating range, such as three-dimensional bumps.

In contrast to 2D bumps, three-dimensional bumps introduce geometric variations in the spanwise direction. Additional design parameters, the width of the three-dimensional bump in the spanwise direction and also the spacing between the bumps are considered. Figure 1.10 illustrates the differences between a 2D and three-dimensional bump. As shown from Figure 1.10, the 2D bump has constant XY-plane in the Z-direction (or spanwise direction), while for the three-dimensional bump, the cross-sectional XY-plane shrinks gradually in the Z-direction, thus it is considered "three dimensional" and will be referred to as "3D bump" for the rest of this work.

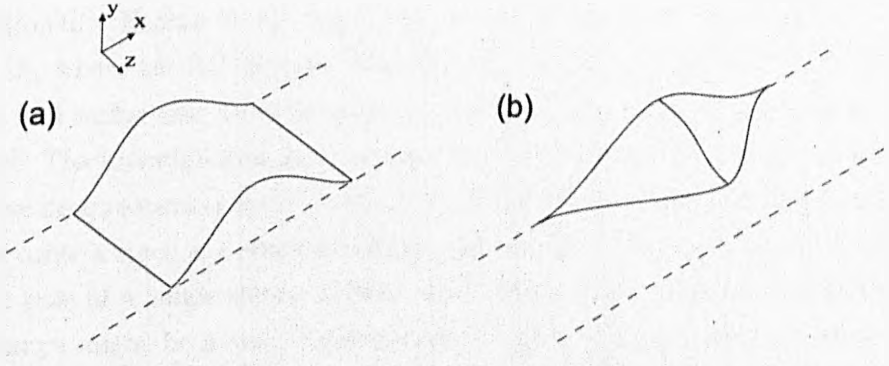


Figure 1.10: a) 2D bump and b) 3D bump

Physically, the most important differences are that the shock wave is now three-dimensional, and that the flow and the boundary layer can now go around the bump, thus, the shock-boundary layer interactions will differ. It is this third dimension geometry variation that might provide further improvement of the shock

control bumps over a wider range of operating conditions.

So far, there have only been a limited number of works reported on shock control studies using 3D bumps. Takahashi [45] briefly studied the inviscid effects of a 3D ramp bump on a RAE 5225 supercritical aerofoil. His results show that at the design point, the 3D ramp bump seems to give a great reduction in wave drag, probably more effective than a 2D bump. These encouraging inviscid results lead to further investigations of the viscous effects of the 3D bump in Refs. [46, 47]. Instead of using the previous supercritical aerofoil employed in Takahashi's investigations, a NLF aerofoil, the RAE 5243 was adopted. Results from Refs. [46, 47] show that unlike 2D bumps, where wave drag reduction is always accompanied by viscous drag or skin friction drag penalty, 3D bumps can reduce wave drag as well as skin friction drag. Thus, these results indicate that the 3D bumps might potentially have a greater drag reduction capability than the 2D bumps. However, it should be noted that the performance of the 3D bump from Monet's investigations has not reached the level of that of the 2D bump. Therefore, it has laid down the groundwork for the present work in this thesis to optimise the design of the 3D bump and also to provide further analysis of its mechanisms and performances.

Additionally, Holden *et al.* have also carried out parallel experimental studies [48, 49], where the 3D devices, including 3D bumps of different shapes, such as ramp and wedge-like, were mounted on the working section of a supersonic wind tunnel. The investigations have demonstrated that these 3D bumps are effective in wave drag reduction by bifurcating the shock-wave. This effect is favourable in shock control since a $\lambda$-shock structure reduces the total pressure losses relative to the case of a single strong normal shock wave. The results also suggest that 3D bumps might be a very beneficial device since they appeared to cause little boundary layer thickening compared to the other 3D devices such as slots and grooves.

## 1.5 Objectives

The encouraging preliminary results of the 3D bumps gives the main motivation behind this project. The objectives of this thesis include the following:

- Validation of the numerical flow solutions with existing wind tunnel experimental data.
- Optimisation of the designs of a three-dimensional bump on infinitely unswept and swept wings.
- Investigations of the mechanisms and performance of the three-dimensional bumps, including detailed drag analyses.
- Applications of the three-dimensional bumps on three-dimensional transonic wings.

Several novelties of this thesis can be derived from this list of objectives. Besides the preliminary work that have been carried out for the initial design of three-dimensional shock control bumps at Cranfield, at least to the author's knowledge, this work is the first to provide detail investigations into the mechanisms and performance of this device. This work has then been extended to applying this device on full three-dimensional transonic wings to demonstrate its feasibility in "real-life" applications.

## 1.6 Outline of this Thesis

The context of various aircraft drag reduction technologies presented in this chapter should provide some knowledge on recent advancements of these methods. The following *Chapter 2* provides the descriptions of the numerical flow solver, which is the main numerical tool employed in this project, with details including the MPI parallelisation and a far-field drag analysis method. The results from the validation of the flow solutions for 3D shock control bumps are presented and discussed in *Chapter 3*. Before presenting the main results, details of the rest of the numerical tools developed for the adjoint-based aerodynamic optimisation are presented in *Chapter 4*. The tools include the grid modeller, the adjoint solver and the Sequential-Quadratic-Programming optimiser. The last three chapters is the core of the thesis, which present the optimisation results and analyses of both the 2D and 3D shock control bumps. *Chapter 5* presents the work carried out for 2D bumps on unswept wings. The results of the 2D bumps from this chapter are then compared with the 3D bumps applied on the same unswept wings in *Chapter 6*. Both chapters detail the optimisations and analysis work carried out for the shock control bumps. *Chapter 7* investigates the performances and optimisations

of employing 3D bumps on an infinite span, a full three-dimensional swept wings and a Blended-Wing-Body. The very last chapter concludes the achievements and findings of this thesis and some suggestions for future work.

# Chapter 2

# Numerical Flow Solver

As mentioned in the previous chapter, the investigations conducted in this project are numerical based. This chapter is aimed at presenting descriptions of the numerical flow solver employed in this project - MERLIN. It is an in-house CFD code developed at the Centre for Computational Aerodynamics of Cranfield College of Aeronautics by Qin *et al.* [26, 50]. MERLIN is a 3D Reynolds averaged Navier-Stokes flow solver. The version employed in this project is a structured multiblock code. The unstructured version of MERLIN has also been developed in Refs. [51, 52]. The author has contributed some modifications to the code including adding some additional boundary conditions and implementing parallel computing capability using MPI into this structured version of MERLIN.

In the code, the governing equations are cast in a cell-centred finite-volume form, the convective flux calculations utilise Osher's approximate Riemann solver [53] to capture flow discontinuity such as shock waves and employs a MUSCL scheme [54] for higher order accuracy. As for time discretisation, both explicit and implicit methods have been implemented. The algebraic turbulence model of Baldwin-Lomax [55], the k-$\omega$ two equation turbulence model [56] and a curvature-based algebraic turbulence model [57] are employed in this work. Before detailing the numerical methods, it is necessary to present the fundamental equations that govern the physics of the flow, which are described in the following section.

## 2.1 The Governing Equations

The Navier-Stokes equations are derived by applying the conservation laws of mass, momentum and energy to an infinitesimally small, moving fluid element.

Complete derivation details are beyond the scope of this thesis and can be found in the literature [17, 58, 59, 60]. In integral form, the full 3D Navier-Stokes equation can be written as below:

$$\frac{\partial}{\partial t}\iiint_{\Omega}\mathbf{Q}d\Omega + \iint_{S}\mathbf{F}\cdot\mathbf{n}dS = \iiint_{\Omega}\mathbf{S}d\Omega \tag{2.1}$$

where **F** is the flux vector, **S** is the source term vector and **Q** is the vector of five conserved variables,

$$\mathbf{Q} = \begin{pmatrix} \rho & \rho u & \rho v & \rho w & \rho E \end{pmatrix}^t \tag{2.2}$$

$\rho$ is the fluid density. $u$, $v$ & $w$ are the three velocity vectors and $E$ is the total energy,

$$E = \frac{1}{2}(u^2 + v^2 + w^2) + e \tag{2.3}$$

and $e$ is the specific internal energy, given by,

$$e = \frac{1}{\gamma - 1}\frac{p}{\rho} \tag{2.4}$$

where $p$ is the static pressure and $\gamma$ is the ratio of specific heats, given as $\gamma$=1.4. However, note that when the k-$\omega$ turbulence model is employed, an additional two more conserved variables need to be solved for and the vector in Eqn. (2.2) becomes

$$\mathbf{Q} = \begin{pmatrix} \rho & \rho u & \rho v & \rho w & \rho E & \rho k & \rho\omega \end{pmatrix}^t$$

where $k$ is the turbulence kinetic energy and $\omega$ is the specific dissipation rate, which will be discussed in more detail in a later section of this chapter. Additionally, it should also be noted that the k-$\omega$ turbulence model is not strongly coupled with the flow equations and is solved sequentially.

The flux vector **F** from Eqn. (2.1) may be subdivided into inviscid and viscous terms:

$$\mathbf{F} = \begin{bmatrix} \mathbf{F}^i - \mathbf{F}^v \\ \mathbf{G}^i - \mathbf{G}^v \\ \mathbf{H}^i - \mathbf{H}^v \end{bmatrix} \tag{2.5}$$

Further details of the flux vector in Eqn. (2.5) can be found in *Appendix A*.

The molecular viscosity is calculated using Sutherland's law in non-dimensional form,

$$\frac{\mu}{\mu_\infty} = \left(\frac{T}{T_\infty}\right)^{\frac{3}{2}} \frac{\frac{110.4}{T_\infty} + 1}{\frac{110.4}{T_\infty} + \frac{T}{T_\infty}}$$

where $T$ is the static temperature and the turbulence viscosity $\mu_t$, will be determined by the turbulence models employed as will be presented in the later section.

The heat flux vector $q$ as seen in the flux matrices (Eqn. (A.1)) is given by

$$q_i = -\kappa \frac{\partial T}{\partial x_i}$$

where $\kappa$ is the coefficient of thermal conductivity.

As for the source term vectors $\mathbf{S}$ in Eqn. (2.1), when the flow is inviscid or laminar, or zero equation turbulence models/algebraic turbulence models like the Baldwin-Lomax and the curvature based turbulence models are employed, this term is simply *0*. Otherwise, if a two-equation model such as the k-$\omega$ model is employed, the source term is given by

$$\mathbf{S} = \begin{pmatrix} 0 & 0 & 0 & 0 & 0 & S_k & S_\omega \end{pmatrix}^t \tag{2.6}$$

In order to close this mathematical system and to enable the solution of Eqn. (2.1) for the components of vector $\mathbf{Q}$, another equation is needed, which is the equation of state of a perfect gas, $p = \rho RT$.

## 2.2 Primitive Variables & Non-dimensionalisation

In MERLIN, the code is actually solving for the vector of primitive variables **P**, which is defined as

$$\mathbf{P} = \begin{pmatrix} \rho & u & v & w & p \end{pmatrix}^t$$

instead of the vector of conservative variables **Q** in Eqn. (A.1). The reasons behind this choice is that it will enhance the robustness of the solver. The transformation between these two sets of variables is achieved via a straightforward matrix multiplication.

All of the mean flow variables, including the turbulence variables are non-dimensionalised. In the current version of MERLIN used in this project, the variables are non-dimensionalised by the freestream conditions as shown below:

$$\begin{aligned} \rho^* &= \frac{\rho}{\rho_\infty} \quad , \quad u^* = \frac{u}{V_\infty} \quad , \\ v^* &= \frac{v}{V_\infty} \quad , \quad w^* = \frac{w}{V_\infty} \quad , \\ p^* = \frac{p}{p_\infty (V_\infty)} &= \frac{p}{p_\infty \gamma M_\infty^2} \quad , \quad \mu^* = \frac{\mu}{\mu_\infty} \quad , \\ T^* &= \frac{T}{T_\infty} \quad , \end{aligned}$$

where $V_\infty = \sqrt{u_\infty^2 + v_\infty^2 + w_\infty^2}$ and the turbulence variables:

$$k^* = \frac{k}{V_\infty^2} \quad \text{and} \quad \omega^* = \frac{\omega l}{V_\infty}$$

where $l$ is the turbulence length scale.

The non-dimensionalised variables will have a similar order magnitude, which increases the accuracy of the calculations because it avoids the computations of numbers of drastically different order of magnitude. The superscript asterisk (*) that denotes non-dimensional variables will be dropped in the following sections for convenience.

## 2.3 Domain Spatial Discretisation

Basically, it is difficult to obtain an analytical solution for the full 3D Navier-Stokes equations (Eqn. (2.1)). Hence, in order to solve this set of equations numerically and efficiently, they are spatially discretised using a finite volume formulation.

### 2.3.1 Finite Volume Formulation

The whole domain is sub-divided into a large finite number of small volumes/cells, and the Navier-Stokes Eqn. (2.1) are applied locally to each of these volumes. In this project, the computational mesh is generated using a commercial meshing package called GRIDGEN [61]. Since the Navier-Stokes equations are satisfied locally at the level of each cell, it would also be valid for the entire domain if the equations were to be applied directly to this domain. Consequently, Eqn. (2.1) is sub-divided into $i$ number of cells and can be simplified as

$$V_i \frac{\partial \mathbf{Q}_i}{\partial t} = -(\mathbf{R}_i + \mathbf{S}_i V_i) \tag{2.7}$$

where $V$ is the cell volume size, $\mathbf{Q}_i$ and $\mathbf{S}_i$ are the cell-averaged state variables for cell $i$ and the residual vector $\mathbf{R}_i$ is the sum of all the fluxes passing through the six cell faces of the cell, as written below

$$\mathbf{R}_i = \sum_{faces} \mathbf{F}(\mathbf{Q}_i) \cdot \mathbf{n} S \tag{2.8}$$

with $n$ as the vector normal to the face pointing outwards and $S$ is the area of the corresponding face.

It is also necessary to point out that the cell-averaged values of the primitive variables are stored at the centre of the cell. Figure 2.1 illustrates a cell (a six-faces hexahedron) with all the eight corresponding grid points, which is defined by GRIDGEN and the metric/normal vectors on the cell faces, where $\xi$, $\eta$ and $\zeta$ represent the $i$, $j$ and $k$ directions respectively.

The right hand side vector $\mathbf{R}$ from Eqn. (2.7), is needed in both the explicit and implicit algorithms that will be described in latter sections. Hence, the next

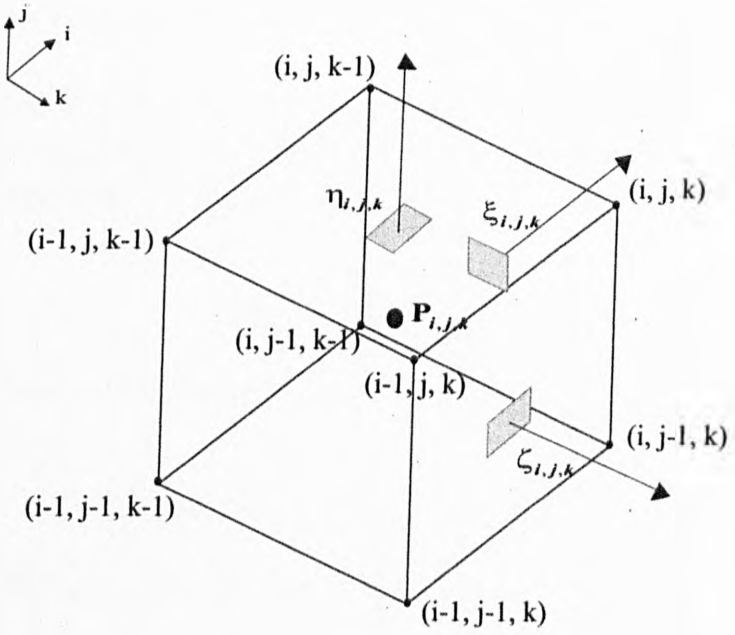


Figure 2.1: A typical computational cell.

subsection details the calculations of the flux terms $\mathbf{F}(\mathbf{Q}_i)$, for the right hand side vector $\mathbf{R}$ in Eqn. (2.8).

### 2.3.2 Convective Flux

Osher's approximate Riemann solver is implemented in MERLIN in order to capture flow discontinuities such as shock waves efficiently, thus, it is particularly useful for most of the aerodynamic cases in this work, which deal with high speed compressible flow with shock waves.

#### 2.3.2.1 Osher's Approximate Riemann Solver

In the approximate Riemann solver, the flux terms at a cell interface are evaluated by incorporating local information on the flow characteristics at this interface. This is achieved by solving an approximate one-dimensional Riemann problem or more trivially known as the shock-tube problem at this interface [62]. The cell interface represents the membrane of the problem with two different flow conditions $\mathbf{Q}_L$ and $\mathbf{Q}_R$ on each side of the membrane. Depending on the state of the flow on each side of the interface, different expressions are provided to calculate

the flux. As a result, any flow discontinuity can be captured with this method.

In contrast to the Godunov method [63, 64] for the exact solution of the Riemann problem, this Riemann solver employs the Osher's flux difference splitting method [53] and assumes that the flux can be split as

$$\mathbf{F}(\mathbf{Q}) = \mathbf{F}^{+}(\mathbf{Q}) + \mathbf{F}^{-}(\mathbf{Q}) \tag{2.9}$$

The original Riemann solver can then be written in the form of

$$\mathbf{F}(\mathbf{Q}_L, \mathbf{Q}_R) = \mathbf{F}^{+}(\mathbf{Q}_L) + \mathbf{F}^{-}(\mathbf{Q}_R) \tag{2.10}$$

Therefore, Eqn. (2.10) can also be re-written as

$$\mathbf{F}(\mathbf{Q}_L, \mathbf{Q}_R) = \frac{1}{2}\left[\mathbf{F}(\mathbf{Q}_L) + \mathbf{F}(\mathbf{Q}_R) - \int_{\mathbf{Q}_L}^{\mathbf{Q}_R} |\mathbf{A}(\mathbf{Q})| d\mathbf{Q}\right] \tag{2.11}$$

where

$$\mathbf{A}(\mathbf{Q}) = \frac{\partial \mathbf{F}(\mathbf{Q})}{\partial \mathbf{Q}} = \mathbf{B}(\mathbf{Q}) \cdot \mathrm{diag}[\lambda_1(\mathbf{Q}), \lambda_2(\mathbf{Q}), \lambda_3(\mathbf{Q})] \cdot \mathbf{B}^{-1}(\mathbf{Q})$$

so,

$$|\mathbf{A}(\mathbf{Q})| = \mathbf{B}(\mathbf{Q}) \cdot \mathrm{diag}[|\lambda_1(\mathbf{Q})|, |\lambda_2(\mathbf{Q})|, |\lambda_3(\mathbf{Q})|] \cdot \mathbf{B}^{-1}(\mathbf{Q}) \tag{2.12}$$

As a result, the Riemann solver is independent of the flux splitting and the flux Jacobian $\mathbf{A}(\mathbf{Q})$ has to be integrated in the state space.

The integrals depend on the particular chosen integration path of $\mathbf{A}(\mathbf{Q})$. Consequently, the Riemann solver is regarded as approximate. This chosen integration path is laid upon where it is tangential to the eigenvectors $\mathbf{B}(\mathbf{Q})$ of $\mathbf{A}(\mathbf{Q})$.

Figure 2.2 illustrates the integration path for a P-variant scheme for the one-dimensional approximation made at the cell interface as described above. The path connects the left and right states $\mathbf{Q}_L$ and $\mathbf{Q}_R$ via three sub-paths $\Gamma_k$, k=1,2,3. The points where the waves $\lambda_1$, $\lambda_3$ intersect with the path defines the sonic points

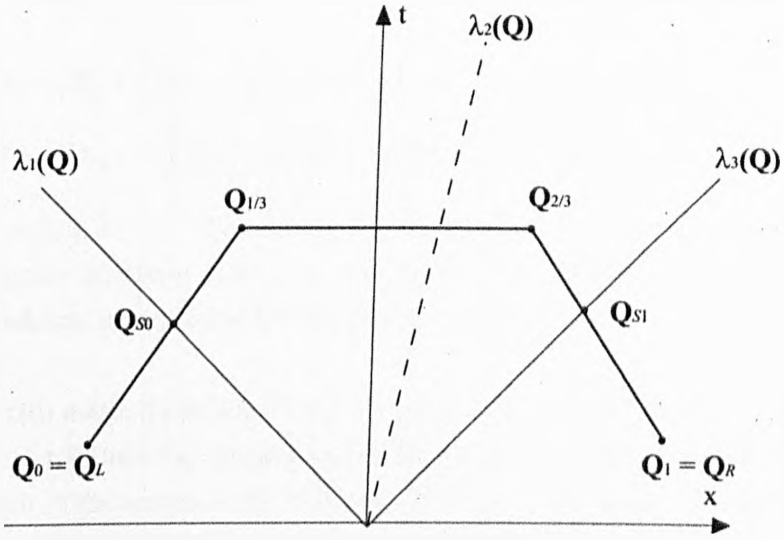


Figure 2.2: Integration path for Osher's approximate Riemann solver (P-variant).

$\mathbf{Q}_{S0}$ and $\mathbf{Q}_{S1}$ while $\mathbf{Q}_{\frac{1}{3}}$ and $\mathbf{Q}_{\frac{2}{3}}$ are the intersection points between the three sub-paths. Along each sub-path $\Gamma_k$, the corresponding Riemann invariants are constants. Thus, the intermediate states $\mathbf{Q}_{\frac{1}{3}}$ and $\mathbf{Q}_{\frac{2}{3}}$ can be evaluated from the initial and final conditions, $\mathbf{Q}_L$ and $\mathbf{Q}_R$ respectively. Therefore, calculating the integrals along the sub-paths is possible and the end results of Eqn. (2.11) are presented in *Appendix B*.

#### 2.3.2.2 MUSCL Scheme

The numerical accuracy for the approximate Riemann solver described in the previous section is just $1^{st}$ order, leading to poor accuracy in smooth regions of the flow. Hence, the MUSCL scheme is utilised as proposed in Refs. [65, 54], in order to obtain higher-order spatial accuracy. Consider the interface between cells $i$ and $i+1$, the numerical scheme performs a linear extrapolation of the flow properties in the two cells adjacent to the interface (cells $i$ and $i+1$) and an additional third cell from each side of the interface (cell $i-1$ or $i+2$), for each respective left and right state. Thus, the generic form of the equation is written as

$$\mathbf{P}_L = \mathbf{P}_i + \frac{1}{4}[(1-\kappa)(\mathbf{P}_i - \mathbf{P}_{i-1}) + (1+\kappa)(\mathbf{P}_{i+1} - \mathbf{P}_i)] \tag{2.13}$$

$$\mathbf{P}_R = \mathbf{P}_{i+1} - \frac{1}{4}[(1-\kappa)(\mathbf{P}_{i+1} - \mathbf{P}_i) + (1+\kappa)(\mathbf{P}_{i+2} - \mathbf{P}_{i+1})] \tag{2.14}$$

for cell $i = 1, 2, 3 \cdots n$. The value of the parameter $\kappa$ is chosen as $\frac{1}{3}$ for a third order accuracy in space. Also note that, as shown in Eqn. (2.13) and (2.14), the MUSCL scheme interpolates for the primitive variables.

Although this method can provide improved accuracy in the smooth regions of the flow field, it will however generate oscillations around discontinuities and could even prevent convergence of the solution. Therefore, the solution to this problem is to retain third order accuracy in the smooth flow field regions whilst switching to the first order scheme in the vicinity of discontinuities. This is achieved by introducing a slope limiter, defined as

$$s_i = \frac{2(\mathbf{P}_{i+1} - \mathbf{P}_i)(\mathbf{P}_i - \mathbf{P}_{i-1}) + \varepsilon}{(\mathbf{P}_{i+1} - \mathbf{P}_i)^2 + (\mathbf{P}_i - \mathbf{P}_{i-1})^2 + \varepsilon} \tag{2.15}$$

where $\varepsilon$ is a small value to prevent the denominator from becoming zero in the smooth flow regions.

Thus, by introducing the limiter above (Eqn. (2.15)) into the MUSCL scheme, Eqn. (2.13) and 2.14 are then re-written as

$$\mathbf{P}_L = \mathbf{P}_i + \frac{1}{4}[(1-s_i\kappa)(\mathbf{P}_i - \mathbf{P}_{i-1}) + (1+s_i\kappa)(\mathbf{P}_{i+1} - \mathbf{P}_i)] \tag{2.16}$$

$$\mathbf{P}_R = \mathbf{P}_{i+1} - \frac{1}{4}[(1-s_i\kappa)(\mathbf{P}_{i+1} - \mathbf{P}_i) + (1+s_i\kappa)(\mathbf{P}_{i+2} - \mathbf{P}_{i+1})] \tag{2.17}$$

In the smooth flow regions, $s_i$ is close to 1 and the scheme remains in third order accuracy. While in the presence of discontinuities where flow gradient is large, $s_i$ is close to 0 and it reverts back to first order scheme.

### 2.3.3 Diffusive Flux

The diffusive flux terms are evaluated directly from $\mathbf{F}^v$, $\mathbf{G}^v$ and $\mathbf{H}^v$ (Eqn. (A.1)) using central discretisation at the centre of the acquired cell face. In order to calculate the stress tensor $\tau$, the velocity and temperature gradients have to be

calculated at this cell face centre. To achieve that, an auxiliary cell is formed at this cell face between the two adjacent cells. Figure 2.3 illustrates the auxiliary cell, which is bounded in dashed lines and the shaded area is the cell face where the fluxes are to be evaluated. With this approach, the gradients are then calculated using Gauss' theorem. So, for the velocity component $u$ in the $x$ direction, from Gauss' theorem,

$$\int_{\Omega} \nabla \cdot u d\Omega = \oint_{S} u \cdot \mathbf{n} dS$$

which, once discretised on the auxiliary cell, becomes

$$\nabla \cdot u = \frac{1}{V} \sum_{l=1}^{6} u_l \cdot \mathbf{n}_l S_l \tag{2.18}$$

where $V$ is the volume of this domain or the averaged value of the volumes of these two cells, $u_l$ is the averaged value of $u$ at the centre nodes of the six faces, illustrated by diagonal crosses in Figure 2.3, $n_l$ is the normal pointing outwards on these faces and $S_l$ is the area of the corresponding faces. The multiplication of $n_l S_l$ is also the corresponding metric vectors $\boldsymbol{\xi}_l$, $\boldsymbol{\eta}_l$ or $\boldsymbol{\zeta}_l$.

The averaged value $u_l$ is evaluated using the known quantities from the four neighbouring cell centres. Take the evaluation of $u_{j1}$ for example,

$$u_{j1} = \frac{1}{4}(u_{i,j,k} + u_{i+1,j,k} + u_{i,j+1,k} + u_{i+1,j+1,k})$$

As for the metric vectors, at this auxiliary cell face at $j1$,

$$\boldsymbol{\eta}_{j1} = \frac{1}{2}(\boldsymbol{\eta}_{i,j,k} + \boldsymbol{\eta}_{i+1,j,k})$$

Finally, with all the needed values calculated at the six auxiliary cell faces, a gradient, for example, $\frac{\partial u}{\partial x}$, expanded from Eqn. (2.18), is given by

$$\left.\frac{\partial u}{\partial x}\right|_o = \frac{1}{V}\left[u_{i2}\boldsymbol{\xi}_{x\,i2} - u_{i1}\boldsymbol{\xi}_{x\,i1} + u_{j2}\boldsymbol{\eta}_{x\,j2} - u_{j1}\boldsymbol{\eta}_{x\,j1} + u_{k2}\boldsymbol{\zeta}_{x\,k2} - u_{k1}\boldsymbol{\zeta}_{x\,k1}\right]$$

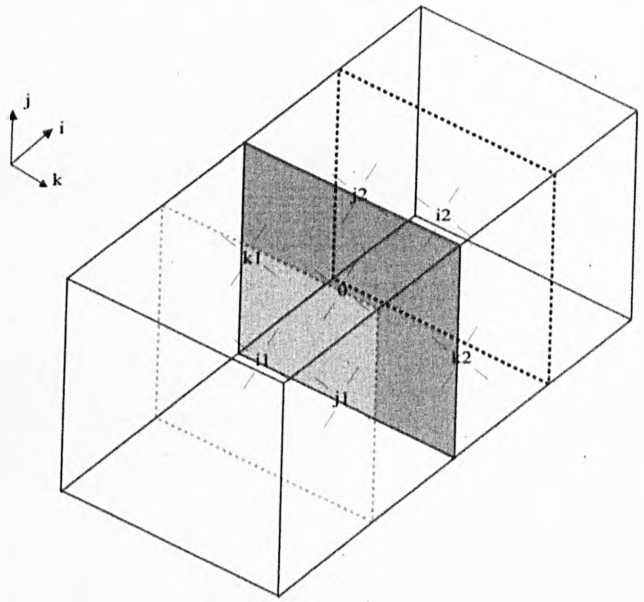


Figure 2.3: The dual volumes for viscous flux calculations.

This is done for the rest of the velocity and temperature gradients. The calculations of the diffusive flux terms in $\mathbf{F}^v$, $\mathbf{G}^v$ & $\mathbf{H}^v$ are then straightforward.

Up to this point, the domain spatial discretisation and the calculations of both convective and diffusive flux terms for the right hand side vector $\mathbf{R}$, have been presented. In order to march the solution in time, Eqn. (2.7) has to be discretised in time as well.

## 2.4 Time Discretisation

In this work, only the steady state of the solution is considered. However, it is common practise in CFD to march the solution in pseudo-time step to the acquired steady state. In MERLIN, a choice of an explicit or implicit method is available.

### 2.4.1 Explicit Update

The spatial discretised Navier-Stokes equation (Eqn. (2.7)) can be re-written as a system of ordinary differential equations that are continuous in time,

$$V\frac{\partial \mathbf{Q}}{\partial t} = -\mathbf{R}(\mathbf{Q}) \tag{2.19}$$

Note that the source term vector $\mathbf{S}$, is not included here. Recall from Eqn. (2.6),

$$\mathbf{S} = \begin{pmatrix} 0 & 0 & 0 & 0 & 0 & S_k & S_\omega \end{pmatrix}^t$$

the first five values in the vector, which corresponds to the five conservative variables that define the essential fluid flow state, are nil. Besides that, the convergence criteria for the steady state requires that

$$\mathbf{R}(\mathbf{Q}) = 0$$

and this criteria does not take the flux terms contribution from the turbulence variables into account.

The temporal discretisation of Eqn. (2.19) can be written as

$$\frac{\mathbf{Q}^{n+1} - \mathbf{Q}^n}{\Delta t} = -\mathbf{R}(\mathbf{Q}^n) \tag{2.20}$$

where the cell volume is incorporated in the time step $\Delta t$. As a result, by re-arranging Eqn. (2.20), the update of the conservative variables at the next time step is simply

$$\mathbf{Q}^{n+1} = \mathbf{Q}^n - \Delta t \mathbf{R}(\mathbf{Q}^n) \tag{2.21}$$

A local time-stepping method is employed to evaluate the value of $\Delta t$. Therefore, its value is not uniform across the domain at the instantaneous global time iteration and is dependant on its volume size and local flow properties. This local time-stepping method can, substantially speed up the convergence rate. Also note that, nevertheless, the turbulence variables ($k$ and $\omega$) are updated using the same Eqn. (2.21), only that the additional source terms $S_k$ and $S_\omega$, are added in the RHS of the equation.

Although this explicit updating method is quite simple, it is only subjected to a small time step $\Delta t$ due to numerical stability restrictions. So, a stability condition where the $CFL$ number is to be less than unity is required in the local time step calculation. However, the speed of the convergence using explicit updates is still considered slow though stable, especially when complex 3D problems are to be dealt with. Hence, a more efficient implicit method is implemented.

### 2.4.2 Implicit Update

In contrast to the explicit method, the implicit method evaluates the residual vector at a future time level, so re-writing Eqn. (2.20),

$$\frac{\mathbf{Q}^{n+1} - \mathbf{Q}^{n}}{\Delta t} = -\mathbf{R}(\mathbf{Q}^{n+1}) \tag{2.22}$$

The RHS residual vector is then expanded using Taylor's expansion,

$$\mathbf{R}(\mathbf{Q}^{n+1}) = \mathbf{R}(\mathbf{Q}^{n}) + \frac{\partial \mathbf{R}(\mathbf{Q}^{n})}{\partial \mathbf{Q}}(\mathbf{Q}^{n+1} - \mathbf{Q}^{n}) + \text{higher order terms} \tag{2.23}$$

By truncating the higher order terms and substituting Eqn. (2.23) into Eqn. (2.22) and defining ${}^{n}\Delta\mathbf{Q} = \mathbf{Q}^{n+1} - \mathbf{Q}^{n}$,

$$\left[\frac{\mathbf{I}}{\Delta t} + \frac{\partial \mathbf{R}(\mathbf{Q}^{n})}{\partial \mathbf{Q}}\right]({}^{n}\Delta\mathbf{Q}) = -\mathbf{R}(\mathbf{Q}^{n}) \tag{2.24}$$

or in primitive variables form,

$$\left[\frac{1}{\Delta t}\frac{\partial \mathbf{Q}}{\partial \mathbf{P}} + \frac{\partial \mathbf{R}(\mathbf{Q}^{n})}{\partial \mathbf{P}}\right]({}^{n}\Delta\mathbf{P}) = -\mathbf{R}(\mathbf{Q}^{n}) \tag{2.25}$$

The linearised system of Eqn. (2.25) is now solving for ${}^{n}\Delta\mathbf{P}$ and the Jacobian $\dfrac{\partial \mathbf{R}}{\partial \mathbf{P}}$ needs to be constructed. Instead of the constructing the exact Jacobian, the Jacobian is actually approximate and Eqn. (2.25) is again re-written as

$$\left[\frac{1}{\Delta t}\frac{\partial \mathbf{Q}}{\partial \mathbf{P}} + \frac{\partial \bar{\mathbf{R}}(\mathbf{Q}^{n})}{\partial \mathbf{P}}\right]({}^{n}\Delta\mathbf{P}) = -\mathbf{R}(\mathbf{Q}^{n}) \tag{2.26}$$

where the symbol ($\tilde{}$) is added to the LHS Jacobian, which denotes the approximation.

With the matrix constructed, the large linear system can also be expressed as the following

$$\mathbf{A}\mathbf{x} = \mathbf{b} \tag{2.27}$$

By using an approximate direct inversion method, the Block Incomplete Lower-Upper decomposition with no fill-in or BILU(0), the block diagonal LHS matrix $\mathbf{A}$ is then approximated as

$$\mathbf{A} \approx \mathbf{L}\mathbf{U}$$

where $\mathbf{L}$ is a lower triangular matrix and the $\mathbf{U}$ is an upper triangular matrix. Hence, the original system (Eqn. (2.27)) can then be inverted as below

$$\mathbf{x} = \mathbf{U}^{-1}\mathbf{L}^{-1}\mathbf{b}$$

Finally, with the solutions of ${}^{n}\Delta\mathbf{P}$ obtained, the update of the primitive variables is just straightforward, where

$$\mathbf{P}^{n+1} = \mathbf{P}^{n} + {}^{n}\Delta\mathbf{P}$$

The main numerical schemes employed in MERLIN solving for the main flow properties have now been presented. The following subsection will then present the boundary condition treatments implemented in the code.

## 2.5 Boundary Conditions

The physical boundary conditions are actually the main driver on the way the solutions evolve. In order to properly simulate the physical boundaries required at each different case, i.e. wall, appropriate numerical treatments have to be implemented at the boundaries. In the current version of MERLIN, ten types of boundary conditions have been employed, including a periodical and a subsonic

outflow boundary condition added by the author.

Before introducing these various boundary conditions, it is necessary to point out that two auxiliary cells or the so-called halo cells are actually added at the boundaries, so that the calculations of the flux terms at these boundaries are practically the same as the ones inside the domain. A schematic diagram of these halo cells at the start of the boundary is depicted in Figure 2.4. The geometry information of these fictitious halo cells are either extrapolated from inside the domain linearly or through mirroring. The numerical treatments are then applied to these halo cells. The various boundary conditions are detailed in *Appendix C*.

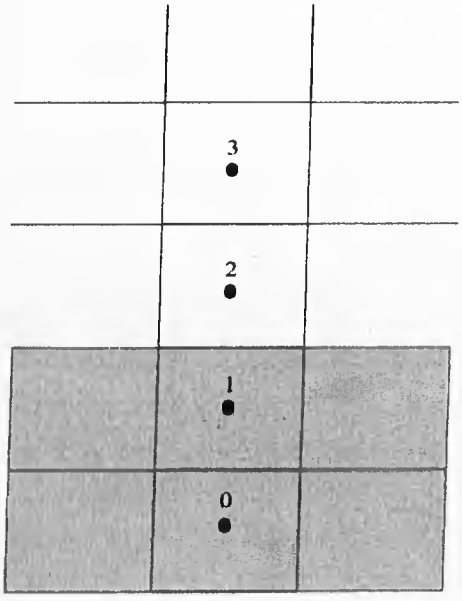


Figure 2.4: Schematic diagram of halo-cells.

## 2.6 Turbulence Models

As presented in Eqn. (A.3), which is for the calculation of the stress tensor, besides the molecular viscosity $\mu$, the turbulence viscosity $\mu_t$ needs to be evaluated as well by using the turbulence models available in the code. To start with, the Baldwin-Lomax algebraic turbulence model will be presented in the following subsection.

### 2.6.1 Baldwin-Lomax Algebraic Turbulence Model

This turbulence model is the most widely used in this project, mainly due to the fact that it takes less time to compute than the two-equation model and that it is currently the only turbulence model implemented in the adjoint solver. This model is based on the turbulence mixing-length hypothesis proposed by Prandtl and is significantly modified from the Cebeci-Smith model [55, 56]. It also has the advantage of modelling the turbulent boundary layer without having to search for the boundary layer edge to determine a length scale for the model. Just like the Cebeci-Smith model, it is a two-layer model, where the turbulence viscosity is divided into an inner and outer layer as given by:

$$\mu_t = \begin{cases} (\mu_t)_{inner}, & y_n \leq y_{n,\,crossover}; \\ (\mu_t)_{outer}, & y_n > y_{n,\,crossover}. \end{cases} \tag{2.28}$$

where $y_n$ is the normal distance from the wall measured at the cell centre and $y_{n,\,crossover}$ is the point which the calculated inner and outer $\mu_t$ are equal.

In the inner layer, the mixing-length hypothesis is applied, hence the turbulence viscosity is defined as

$$(\mu_t)_{inner} = \rho l_{mix}^2 |\omega| \tag{2.29}$$

and by using the van Driest damping function, the mixing length $l_{mix}$ is given by

$$l_{mix} = \kappa y_n \left[1 - e^{-y^+/A^+}\right] \tag{2.30}$$

where $\kappa$ & $A^+$ are the von Karmann constant and van Driest constant respectively. While $y^+$ is the non-dimensional normal wall distance,

$$y^+ = \frac{\rho_w u_\tau y_n}{\mu_w} = y_n \frac{\sqrt{\rho_w \tau_w}}{\mu_w}$$

with $u_\tau$ as the friction velocity and $\tau$ as the shear stress at the wall. The subscript $w$ above denotes the values evaluated at the wall. Finally, the vorticity magnitude $|\omega|$ in Eqn. (2.29), is evaluated as below for a three-dimensional flow

$$|\omega| = \sqrt{\left(\frac{\partial u}{\partial y} - \frac{\partial v}{\partial x}\right)^2 + \left(\frac{\partial v}{\partial z} - \frac{\partial w}{\partial y}\right)^2 + \left(\frac{\partial w}{\partial x} - \frac{\partial u}{\partial z}\right)^2}$$

The turbulence viscosity in the outer layer is given by

$$(\mu_t)_{outer} = \rho \alpha C_{cp} F_{wake} F_{Kleb}(y_n) \tag{2.31}$$

where $\alpha$ is the Clauser constant, $C_{cp}$ is an additional closure coefficient, and the wake function

$$F_{wake} = \min\left(y_{max} F_{max}, \frac{C_{wake} y_{wake} U_{diff}^2}{F_{max}}\right) \tag{2.32}$$

Here, $U_{diff}$ is the maximum difference of the velocity magnitude across the boundary layer

$$U_{diff} = \max\left(\sqrt{u^2 + v^2 + w^2}\right) - \min\left(\sqrt{u^2 + v^2 + w^2}\right)$$

and the value of $F_{max}$ is given by the maximum of the function

$$F(y_n) = y_n |\omega| \left(1 - e^{-y^+/A^+}\right) \tag{2.33}$$

Thus, $y_{max}$ refers to the value of $y_n$ where $F_{max}$ is found. The Klebanoff function from Eqn. (2.31) is defined as

$$F_{Kleb}(y_n) = \left[1 + 5.5\left(\frac{C_{Kleb} y_n}{y_{max}}\right)^6\right]^{-1} \tag{2.34}$$

The closure coefficients that have been presented above are summarised as follows:

$$\begin{array}{lll} \kappa = 0.41 & A^+ = 26 & \alpha = 0.0168 \\ C_{cp} = 1.6 & C_{Kleb} = 0.3 & C_{wake} = 0.25 \end{array}$$

Although the Baldwin-Lomax model is easy to implement and efficient, it is more suitable for steady flows with little or no separation since it performs relatively poor when there is large separation, i.e. vortical separation, in the flow. Consequently, the curvature-based turbulence model was proposed to improve the ability of the algebraic model in capturing vortical flow structure.

### 2.6.2 Curvature-Based Algebraic Turbulence Model

Degani and Schiff have proposed some modification on the Baldwin-Lomax algebraic turbulence model that has significantly improved the turbulent vortical flow simulation for many vortical flow test cases [66]. The modification is based on the observation that under the separated vortical flow, there remains an attached boundary layer, which the Baldwin-Lomax model works well on. Therefore, it is important to select the appropriate length scale for these attached boundary layers.

In the Degani-Schiff model, the criterion is that the first peak of the moment of vorticity distribution away from the wall should be used to represent the underlying attached boundary layer. However, weaknesses of the model is realised within the vicinity of the crossflow separation where the peak representing the attached boundary layer and the vortical sheet are very close to each other. Besides that, the accuracy of the model decreases as the region with a frozen length increases [67].

Another study by Panaras and Steger suggested that the Degani-Schiff model might have picked up the wrong peak in the $F(y_n)$ profile, hence they proposed an empirical way called the Kcut method to separate the outside vortical flow from the attached boundary layer [68]. By doing so, an absolute maximum can be found between the wall and the Kcut position. As a result, both the vortex and the possible sublayer peaks can be avoided in the search. However, again, the possible setback of this approach is the difficulty in determining the corresponding Kcut position in advance for different streamwise stations or different flow conditions.

Consequently, based on the same basic concept as that of the Degani-Schiff model and with the findings from the Kcut method, Qin and Jayatunga [57] suggested that a more well-established and accurate criterion needs to be defined to search for the appropriate length scale using the $F(y_n)$ profile. Instead of using the peaks in the $F(y_n)$ curve, it is then proposed to use the curvature of the $F(y_n)$ curve, which is defined as

$$\kappa_{curve} = \frac{F''(y_n)}{[1 + (F'(y_n)^2]^{3/2}} \tag{2.35}$$

where the derivatives are evaluated using central differencing. By assuming that regardless of the number of possible peaks that could exist in the $F(y_n)$ profile, the second convex region in the profile or the second minimum dip in the curvature function profile will represent the appropriate length scale for the attached boundary layer. Thus, the idea is then to search for the second negative region in the $\kappa_{curve}$ profile, which will refer to the second convex region in the $F(y_n)$ profile and hence where $y_{max}$ and $F_{max}$ are to be defined.

So, it is practically easy to implement this concept into the code, because most of the existing numerical routines in the Baldwin-Lomax model do not need to be modified. Only minor parts of the code need to be added, which is where the values of $y_{max}$ and $F_{max}$ are determined by the above curvature-based criterion instead of the original Baldwin-Lomax approach that will always lead to a global maximum in $F(y_n)$.

The numerical noise in the straight part of $F(y_n)$ could cause misjudgement of the second minimum dip during the numerical search as $\kappa_{curve}$ could oscillates in a very small band around the 0-axis. This problem is tackled by introducing a noise band,

$$|\kappa_{curve}| \leq \varepsilon_{noise} \tag{2.36}$$

where $\varepsilon_{noise}$ is a small number but greater than the numerical noise associated with the curvature. This noise band value is case dependent though but with some trial and error, the reasonable value for $\varepsilon_{noise}$ was found in this work to be 0.75.

### 2.6.3 The k-$\omega$ Turbulence Model

The k-$\omega$ model is developed by Wilcox [56], it is wall distance free and should be able to accurately predict flows with various characteristics including adverse pressure gradient and free shear layers. This model is also advantageous over other high Reynolds number k-$\epsilon$ models since it can be integrated through the

viscous sublayer without having to use some damping functions.

Referring back to Eqn. (2.6), the source terms in the vector are given here by

$$\begin{bmatrix} S_k \\ S_\omega \end{bmatrix} = \begin{bmatrix} C_{k1}\tau_{ij}\frac{\partial u_i}{\partial x_j} - C_{k2}\rho\omega k \\ C_{\omega 1}\frac{\omega}{k}\tau_{ij}\frac{\partial u_i}{\partial x_j} - C_{\omega 2}\rho\omega^2 \end{bmatrix} \tag{2.37}$$

Hence, the governing equations for the two conserved turbulence variables can be written as:

$$\rho\frac{\partial k}{\partial t} + \rho u_j\frac{\partial k}{\partial x_j} = S_k + \frac{\partial}{\partial x_j}\left[(\mu + \frac{\mu_t}{\sigma_k})\frac{\partial k}{\partial x_j}\right] \tag{2.38}$$

$$\rho\frac{\partial \omega}{\partial t} + \rho u_j\frac{\partial \omega}{\partial x_j} = S_\omega + \frac{\partial}{\partial x_j}\left[(\mu + \frac{\mu_t}{\sigma_\omega})\frac{\partial \omega}{\partial x_j}\right] \tag{2.39}$$

where the constants are given by

$$\begin{array}{lll} C_{k1} = 1.0 & C_{k2} = 0.09 & \sigma_k = 2.0 \\ C_{\omega 1} = 0.555 & C_{\omega 2} = 0.075 & \sigma_\omega = 2.0 \end{array}$$

Finally, the turbulence viscosity is calculated with the following relationship

$$\mu_t = \frac{\rho k}{\omega} \tag{2.40}$$

## 2.7 Far-field Drag Analysis

The most straightforward approach to computations of drag from CFD solutions are by surface integration of pressure and shear stresses, which is also known as the near-field method. In contrast, far-field methods, often used in experiments, provide breakdown of the drag into other useful components, such as viscous drag (also known as profile drag or the sum of form and skin friction drag), wave drag (associated with shock waves) and lift-induced or vortex drag.

Giles & Cummings [69] and Hunt *et al.* [70] introduced a far-field method that uses a Trefftz-plane situated downstream of the wing to integrate the drag components. Therefore, this method requires the extraction of a downstream cutting plane orthogonal to the direction of the flow using flow visualisation techniques.

Instead another method developed by Paparone & Tognaccini [71], which is based on a Taylor expansion of the far-field drag expression has been chosen. This method does not require the computation of intersections of the flowfield with given planes, thus it is easier to implement. Its ability to identify local shock wave and viscous regions for the computation of the two drag components reduces the contribution of numerical errors to the physical drag.

As a result, it is possible to evaluate the wave drag accurately even on a coarse grid using this method. The only drawback of this method is that it does not incorporate the evaluation of vortex drag. Nevertheless, at the moment, we are mainly concern of extracting wave drag in this study and combining it with surface drag integration method for this further drag analysis. The following part introduces some details of the method.

### 2.7.1 Derivation of the Far-Field Method

Define $S_{far}$ as the external surface bounding the volume $\Omega$, if this surface is sufficiently far from the body, the viscous stresses can be neglected and the far-field expression of the drag is given by,

$$D_{far} = -\int_{S_{far}} \left[(p - p_\infty)\, n_x + \rho u\, (\boldsymbol{V} \cdot n)\right] dS \tag{2.41}$$

where $u$ is the x-component of the velocity. In three-dimensional flows, Eqn. (2.41) can be re-written as

$$D_{far} = -\int_{S_{far}} \left[\rho V_\infty^2 \frac{1}{\gamma M_\infty^2} \frac{\Delta p}{p_\infty} + V_\infty \frac{V}{V_\infty} \rho\, (\boldsymbol{V} \cdot n)\right] dS \tag{2.42}$$

For a perfect gas, it is possible to express the velocity term $\frac{V}{V_\infty}$ in terms of variations of total enthalpy $\Delta H$, entropy $\Delta s$, and static pressure $\Delta p$. By expanding this term in Taylor's series and substituting it (with third and higher order truncated) into Eqn. (2.42), to give the entropy drag with the other two terms ignored:

$$D_{far} = V_\infty \int_{S_{far}} \left[f_{s1} \frac{\Delta s}{R} + f_{s2} \left(\frac{\Delta s}{R}\right)^2\right] \rho\, (\boldsymbol{V} \cdot n)\, dS \tag{2.43}$$

Here, the coefficients $f_{s1}$ and $f_{s2}$ are defined as

$$f_{s1} = -\frac{1}{\gamma M_\infty^2} \quad , \quad f_{s2} = -\frac{1+(\gamma-1)M_\infty^2}{2\gamma^2 M_\infty^4}$$

Furthermore, with the function

$$g\left(\frac{\Delta s}{R}\right) = -f_{s1}\left(\frac{\Delta s}{R}\right) - f_{s2}\left(\frac{\Delta s}{R}\right)^2 \tag{2.44}$$

Eqn. (2.43) can be expressed in divergence form by applying the Gauss's theorem to the vector field $\rho g \boldsymbol{V}$ in the finite flow domain $\Omega$. Since on $S_{body}$, $\boldsymbol{V} \cdot n = 0$, the entropy drag expression becomes

$$D_{\Delta s} = V_\infty \int_\Omega \nabla \cdot (\rho g \boldsymbol{V}) d\Omega \tag{2.45}$$

Further analysis indicates that the integrand in Eqn. (2.45) can be defined as the local production rate of entropy drag, therefore allowing the breakdown of the domain $\Omega$ into three separate regions, the shock wave, viscous (boundary layer and wake) and spurious regions. The spurious entropy production associated with the artificial dissipation and with the discretisation error of the numerical scheme. Separating this spurious region thus cut down the level of numerical error contributed to the physical entropy drag evaluation.

### 2.7.2 Algorithm for Region Selection

A hierarchy has been employed in the selection criteria of each computational cell for the various regions. First, the shock wave region test is performed; if not satisfied, the viscous region test follows and if it is not satisfied as well, the cell is then assumed to belong to the spurious region. The shock wave region sensor is based on the following non-dimensional function:

$$F_{shock} = (\boldsymbol{V} \cdot \nabla p)/(a|\nabla p|) \tag{2.46}$$

where $a$ is the local speed of sound. This sensor is negative in the expansion zones and positive in the compression zones. Given the knowledge of the upstream Mach number of the shock wave, the Mach number downstream of the

shock wave can be estimated using Rankine-Hugoniot relations. This downstream Mach number value is adopted as the value $K_{cw}$ for the selection criterion of function $F_{shock}$. Therefore, the selection of the cells in the shock wave region is based on the satisfactory of the criterion $F_{shock} > K_{cw}$.

Next for the selection of the cells in the boundary layer and wake region, the following sensor works for turbulent flows:

$$F_{bl} = (\mu_l + \mu_t)/\mu_l \tag{2.47}$$

where $\mu_l$ and $\mu_t$ are the molecular and eddy viscosities respectively. From Eqn. (2.47), it can be perceived that the value of $F_{bl}$ is very high in the boundary layer and wake, whereas it remains around the value 1 in the remaining parts of the domain. The criterion adopted is to select cells that satisfy $F_{bl} > K_{bl} \times F_{bl}$, where $K_{bl}$ is a cutoff value. Since Paparone & Tognaccini found that the drag region breakdown is not sensitive to the cutoff value $K_{bl}$, in all present studies; a value of 1.1 has been selected [71].

### 2.7.3 Validation with NACA0012 Test Cases

In order to test the algorithm implemented, two cases at different lift conditions have been tested on the NACA0012 aerofoil as investigated in the experiments by McCroskey [72] and Paparone and Tognaccini [71]. The flow solutions are computed at freestream conditions, $M_\infty = 0.7$ and $Re_c = 9 \times 10^6$. The computational grid is a C-type grid with a very fine resolution of 640 × 256 cells, which corresponds to the highest grid resolution level as tested in Ref. [71]. The computed wave drag and viscous drag from the present study, Paparone and Tognaccini and the total drag from the experiment are compared in Table 2.1 below:

| | $C_L = 0.000$ | | | $C_L = 0.424$ | | |
|---|---|---|---|---|---|---|
| | $C_{Dw}$ | $C_{Dv}$ | $C_{Dtotal}$ | $C_{Dw}$ | $C_{Dv}$ | $C_{Dtotal}$ |
| **Present study** | 0.000 | 0.00781 | 0.00781 | 0.00169 | 0.00853 | 0.01022 |
| **Paparone *et al.*** | 0.000 | 0.00786 | 0.00786 | 0.00175 | 0.00868 | 0.01043 |
| **Experiment** | - | - | 0.00780 | - | - | 0.01030 |

Table 2.1: Comparisons of the drag components with previous studies.

At zero lift, no shock waves are formed on the aerofoil at this freestream condition, thus, no shock wave region is detected and the computed wave drag is nil. On the other hand, the predicted viscous drag by the present study agrees very well with that of Paparone's. For a two-dimensional flow, with no lift-induced drag, the total drag is then the sum of the wave drag and the viscous drag. The predictions from both studies agree particularly well with the experiment with less than 1 drag count difference.

As the lift coefficient is increased to 0.424, a reasonably strong normal shock is formed on the upper surface of the aerofoil. The selection of shock wave region is shown in Figure 2.5.

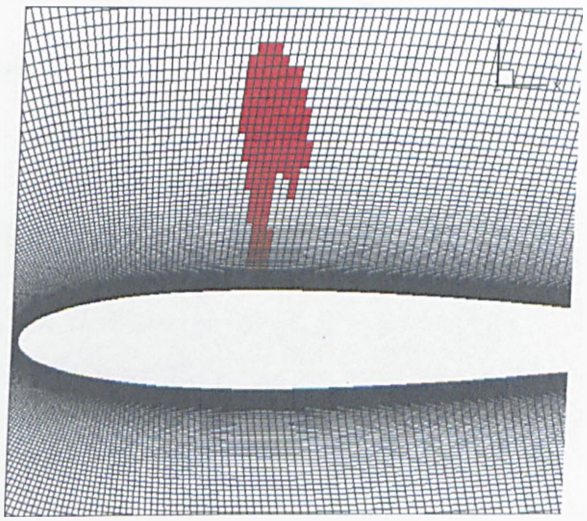

Figure 2.5: Selection of the shock wave region.

Again from Table 2.1, the computed wave and viscous drag from the present study agrees very well with that of Paparone's with less than 1 drag count difference for the wave drag and just around 1 drag count for the viscous drag. As for the total drag, the discrepancies between the experiment and the computations are still low, retaining about one drag count difference. Although both results from present study and Paparone's were computed with the same level of grid resolution, the discrepancy occurs might be due to a slightly different grid distribution strategy adopted.

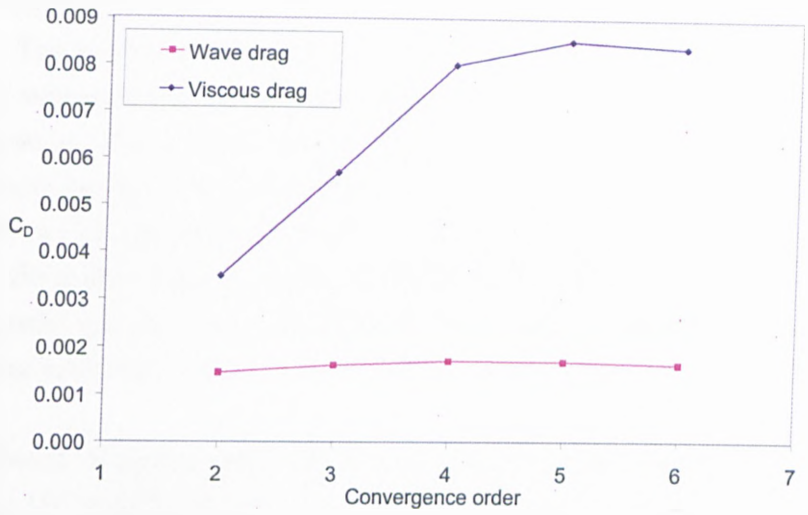


Figure 2.6: Sensitivity of the farfield drag analysis with the flow solution convergence.

Figure 2.6 plots out the sensitivity of the computed drag components with respect to the order of convergence of the flow solution. It is suggested by the plot that the wave drag is not sensitive to the level of convergence of the flow solution, which also implies that even with a bad level of convergence, the predicted wave drag is still reasonably accurate. In contrast, the computed viscous drag only starts to converge when the flow solution converges to fourth order or less. In this report, all the flow solutions are converged to at least fourth order or lower.

## 2.8 Parallel Implementation

MERLIN had already been parallelised with OpenMP [74, 50]. OpenMP is a directive based language for simplified implementations of application level parallelism [75]. It is hence easier to implement in the code. However, in order for the code to achieve good data parallel efficiency when solving very large problems on the available distributed-memory clusters, it was decided to implement Message-Passing-Interface (abbreviated as MPI) into MERLIN.

MPI allows efficient information exchange via a fast internal network between the nodes of the computing cluster. Extensive literature of implementing MPI can be found on the web [81, 82]. In this work, the *Intel*, *Portland Group* or

*IBM* compilers have been employed. The *IBM* compiler is only available on the HPCx. The parallel environment in which the MPI code runs, is the common *MPICH* environment. In addition to that, for the nodes that consist of more than one processor, the processors within the node still maintain the shared-memory architecture as that of a typical shared-memory system as discussed above. Consequently, a code can in fact be parallised with mixed MPI-OpenMP calls. In this project, the author has only implemented MPI into MERLIN. In fact, many clusters do make use of this shared-memory advantage via enhancing the efficiency of message exchange between the processors located on the same node.

The approach of implementing MPI into MERLIN is straightforward. The idea is to exploit the multiblocks structure of MERLIN, where the blocks are exchanging information using the interface boundary condition as presented in *Section 2.5.5*. Therefore, the domain is decomposed into a number of node-balanced sub-domains that correspond to the number of processors used on a computing cluster, thus each processor is assigned to a block. Each processor then only has to calculate the block that it has been assigned to. The computer routine will determine which other blocks are adjacent to each particular blocks and the information at the interface are "sent" and "received" via MPI between the blocks. Thus, only the original interface boundary condition is needed to be extensively modified with additional MPI routines, the rest of the MERLIN main routines just require some degree of modifications to work properly in the MPI parallel environment, i.e. the routine that reads in the grid information.

In order to assess the parallel efficiency of the code on HPCx, the wall-clock time taken to run on 32 processors is taken as the reference. A node on HPCx consists of 32 processors; hence it is reasonable that the scaling of the number of processors is a multiple of 32. Thus, the speed-up expression is written as

$$S_{speedup,N} = \frac{t_N}{t_{32}} \tag{2.48}$$

where the subscript $N$ is the number of processors and $t$ is the wall-clock time required to perform 100 implicit iteration for this number of processors. Note that the chosen test case has a resolution of around 2 million grid points. Figure 2.7 shows the parallel efficiency of the code with comparison to the ideal speed-up values. From the graph, by scaling the flow solver up to 128 processors, the actual

speed-up is quite close to the ideal value. Thus, from this test, it is shown that the parallel efficiency of the flow solver is reasonably good. It is obvious that, for domain decomposition based parallelisation, the efficiency depends strongly on the overall grid size. Although the current problem is very large in the sense of design variables and CPU time, the grid size of 2 million points is not large enough for high parallel efficiency beyond 256 processors. Nevertheless, this parallel version of MERLIN has been awarded a Bronze level award by the HPCx team for its scaling capability of running more than 1.7 times faster on 256 processors than on 128 processors.

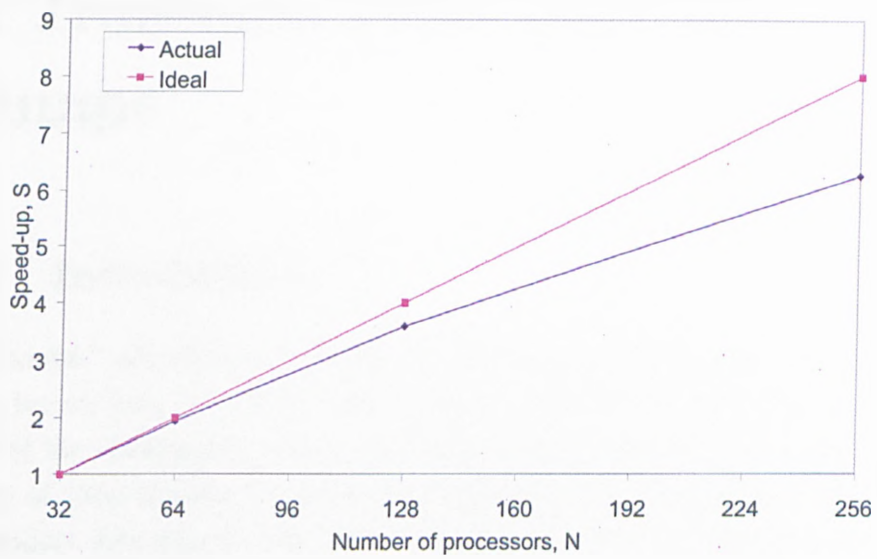


Figure 2.7: Speed-up with respect to the number of processors for the flow solver.

Finally, here ends this long chapter that provide details of the CFD code–MERLIN, which is used to compute all the numerical solutions in this work. Understanding a code that is not largely written by the author from scratch is important as it provide some level of confidence for the author to conduct any modifications. The code has been parallelised successfully with MPI. Although MERLIN has already been validated extensively with various aerodynamic test cases, e.g. the RAE 2822 aerofoil and ONERA M6 wing [83], it is still essential to validate this code on its ability to simulate the transonic flow over 3D bumps, which will be presented and discussed in the next chapter.

# Chapter 3

# Validation and Numerical Study of Transonic Flow Over 3D Bumps

## 3.1 Introduction

The mutual validation and verification between numerical simulations and the wind tunnel tests of such complex flows is essential and complementary. The aims of the investigation presented in this chapter were then to determine the ability of computations to capture the complex physics of transonic shock wave / boundary layer interactions with bump control as well as improving the understanding of such devices.

In previous investigations involving wind tunnel computational modelling [84, 85], periodical boundary conditions have been implemented in the spanwise direction. However, this assumption has been found to be inadequate for both uncontrolled (empty tunnel tests) and controlled cases in a transonic flow wind tunnel, because the lack of modelling of the blockage effect of the side wall boundary layer causes the backpressure to be greater than the experimentally observed value at a given shock-wave position. As a result, it is difficult to make a quantitative comparison between the experiment and computation. Hence, in this study, the sidewall and its associated boundary layers were taken into account for a closer match of the wind tunnel and the simulation conditions.

Since the experimental measurements did not provide all of the required boundary layer properties to completely specify the inflow conditions, a flat plate boundary layer was computed under wind tunnel conditions to be used as the initial boundary condition. The study highlights the importance of matching the simulation and experimental conditions as closely as possible in validation studies. The combined surface and flowfield data provide insight into the flow physics on the shock control bump.

## 3.2 Experimental Arrangements

The numerical results are compared with experimental data obtained in a supersonic wind tunnel at the Engineering Department of Cambridge University. The tunnel arrangement and control region are shown in Figure 3.1 where the thick-dashed lines outline the domain modelled numerically. Shaped liners on the upper and lower faces of the tunnel were used to generate supersonic flow in the working section. A manual control valve regulates the tunnel reservoir pressure, which allows a recovery shock to be held at a given streamwise location in the tunnel.

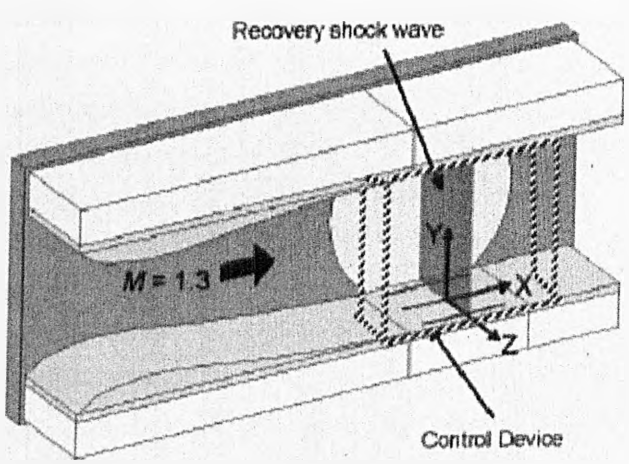


Figure 3.1: Cambridge supersonic wind tunnel.

All results presented here were obtained with the shock positioned above the centre of the control region, at x = 0 mm. The tunnel was operated at a Mach

number of 1.29, a total temperature of 300 K and a freestream Reynolds number of $28 \times 10^6$ $m^{-1}$. The control devices are fitted on the floor of the working section. Schlieren photography and surface oil-flow visualisation are used to determine the flow structure. Surface pressures were measured using surface pressure tappings connected to pressure transducers mounted just underneath the wind tunnel floor (all results presented here are time averaged mean flow values). Boundary layer velocity profiles and stagnation pressure profiles were obtained using Pitot pressure probes attached to a mechanical traverse system. However, when the traverse system is mounted downstream of the bump devices the additional blockage caused tunnel unstart. For this reason, profile data downstream of the bumps could only be recorded with only a single device in the tunnel. The lack of outer bumps was found not to affect the overall flow features around the control, but it did change the spanwise development of the flow downstream as discussed in a later section.

The shape and the geometry details of the bumps used in this study can be seen in Figure 3.2. This particular bump geometry has been selected for its relative simplicity and because it bears close resemblance to the 3D bump investigated in Refs. [46, 47]. The streamwise length of the bumps is 100 mm (centred around x = 0 mm) with a maximum height of 5.25 mm, which is lower than the thickness of the incoming boundary layer (about 7 mm). Generally, three devices were fitted side by side along the tunnel floor with a spanwise spacing between the device centrelines being 44 mm. Figure 3.3 also illustrates the coordinate system that have been employed in the experiment, which is useful as a reference to pinpoint the acquired positions in the discussion of the results later.

The largest source of experimental error is caused by the difficulties of accurately controlling the shock location. At the centre of the bump, the shock did experience some unsteadiness, which was found to be of the order of ±3mm. Surface pressure measurements were subject to an uncertainty of ±2%, while Pitot pressures traverses are subject to uncertainties of ±4% close to the surface and ±1% outside the boundary layers.

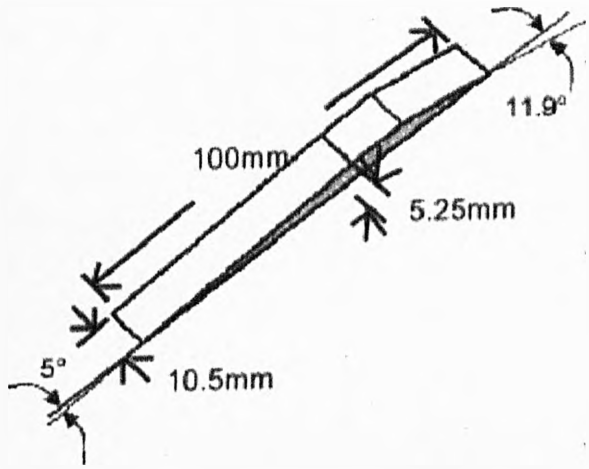


Figure 3.2: Geometries of the ramp bump

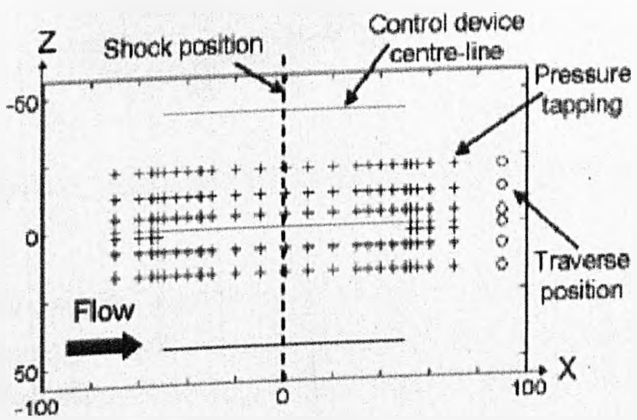


Figure 3.3: Coordinate system of the experiment.

## 3.3 Numerical Approach

For the uncontrolled case, only a quarter of the wind tunnel spanwise geometry has been modelled, where the top plane of the computational mesh is specified as a symmetry plane. This is shown in Figure 3.4, which depicts the computational mesh employed for the empty wind tunnel calculations. The mesh consists of three separate blocks with a total resolution of 69×48×48. The outflow plane of the computational domain for the uncontrolled case extends 100 mm downstream of the shock position; the most aft location where the experimental wall pressure data is available for the specification of the subsonic boundary condition. The full detailed dimensions for this mesh are illustrated in the schematic diagram of Figure 3.5.

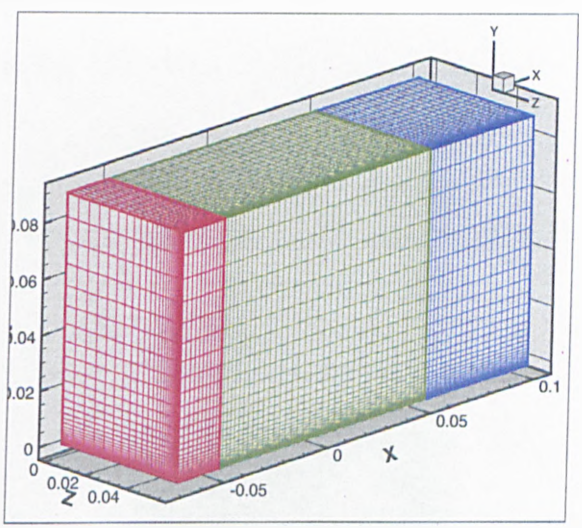


Figure 3.4: Computational mesh for the clean wind tunnel.

However, the assumption of setting the boundary condition at the top plane as symmetry is inappropriate for the controlled case and hence half of the full wind tunnel is modelled with a single spanwise symmetry plane specified in the middle of the wind tunnel as shown in Figure 3.6. The computational mesh generated for the controlled case has more blocks in order to cope with the complex geometries and it has around a million cells. The closeup of the generated one and a half ramp bumps is also shown in Figure 3.7. The dimension details for the controlled case mesh are similar to those of Figure 3.5, only the height of the mesh is now

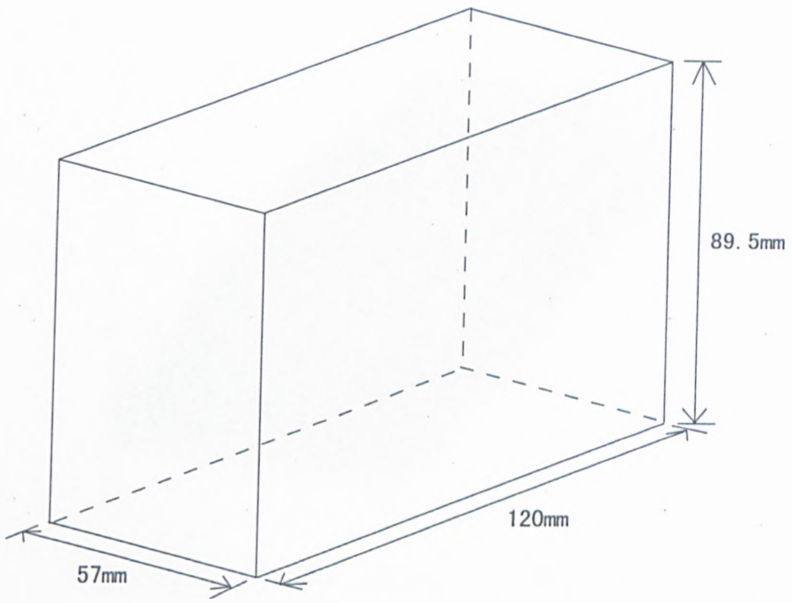


Figure 3.5: Dimensions for the clean wind tunnel mesh.

the full height of the wind tunnel working section, which is 179 mm. Note that for the controlled case, the experimental wall pressure data is only available up to x = 70 mm.

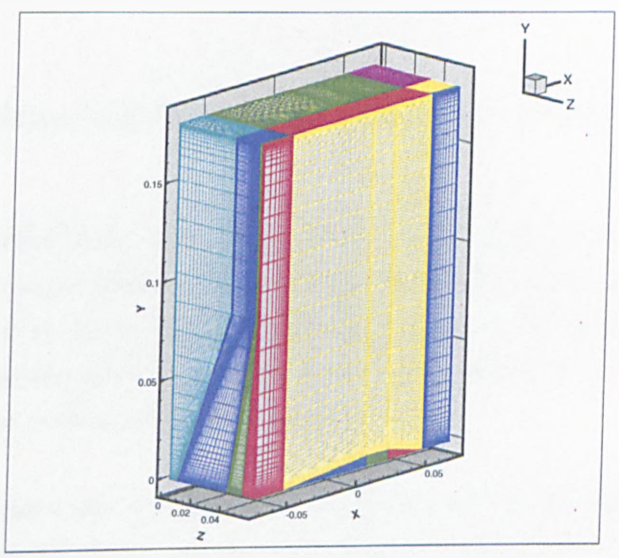


Figure 3.6: Computational mesh for the controlled case.

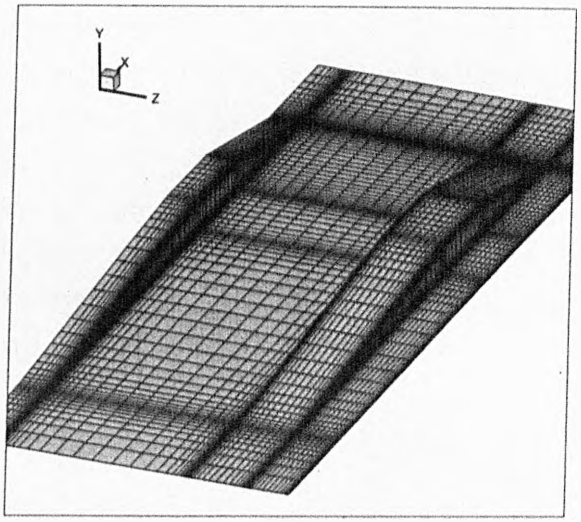


Figure 3.7: Closeup of the ramp bumps mesh.

The inflow plane for both of the cases is situated at x = -70 mm. The incoming flow is specified at the inflow plane where the boundary layer profile is extracted from a flat plate turbulent boundary layer simulation. The boundary layer profiles for all three walls are assumed to be identical. At the outflow plane, a subsonic boundary condition has been specified where all the conservative variables are allowed to float except for the pressure, which is specified at the given experimental value.

### 3.3.1 Implementation of the Algebraic Turbulence Models

Both the Baldwin-Lomax and the curvature-based algebraic models are wall-distance dependant, therefore, in the controlled case, three values of the turbulence viscosity $\mu_t$ for a cell in the flowfield have to be calculated using the distances from all the three walls. The $\mu_t$ that is calculated from the nearest wall to this cell centre is then selected as the final value.

Figure 3.8 illustrates the topology and the front view of the initially generated structured grid at the vicinity of the edge of a 3D bump, where all the numbered areas shown in the figure are separated into different blocks. This topology works fine for the k-$\omega$ model, however, it causes trouble for the algebraic models, since

the $\mu_t$ for the cells at the vicinity of the sharp edge of the 3D bump in block *2* have to be copied from block *1* & *3* to maintain the continuity of the value of $\mu_t$ in that area. Unfortunately, this solution did not work particularly well. Thus, to tackle this problem, the whole solid surface of the 3D bumps and the bottom walls are integrated as a single bottom surface and hence merged as one block as illustrated in Figure 3.9. The $\mu_t$ for the cells at the vicinity of the sharp edge of the 3D bump in block *2* are now calculated from the solid surface distances instead of being copied from different blocks.

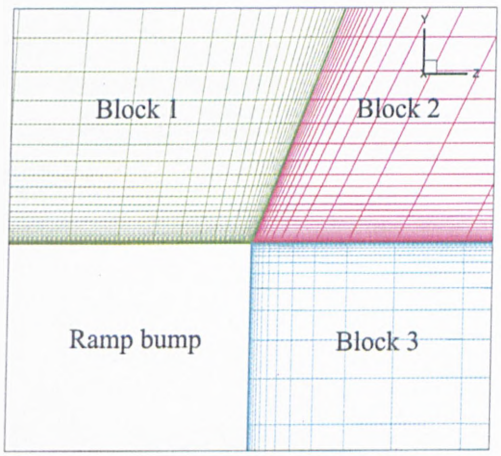


Figure 3.8: Topology of the initially generated grid

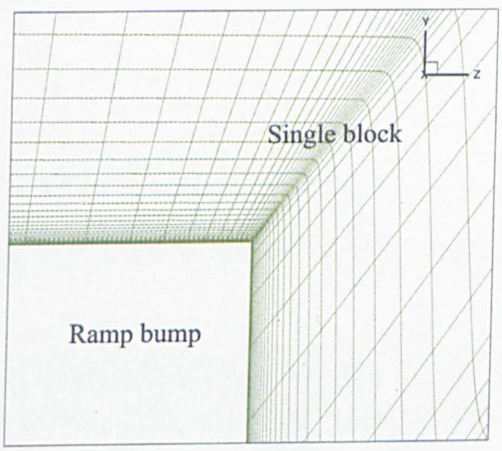


Figure 3.9: Topology of the revised grid

## 3.4 The Flat Plate Simulation

In order to match the wind tunnel experimental conditions, it is necessary to simulate the boundary layer at the inlet of the computational domain. While the streamwise mean velocity profile was available from experiment, the numerical simulation also required knowledge of wall normal velocities, density, pressure, turbulence viscosity for the algebraic models and an additional two turbulence variables for the k-$\omega$ model. For this reason, it was decided to extract the inflow boundary layer profiles from a flat plate simulation at the wind tunnel conditions.

The computational mesh generated for this flat plate simulation is shown in Figure 3.10. Note that the flow direction is from left to right. The downstream of the mesh is extended to a sufficient distance to allow the boundary layer to fully develop. The distribution of the grid near the wall has also been adjusted so that the near wall mesh spacing has a $y^+$ value of *1*.

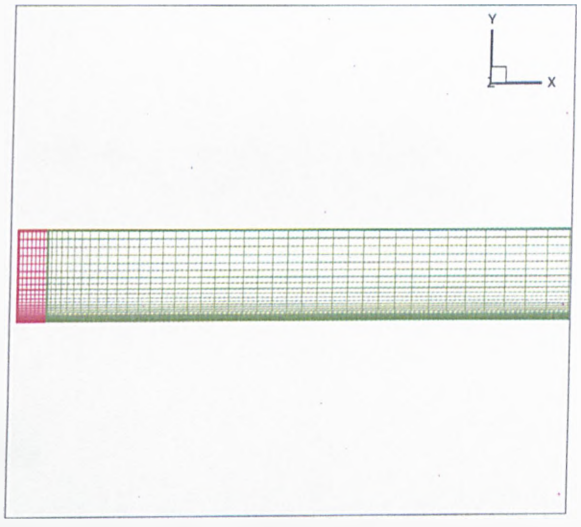


Figure 3.10: The mesh for flat plate simulation.

The simulation is run at a freestream Mach number of 1.29 and a Reynolds Number of 28 million per meter, both matching the experimental conditions. The boundary layer is then extracted at the station where the thickness is around 7 mm in accordance with the experimental data. Here, it was decided to slightly scale the inflow boundary layer to achieve the correct shock position because

the shock location proved to be highly sensitive to this parameter, which will be further discussed in later sections (and thus only small modifications were required). Figure 3.11 shows an $y^+$ vs $U^+$ graph that is plotted at a station where the boundary layer is fully developed to demonstrate that the simulations from both models have as expected (see Ref. [56]) captured the log-law region of a typical turbulent flow well.

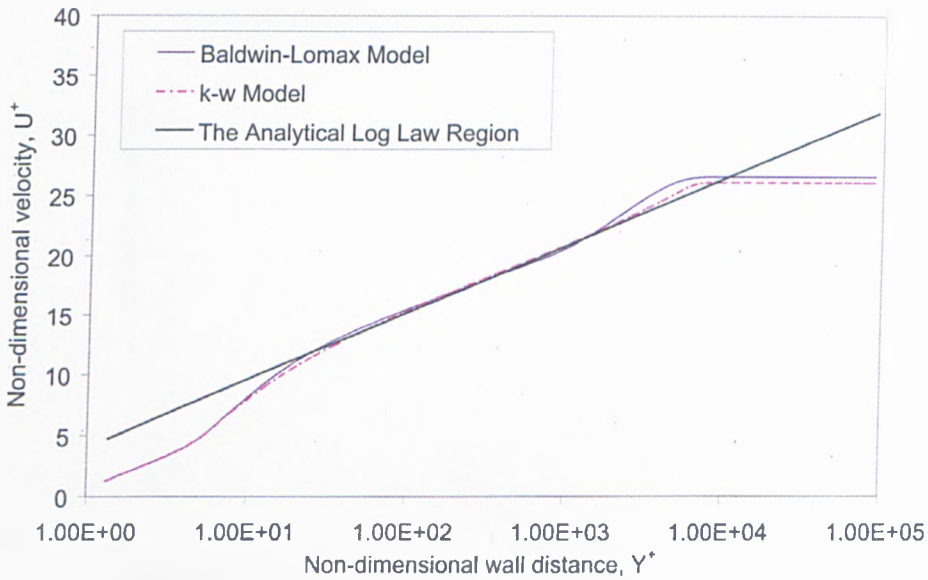


Figure 3.11: $y^+$ vs $U^+$ graph plot.

## 3.5 Results

### 3.5.1 Uncontrolled Case (Empty Wind Tunnel)

Figure 3.12 shows the comparison between the simulations and the experiment data of the incoming flow velocity profiles at x= -30mm. Note that in the experiment, the incoming boundary layer is developed through a converging-diverging nozzle instead of a flat plate, and this is likely to contribute to the differences between the computation and the experiments, in particular the slightly increased shape factor of the experimental profile. To achieve the correct shock position in the simulations, it was necessary to adjust the incoming flow boundary layer,

i.e. to extract the turbulent boundary layer solution at a particular streamwise location. The incoming boundary layer determined in this way has a boundary layer thickness of about 7mm, consistent with the experiment data. This also corresponds to a displacement thickness of 0.928mm, closely matching that of the experimental value of 0.94mm.

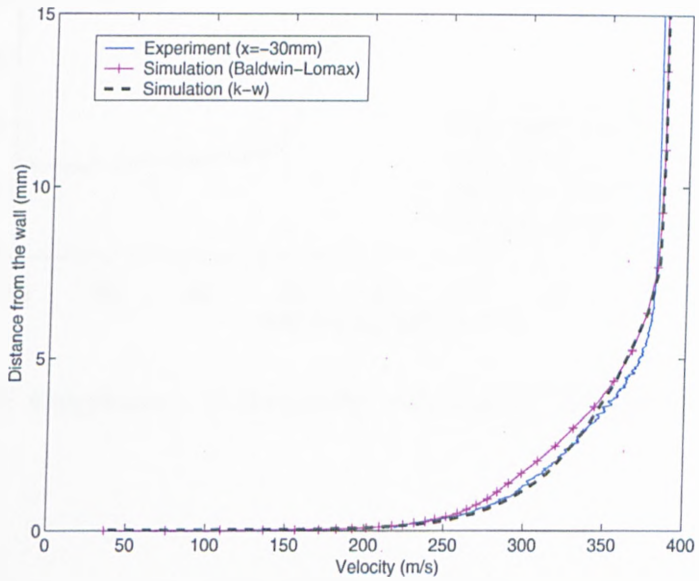


Figure 3.12: Incoming velocity profile at x=-30mm.

The streamwise surface pressure along the tunnel floor (z=0mm) is plotted in Figure 3.13. Previous simulations by Schumacher [85] as well as the present study have shown good agreement with the experiment in the upstream part of the interaction. In particular, the upstream influence length is reasonably well captured. However, downstream of the shock, x > 0mm, the surface wall pressure predicted by Schumacher's calculations recovered to a value greater than that of the experiment. This is because a higher backpressure has to be specified to match the shock position in the absence of the sidewall blockage effect. In contrast, the results from the present study are in very good agreement with the experiment and the surface wall pressure recovers to the specified level of the experiment. Figure 3.14 shows the static pressure contours for the controlled case. Along the floor and side-wall, the smearing at the foot of the normal shock wave can be observed, which is typical for weak shock boundary layer interactions.

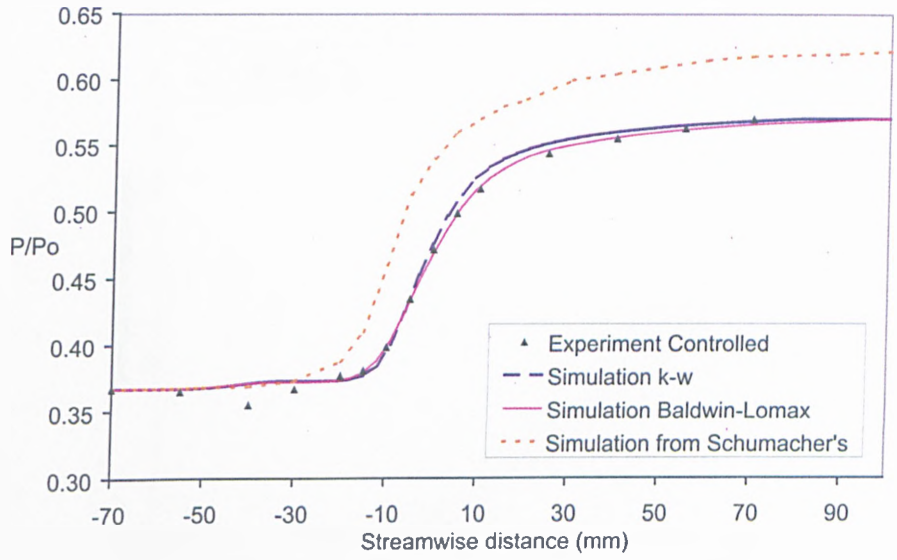


Figure 3.13: Comparisons of streamwise wall pressure distribution (z=0mm).

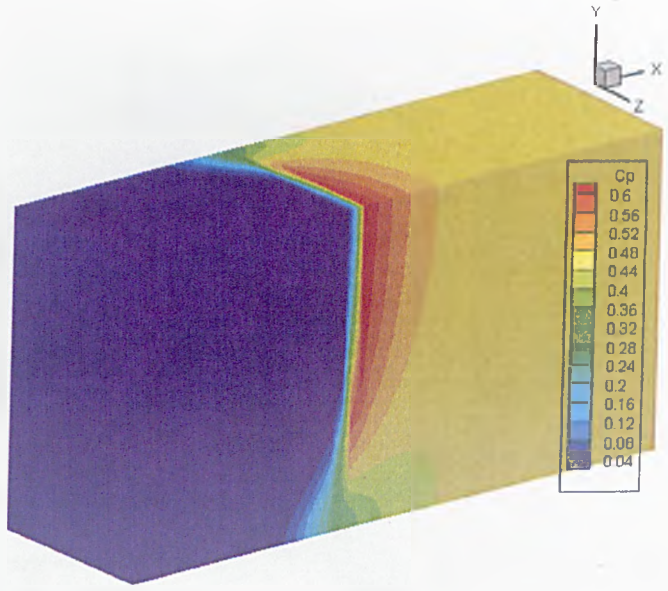


Figure 3.14: Pressure contour plot for the uncontrolled case.

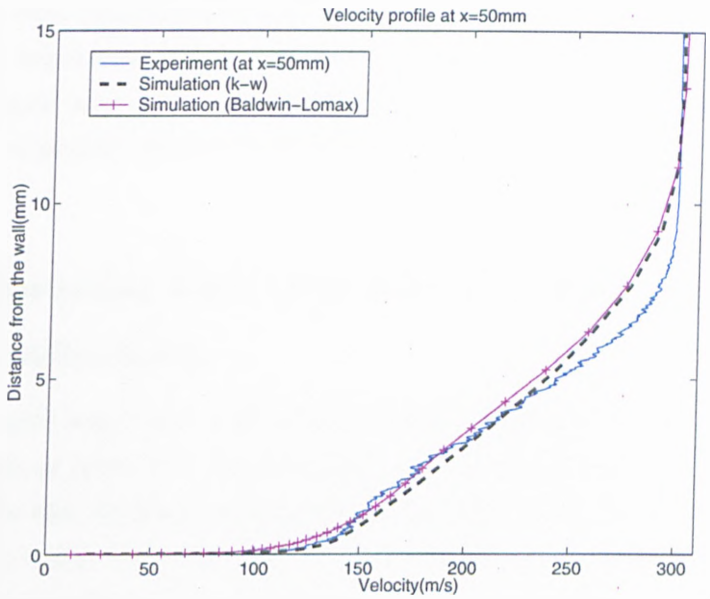


Figure 3.15: Velocity profiles at x=50mm.

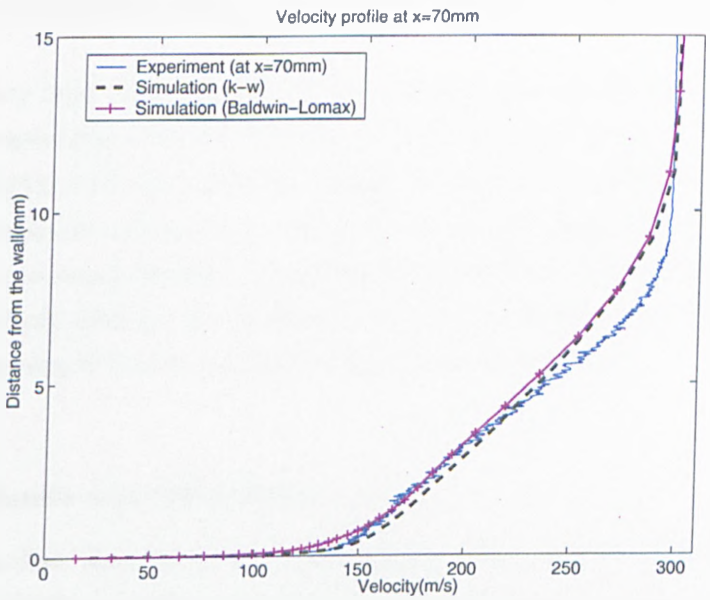


Figure 3.16: Velocity profiles at x=70mm.

Shown in Figures 3.15 and 3.16 are the velocity profiles downstream of the shock / boundary layer interaction along the symmetry plane in the streamwise direction at x = 50mm and 70mm respectively. Although the profiles are found in reasonably good agreement, the computed boundary layer after the interaction is found to be slightly thicker than that of the experiment.

## 3.5.2 Controlled Case (with 3D Ramp Bumps)

### 3.5.2.1 Grid Sensitivity

A study on grid sensitivity was conducted for the controlled case with the 3D bumps. Solutions have been obtained from a fine grid with a resolution of around 1 million cells and relatively coarser grid with around 300 thousand cells. It is found that, by using the same inflow boundary layer profile and backpressure for both cases, the position of the shock wave (a sensitive parameter to boundary conditions as mentioned earlier) is relatively insensitive to the grid resolution. The streamwise pressure distribution plots in Figure 3.17 show that the result from the coarser grid is in good agreement with the experimental data. However, a lack of streamwise grid resolution in the vicinity of the shock wave is depicted by the pressure rise discrepancy in the region between 10mm and 30mm.

The boundary layer development station also shows some sensitivity to the grid resolution, especially with the presence of vortical flow as shown in velocity profiles from Figure 3.19. Nevertheless, generally, the study provides some grid sensitivity information indicating a reasonable resolution on the grids used. Based on the balanced requirements of numerical accuracy and computational time, the fine grid has been used for all the cases. Even finer grids have not been attempted in the present study due to computational resources available.

### 3.5.2.2 Results and Discussions

For the controlled case, the shock wave position was found to be even more sensitive to flow field variations and the experimental data was subject to an error band of ±3mm. As a result, the incoming flow boundary layer prescribed in the simulations needed some readjustments to match the experimental shock position for a given backpressure. Figure 3.20 compares the experimental Schlieren

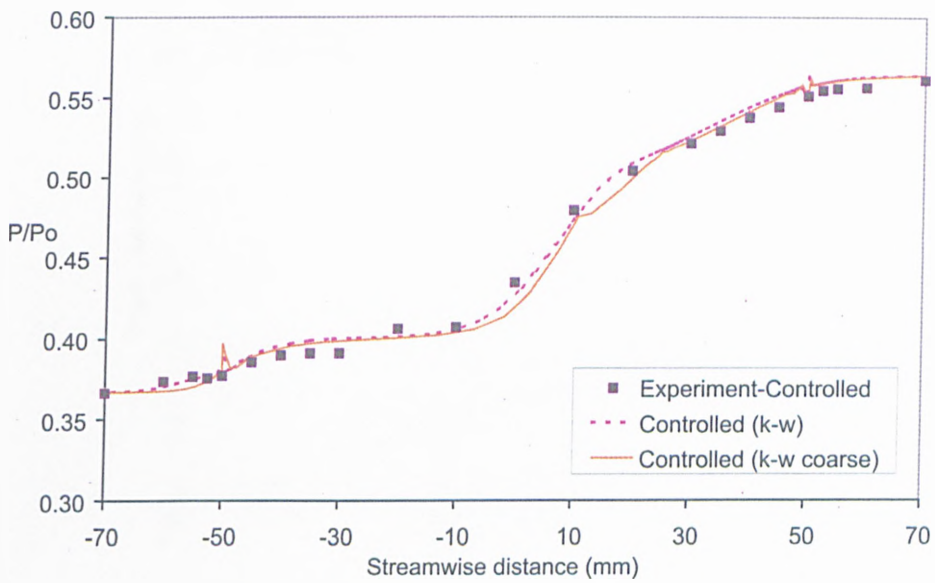


Figure 3.17: Wall surface pressure distribution at z=17mm, for a fine and a coarse grid.

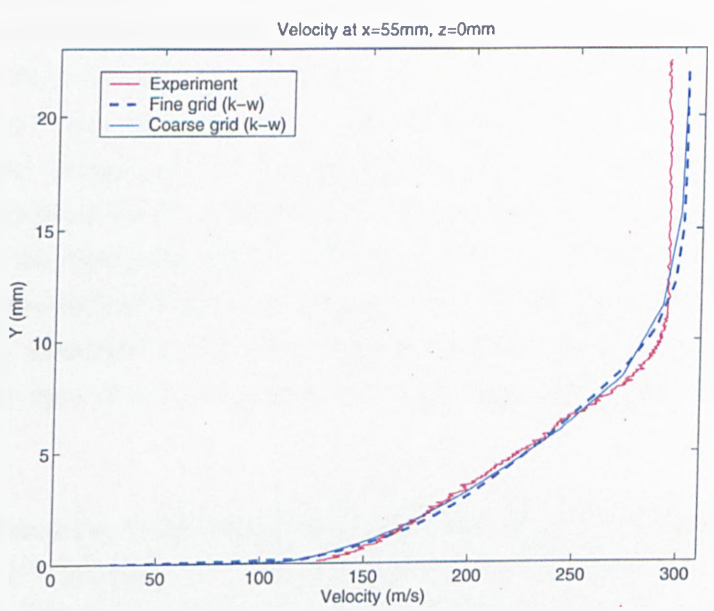


Figure 3.18: Velocity profile at x=55mm, z=0mm.

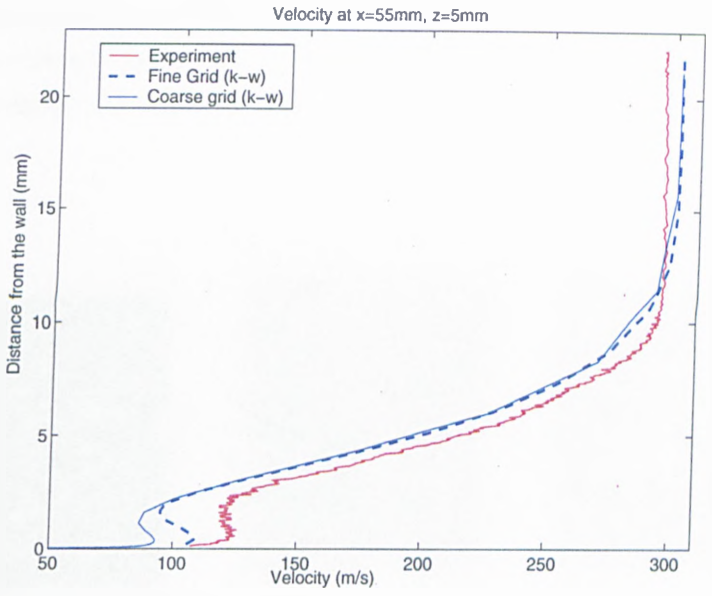


Figure 3.19: Velocity profiles at x=55mm, z=5mm.

picture with numerically generated density gradients in the x and y directions using CFD data at the symmetry plane. It can be seen that the CFD simulation has been successful in capturing the flow features seen in the experimental image. The main shock is split into a lambda-structure, where the leading leg is attached to the upstream edge of the bumps. The rear shock leg appears slightly smeared close to the bump surface in both images and there is a clear evidence of a post-shock expansion, with a secondary shocklet, over the rear of the device just after the second corner of the bump. The density gradient in the wall normal direction on the symmetry plane in Figure 3.20 (c) shows the boundary layers on the bottom and top walls of the wind tunnel. It can be seen that the ramp bump is fully immersed in the incoming flow boundary layer. The thickening of the boundary layer due to the shock/boundary layer interaction is also clearly visible.

Figure 3.21 compares experimental and numerical streamwise pressure distributions at $z = 17$ mm, which is located in between the 3D bumps. Generally, the turbulence models give good agreement with the experiment. The initial pressure increase due to the leading leg of the lambda-shock is well predicted and the subsequent pressure rise across the rear shock leg is also captured in its magnitude

as well as in its streamwise location. This suggests that the computations have captured the shock structure above the bumps in its geometry as well as in the relative strengths of both shock legs.

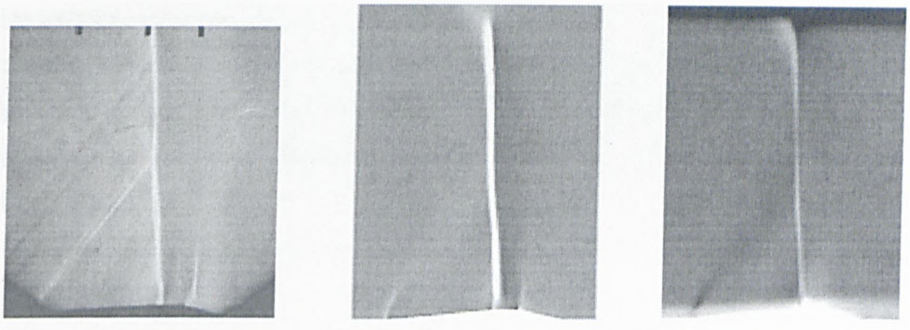

Figure 3.20: Images of flow over bump (a) Experimental Schlieren (b) CFD x-density gradient (c) CFD y-density gradient.

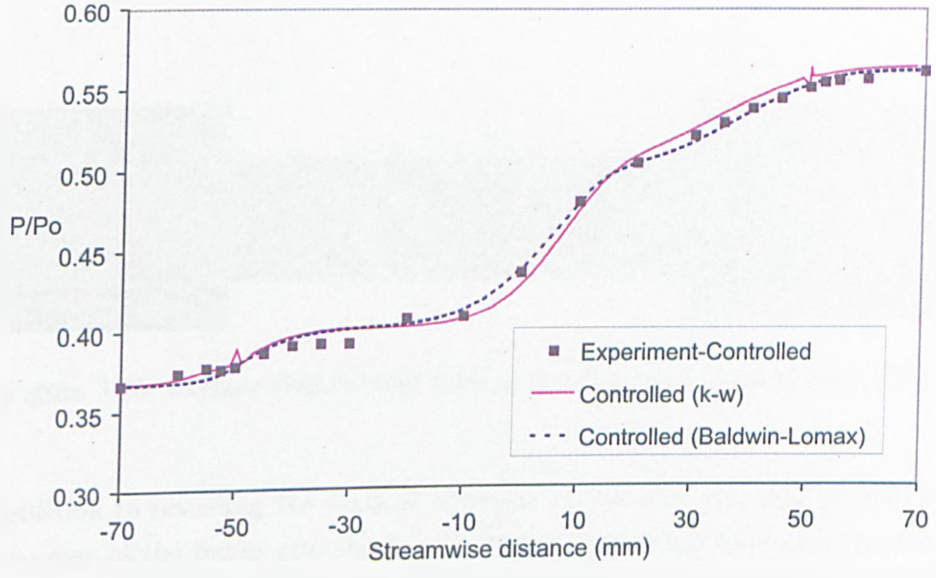


Figure 3.21: Wall surface pressure distribution at z=17mm.

Figure 3.22 and 3.23 compare the surface oil-flow visualisation from the experiment with surface skin friction lines from the simulation. In the enlargement of the upstream section it can be seen that the oil-flow just after the leading edge of the bump slightly diverges on the ramp surface. The same flow pattern is observed from the computed skin friction lines. This suggests that the flow is 'spilling' over the sides, which is likely to cause flow separation and the generation of streamwise vortices. This is confirmed in the flow field plots from numerical simulation as shown in Figure 3.24. A weak vortical flow is observable on the side of the ramp bump. Similarly, both the oil flow pattern and the skin friction lines downstream of the bump show clear separation lines and traces of cross flow separation and vortical flow. Once again, the presence of vortical flow is confirmed by the streamlines in Figure 3.25. Note that this downstream vortex is stronger and has the opposite sense of rotation from the weaker vortex generated upstream.

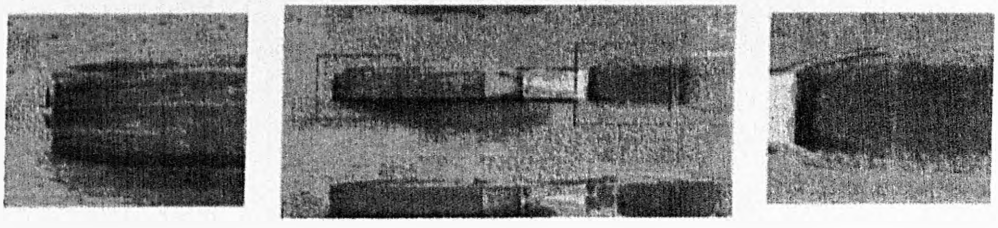

Figure 3.22: Surface oil flow visualisation of the flow with control.

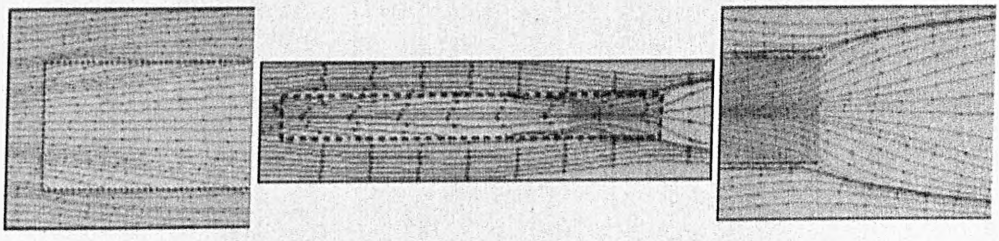

Figure 3.23: Surface skin friction lines of the flow with control from CFD.

In addition to revealing the vortical structure of the flow, the skin friction lines at the rear of the bump also show some degree of reversed flow near the foot of the bump, which indicates a small separation bubble at the intersection between the bump and the wind tunnel floor. Therefore, Figure 3.26 presents a clearer picture of this separation bubble with an enlargement of the region downstream

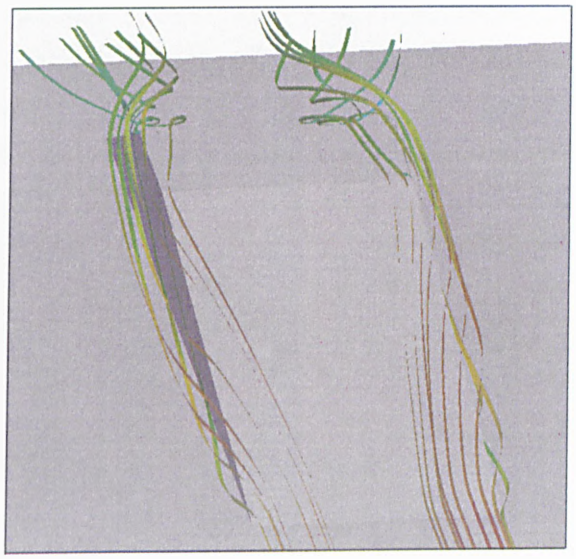

Figure 3.24: Streamtraces of the vortices

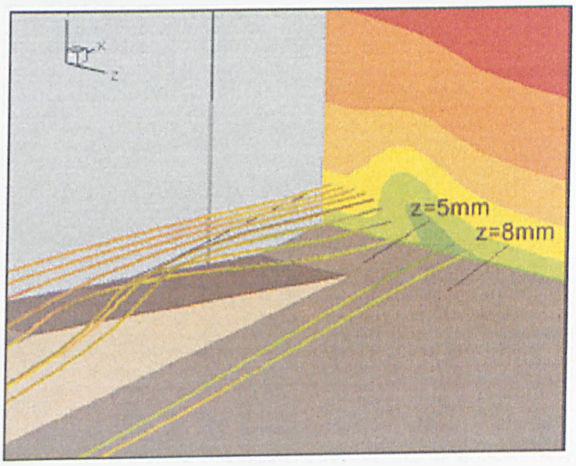


Figure 3.25: Streamtraces of the downstream vortex.

of the bump shown previously in Figure 3.23. A closer examination of Figure 3.26 indicates that the sharp geometric change at the intersection between the bump and the wind tunnel floor contributes to separation of the flow. However, recalling the shape of the bump in Figure 3.2, where the height of the bump gradually shrinks at the downstream end of the bump and by backtracking the separation line, it shows that the cross flow separation also bears significant influences from the vortex shed from the sharp edge of the bump since the sharp edge is relatively closer to the foot of the bump in this downstream region. Viewing this region in a different angle with Figure 3.27 gives a clearer picture of the skin friction line 'spilling' off the sharp edge and into the separation bubble before converging to form the separation line downstream. Another plot of the skin friction line of the same region but at the side of the bump is presented in Figure 3.28. It again shows the reversed flow at the foot of the bump and that it spans across almost the entire length of the bump. This is undesirable in the bump design and can be avoided with a smoother geometry change at the mounted base of the bump.

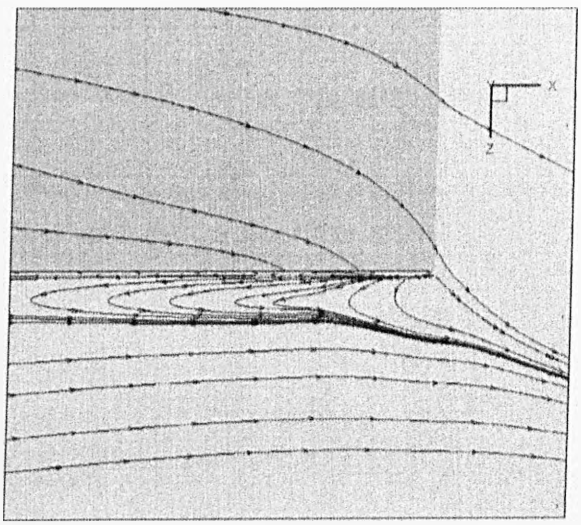


Figure 3.26: Enlargement of the skin friction line at the downstream of the bump.

As mentioned earlier, the velocity profiles were measured with only a single bump in the tunnel. In order to eliminate the potential difference in these profiles caused by the bump numbers for a more reasonable quantitative comparison of the velocity profiles, calculations have also been done with just one bump in the working section using the k-$\omega$ turbulence model. According to the experimental

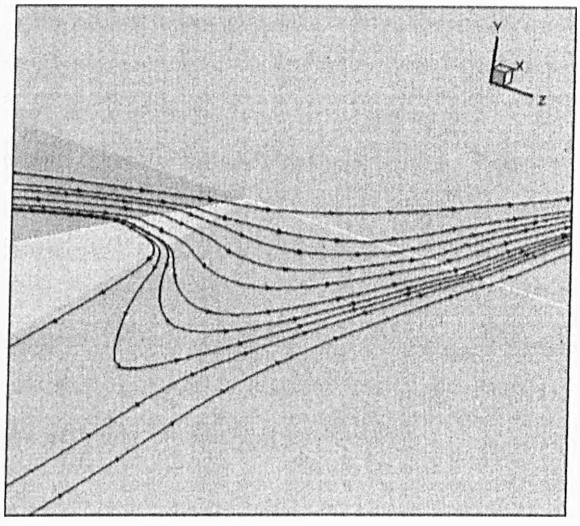


Figure 3.27: Oblique view of the downstream separation region.

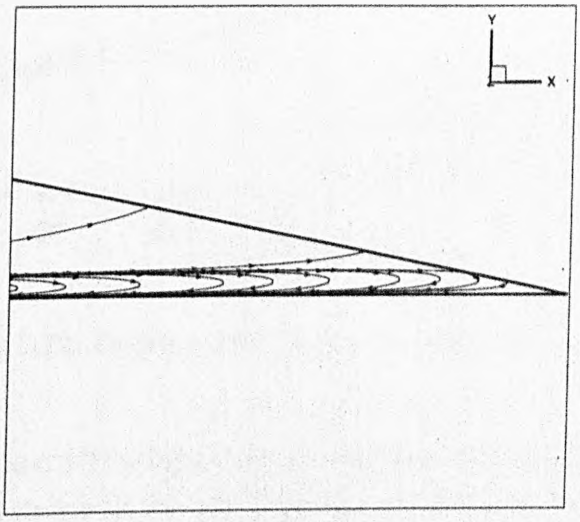


Figure 3.28: Skin friction lines on the side of the bump.

conditions, the backpressure and the inflow boundary layer profile are set to be the same as that of the multiple bumps case. Observations on the position of the shock wave in the flow field suggested that the main normal shock in the freestream has not displaced much relative to the multiple bumps case. This is consistent with what was observed in the experiments. It is also observed that the bifurcated $\lambda$-shock structure is less pronounced, which is expected since the flow displacement is slightly reduced with just one bump in place. This is further confirmed in the streamwise pressure distribution plot shown in Figure 3.29. It is obvious from the plot that the normal branch of the shock from the single bump control is significantly stronger, which implies that an array of 3D bumps clearly work better than one and that the spacing between them is crucial. Besides that, the overall flow field did not change significantly.

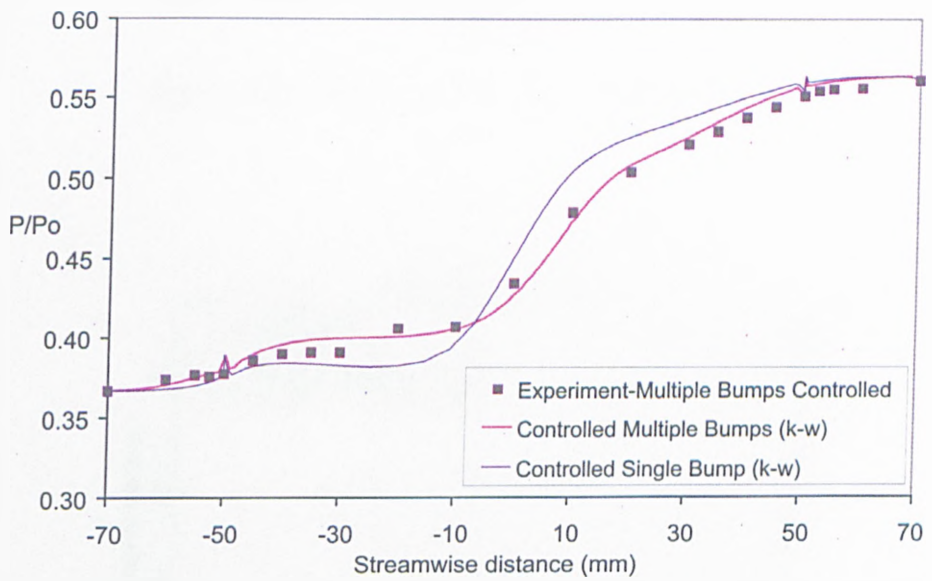


Figure 3.29: Pressure distribution plot with single bump.

Figures 3.30, 3.31 and 3.32 compare velocity profiles at various spanwise locations immediately downstream of the interaction at x = 55 mm. For clarity, velocity profiles comparison for the multi and single bump cases are plotted separately in Figures 3.33, 3.34 and 3.35. On the whole it can be seen that the simulations have slightly over-predicted the boundary layer growth through the interaction. A closer examination of Figures 3.31 and 3.32 reveals significant inflexion in the

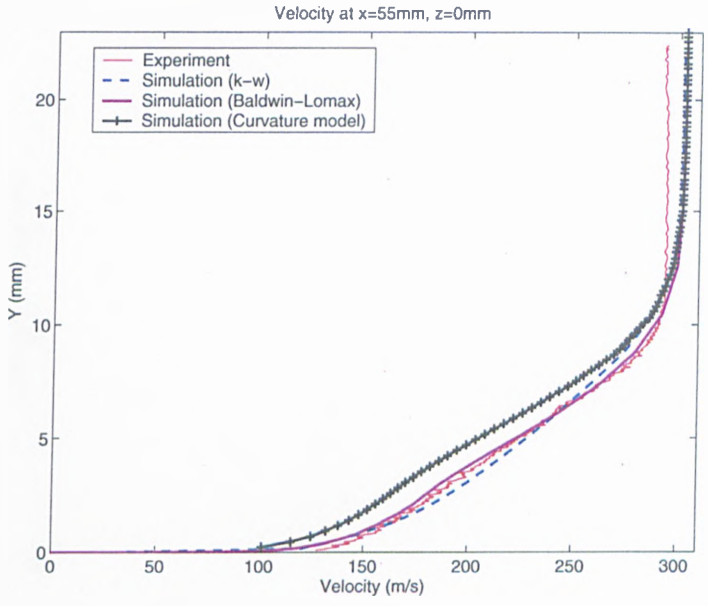


Figure 3.30: Velocity profiles at x=55mm, z=0mm.

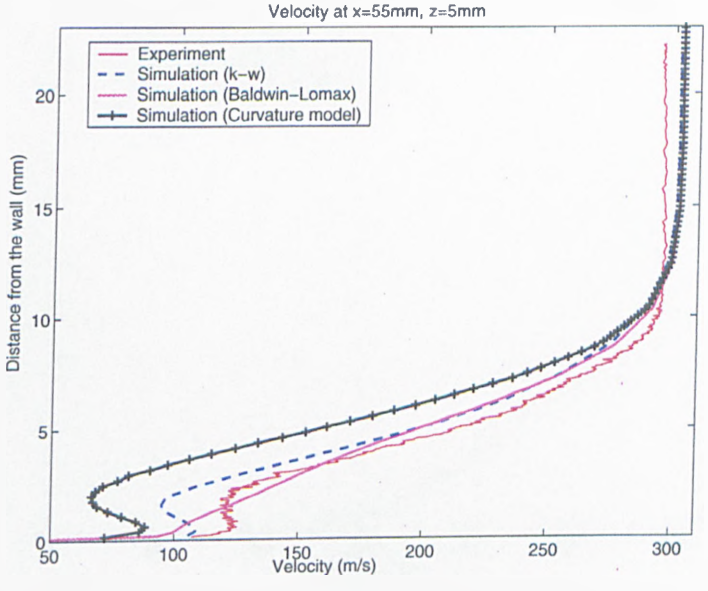


Figure 3.31: Velocity profiles at x=55mm, z=5mm.

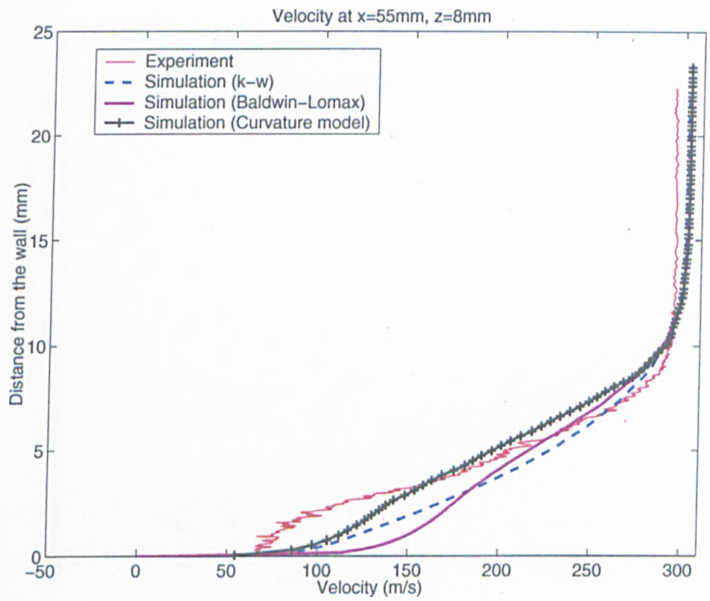


Figure 3.32: Velocity profiles at x=55mm, z=8mm.

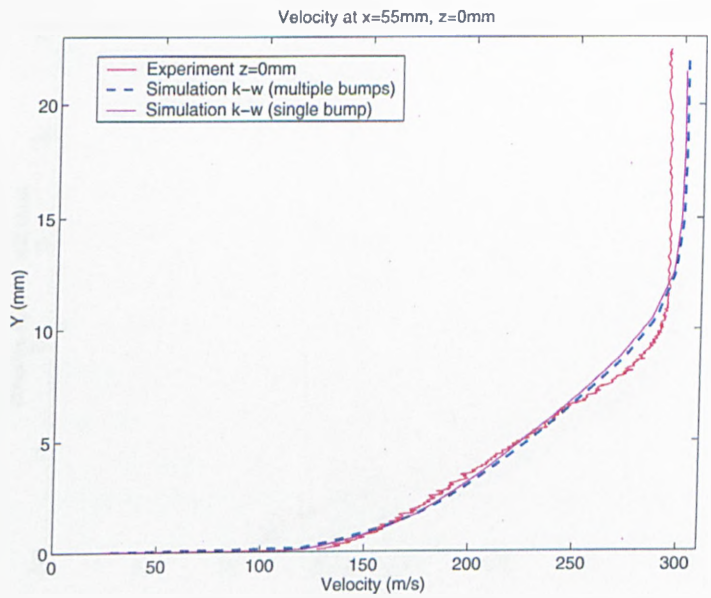


Figure 3.33: Velocity profiles with single bump at x=55mm, z=0mm.

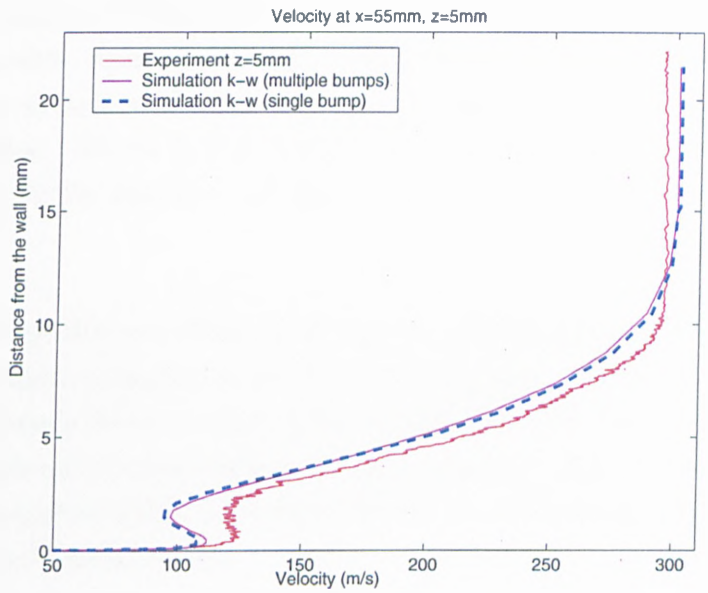


Figure 3.34: Velocity profiles with single bump at x=55mm, z=5mm.

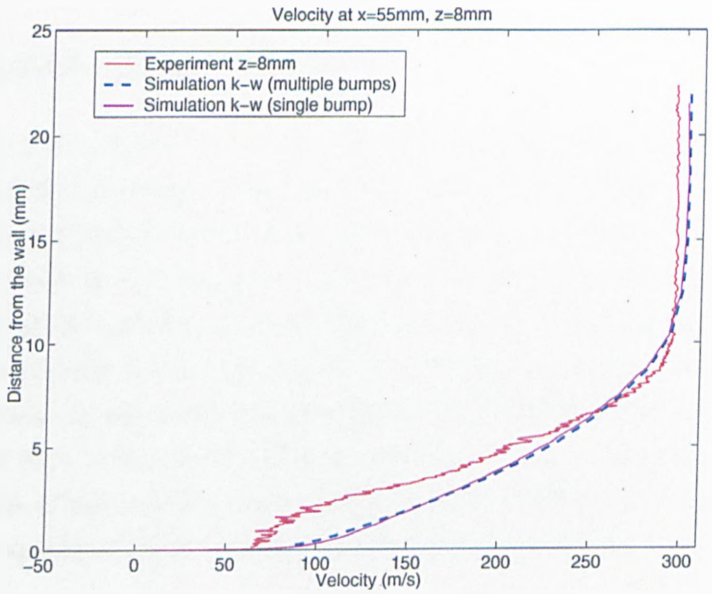


Figure 3.35: Velocity profiles with single bump at x=55mm, z=8mm.

profiles, which indicates the presence of crossflow separation and vortical flows. While in general the shape of the profiles is well captured by the k-$\omega$ and the curvature models, there are no obvious inflexions in the results obtained with the Baldwin-Lomax model. The improved performance of the curvature model is due to the modified criterion in the model, which carefully chooses the appropriate length scales for the attached turbulent boundary layer under the vortical structure.

There are no significant changes in the velocity profiles extracted from the single bump calculation compared to the multiple bump case. Further examination of Figure 3.34 reveals that the velocity profiles from both calculations are seemingly close with just some minor difference, suggesting that the spanwise position of the vortices generated from the centre bump is not displaced significantly from a single bump to multiple bumps.

Finally, the origin and trajectories of streamwise vortices can be determined again from Figures 3.24 and 3.25. This shows that the flow separates over the trailing edge of the bump, which leads to the generation of a pair of counter-rotating vortices downstream.

## 3.6 Concluding Remarks

This chapter has demonstrated that careful matching of the experimental parameters and the boundary conditions of a numerical simulation is crucial for mutual validation and further understanding of the flow physics. In the study of a transonic shock wave / boundary layer interaction it was found that the back pressure, the wind tunnel sidewall and the incoming flow boundary layers all had to be matched closely due to the sensitivity of the shock position and structure to these conditions. In the numerical simulation, the incoming flow boundary layer was obtained from a flat plate turbulent boundary layer simulation, which is an approximation of the realistic wind tunnel boundary layers from the supersonic nozzle. This approximation was found to work reasonably well.

All turbulence models used in the computation have captured the flow features well for the uncontrolled baseline case. They also correctly resolved the shock

structure and streamwise wall pressure distribution in the controlled case. However, the Baldwin-Lomax algebraic model was not successful in capturing the details of the viscous flow, particularly the streamwise vortices generated by flow separations downstream of the three-dimensional bump. In contrast, the k-$\omega$ model and the curvature model were both able to model this flow feature.

This study shows how difficult a seemingly straightforward validation can be. For complicated turbulent flow problems, detailed quantitative comparison is crucial. This in turn requires careful matching of the simulation with the experimental conditions. Incorporating the correct backpressure, the sidewall boundary layers and the incoming boundary layer, made it possible to improve the quantitative agreement between the experiments and the numerical simulation. However, the final solution is still short of an "exact" match, due to the lack of detailed information about the incoming boundary layers on all sides of the wind tunnel. To improve the simulations it is necessary to either measure detailed boundary layer profiles at these walls or model the whole converging-diverging nozzle with detailed geometrical input.

Nevertheless, the study demonstrates how the combination of experiments and a careful numerical investigation can provide additional insight into a complex flow, which might not have been obtained from either approach alone. Based on the agreements with the surface pressure and oil flow provide confidence, the flowfield plots from the simulation have greatly assisted in the interpretation of the experimental oil-flow patterns by revealing the existence of upstream weak vortices that cause the oil-flow pattern to diverge towards the side of the bump. Further evidence of the strong downstream vortex and indications of flow separation near the rear of the bump are significant for the design of improved shock control bumps. These findings suggest a possible design of a shock control bump that also incorporates the benefits of a sub-boundary layer vortex generator in controlling or suppressing trailing edge separation. On the other hand, if significant viscous drag is to be avoided the current ramp bump shape is unlikely to be a successful design due to the number of separations observed along the sharp edges. An optimum design is likely to feature a more curved shape to avoid flow separation.

With the numerical flow solver proven to be able to capture the complex flow features of transonic flow over 3D bumps, we can now move on to investigating and optimising the performance of the 3D bumps on wings. However, before that, it is necessary to include the descriptions of the additional numerical tools needed to perform aerodynamic optimisation in the following chapter.

# Chapter 4

# Adjoint-based Aerodynamic Optimisation

## 4.1 Introduction

Progressive improvements in CFD over the years and powerful computing resources that are readily available at affordable costs have made it possible to evaluate alternative designs rapidly and effectively through computer simulations without the need to build numerous wind tunnel models. However, it is almost impossible for the designer to find an optimum design through trial and error. Therefore, numerical optimisation procedures are used in conjunction with CFD to optimise aerodynamic design problems. In recent years, aerodynamic optimisations and even multidisciplinary optimisations has been emerging as essential design tools in both academia and the industry.

The various aerodynamic optimisation methods can be largely divided into two main categories, gradient and non-gradient-based methods. For the gradient-based methods, the sensitivities are calculated by finite-difference methods, complex variable methods, automatic differentiation methods and quasi-analytical methods. The adjoint method employed in this project is one of the quasi-analytical methods. In the other category, the non-gradient-based or function evaluation methods consist of the response surface technique [86] and genetic algorithms [87, 88].

The function evaluation methods have the advantage over the gradient-based methods of finding the possible global optimum of the objective function, but

the methods require a large number of CFD calculations. The computing cost will be very high as well, especially when complex three-dimensional aerodynamic problems are involved. As for the adjoint method, the sets of adjoint equations derived from differentiating the governing equations of the flow field only need to be solved once for each objective function and constraints [89]. Therefore, when the number of design variables is greater than that of the number of constraints plus objective function, which is likely to be the case in most aerodynamic optimisation problems, the adjoint method is quite efficient compared to the other methods. For example, for the optimisation of the blended wing-body configuration as investigated in Ref. [83], there are hundreds of control points or design variables that define the shape of the wing, while the aerodynamic constraints considered only include the lift and pitching moment and the objective function is the drag.

The aim of this chapter is to present the numerical optimisation tools that have been employed in this project, instead of introducing and detailing the various optimisation methods. Thus, besides the discrete adjoint solver developed by Le Moigne and Qin [74, 83] that will be described in later sections, the other methods listed above are considered to be beyond the scope of this thesis.

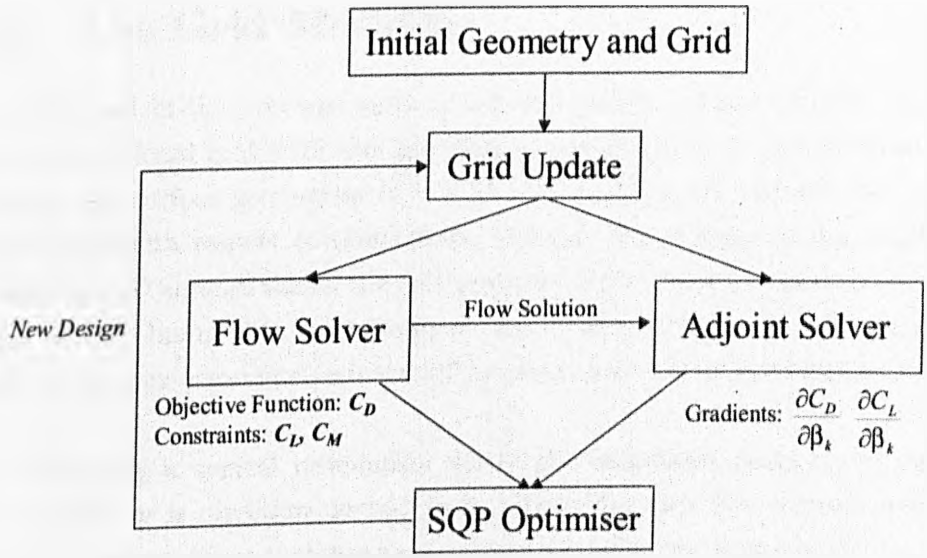


Figure 4.1: Schematic of the optimisation chain.

The optimisation chain is an automatic iterative process as shown in the schematic diagram in Figure 4.1. To kick-start the optimisation process, an initial design is fed into the top of the chain, which is the grid modeller that updates the computational grid from the provided design sets. The flow solver MERLIN, then solves for the flow on the updated grid including the objective functions and constraints, i.e. drag and lift. Moving on, provided with the converged flow solution, the adjoint solver can then solve for the gradients of the objective functions or constraints. Note that the flow solver and the adjoint solver do not run simultaneously although they are placed in parallel in the schematic diagram. Finally, all the essential information including the objective functions, constraints and gradients are supplied to the Sequential-Quadratic-Programming or SQP optimiser. The optimiser then searches for the subsequent improved designs which will be updated by the grid modeller again and the whole process iterates until the optimiser find the best converged design.

One by one, all the four main elements in the optimisation chain excluding the flow solver, which has already been presented earlier in *Chapter 2*, will be introduced in the following sections. Starting with the grid modeller at the top of the chain.

## 4.2 The Grid Modeller

As mentioned in the previous section, the grid modeller automatically updates the computational grid with the new design sets acquired by the optimiser. It modifies the surface geometries of the aerofoil or wing and updates the whole volume grid with respect to these shape changes. In addition to the ability of modifying a 2D aerofoil shape, the grid modeller is also extend to add either a 2D bump or a 3D bump onto an unswept or swept wing. The details of the aerofoil shape and bumps parameterisations will be presented at later appropriate stages.

By considering a typical orientation where the chordwise direction is the x-direction and y is direction normal to it. Basically, only the y-coordinates of the grid points on the x-y planes are modified to define the shape of the bumps, i.e. 2D bumps on un-swept wings. In the case of swept wings where the sweep angle can be considered as a variable, the x-coordinates of the surface grid points are displaced accordingly with respect to the defined sweep angle. On the other

hand, when defining the shape of the 3D bump, not only the y-coordinates of the x-y planes have to be modified, but the z-coordinates (spanwise direction) too because one of the 3D bump parameters defines the width or spanwise spacing between the subsequent 3D bumps (further details of the parameterisations of the bumps will be presented in a later chapter), which will therefore be shrinking or expanding the width of the grid. With sufficient spanwise grid resolution, the z-coordinates are just distributed equally with respect to the width of the grid.

As for the wake surface grid for a C-type grid, again, this usually need not be dealt with when the sweep angle is disregarded as a variable. In case it is, since the grid lines connecting both the symmetry boundaries should be straight, so the distance between the trailing edge and the corresponding wake surface grid points are kept constant. Thus, considering the grid points along the grid line connecting the trailing edge and the outer far-field boundary, with $i = 2, \cdots, in$ and $x_{TE} = x_1$, the x-coordinates of these grid points are simply

$$x_i^{new} = x_{TE}^{new} + \left(x_i^{old} - x_{TE}^{old}\right) \tag{4.1}$$

Once the surface grids are generated, the modifications to it will have to be propagated to the volume grid. This is done by updating the grid points along the grid lines that connect the surface boundary and the far-field boundary using an analytical method as employed by Le Moigne [83]. Therefore, the deformation of the y-coordinate of one of these grid points, where $j = 1, \cdots, jn$ are achieved by

$$y_j^{new} = y_j^{old} + [1 - arc(j)] \left(y_{surface}^{new} - y_{surface}^{old}\right) \tag{4.2}$$

where

$$arc(j) = \frac{\sum_{l=2}^{j} L_l}{\sum_{l=2}^{jn} L_l}$$

and

$$L_l = \sqrt{(x_l - x_{l-1})^2 + (y_l - y_{l-1})^2 + (z_l - z_{l-1})^2}$$

Note that $y_{surface} = y_1$. If the x-coordinates of the surface grid were modified, the volume grid is updated using the same idea from Eqn. (4.1), only that $x_{TE}$ is now replaced with $x_{surface}$. When z-coordinates are modified, in order to keep the grid lines connecting the surface boundary and the far-field boundary in parallel as they have been initially, instead of using Eqn. (4.2), the volume grids are updated by copying the z-coordinates of the spanwise-displaced surface grid,

$$z_j^{new} = z_{surface}^{new}$$

## 4.3 Discrete Adjoint Solver

The discrete adjoint solver developed by Le Moigne and Qin [74, 83] has several unique features. The solver has been entirely hand-differentiated for the calculations of the components of the Jacobians and the grid sensitivities. It is also one of the rare adjoint solvers developed that uses Osher's approximate Riemann solver to calculate the inviscid fluxes. Besides that, the adjoint solver is also novel for its choice of turbulence model, which is the Baldwin-Lomax algebraic turbulence model. In Ref. [74], Le Moigne noted that the rarity of adjoint solvers implemented with algebraic turbulence models might be due to the reasons that two-equation turbulence models are relatively easier to implement. Although there were some difficulties in the linearisation of the turbulence model, nevertheless, this adjoint solver has been successfully used in the optimisation of both 2D and 3D aerodynamic problems including the blended-wing body configuration as published in Ref. [83].

Due to the requirements of this project, the author has also contributed some modifications to the adjoint solver. This includes the periodical boundary condition and adding in the influence of the reference area (which is required in the calculations of the aerodynamic coefficients, i.e. lift and drag coefficients) on the sensitivity derivatives. Besides this, the adjoint solver has also been parallelised with the same MPI implementation that has been used on the flow solver.

At the start of this section, the derivation of the adjoint equations will be presented. A few chosen examples on the calculation of the exact RHS Jacobian are also presented. After showing some details on the linearisation of the turbulence model, the calculations of the sensitivity derivatives when the adjoint solution is converged will be discussed. Finally, some remarks are made on the way the adjoint solver is parallelised using MPI.

### 4.3.1 The Adjoint Variable Formulation

This formulation is one of the quasi-analytical methods that are based on the differentiation of the governing equations of the flow field. The objective function is written as

$$F = F\left(\mathbf{Q}^*(\beta), \mathbf{X}(\beta), \beta\right) \tag{4.3}$$

where $\mathbf{Q}$ is the vector of fluid variables. The superscript * indicates that this vector is the converged values from the flow solution. The vector $\mathbf{X}$ is for the grid variables and $\boldsymbol{\beta}$ is the vector of design variables. As presented, $F$, $\mathbf{Q}$ and $\mathbf{X}$ are functions of $\beta$.

By differentiating Eqn. (4.3), the gradients or the sensitivity derivatives can be expressed as

$$\frac{dF}{d\beta_k} = \left(\frac{\partial F}{\partial \mathbf{Q}}\right)^t \frac{d\mathbf{Q}^*}{d\beta_k} + \frac{\partial F}{\partial \mathbf{X}}^t \frac{d\mathbf{X}}{d\beta_k} + \frac{\partial F}{\partial \beta_k} \tag{4.4}$$

Since the differentiation of the governing flow equations is in a residual form,

$$\frac{d\mathbf{R}}{d\beta_k} = \frac{\partial \mathbf{R}}{\partial \mathbf{Q}} \frac{d\mathbf{Q}^*}{d\beta_k} + \frac{\partial \mathbf{R}}{\partial \mathbf{X}} \frac{d\mathbf{X}}{d\beta_k} + \frac{\partial \mathbf{R}}{\partial \beta_k} = 0 \tag{4.5}$$

and adding this equation to Eqn. (4.4) by multiplying it with an adjoint vector $\boldsymbol{\lambda}$ gives

$$\frac{dF}{d\beta_k} = \left(\frac{\partial F}{\partial \mathbf{Q}}\right)^t \frac{d\mathbf{Q}^*}{d\beta_k} + \frac{\partial F}{\partial \mathbf{X}}^t \frac{d\mathbf{X}}{d\beta_k} + \frac{\partial F}{\partial \beta_k} + \boldsymbol{\lambda}^t \left(\frac{\partial \mathbf{R}}{\partial \mathbf{Q}} \frac{d\mathbf{Q}^*}{d\beta_k} + \frac{\partial \mathbf{R}}{\partial \mathbf{X}} \frac{d\mathbf{X}}{d\beta_k} + \frac{\partial \mathbf{R}}{\partial \beta_k}\right)$$

which is rearranged as

$$\frac{dF}{d\beta_k} = \left[\left(\frac{\partial F}{\partial \mathbf{Q}}\right)^t + \boldsymbol{\lambda}^t \frac{\partial \mathbf{R}}{\partial \mathbf{Q}}\right] \frac{d\mathbf{Q}^*}{d\beta_k} + \left[\left(\frac{\partial F}{\partial \mathbf{X}}\right)^t + \boldsymbol{\lambda}^t \frac{\partial \mathbf{R}}{\partial \mathbf{X}}\right] \frac{d\mathbf{X}}{d\beta_k} + \frac{\partial \mathbf{F}}{\partial \beta_k} + \boldsymbol{\lambda}^t \frac{\partial \mathbf{R}}{\partial \beta_k} \tag{4.6}$$

To solve for the adjoint vector, the following term in the RHS of Eqn. (4.6) is simply set to zero,

$$\left[\left(\frac{\partial F}{\partial \mathbf{Q}}\right)^t + \boldsymbol{\lambda}^t \frac{\partial \mathbf{R}}{\partial \mathbf{Q}}\right] = 0$$

which then leads to the adjoint equation

$$\left(\frac{\partial \mathbf{R}}{\partial \mathbf{Q}}\right)^t \boldsymbol{\lambda} = -\frac{\partial F}{\partial \mathbf{Q}} \tag{4.7}$$

Once Eqn. (4.7) has been solved for $\boldsymbol{\lambda}$, the sensitivity derivatives are calculated by

$$\frac{dF}{d\beta_k} = \left[\left(\frac{\partial F}{\partial \mathbf{X}}\right)^t + \boldsymbol{\lambda}^t \frac{\partial \mathbf{R}}{\partial \mathbf{X}}\right] \frac{d\mathbf{X}}{d\beta_k} + \frac{\partial F}{\partial \beta_k} + \boldsymbol{\lambda}^t \frac{\partial \mathbf{R}}{\partial \beta_k} \tag{4.8}$$

Note that in the form of Eqn. (4.7), the adjoint equation is presented in the discrete formulation since the residual vector $\mathbf{R}$ has been discretised as in Eqn. (2.8) and that the Jacobian $\dfrac{\partial \mathbf{R}}{\partial \mathbf{Q}}$ is of the same form as in Eqn. (2.24), which justify the formulation above as a discrete adjoint method since the adjoint equation has been discretised before being differentiated.

### 4.3.2 Solution Methodology

In the adjoint solver, the vector of conservative variables $\mathbf{Q}$ in Eqn. (4.7) is actually replaced by the vector of primitive variables $\mathbf{P}$. Thus, rewriting the adjoint equation again,

$$\left(\frac{\partial \mathbf{R}}{\partial \mathbf{P}}\right)^t \boldsymbol{\lambda} = -\frac{\partial F}{\partial \mathbf{P}} \tag{4.9}$$

A major advantage of using the discrete adjoint method is that the same solution methodology as employed in the flow solver can be applied to the adjoint Eqn.

(4.9). Hence, in order to use the same Jacobian as in the flow solver, the adjoint equation is expressed in the incremental form:

$$\left[\frac{\partial \widetilde{\mathbf{R}}\left(\mathbf{Q}^{*}\right)}{\partial \mathbf{P}}\right]^{t} {}^{n}\Delta\boldsymbol{\lambda} = -\left\{\frac{\partial F}{\partial \mathbf{P}} + \left[\frac{\partial \mathbf{R}\left(\mathbf{Q}^{*}\right)}{\partial \mathbf{P}}\right]^{t} \boldsymbol{\lambda}^{n}\right\} \tag{4.10}$$

with

$$\boldsymbol{\lambda}^{n+1} = \boldsymbol{\lambda}^{n} + {}^{n}\Delta\boldsymbol{\lambda}$$

Here, again note that the LHS Jacobian has a tilde symbol $\widetilde{\ }$ above it, which indicates that it is simplified and approximated. This approximation is acceptable since it is the RHS of Eqn. (4.10) that carries the physics of the equation whilst the LHS is only driving ${}^{n}\Delta\boldsymbol{\lambda}$ to zero. Therefore, by adding a fictitious time term, Eqn. (4.10) is transformed into

$$\left[\frac{1}{\Delta t}\frac{\partial \mathbf{Q}}{\partial \mathbf{P}} + \frac{\partial \widetilde{\mathbf{R}}\left(\mathbf{Q}^{*}\right)}{\partial \mathbf{P}}\right]^{t} {}^{n}\Delta\boldsymbol{\lambda} = -\left\{\frac{\partial F}{\partial \mathbf{P}} + \left[\frac{\partial \mathbf{R}\left(\mathbf{Q}^{*}\right)}{\partial \mathbf{P}}\right]^{t} \boldsymbol{\lambda}^{n}\right\} \tag{4.11}$$

It can now be noticed that Eqn. (4.11) has actually the same structure as that of Eqn. (2.26), where both equations can be expressed in the form $\mathbf{A}\mathbf{x} = \mathbf{b}$ with the same banded matrix $\mathbf{A}$. As a result, the same implicit solution methodology is employed to solve the adjoint equations, which is the approximate direct inversion method or BILU(0) technique as presented in *Section 2.4.2*. To save some computing time, the terms $\frac{\partial \widetilde{\mathbf{R}}\left(\mathbf{Q}^{*}\right)}{\partial \mathbf{P}}$ at the LHS and $\frac{\partial F}{\partial \mathbf{P}}$ at the RHS in Eqn. (4.11) are calculated once at the beginning of the computation and then stored in the memory for the rest of the iterations. The time-term on the LHS depends on $\Delta t$ that changes at each iteration with respect to the value of the total residual as in the flow solver. As for the RHS term, a term by term multiplication is performed and the Jacobian has to be exact. Examples on the calculation of this exact RHS Jacobian are presented in *Appendix D*.

### 4.3.3 Sensitivity Derivatives

Finally, once the solution of the adjoint vector $\boldsymbol{\lambda}$ has converged, the sensitivity derivatives can then be evaluated using Eqn. (4.8). However, for a pure aerodynamic shape optimisation, the design variables $\beta_k$ only influence the flow field

solution, and hence the objective function through the modifications of the computational grid. Consequently, the terms $\frac{\partial F}{\partial \beta_k}$ and $\frac{\partial \mathbf{R}}{\partial \beta_k}$ can be discarded, so that the sensitivity Eqn. (4.8) is rewritten as

$$\frac{dF}{d\beta_k} = \left(\frac{\partial F}{\partial \mathbf{X}}\right)^t \frac{d\mathbf{X}}{d\beta_k} + \boldsymbol{\lambda}^t \frac{\partial \mathbf{R}}{\partial \mathbf{X}} \frac{d\mathbf{X}}{d\beta_k} \tag{4.12}$$

Instead of a first differentiation with respect to the coordinates of the grid points and then a multiplication between the resulting matrix and the grid sensitivity matrix $\frac{d\mathbf{X}}{d\beta_k}$ as suggested above in Eqn. (4.12), the differentiation is done directly in the code by the use of chain rule. Consider the term $\frac{\partial \mathbf{R}}{\partial \mathbf{X}} \frac{d\mathbf{X}}{d\beta_k}$ as an example, it is actually calculated in the form

$$\frac{\partial \mathbf{R}}{\partial(\xi, \eta, \zeta)} \frac{\partial(\xi, \eta, \zeta)}{\partial \mathbf{X}} \frac{d\mathbf{X}}{d\beta_k} \tag{4.13}$$

where $(\xi, \eta, \zeta)$ are the metric terms. All these terms are already present in the flow solver and can be differentiated directly by hand in the code.

As mentioned earlier in *Section 4.3*, one of the modifications contributed by the author is adding the influence of the reference area on the sensitivity derivatives. Since the total projected area in the $\eta$-direction is taken as the reference area, this is achieved simply by adding another term into Eqn. (4.13) as

$$\frac{\partial \mathbf{R}}{\partial(\xi, \eta, \zeta)} \frac{\partial(\xi, \eta, \zeta)}{\partial A_{area}} \frac{\partial A_{area}}{\partial \mathbf{X}} \frac{d\mathbf{X}}{d\beta_k}$$

where $A_{area}$ is the reference area.

### 4.3.4 Parallel Implementation

Similar to the serial version of the flow solver, the adjoint solver has already been implemented with OpenMP. In addition to the task of speeding up the calculations of the adjoint vector, a certain amount of effort has also been put in to parallelise the calculation of the derivatives. The reasons are that the calculation of the sensitivity derivatives in Eqn. (4.12) is looped over the number design variables. As indicated in this equation, each calculation of the derivatives involves

large and time-consuming matrix multiplications. Therefore, parallelisation of this part is essential to avoid a bottleneck in the optimisation process when the grid resolution and the number of design variables are very large.

*Section 4.3.2* and *4.3.3* have already shown that the structure of the adjoint solver is similar to that of the flow solver MERLIN, i.e. the boundary conditions set-up and the usage of halo cells. Therefore, when solving for the adjoint vector, the same approach to that of parallelising MERLIN has been employed, which is to exploit the multiblock structure and hence the interface boundary condition. As a result, generally, the modifications involved in the code are very similar to what has been described in *Section 2.8*, only that now, instead of exchanging the flow variables, the blocks are exchanging the adjoint vector $\boldsymbol{\lambda}$.

The parallel efficiency of the adjoint solver has also been tested using the similar assessment method of Eqn. (2.48). The speed-up graph for the adjoint solver is shown in Figure 4.2. From this graph, it is observed that the parallelisation performance of the adjoint solver is found to be at similar level as that of the flow solver. Consequently, this parallel version of the adjoint solver has also been awarded a Bronze level award by the HPCx team for this level of scaling capability.

However, it should be pointed out that the interface boundary condition in the adjoint solver actually involves an extra layer of halo cells for an inviscid higher-order scheme (as described in *Section 4.3.3.1*). This did not cause any further difficulties in the coding since the same solution methodology can be used.

The calculations of the sensitivity derivatives are only carried out after the solution of the adjoint solver is converged and can be considered as a separate module from the main core of the adjoint vector calculations. As discussed earlier in this section, it is necessary to parallelise this part to avoid a bottleneck in large optimisation problems. Again, from Eqn. (4.12), the grid sensitivities $\frac{d\mathbf{X}}{d\beta_k}$ of the whole volume grid, which is updated by employing an analytical grid deformation technique as pointed out in *Section 4.2*, has to be recalculated for each of the design variables $\beta_k$. For the code to be data-parallel efficient, each processor only stores the grid for its own block. However, each $\beta_k$ could have influences in multiple blocks because the wing surface has to be modified as a whole. Take the twisting angle of a master section and a block that is situated across this section

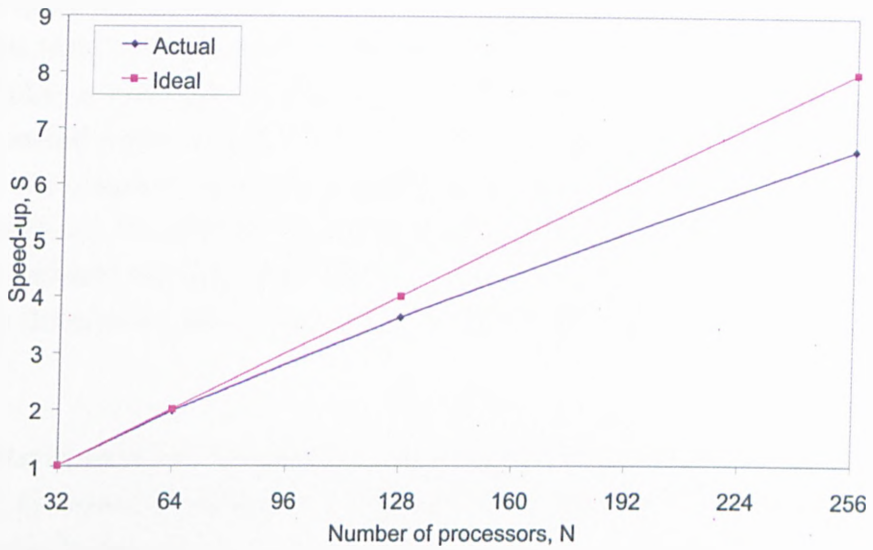


Figure 4.2: Speed-up with respect to the number of processors for the adjoint solver.

as shown in Figure as an example.

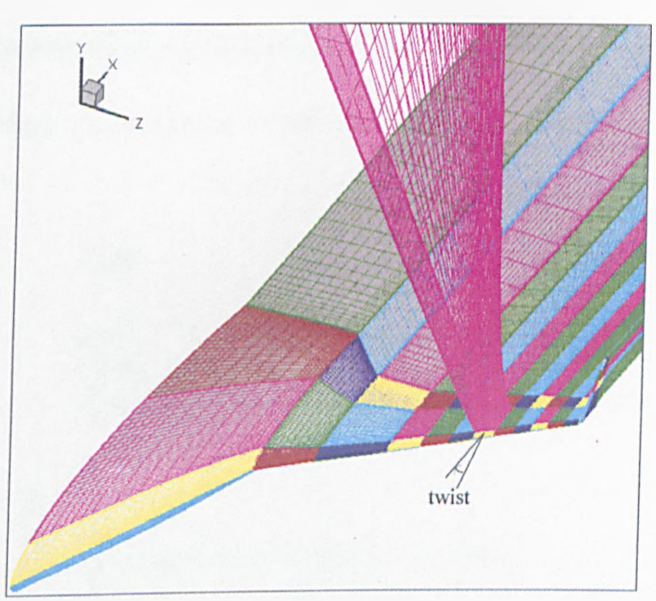


Figure 4.3: Dependency of the grid sensitivities in a block.

A change in this design variable will affect at least the whole section, which in

turn spans across multiple blocks. Thus, the grid sensitivities in the volume grid of this block are influenced by this design variable and also several other design variables as well, such as the Bézier control points on the master sections that are located within this block. Consequently, each processor has to be provided with the complete surface grid modified by $\beta_k$ so that the grid sensitivities in its block can be computed properly. Each processor then computes Eqn. (4.12) independently but simultaneously. The values from each processors are summed up on the master node to form the final value of the sensitivity derivatives for $\beta_k$.

Here terminates the descriptions of the adjoint solver employed in this project, which has basically explained how the sensitivity derivatives have been calculated. Referring back to the optimisation chain (Figure 4.1) again, by following the route of the chain, first the grid modeller, followed by the flow solver MERLIN which has already been detailed in *Chapter 2* and then the adjoint solver. We have now reached the bottom of the chain or rather the essential part of the optimisation chain, that is the Sequential Quadratic Programming or SQP optimiser, which will be presented in the next section.

## 4.4 Sequential Quadratic Programming Optimiser

A general problem of a constrained optimisation can be expressed mathematically as [90]:

$$\begin{array}{lllll} \text{Minimise} & F(\boldsymbol{\beta}) & & & \text{objective function} \\ \boldsymbol{\beta} & & & & \\ \text{Subject to:} & g_i(\boldsymbol{\beta}) \leq 0 & i = 1, l & & \text{inequality constraints} \\ & h_j(\boldsymbol{\beta}) = 0 & j = 1, m & & \text{equality constraints} \\ & \beta_k^l \leq \beta_k \leq \beta_k^u & k = 1, NDV & & \text{side constraints} \end{array} \tag{4.14}$$

where $\boldsymbol{\beta} = \left\{ \begin{array}{c} \beta_1 \\ \beta_2 \\ \vdots \\ \beta_{NDV} \end{array} \right\}$ is the vector of design variables.

For aerodynamic optimisation, the objective function can be the drag coefficient (which is mostly the case in this thesis) or the lift-drag ratio. Although the expressions above indicate that the objective function is to be minimised, bear in

mind that minimising $-F(\boldsymbol{\beta})$ is the same as maximising it, which shall be employed if the lift-drag ratio were chosen to be maximised. An example for the inequality constraints is the limit on the volume of a wing. One of the most common practise in aerodynamic optimisation is to minimise drag at a given fixed lift, hence here, the lift is an equality constraint. Finally, the side constraints are just the lower and upper bound limits for the design variables in the design space.

As indicated in the introduction of this chapter and Figure 4.1, throughout this project, the optimisation problem is solved using an iterative method. The optimisation process starts from an initial value of the vector of design variables $\boldsymbol{\beta}$, which is commonly referred as the baseline configuration, the design is then updated iteratively until a minimum of the objective function $F$ is reached. The vector of design variables are updated by:

$$\boldsymbol{\beta}^q = \boldsymbol{\beta}^{q-1} + \alpha^q \mathbf{S}^q \tag{4.15}$$

Here, $q$ is the iteration number, $\alpha^q$ is a scalar which defines the step-size taken in the search direction within the design space that is defined by the vector $\mathbf{S}^q$. Consequently, two unknown values of $\alpha^q$ and $\mathbf{S}^q$ need to be solved for. This is where the SQP optimiser comes in. Detailed descriptions of the SQP optimiser can be found in *Appendix E.*

In this project, two SQP optimiser subroutines have been employed. They are the subroutine E04UCF from the NAG library [91] and the subroutine FFSQP provided by AEMDesign [92]. Both the subroutines are designed to solve the non-linear programming problem of minimising a smooth non-linear objective function of $n$ variables subject to some constraints. These constraints are lower and upper bounds on the variables, linear and non-linear inequality or equality constraints. As already stated, both of them require the gradients of the objective function and of the constraint, which are provided by the adjoint solver.

The main difference between these two subroutines is that the subroutine E04UCF allows designs that do not satisfy the non-linear constraints during the optimisation process until the final optimal design point is reached. In contrast, the subroutine FFSQP, which is an abbreviation for FORTRAN Feasible Sequential Quadratic Programming, will always generate a feasible design that satisfies the

non-linear constraints for every optimisation iteration.

Despite this difference, an investigation conducted by Le Moigne in Ref. [74] has shown that, at the same design conditions and starting from the same design sets, the optimal aerofoil design found by the two optimisers were very similar with little discrepancies. In this project, the FFSQP is the chosen subroutine for most of the optimisations. Nevertheless, the possible inconsistencies on the outcome of the results of using different subroutines are then minimal.

This chapter has introduced the optimisation methodologies employed to optimise the performance of both the 2D and 3D shock control bumps, which is the main interest of this project. In the following chapter, the results on the performance of the 2D bump will first be presented.

# Chapter 5

# Mechanisms and Optimisations of 2D Bumps on Unswept Wings

Extensive research has already been carried out on the performance of 2D bump including optimisation, and it has been proven to work particularly well. However, the author has not so far encountered literature that involved optimisation of the 2D bump using adjoint methods. Therefore, this chapter sets out to optimise the performance of the 2D bump using the adjoint-based optimisation method and to provide some insight into the mechanism of this kind of device as well. Besides that, this is also a reasonable way to start the project, gaining essential experiences in using the numerical tools.

The following results will only include the performance of a 2D bump on an unswept wing with two different types of aerofoil sections. The chosen aerofoil types include the RAE 5243 NLF aerofoil and the RAE 2822 turbulent aerofoil. The next section presents the parameterisation of the 2D bump employed in this project.

## 5.1 Initial 2D Bump Parameterisations

There are various possible shapes for 2D bumps, i.e. loaded beam, triangular shape or ramp, concave polynomial and polynomial as investigated by Sommerer *et al.* [38]. However, it has been concluded that the shape of the bump has minor effects on the drag reduction [38, 11]. Consequently, for simplicity, the author has chosen to define the shape of the bump with a simple cubic polynomial as written below:

$$y = bx^3 + cx^2 + dx + e \tag{5.1}$$

As shown in Figure 5.1, the bump is parameterised by four essential design variables, the upstream and downstream points of the bump, $x_{st}/c$ and $x_{end}/c$, the position of the crest of the bump, $x_{cre}/c$ and the maximum height of the bump, $\Delta y_h/c$. Here, the subscripts $st$, $cre$ and $h$ are abbreviations denoting *start*, *crest* and *height* respectively.

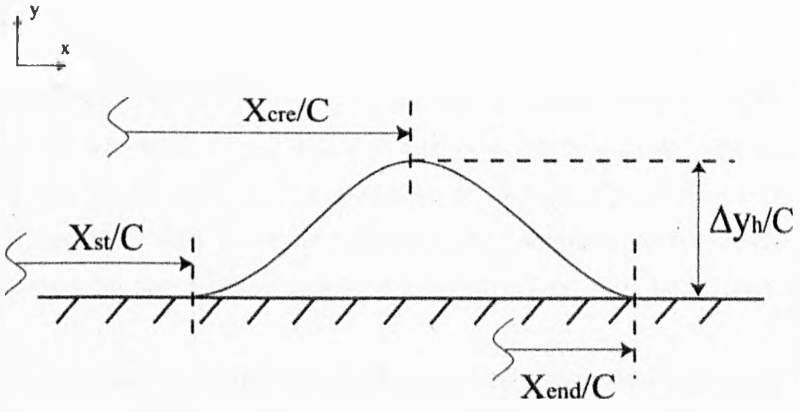


Figure 5.1: Parameterisations of 2D bump.

Note that the 2D bump is added on top of the aerofoil profile. Hence, the gradient at the crest of the 2D bump is evaluated such that it is aligned with a line connecting $x_{st}/c$ and $x_{end}/c$, hence tangential to the local aerofoil profile. The gradients at both ends of the 2D bump are evaluated such that the local curvature is maintained. Therefore, the cubic spline equation (Eqn. (5.1)) can then be solved via a set of equations with these known design parameters and gradients.

For the sake of convenience, the designation of the 2D bump can be expressed in abbreviated form, for example, *st48.5-e68.5-cre60-h0.6* defines a bump that starts at $x_{st}/c = 48.5\%$, ends at $x_{end}/c = 68.5\%$, its bump crest is located at $x_{cre}/c = 60\%$ and with a height of $\Delta y_h/c = 0.6\%$.

These are the parameters that have been defined at the preliminary stage of the investigations. However, in order to tackle several optimisation issues, the

parameters have indeed been revised, which will be discussed in further detail at appropriate stages of this chapter.

## 5.2 Unswept Wing with RAE 5243 NLF Aerofoil Section

The RAE 5243 NLF blunt trailing edge aerofoil has been adopted in various references involving investigation into shock control [26, 31, 30, 27, 47]. It has a maximum thickness to chord ratio of 14% and was designed at a freestream Mach number of 0.68. This type of aerofoil is of particular interest for shock control purposes for several reasons. First of all, it will be even more beneficial to combine the potential of wave drag reduction from the shock devices with the laminar flow nature of the aerofoil that reduces the skin friction drag. Besides that, the position of the shock wave is less sensitive to the change of flow conditions for this type of aerofoil. This is important since the performance shock control bump largely depends on the relative position between them and the shock wave.

In order to save some computational effort and to enable the turbulent viscosities at the wake to be copied from the neighbouring block, the blunt trailing edge of the aerofoil has been sharpened by employing the method suggested by Zhu [30]. As a result, without the extra block that would have been needed if the trailing edge were blunt, Figure 5.2 shows a typical C-type grid with four blocks. Note that the grid shown here is generated for inviscid two-dimensional investigations, therefore the grid only consists of around 248×31 cells. Here, the far-field boundary is more than 20 times chord distance away from the aerofoil surface. On the other hand, Figure 5.3 shows the trailing edge of the aerofoil that has been sharpened. The grid resolution is not clustered close to the aerofoil surface since the boundary layer need not be modelled yet. The grids are however clustered at the vicinity of the known location of the shock wave to enable better capturing of the shock structure.

The freestream Mach number is set to 0.68 and a Reynolds number of 19 million based on chord. These conditions correspond to the cases studied in the literature mentioned in the earlier paragraph of this section. Without the viscous effects, at

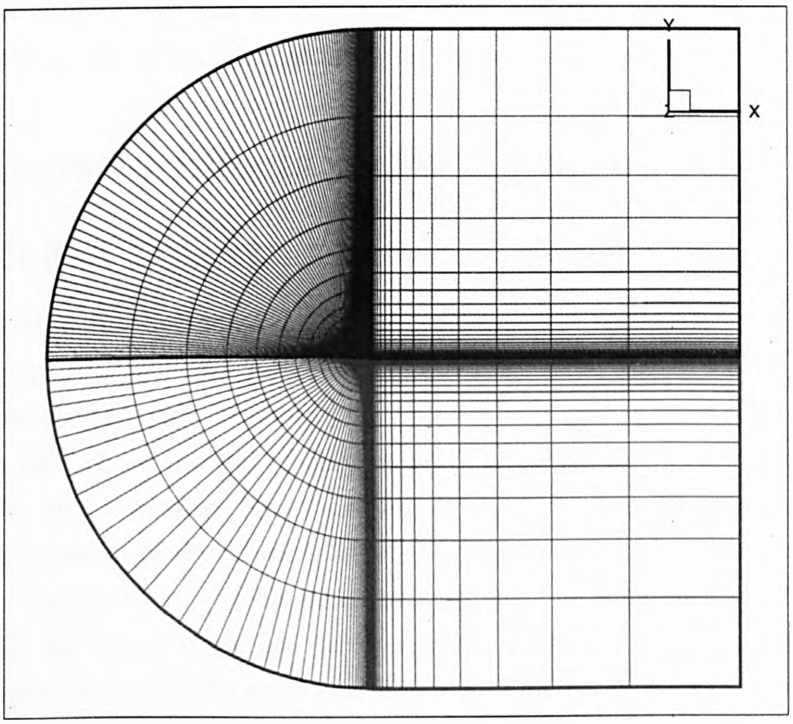


Figure 5.2: A typical C-type grid with four blocks. (RAE 5243)

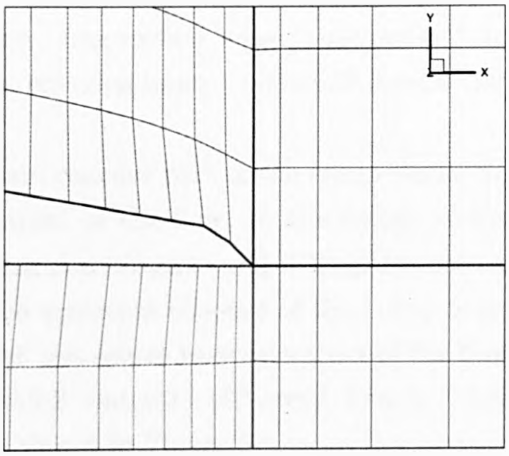


Figure 5.3: The sharpened TE on the RAE 5243 aerofoil.

an angle of attack of $1.5^0$, the calculated lift coefficient is 0.823. Hence, throughout the investigation of the inviscid performance of the 2D bump, $C_L = 0.823$ serves as the target lift coefficient that has to be constrained.

## 5.3 Inviscid Effects of 2D Bump on RAE 5243

### 5.3.1 Initial Designs

Before starting the optimisation, some preliminary investigations were carried out. A design of *st48.5-e68.5-cre60-h0.2* is derived from Monet's brief 2D bump viscous investigation [46]. However, the bump is modified to have the bump crest located at 62% chord instead of 60% chord, due to the following reasons. With the absence of a boundary layer, a strong normal shock is formed on the aerofoil, so the position of the shock is located further downstream compared to the position of the shock in viscous flow. Besides that, as suggested by Birkemeyer *et al.* [36], the bump crest has to be located slightly downstream relative to the position of the shock for good performance. The computed pressure distribution on the surface of the aerofoil with and without bumps is shown in Figure 5.4.

For the bump *st48.5-e68.5-cre62-h0.2*, the pressure distribution plot shows that a compression wave is indeed generated since the flow just upstream the shock is slowed down. However, the flow re-accelerates before reaching the bump crest and hence shifting the shock downstream. As the bump height is increased to 0.3% chord, a stronger compression wave is generated. However, the flow still re-accelerates like the previous bump *st48.5-e68.5-cre62-h0.2*.

Since the long upstream concave part of the bump seems to be the reason behind the severe re-acceleration of the flow, so the design of the bump is revised to consist of a short upstream concave and a long downstream concave. Hence a steeper gradient at the upstream concave of the bump to generate stronger compression wave but with less severe re-acceleration of the flow. The revised bumps are *st55-e80-cre61.9-h0.2* and *st55-e80-cre61.9-h0.3*. Their computed pressure distribution plots are shown in Figure 5.5.

Figure 5.5 indicates that the previous hypothesis on the revised bump is sensible. Without the severe re-acceleration of the flow, the maximum Mach number is

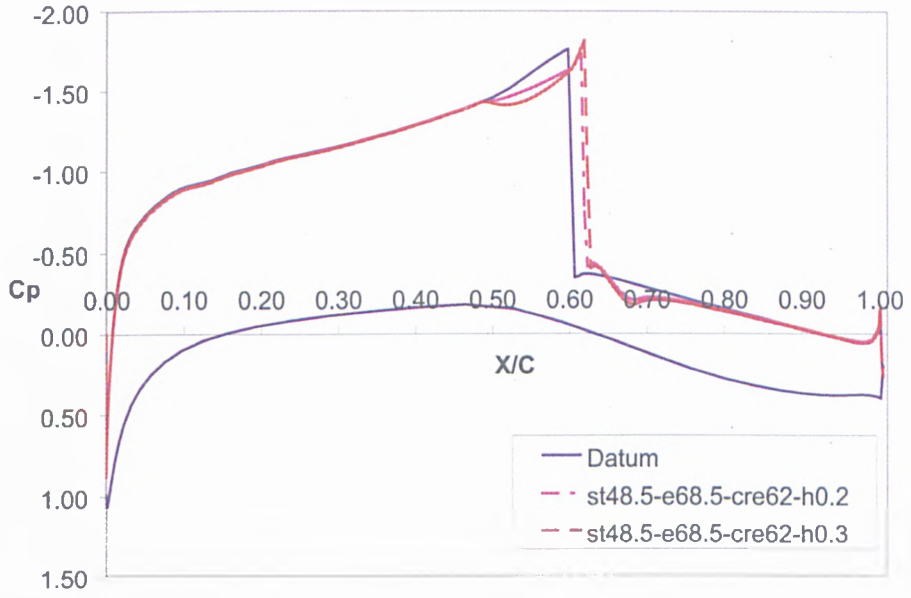


Figure 5.4: Computed pressure distribution for the preliminary designed bumps. (RAE 5243, $M_\infty = 0.68$, $C_L = 0.82$)

lowered, hence the strength of the shock is weakened. Note that the speed of the flow after the shock or at the long downstream concave part of the bump is higher compared to the clean aerofoil; hence the entropy increase across the shock is lowered. Consequently, wave drag is reduced.

## 5.3.2 Optimisation Results

### 5.3.2.1 Unconstrained and Constrained Bump Length

The context of this optimisation task is to minimise the objective function, which is here the total drag coefficient, $C_D$, while constrained at the target lift coefficient, $C_L = 0.823$ by changing the incidence $\alpha$. Initially the four design variables to be optimised are the four essential parameters that define the shape of the bump as described in *Section 5.1*. So, the four design variables are able to move freely and independently. Subsequently, it was soon realised that the optimiser would then allow the bump to grow over almost the whole aerofoil upper surface, starting from 36%c to 80%c. In other words, the optimiser is optimising the geometry of the whole aerofoil upper surface using the geometrical definition of

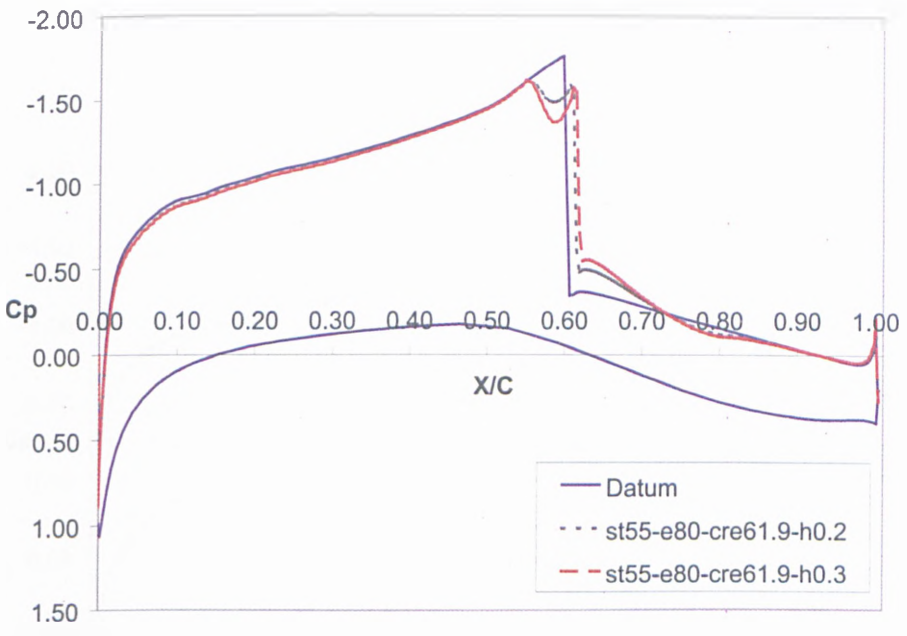


Figure 5.5: Computed pressure distribution for the revised designed bumps. (RAE 5243, $M_\infty = 0.68$, $C_L = 0.82$)

the bump. Thus, obviously, the length of the bump has to be constrained for a more reasonable optimisation.

The first attempt was to constrain the upper and lower boundaries of $x_{st}/c$ and $x_{end}/c$ within a specific region, e.g. bounded within 55%c and 80%c. By doing so, the bump is fixed within a definite region with the maximum length of 25% chord, but still allowed to shrink. Both these design parameters are not allowed to move freely over the aerofoil, because they might crossover with each other and possibly with $x_{cre}/c$ too. This approach was first considered because minor modifications were only needed in the optimiser. Hence, in this case, $x_{st}/c$ has a maximum upstream boundary at 55% chord and $x_{end}/c$ is allowed to grow up to 80% chord. Figure 5.6 displays the computed pressure distribution plots for the optimised bump found using this method and also the case where the bump length was not constrained.

For the 2D bump optimised with the bump length as a constraint, the upstream maximum Mach number of the shock is further reduced, and the speed of the flow

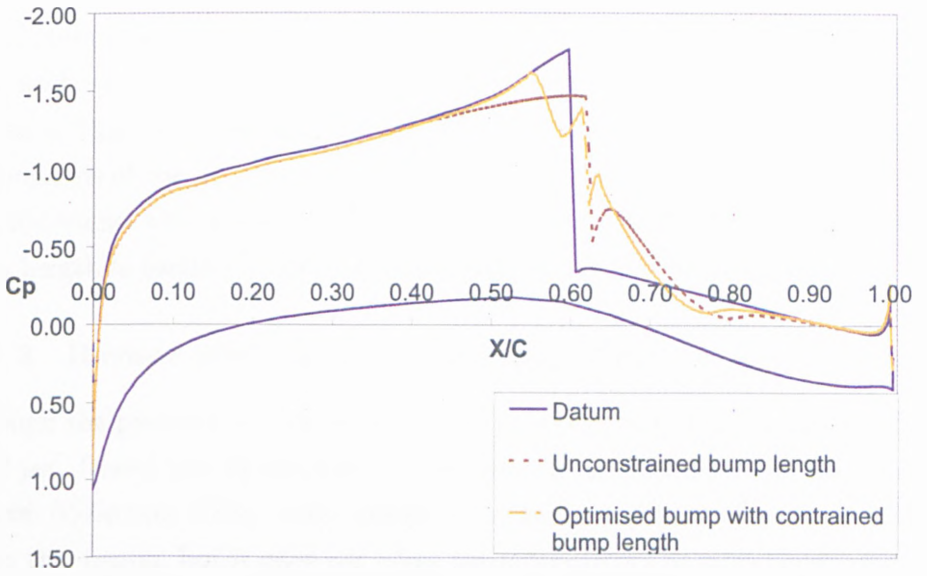


Figure 5.6: Computed pressure distribution for the optimised bumps with and without bump length constraint. (RAE 5243, $M_\infty = 0.68$, $C_L = 0.82$)

| | $C_{Dpressure}$ | Total Drag Reduction |
|---|---|---|
| Datum aerofoil | 0.011681 | - |
| ***Unconstrained bump length*** | 0.006747 | 42.2% |
| ***Constrained bump length*** | 0.007442 | 36.3% |

Table 5.1: Comparisons of performance for the optimised 2D bump without and with constrained bump length. (RAE 5243, $M_\infty = 0.68$, $C_L = 0.82$)

aft of the shock is higher than before, hence resulting in a relatively weakened shock. The inviscid drag reduction achieved by this optimised bump is up to 36%. As observed from the pressure distribution plot for the optimised bump that is unconstrained by the bump length, instead of weakening the shock by a compression wave, the geometry of the aerofoil was optimised to weaken the shock such as that of a supercritical aerofoil. Thus, the strength of the shock is lowered so that the upstream pressure distribution tends to be a "rooftop" trend. Comparisons of the performance in Table 5.1 indicate that it also performs better than the bump with constrained bump length. This method of constraining the bump length is further revised and discussed in the following section.

#### 5.3.2.2 Revised Method for Constraining Bump Length

Although the previous optimisation results look promising, the bump is not optimised yet. Recall that the location of the bump is restricted to a particular region between 55%c and 80%c, even though $x_{st}/c$ and $x_{end}/c$ are allowed to translate within this region, but it does not allow the entire bump to move freely elsewhere on the aerofoil. Instead, for a better and more sensible optimisation, the location of the bump should be allowed to move freely within the aerofoil upper surface while the maximum bump length is still constrained. The method should also be able to avoid possible crossovers between $x_{st}/c$, $x_{end}/c$ and $x_{cre}/c$ effectively. By referring to Birkemeyer's efforts in Ref. [36], an additional bump parameter, which is the relative position of the bump crest with respect to the bump length, is defined as

$$bump_{relative} = \frac{x_{cre}/c - x_{st}/c}{x_{end}/c - x_{st}/c} \tag{5.2}$$

Consequently, the original design variables $x_{st}/c$ and $x_{end}/c$ are then replaced by the bump length, $bump_{length} = x_{end}/c - x_{st}/c$ and $bump_{relative}$ respectively in the optimiser. Therefore, the total number of design variables still remains as four. Although the two original bump design variables have been replaced in the optimiser, the bump is actually still generated by the grid modeller using the same four parameters as described in *Section 5.1*. In other words, the two new parameters described above, $bump_{length}$ and $bump_{relative}$ actually define the values of both $x_{st}/c$ and $x_{end}/c$. As a result, the parameterisations illustrated in Figure 5.1 are being replaced with the following illustration:

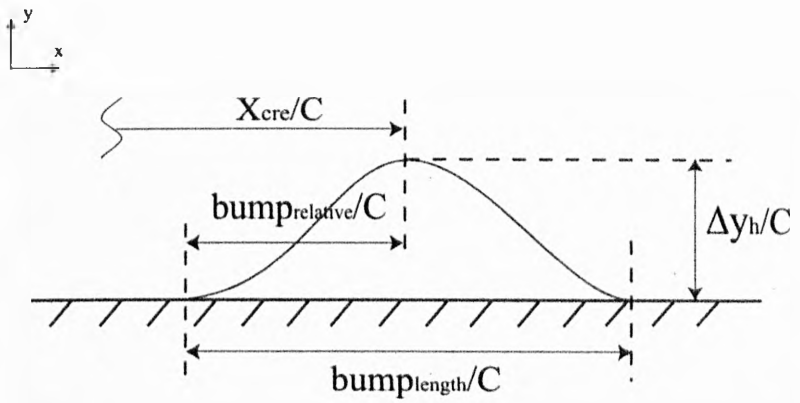


Figure 5.7: Revised parameterisations of 2D bump.

Without having to define the upper and lower boundaries for $x_{st}/c$ and $x_{end}/c$, the bump length and the shape of the bump (i.e. bump with longer upstream and shorter downstream shape) being defined by $bump_{length}$ and $bump_{relative}$ respectively and that the location of the bump is determined by $x_{cre}/c$; the bump is now allowed to move anywhere within the aerofoil upper surface whilst having the length constrained. Any possible crossover or violation between the design parameters is also avoided with this approach. The designation of the bump is modified as, for example, a *l20-cre63-cb50-h0.6* bump has a bump length of 20%c with the bump crest located at 63%c and at 50% of the bump length (hence a symmetrical bump), and a bump height of 0.6%c. There are additional benefits to these modifications as well. As demonstrated in this bump designation example, it would provide a more convenient and direct interpretation of the shape of the bump, i.e. symmetrical or asymmetrical with longer upstream, etc.

Two optimisation cases have been run using this revised method, one with a maximum allowable bump length of 20%c and another with 25%c. Note that the previous optimised bump has a designation of *l20-cre63.2-cb33-h0.6* and by taking this as the initial design for the optimisation, Figure 5.8 below plots the convergence history of the objective function (total drag coefficient, $C_D$) for the optimisation case with 25%c maximum allowable bump length.

The optimised bumps obtained from both cases have the designation *l20-cre63.3-cb66.8-h0.61* and *l25-cre63.6-cb54.5-h0.75*. The location of the bump crest is similar to that of the previous effort, but the shape of the bump has now changed.

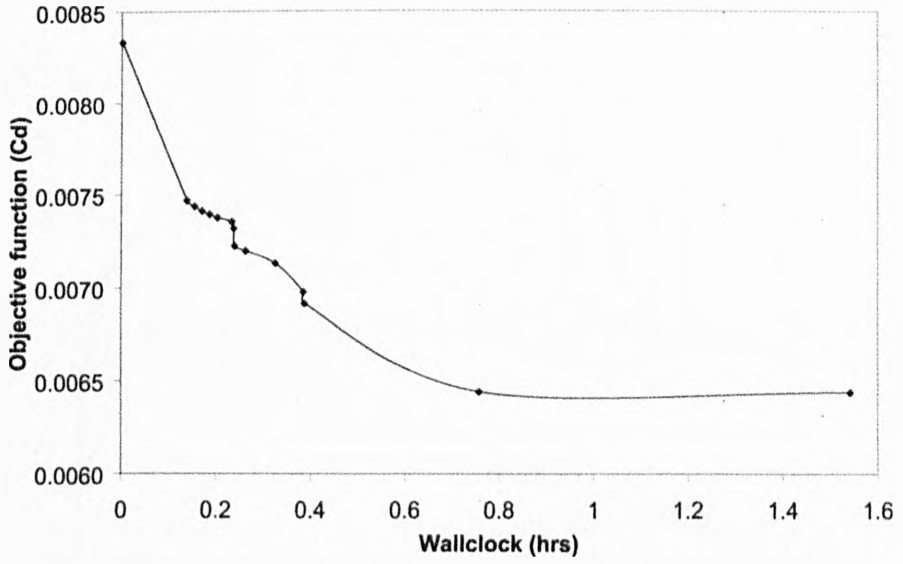


Figure 5.8: Convergence history of the objective function.

Instead of an asymmetric short upstream shape, both bump crests of the optimised bumps are located at 67% and 55% relative to the bump length, hence they are still asymmetric but with longer upstream and shorter lee side. A further pressure drag reduction of about 43% and 45% have been achieved by the optimised bumps with maximum allowable bump length of 20%c and 25%c respectively.

| | $C_{Dpressure}$ | **Total Drag Reduction** |
|---|---|---|
| Datum aerofoil | 0.011681 | - |
| ***l20-cre63.3-cb66.8-h0.61*** | 0.006582 | 43.1% |
| ***l25-cre63.6-cb54.5-h0.75*** | 0.006338 | 45.2% |

Table 5.2: Comparisons of performance for the optimised 2D bump with revised bump length constraint method. (RAE 5243, $M_\infty = 0.68$, $C_L = 0.82$)

The predicted pressure distribution plots in Figure 5.9 depict the generation of a strong isentropic compression wave. The remaining shock waves shown in the pressure contour plots in Figures 5.11 (a) and (b) for both the optimised 2D bumps are relatively much weaker compared to the datum aerofoil shown in Figure 5.10 since the isobar contours are not as dense as before at the vicinity of

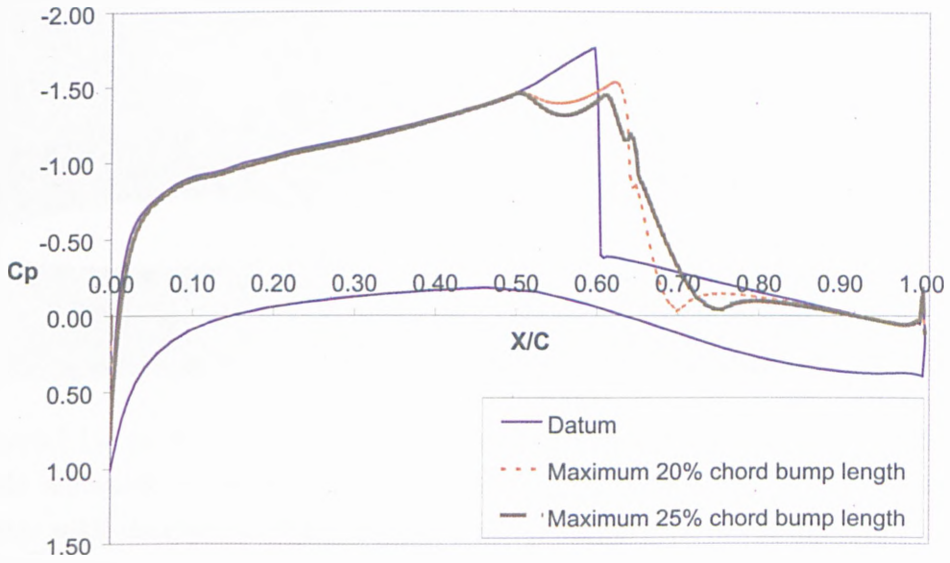


Figure 5.9: Computed pressure distribution plots for both the optimised 2D bumps in inviscid flow. (RAE 5243, $M_\infty = 0.68$, $C_L = 0.82$)

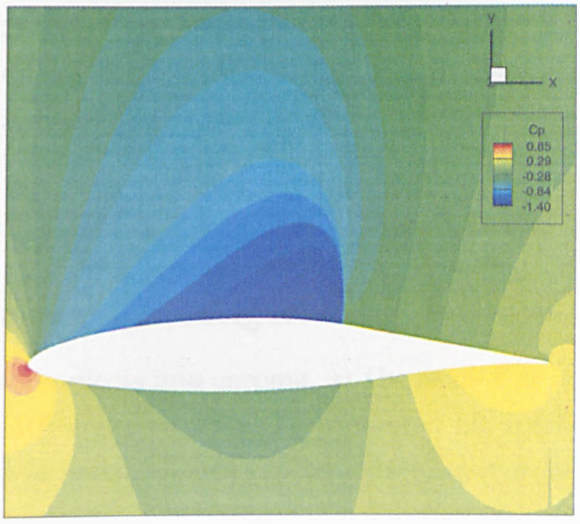


Figure 5.10: Pressure contour plots for the datum aerofoil. (RAE 5243, $M_\infty = 0.68$, $C_L = 0.82$)

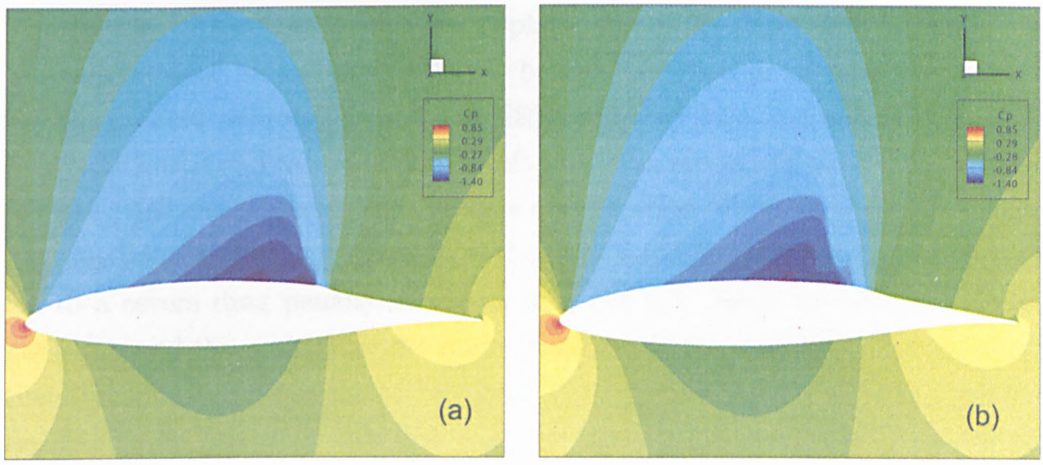


Figure 5.11: (a) Pressure contour plots for the optimised 2D bump with maximum 20%c allowable bump length. (b) Pressure contour plots for the optimised 2D bump with maximum 25%c allowable bump length. (RAE 5243, $M_\infty = 0.68$, $C_L = 0.82$)

the shock. It is demonstrated here that proper design of the 2D bump can be achieved through appropriate bump parameterisations and aerodynamic optimisations. Both the optimised 2D bumps are found to be effective in weakening the shock wave. Building on the experiences gained from this inviscid study, we optimise the design the of the 2D bump with the presence of the boundary layer in the following section. Viscous effects from the 2D bump and its mechanisms are then investigated and analysed.

## 5.4 Viscous Effects of 2D Bump on RAE 5243

### 5.4.1 Preliminary Investigations

By taking the viscous effects into account, at the same flow conditions of $M_\infty = 0.68$, $Re_c = 19 \times 10^6$ and $\alpha = 1.5°$, the computed lift coefficient, $C_L$ becomes 0.69. Note that it is assumed that the boundary layer is fully turbulent right from the LE of the aerofoil. The resolution in the direction normal to the flow or the $\eta$-direction has to be refined to properly model the turbulent boundary layer. Therefore, grid points are clustered near the aerofoil surface so that $y^+$ is around 1. As a result, the total resolution of the grid is increased to around 248×61 cells.

The position of the shock wave has displaced about 3%c upstream compared to the inviscid case. Hence, one of the 2D bumps optimised in the previous section for the inviscid investigations, bump *l20-cre63-cb67-h0.6* was modified as *l20-cre60-cb67-h0.6* and tested under the lift condition mentioned above, $C_L = 0.69$. However, the result shows that there are deterioration effects from the 2D bump, a strong double-shock system is formed on the aerofoil upper surface, which has led to a severe drag penalty as shown in Table 5.3. Since the location of the 2D bump and the position of the bump crest should be reasonable, this suggests that the bump height might be too high. Through some numerical tests, a more sensible bump height for this flow condition and bump configuration was found to be around 0.25%c, which gives around a 6% reduction of drag from the datum case as listed in Table 5.3.

| | $C_{Dtotal}$ | $C_{Dpressure}$ | $C_{Dfriction}$ | **Total Drag Reduction** |
|---|---|---|---|---|
| Datum aerofoil | 0.01282 | 0.007023 | 0.005794 | - |
| *l20-cre60-cb67-**h0.6*** | 0.01725 | 0.011746 | 0.005503 | -34.6% |
| *l20-cre60-cb67-**h0.25*** | 0.01205 | 0.006255 | 0.005837 | 6.3% |

Table 5.3: Comparisons of the viscous test cases for 2D bump, $M_\infty = 0.68$, $C_L = 0.69$.

| | $C_{Dtotal}$ | $C_{Dpressure}$ | $C_{Dfriction}$ | **Total Drag Reduction** |
|---|---|---|---|---|
| Datum aerofoil | 0.01622 | 0.010630 | 0.005586 | - |
| *l20-cre60-cb67-**h0.6*** | 0.01764 | 0.012165 | 0.005474 | -8.8% |
| *l20-cre60-cb67-**h0.4*** | 0.01398 | 0.008555 | 0.005425 | 16.2% |

Table 5.4: Comparisons of the viscous test cases for 2D bump, $M_\infty = 0.68$, $C_L = 0.82$.

The same bump *l20-cre60-cb67-h0.6* is again tested under a relatively higher lift coefficient at $C_L = 0.82$, where the strength of the shock is consequently stronger as well. In terms of performance in drag reduction, the results in Table 5.4 indicates that this bump height is still inappropriate, which has a 8% drag penalty compared to the datum case. The double-shock incurred by this bump is depicted in Figure 5.12 (a), with the secondary shock formed at the 2D bump.

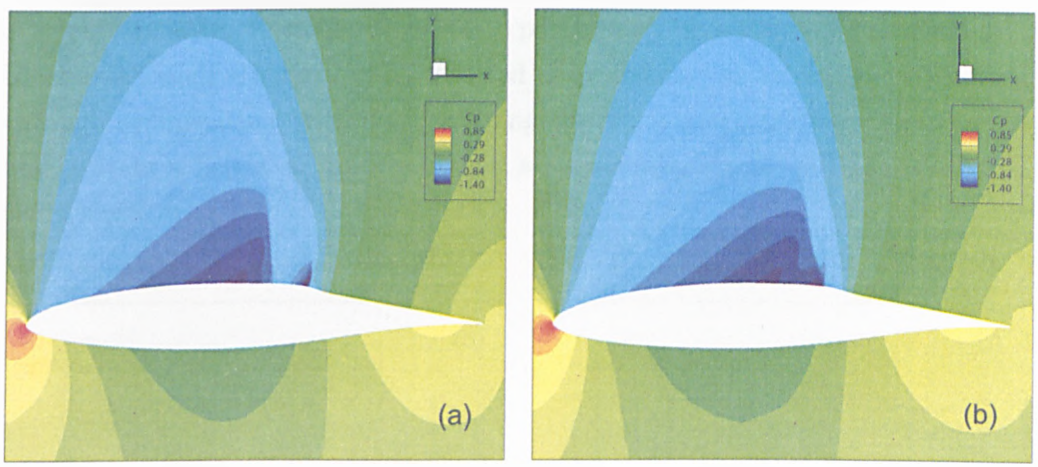


Figure 5.12: (a) Pressure contour plots for the bump *l20-cre60-cb67-h0.6*. (b) Pressure contour plots for the bump *l20-cre60-cb67-h0.4*, $C_L = 0.82$.

Again, with some trial and errors, the possible "optimum" bump height for this 2D bump configuration at this higher lift condition is around 0.4%c. From Table 5.4, this 2D bump with a lowered height can provide 16% reduction in drag. Figure 5.12 (b) demonstrates that with the appropriate bump height, there is no double-shock and the original main shock is smeared and weaken. Therefore, these preliminary investigations suggest that the optimum height of the 2D bump varies with respect to the lift coefficient and the strength of the shock wave. These findings correspond to the conclusions in Birkemeyer's report [36]. In other words, for optimum performance, the 2D bump has to be adaptive to the flow conditions.

### 5.4.2 Optimisation Results

The constrained lift coefficient is chosen as $C_L = 0.82$, to provide a stronger shock wave and hence highlights the off-design performance of the 2D bump. In addition, instead of confining the maximum bump length to 25%c, it was decided to relax the design space constraint and allow the bump to grow to up to 40%c. The obtained optimised 2D bump has a designation of *l31.3-cre59.7-cb66.1-h0.59*.

Figure 5.13 (a) illustrates the optimised 2D bump generated on the upper surface of the aerofoil with figure 5.13 (b) showing a closeup picture of the 2D bump. By referring back to the 2D bump designation of *l31.3-cre59.7-cb66.1-h0.59*, it can be observed that the shape of the 2D bump has a longer upstream concave with

a height of ~6%c. Recalling that in the preliminary investigations, the tested 2D bump with such a height gave increased drag and had to be lowered. However, through optimisation, with a slight change in bump shape and size, the flow can now sustain a height of 6%c without a strong double-shock and hence substantially lower drag.

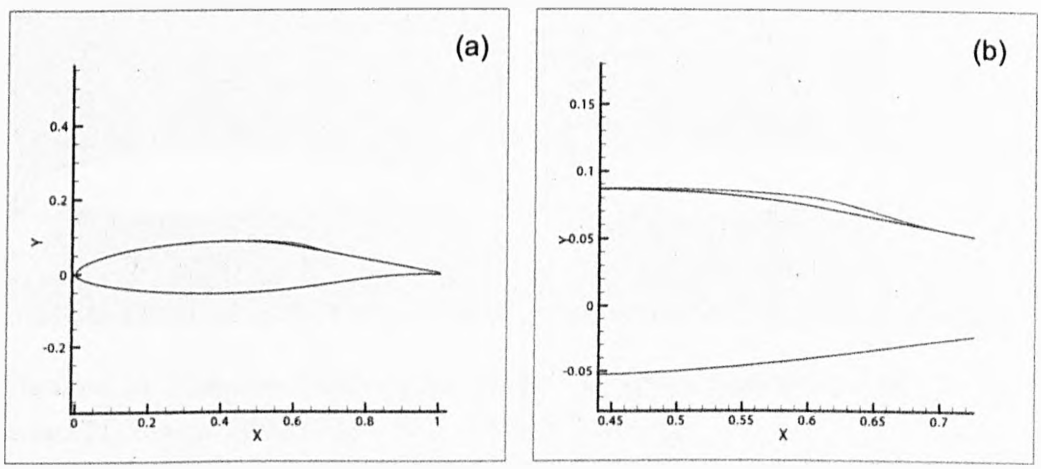


Figure 5.13: (a) Aerofoil with the optimised 2D bump generated on the surface. (b) Closeup on the 2D bump.

| | $C_{Dtotal}$ | $C_{Dpressure}$ | $C_{Dfriction}$ | **Total Drag Reduction** |
|---|---|---|---|---|
| Datum aerofoil | 0.01622 | 0.010630 | 0.005586 | - |
| ***Optimised 2D bump*** | 0.01326 | 0.007563 | 0.005700 | 18.2% |
| ***l20-cre60-cb67-h0.4*** | 0.01398 | 0.008555 | 0.005425 | 16.2% |

Table 5.5: Comparisons of the drag components for the optimised 2D bump. (RAE 5243, $M_\infty = 0.68$, $C_L = 0.82$)

Table 5.5 compares the computed drag components for the datum aerofoil, the optimised 2D bump and also along with the 2D bump from the preliminary investigations. From the table, the optimised 2D bump achieved a 18% total drag reduction from the datum aerofoil or about 30 drag counts. Compared to the manually designed 2D bump *l20-cre60-cb67-h0.5*, a further reduction of 13 drag counts has been obtained from the optimisation. Although there is a 1~2% increase in skin friction drag, nonetheless, this viscous drag penalty is insignificant

when compared to the huge pressure drag reduction achieved by the optimised 2D bump, which is over 25%.

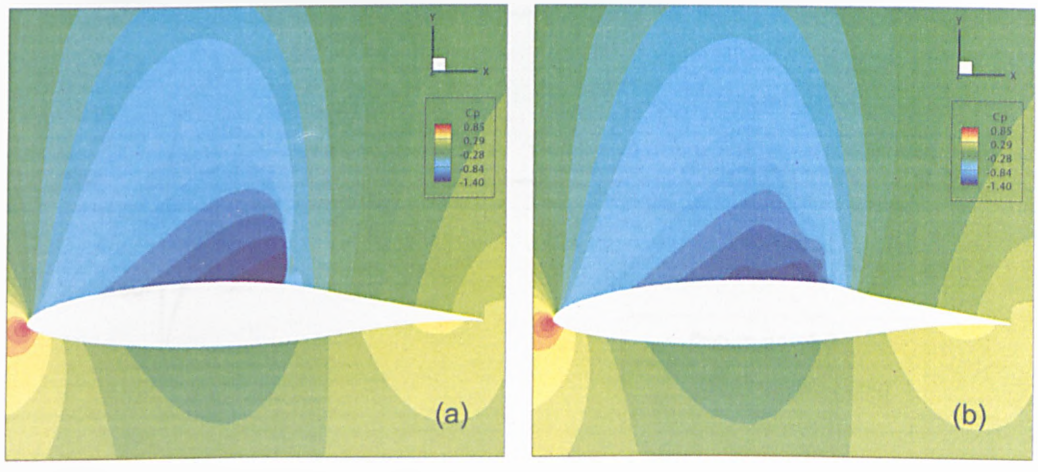


Figure 5.14: Pressure contour plots for the (a) datum aerofoil and the (b) optimised 2D bump. (RAE 5243, $M_\infty = 0.68$, $C_L = 0.82$)

Figure 5.14 (a) depicts clearly a reasonably strong normal shock formed on the upper aerofoil surface. With the presence of the optimised 2D bump, a compression wave is generated upstream of the bump, which substantially weakens the normal shock wave. Therefore, it can be seen that even in the presence of a boundary layer, the effects of the 2D bump on the flow is largely inviscid. The streamwise pressure distribution plot for the optimised 2D bump as shown in Figure 5.15 reassembles some similarities observed from the preceding inviscid investigations in Figure 5.9. The upstream flow ahead of the bump is slowed down before re-accelerating to the crest of the bump, hence shifting the position of the main shock. The speed of the flow on the lee side of the bump is slightly higher compared to the datum, which explains the slight increase in skin friction drag. The modified local curvature could induce flow separations, however, a closer view of the streamtraces around the 2D bump in Figure 5.16 confirms there are no such feature in the flowfield.

#### 5.4.2.1 Mechanisms and Further Drag Analysis

In this section, we will try to analyse the mechanism of the optimised 2D bump from flowfield visualisations and with the help of some further pressure drag analy-

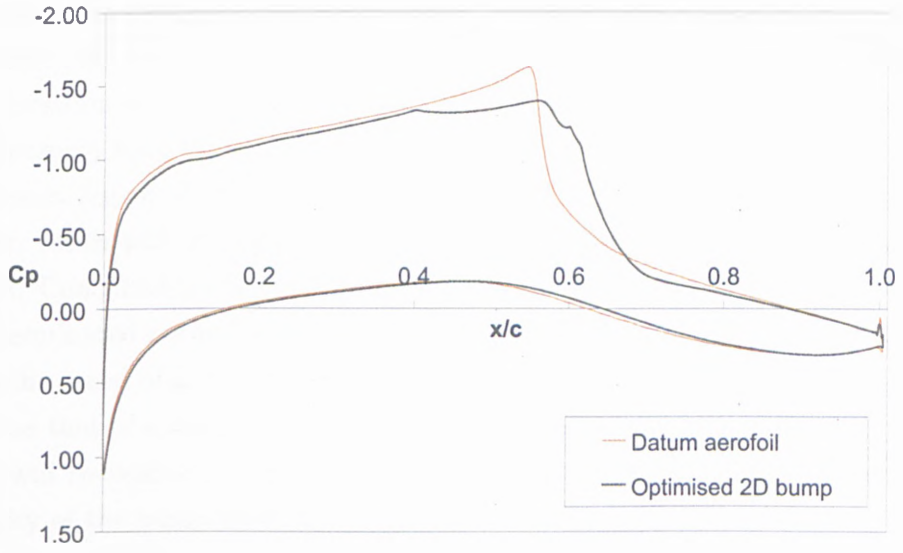


Figure 5.15: Streamwise pressure distribution for the optimised 2D bump. (RAE 5243, $M_\infty = 0.68$, $C_L = 0.82$)

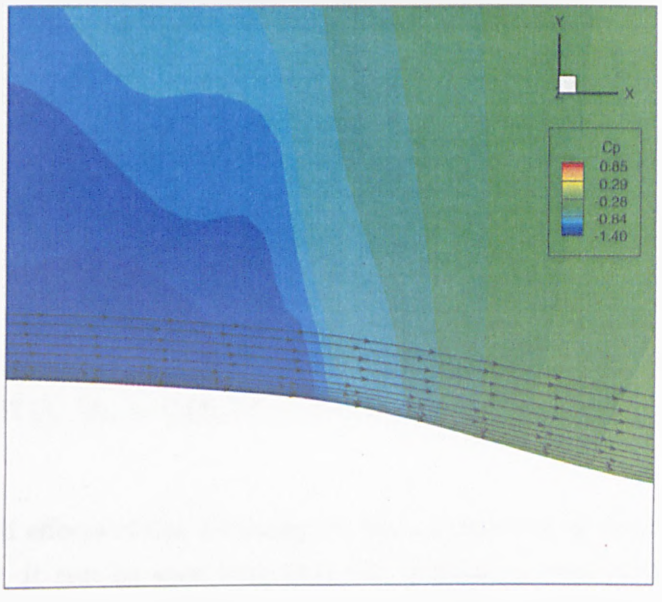


Figure 5.16: Closeup view of the streamtraces around the optimised 2D bump. (RAE 5243, $M_\infty = 0.68$, $C_L = 0.82$)

sis. Figure 5.17 presents the pressure contour lines of the datum case without the 2D bump. In this figure, the solid red-line represents the would-be position of the optimised 2D bump superimposed on top of the solid blue-line of the datum wing. The position of the bump crest is marked in this figure, which is placed ~3%c downstream from the original strong normal shock wave. Notice that part of the upstream region of the 2D bump lies within the supersonic region of the normal shock, which will generate an isentropic compression wave to weaken the normal shock. Concurrently, the remaining upstream region of the 2D bump lies between the terminated normal shock and the crest of the 2D bump. In this region, recall that the speed of a subsonic flow will increase when going through a compression such as that of a compressor (decreasing cross-sectional area); thus, the subsonic flow will re-expand to supersonic flow and terminate as a weaker shock in the vicinity of the bump crest.

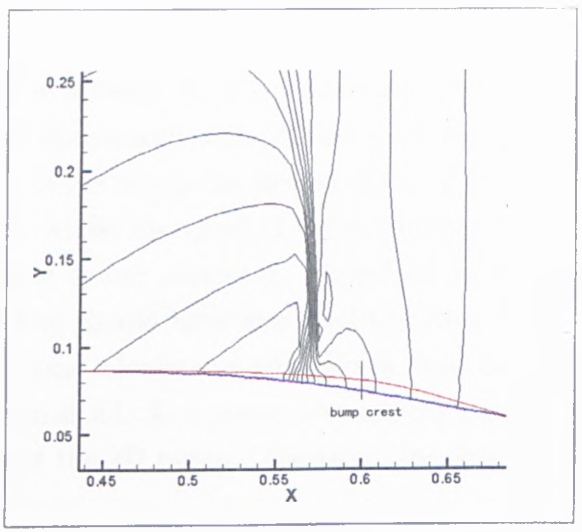


Figure 5.17: Closeup of the pressure contour lines of the datum case without 2D bump. (RAE 5243, $M_\infty = 0.68$, $C_L = 0.82$)

These described effects of the 2D bump on the original normal shock are depicted in Figure 5.18. It can be seen here that the original normal shock is converted into a weaker "knee"-shape shock. Its position has also displaced slightly downstream close to the bump crest.

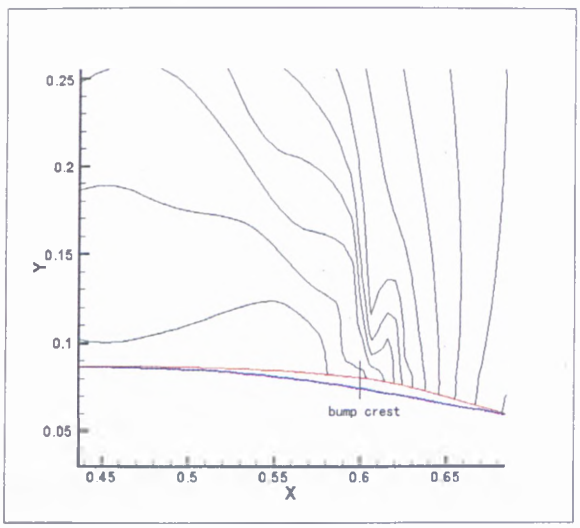


Figure 5.18: Closeup of the pressure contour lines of the case with 2D bump. (RAE 5243, $M_\infty = 0.68$, $C_L = 0.82$)

Recall the streamwise pressure plots and the contour plots from Figures 5.15 and 5.14. Locally within the vicinity of the 2D bump, it is observed that the upstream flow disturbed by the 2D bump has slowed down (higher pressure compared to the datum aerofoil), whilst the speed of the downstream flow aft the bump crest has slightly increased (lower pressure). Therefore, in this sense, the flow field modified by the bump should have increased the drag. However, it has already been proved by various calculations and also in experiments that the effects of the 2D bump are beneficial. As a result, a somewhat paradoxical situation arises on the mechanism of the 2D bump. Therefore, the following analysis is carried out to clarify this.

With reference to Figure 5.19 [93], integration of the enclosed areas of both cases (datum aerofoil and 2D bump) in Figure 5.15 will give the force component $C_y$:

$$C_y = \oint_c C_p d(x/c) \tag{5.3}$$

It can be observed from the plot that the enclosed areas from both cases are quite similar. Whilst from calculations, for a given lift, the calculated $C_y$ component from both the datum aerofoil and the one with the 2D bump are very close (Table 5.6). Due to the change of camber imposed by the 2D bump on the aerofoil, the

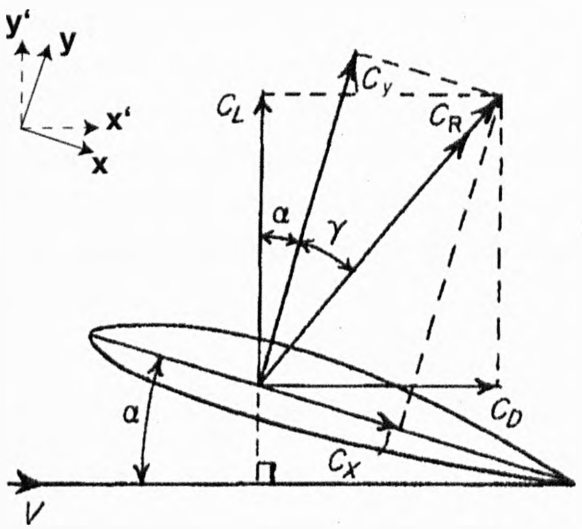


Figure 5.19: Aerodynamic forces.

wing can now achieve the same lift coefficient at a lower incidence 2.207°, which is about 0.2° lower compared to 2.417° of the datum case.

| Datum, $\alpha = 2.417°$ | 2D Bump, $\alpha = 2.207°$ |
|---|---|
| $C_x$= -0.02393 | $C_x$= -0.02400 |
| $C_y$= 0.81899 | $C_y$= 0.81904 |

Table 5.6: Calculated values for the $C_x$ and $C_y$ components. (RAE 5243, $M_\infty = 0.68$, $C_L = 0.82$)

On the other hand, the streamwise pressure distribution can be comprehended through a different plotting approach. Figure 5.20 demonstrates this method by plotting the $y$-coordinates of the sections against pressure $Cp$. The integration of the areas in this figure will provide the other force component $C_x$ (with reference to Figure 5.19 as well):

$$C_x = \oint_c C_p d(y/c) \tag{5.4}$$

In this plot, it is shown that for the datum aerofoil, after the point of maximum $y/c$ of the datum aerofoil, the existence of a fairly strong shock wave pushes the minimum pressure further and hence increases the drag contribution of this

component. The bump significantly weakens the shock strength and pulls the minimum $C_p$ back to a lower value. Consequently, the small enclosed area at the upper right of the plot, which is the drag contribution from the shock wave is now considerably smaller than the datum aerofoil. Calculations shown in Table 5.6 suggest that the $C_x$ component from them are quite similar too. Once again, both cases are at the same lift condition, where the 2D bump case is calculated at a lower incidence.

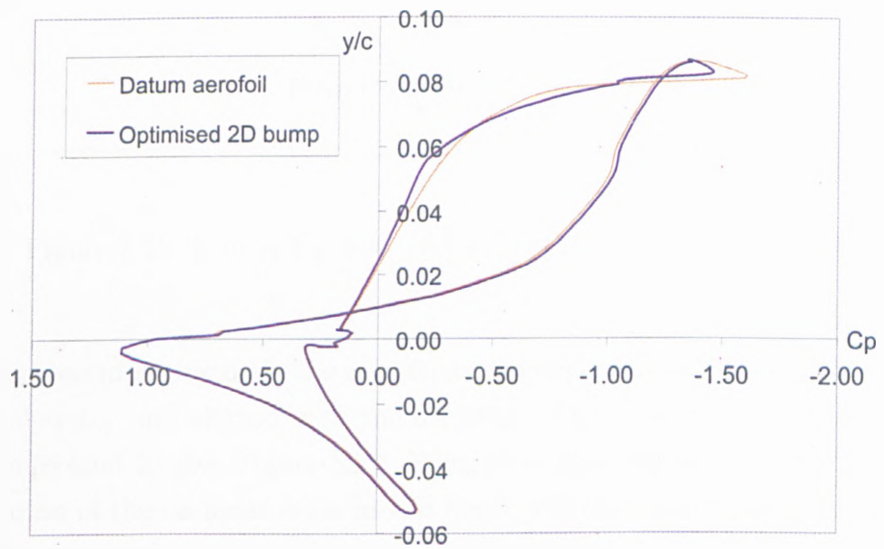


Figure 5.20: $y/c$ vs $C_p$ plot. (RAE 5243, $M_\infty = 0.68$, $C_L = 0.82$)

Since the actual drag coefficient $C_D$ is calculated via

$$C_D = C_y sin\alpha + C_x cos\alpha \tag{5.5}$$

and the bump could sustain the same lift at a lower incidence $\alpha$, therefore even with a similar magnitude of $C_y$ and $C_x$, the drag component $C_y sin\alpha$ is now much smaller with a reduced incidence, $\alpha$. In contrast, the component $C_x cos\alpha$ that actually provides thrust has now increased. As a result, substantial drag reduction has been achieved by the 2D bump. Note that, this analysis did not take the skin friction contributions into account, nonetheless, the contributions are relatively insignificant anyway.

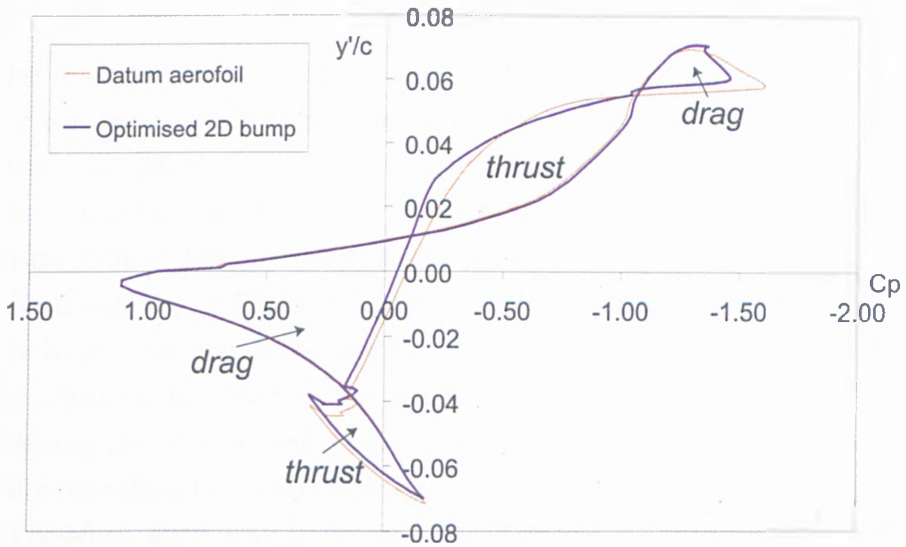


Figure 5.21: $y'/c$ vs $C_p$ plot. (RAE 5243, $M_\infty = 0.68$, $C_L = 0.82$)

As indicated in Figure 5.19, the coordinate system can be adjusted such that the axes, $x'$ and $y'$ are aligned with the direction of the freestream. Figure 5.20 is then re-plotted to give Figure 5.21. From here, ignoring skin friction drag, the integration of the enclosed areas in this figure will then lead directly to the drag coefficient, $C_D$, which is the dominant drag component here. This plot also gives a clearer and straightforward projection of the forces (drag or thrust) acting on the aerofoil, which are labeled in this figure. Once again, the upper region that provides drag is significantly reduced and that the thrust regions on the upper surface from both cases had slightly varied between them. In addition, the lowest enclosed region at the lower surface of the aerofoil, which actually provides thrust slightly increases compared to the datum case.

The analysis carried out here has provided deeper insight into the mechanisms of the 2D bump on drag. It has also clarified the paradox stated earlier by looking at the contribution of the local forces to the total drag such as that in Figure 5.21. The $y'$-pressure distribution analysis shows how the 2D bump alters the various contributions to drag at different part of the wing. The fact that both the shock wave is weakened by the 2D bump and the wing is at a lower incidence explains the substantial drag reduction gained.

#### 5.4.2.2 Wave Drag Analysis

In order to assess the wave drag reduction performance of the 2D bump. The entropy contour plots from the optimised 2D bump are compared to those of the datum aerofoil in Figures 5.22 over the same range of contour levels. Note that the computed entropy shown in the figures is non-dimensionalised by the freestream value. Thus, besides the boundary layer region with high contour values (red regions) in Figure 5.22 (a), it is observed that there is a substantial increase in entropy across the original strong normal shock wave, which forms the red region at the back of the shock. On the other hand, Figure 5.22 (b) demonstrates the effectiveness of the 2D bump in reducing wave drag, where the originally red region behind the shock wave is mostly converted to a lower contour level. Therefore, wave drag is clearly reduced by the 2D bump since the entropy increase behind the shock wave is now much lower than the datum aerofoil.

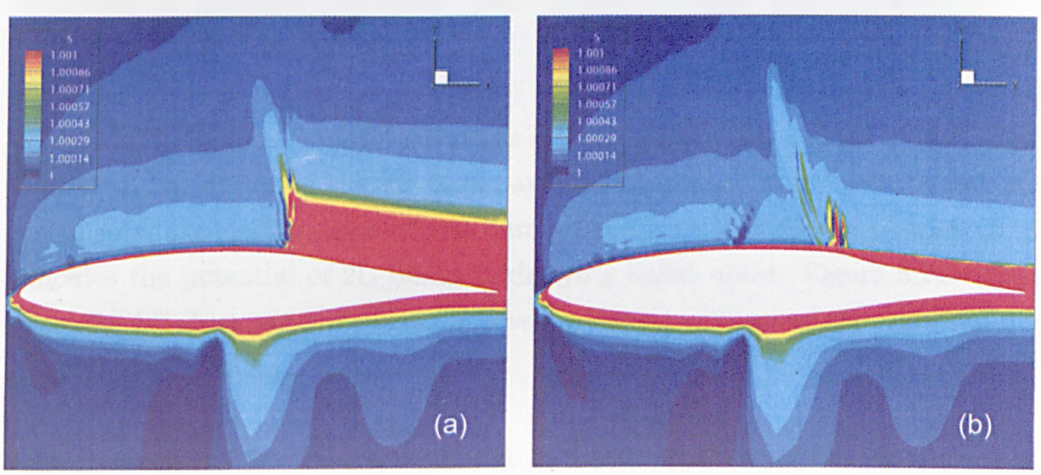


Figure 5.22: Entropy contour plots for the (a) datum aerofoil and the (b) optimised 2D bump. (RAE 5243, $M_\infty = 0.68$, $C_L = 0.82$)

By employing the far-field method introduced in *Chapter 2*, the wave drag and viscous drag (form + skin friction) components extracted from this optimised 2D bump are shown in Table 5.7 below:
From the table above, the computed values again confirm the substantial wave drag reduction achieved by the 2D bump. This corresponds to the previous entropy contour plots of Figure 5.22, which have already suggested that the shock wave has been largely eliminated. In addition to that, viscous drag is also being

| | $C_{Dwave}$ | $C_{Dviscous}$ |
|---|---|---|
| Datum aerofoil | 0.003126 | 0.01026 |
| ***Optimised 2D bump*** | 0.000848 | 0.01011 |

Table 5.7: Comparisons of the wave drag component for the optimised 2D bump. (RAE 5243, $M_\infty = 0.68$, $C_L = 0.82$)

reduced compared to the datum case. Since viscous drag comprises of form drag and skin friction drag, this reduction should be contributed by a reduced form drag because it has already been shown earlier that skin friction drag actually increases slightly.

### 5.4.3 Performance over a Range of $C_L$

The performance of the optimised 2D bump has been tested over a range of lift coefficients at the same freestream Mach number of 0.68. This is plotted out in the drag polar in Figure 5.23.

Note that the bump is optimised at the design point of $C_L = 0.82$. Higher than this point, the effects of the 2D bump are still beneficial. However, at lower lift coefficients, the performance of the bump rapidly deteriorate. Nevertheless, it indicates the potential of 2D bump in delaying buffet onset. Figure 5.24, which plots the lift-drag ratio against $C_L$ gives a clearer picture of the performance range of the 2D bump.

Beyond the optimisation design point at higher lift coefficients, the lift-drag ratio of the bump has substantially improved from the datum aerofoil. At low lift coefficients, the lift-drag ratio of the bump is lower than that of the datum case. As a result, the study here again implies the requirement of employing an adaptive 2D bump for optimum performance especially within the lift coefficients range that is below the design point.

### 5.4.4 Performance over a Range of Mach Number

This section investigates the performance of the optimised 2D bump over a range of freestream Mach numbers. A range of Mach number cases were run with a fixed incidence at $\alpha = 2.42°$. Since the lift coefficients are not fixed, the results

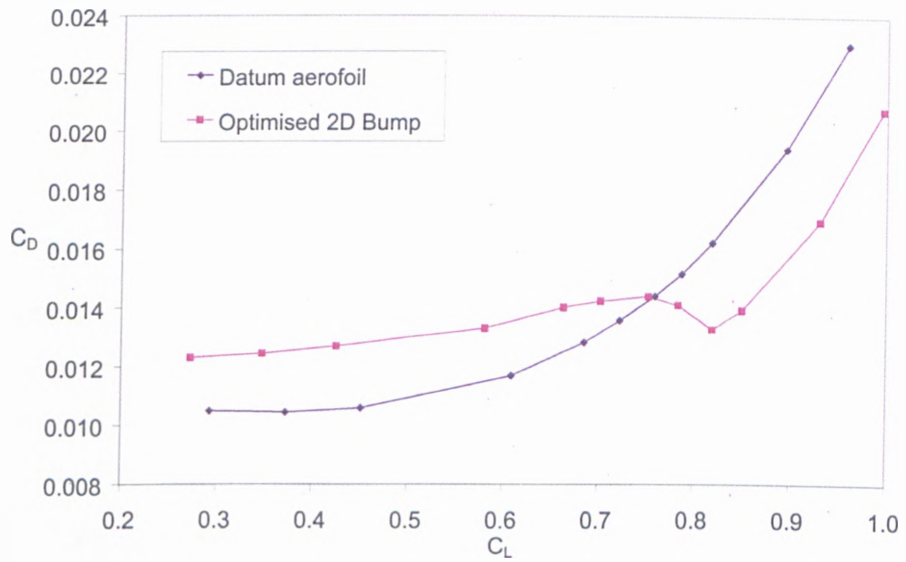


Figure 5.23: Drag polar for the optimised 2D bump. (RAE 5243, $M_\infty = 0.68$)

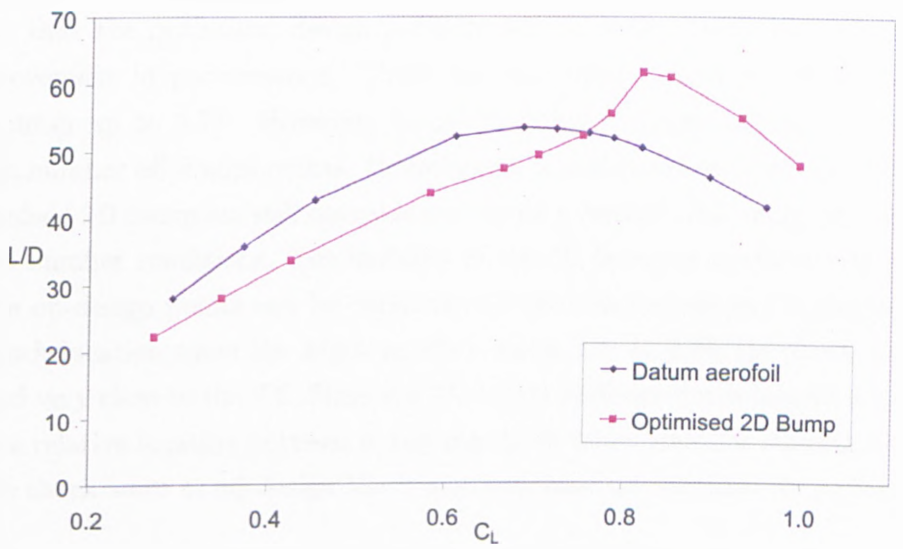


Figure 5.24: Lift-drag ratio against $C_L$ for the optimised 2D bump. (RAE 5243, $M_\infty = 0.68$)

are plotted in Figure 5.25 as the lift-drag ratio against the range of Mach number.

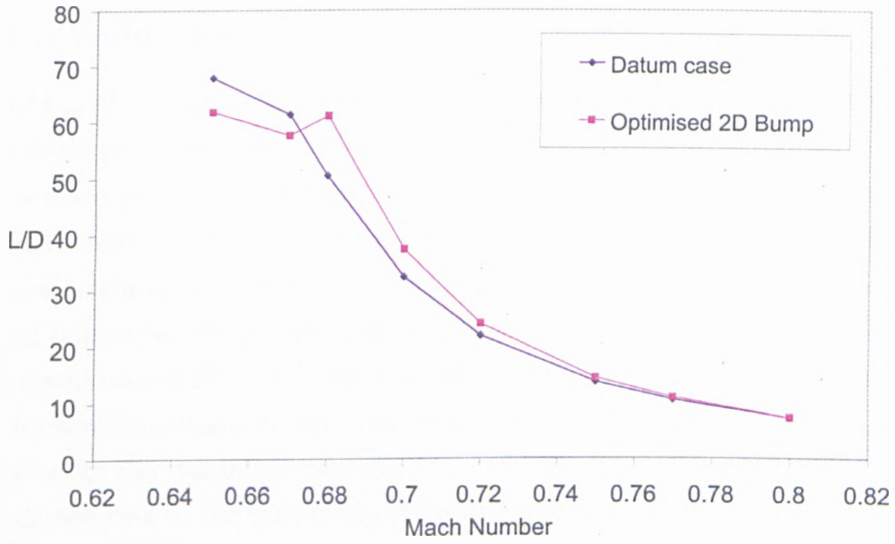


Figure 5.25: Performance over a range of Mach number for the optimised 2D bump. (RAE 5243, fixed at $\alpha = 2.42°$)

Note that the optimised design point is $M_\infty = 0.68$, which has a significant improvement in performance. There are still some beneficial effects from the 2D bump up to 0.77. However, its performance dropped off slightly at lower Mach number off-design points. Nonetheless, it is shown here that the one-point-optimised 2D bump are still operable over quite a considerable range of freestream Mach number conditions. The inability of the 2D bump to perform well at some of the off-design points can be explained by the observation of the displacement of shock location when the Mach number varies, i.e. at 0.85, the shock wave has moved very close to the TE. Since the 2D bump performance is largely dependant on the relative location between it and the shock wave, thus the shifting locations of the shock wave at off-design Mach numbers have undermined its performance.

## 5.5 Unswept Wing with RAE 2822 Transonic Aerofoil Section

### 5.5.1 Validation

The RAE 2822 transonic aerofoil is one of the most widely investigated aerofoils in the research community. It has a maximum thickness to chord ratio of 12% and it is designed for a higher Mach number at 0.729, as compared to the previous RAE 5243 aerofoil. Nonetheless, it still exhibits a fairly strong normal shock on the upper-surface. A different aerofoil is chosen to demonstrate the versatility of using bumps on wings with different type of aerofoil section. A C-type grid with a resolution of 220 × 61 cells was generated. Once again, the grid resolution near the aerofoil surface is adjusted to obtain $y^+$ values at around 1. The flow conditions for the validation case are $M_\infty = 0.729$, $Re_c = 6.5 \times 10^6$ and $\alpha = 2.31$, which correspond to the case study #4 found on the *NPARC Alliance Validation Archive* website [94].

The experimental pressure distribution data plotted in Figure 5.26 shows extracted from the *NPARC* website and the solid line is the results predicted by MERLIN. The comparison of the pressure distributions has shown good agreement between these two sets of data. Although the suction peak at the LE of the aerofoil is slightly under-predicted by MERLIN, but the position of the shock wave and the suction peak at the shock wave are predicted reasonably well.

Nevertheless, this is yet another brief validation exercise in conjunction with the main validation study already presented in *Chapter 3*. Once again, this exercise has demonstrated the ability of MERLIN to resolve transonic flow features with reasonable accuracy.

### 5.5.2 Optimisation Results

Instead of carrying out the optimisations at $M_\infty = 0.729$, the author decided to increase the freestream Mach number slightly to 0.75. The Mach number is now significantly higher than the Mach number design point chosen for the previous RAE 5243 NLF aerofoil cases and hence the strength of the shock wave is considerably stronger. As a result, at flow conditions of $M_\infty = 0.75$, $\alpha = 2.31$, the

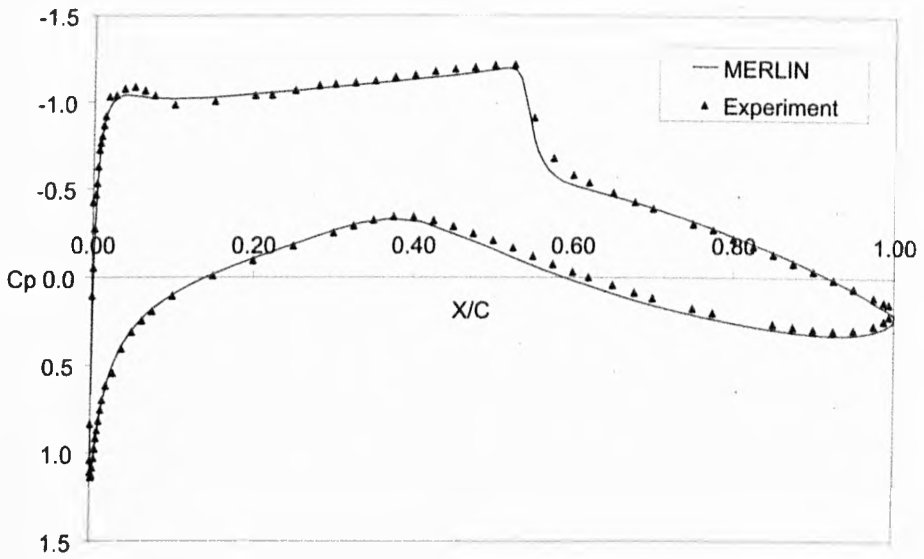


Figure 5.26: Comparison of the pressure distributions computed by MERLIN and experiment for RAE 2822 transonic aerofoil, $M_\infty = 0.729$

calculated $C_L$ is 0.75, which is taken as the target lift-coefficient for the optimisations.

The maximum allowable bump length is still 40%c, by employing the same optimisation methods as before, the final optimised bump has a designation of *l40-cre70.6-cb57.5-h1.14*. Note that the designation indicates that the optimised bump has a height of around 1%c. The aerofoil with the optimised 2D bump on the upper surface is shown in Figure 5.27 (a). The following Figure 5.27 (b) is the close-up of this 2D bump on the aerofoil. The bump designation indicates that this optimised 2D bump is asymmetric and consists of a longer upstream concave.

The obtained optimised 2D bump achieved around 32% total drag reduction from the datum reference case. Table 5.8 below provides further details on the computed drag components. Similar to that of the NLF aerofoil studies, it is noticed that there is a slight increase in skin friction drag. However, this viscous drag penalty is again eclipsed by a pressure drag reduction achieved by the optimised 2D bump, which is around 42%.

Figures 5.28 (a) & (b) compare the pressure contour plots from both the datum

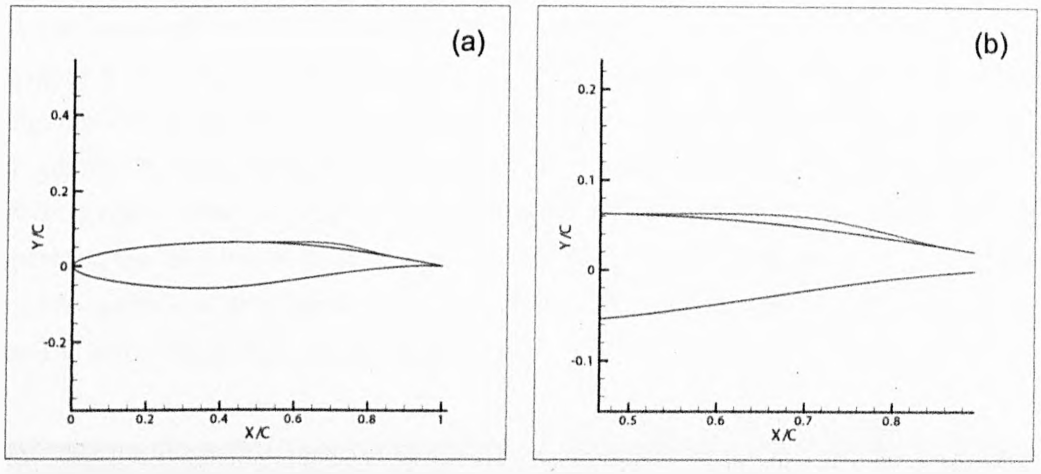


Figure 5.27: (a) RAE 2822 aerofoil with the optimised 2D bump generated on the surface. (b) Closeup on the optimised 2D bump.

| | $C_{Dtotal}$ | $C_{Dpressure}$ | $C_{Dfriction}$ | **Total Drag Reduction** |
|---|---|---|---|---|
| Datum aerofoil | 0.02296 | 0.017146 | 0.005813 | - |
| ***Optimised 2D Bump*** | 0.01555 | 0.009576 | 0.005978 | 32.3% |

Table 5.8: Comparisons of the drag components for the optimised 2D bump. (RAE 2822, $M_\infty = 0.75$, $C_L = 0.75$)

reference case and the optimised 2D bump. It can be observed that the strong normal shock wave on the upper aerofoil surface in Figure 5.28 (a) is very much weakened by the presence of upstream compression wave generated by the 2D bump as shown in Figure 5.28 (b). The effects of the 2D bump on the shock wave is further confirmed in the streamwise pressure distribution plots of both cases in Figure 5.29. Once again, with the presence of the 2D bump, the suction side of the aerofoil is left with a significantly weaker shock wave since the suction peak is greatly reduced. The position of the main shock has been displaced about 5%c downstream, thus increasing the supersonic region on this suction side. Consequently, the aerofoil with the optimised 2D bump is able to sustain the same level of lift coefficient at a lower incidence. Here, the incidence for the 2D bump case is 0.4° lower than that of the datum case.

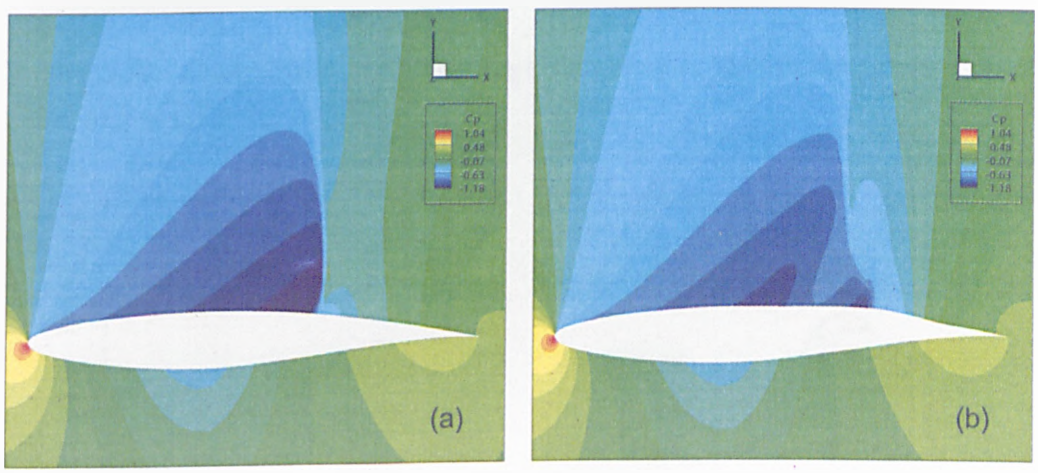


Figure 5.28: (a) Pressure contour plots for the datum reference case and (b) the optimised 2D bump. (RAE 2822, $M_\infty = 0.75$, $C_L = 0.75$)

Accompanying the pressure distribution plot of Figure 5.29 is the alternative $y$'-coordinates against pressure plot of Figure 5.30. Since the $y$'-coordinates are aligned normal to the direction of the freestream, the integration of the enclosed areas in Figure 5.30 directly relates to the drag. As before, skin friction drag is ignored here in the analysis. Nevertheless, it can be seen in Figure 5.30 that at the shock wave drag pocket (upper-right corner), the original normal shock is undergoes a re-compression and expansion before terminated as a much weakened shock. The thrust areas of both the upper and lower surface increase slightly as

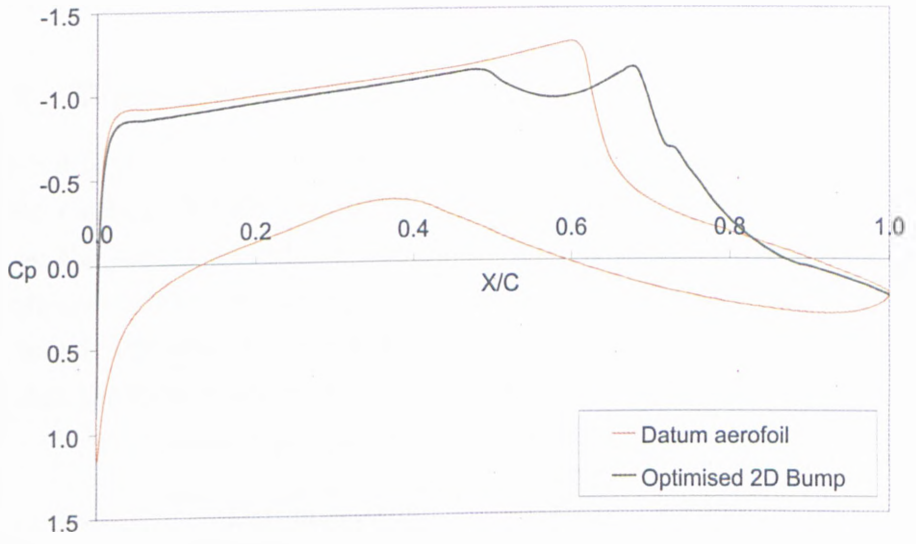


Figure 5.29: Comparison of the streamwise pressure distribution plots. (RAE 2822, $M_\infty = 0.75$, $C_L = 0.75$)

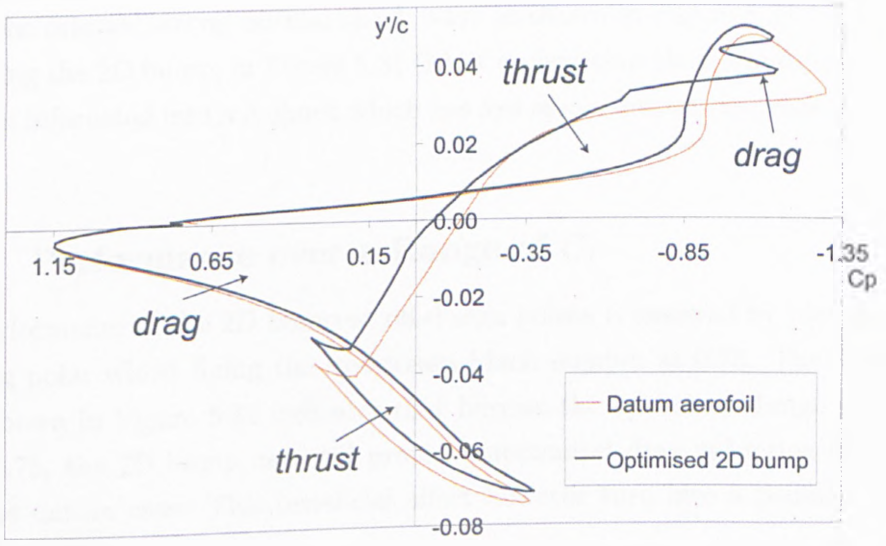


Figure 5.30: Comparison of the $y'$ *vs* $Cp$ plots. (RAE 2822, $M_\infty = 0.75$, $C_L = 0.75$)

well. In addition to that, the main drag region on the lower surface is reduced considerably.

### 5.5.3 Wave Drag Analysis

Table 5.9 lists out the wave and viscous drag components extracted using the far-field method. It indicates that the bump has significantly reduced the wave drag on the datum aerofoil by more than 69 drag counts. This corresponds to the entropy contour plots of Figure 5.31, which suggests that the shock wave has been largely eliminated. Additionally, it is also implied by the reduced viscous drag that the form drag has been reduced as well.

| | $C_{Dwave}$ | $C_{Dviscous}$ |
|---|---|---|
| Datum aerofoil | 0.009494 | 0.01097 |
| ***Optimised 2D bump*** | 0.002543 | 0.01031 |

Table 5.9: Comparisons of the wave & viscous drag components for the optimised 2D bump. (RAE 2822, $M_\infty = 0.75$, $C_L = 0.75$)

The effects of the 2D bump on the wave drag are shown in the entropy plots of Figures 5.31. Without the 2D bump, there is a substantial entropy increase across the original strong normal shock wave as shown in Figure 5.31 (a). While employing the 2D bump, in Figure 5.31 (b), it is clear that the normal shock wave has been bifurcated into a $\lambda$-shock which has less severe entropy increase across it.

### 5.5.4 Performance over a Range of $C_L$

The performance of the 2D bump at off-design points is assessed by plotting out the drag polar whilst fixing the freestream Mach number at 0.75. The drag polar as shown in Figure 5.32 indicates that beyond the optimised design point at $C_L = 0.75$, the 2D bump can still provide substantial drag reduction from the reference datum case. This beneficial effect however turn into a penalty at the lower $C_L$ region.

Figure 5.33, which is the lift-drag ratio plot against $C_L$ again highlights the performance of the 2D bump over the range of $C_L$. Nevertheless, this result also

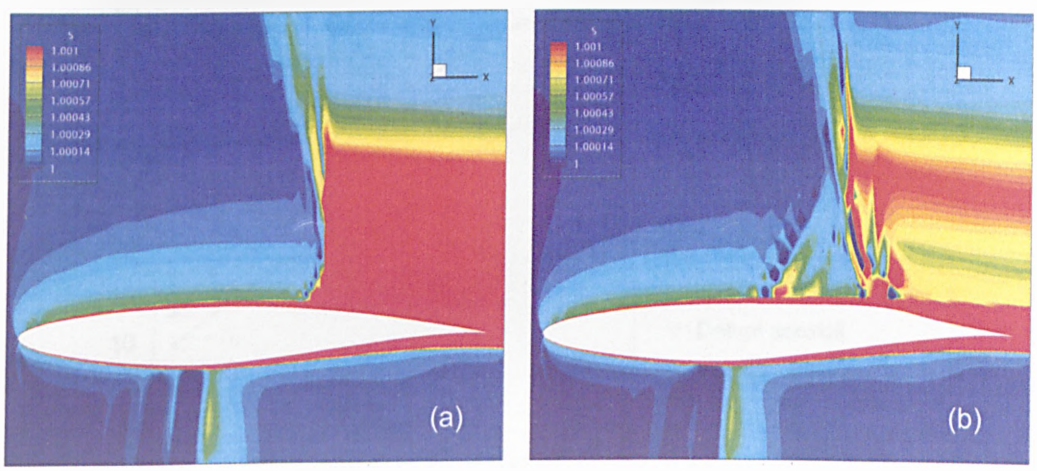


Figure 5.31: (a) Entropy contour plots for the datum reference case and (b) the optimised 2D bump. (RAE 2822, $M_\infty = 0.75$, $C_L = 0.75$)

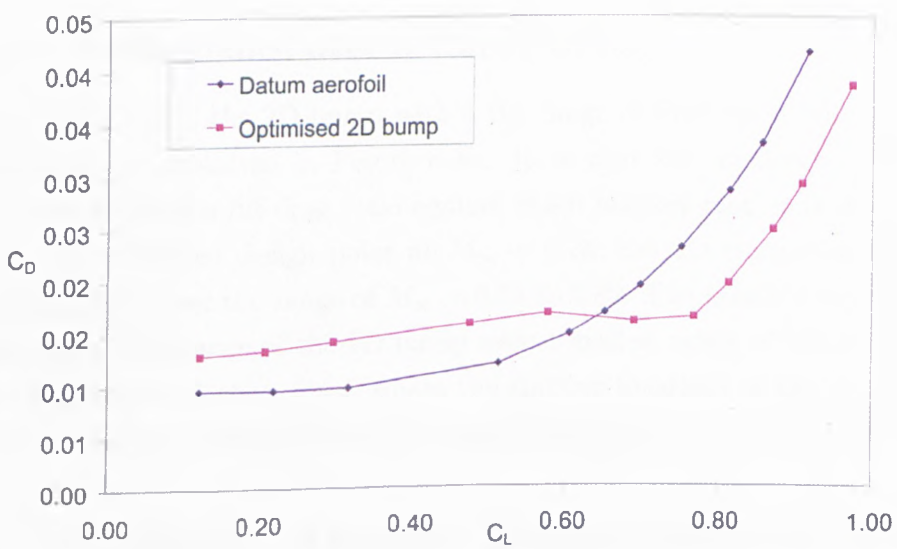


Figure 5.32: Drag polar for the optimised 2D bump on RAE 2822, $M_\infty = 0.75$.

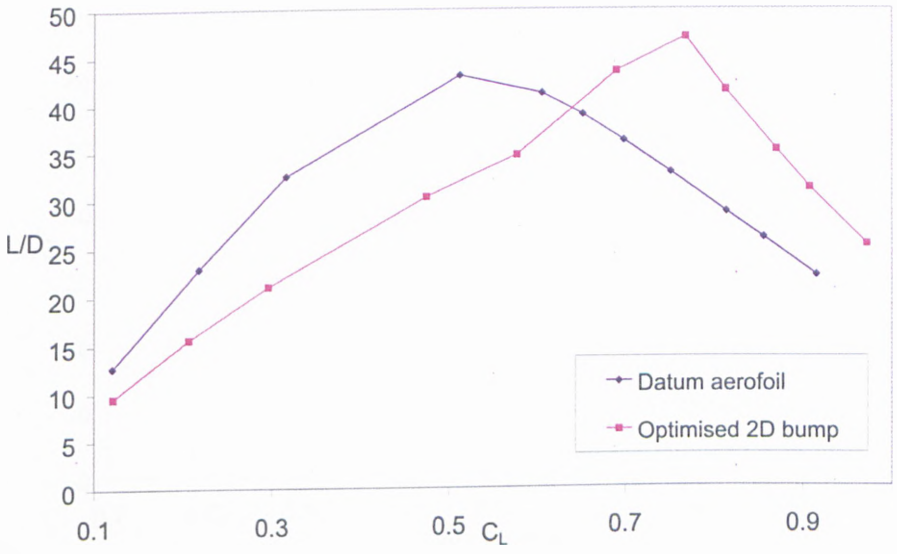


Figure 5.33: Lift-drag ratio plot against lift coefficient for the optimised 2D bump on RAE 2822, $M_\infty = 0.75$.

implies the potential of employing the 2D bump to delay buffet onset and that the 2D bump needs to be adaptive as discussed earlier in *Section 5.4.3*.

### 5.5.5 Performance over a Range of $M_\infty$

The performance of the 2D bump within the range of freestream Mach number of 0.72 to 0.85 is plotted in Figure 5.34. Note that the incidence is fixed at $\alpha = 2.31°$. From this lift-drag ratio against Mach number plot, it is shown that besides the optimised design point at $M_\infty = 0.75$, the 2D bump maintains its beneficial effects over the range of $M_\infty = 0.74$ to 0.82. The possible explanations behind the performance of the 2D bump over a limited range of Mach numbers areas discussed in *Section 5.4.4*, where the shifting locations of the shock wave due to the varying Mach numbers have significant impact on its performance.

## 5.6 Combined Aerofoil Shape with 2D Bump Optimisation

*Chapter 4* has already discussed some aspects of aerodynamic optimisation. In Ref. [83], Le Moigne *et al.* have successfully optimised an aerofoil shape based on

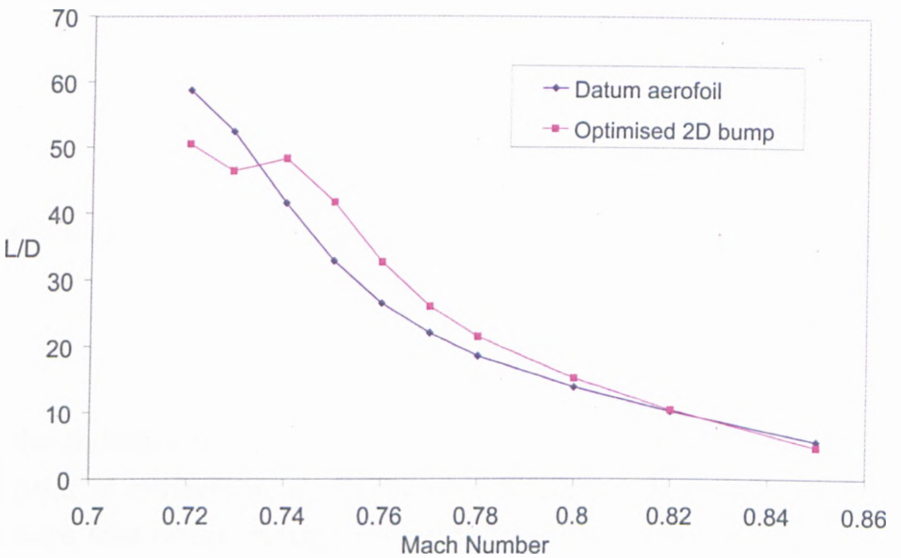


Figure 5.34: Performance over a range of Mach number for the optimised 2D bump on RAE 2822, incidence fixed at 2.31°

the RAE 2822 aerofoil section at its design condition using the efficient adjoint method. While Nemec and Zingg have also attempted to optimise aerofoils based on the NACA 0012 aerofoil [95]. Even though most of the efforts are successful in shaping the aerofoil that would give little or no remaining shock wave, the optimisation is mostly limited within a relatively low transonic Mach number range about 0.7~0.75. It is very difficult to eliminate the shock wave on a unswept wing at higher transonic Mach numbers over 0.8 or 0.85, which are usually the cruising speed range for current modern aircraft. Therefore, it is proposed to conduct a preliminary study on coupling the optimisation of the aerofoil shape with the 2D bump on an unswept wing.

### 5.6.1 Aerofoil Shape Parameterisation

The Bézier-Bernstein parameterisation is employed to represent the variation around an initial 2D aerofoil shape. The parameterisation is applied to a perturbation that is added to the original shape. For a two-dimensional aerofoil, only the vertical coordinates y are considered for deformation, thus

$$y_{current} = y_{initial} + \delta y$$

where

$$\delta y = \sum_{k=0}^{N} B_{k,N}(u) P_{yk}$$

Here, $P_{yk}$ are the Bézier control points and the Bernstein polynomials are

$$B_{k,N}(u) = \frac{N!}{k!(N-k)!} u^k (1-u)^{N-k}$$

where the arclength $u = \sqrt{x}$, with $x$ the non-dimensionalised chordwise position of the point of ordinate $y_{initial}$ for an aerofoil section. This arclength has been chosen such that design changes are concentrated at the leading edge region of the aerofoil where $x$ is small. From this representation, the design variables are then the Bézier control points, $P_{yk}$. In the present study, the upper and lower shapes are represented with 10 Bézier control points each. Note that the leading- and trailing-edge points are kept fixed, therefore only a total of 16 Bézier control points are active design parameters.

### 5.6.2 Optimisation Results

The initial aerofoil shape chosen is the RAE 2822 transonic aerofoil. This aerofoil is preferred to the RAE 5243 NLF aerofoil because it is designed at a higher Mach number. At this Mach number and $\alpha = 1.0$, the computed lift is $C_L = 0.498$. This is a reasonable choice of target lift coefficient such that the shock wave on the upper surface is strong but without severe shock-induced boundary layer separation.

In addition to the lift constraint, a geometrical constraint has also been imposed in the optimisation, where the internal volume of the aerofoil excluding the 2D bump is to be no less than the initial volume. By excluding the additional volume of the 2D bump, the possible thinning of the original aerofoil profile can then be avoided. The objective function remains to reduce the total drag and lift is constrained at the target value stated above. The initial bump has a chordwise length of 20%c and a height of 0.3%c. The maximum allowable bump length is still set to 40%c. In addition to the optimised aerofoil shape, the designation of the optimised 2D bump for this case is *l25.8-cre79.6-cb51.7-h0.55*. Thus, it is shown that the size of the bump has grown about 6%c in the streamwise length

and 0.2%c in height.

An aerofoil shape optimisation has also been carried out without the 2D bump. The freestream conditions and constraints remain the same. Comparisons of the performance of each of the cases are shown in Table 5.10 below:

| | $C_{Dtotal}$ | $C_{Dpressure}$ | $C_{Dfriction}$ | **Total Drag Reduction** |
|---|---|---|---|---|
| Datum aerofoil shape | 0.03183 | 0.02615 | 0.005684 | - |
| ***Coupled optimised shape and bump*** | 0.01477 | 0.00869 | 0.006084 | 53.6% |
| ***Coupled optimised shape and bump*** **(bump removed manually)** | 0.01553 | 0.00952 | 0.006006 | 51.2% |
| ***Optimised shape*** | 0.01480 | 0.00873 | 0.006075 | 53.5% |
| ***Optimised shape*** **(bump added manually)** | 0.01355 | 0.00739 | 0.006157 | 57.4% |

Table 5.10: Comparisons of the drag components for the combined aerofoil shape-bump optimisations, $M_\infty = 0.8$, $C_L = 0.498$.

From this table, in addition to the two optimisation cases, there are two other manually tested cases. For the coupled optimised shape and bump case, the bump is removed manually to investigate the level of drag reduction contributed by the bump. It is found that the bump contributes an additional 2% of drag reduction to the improved aerofoil shape. Overall, this coupled optimisation of aerofoil shape and bump achieves around 53% improvement from the datum case. On the other hand, the aerofoil shape optimisation without bump optimisation can also achieve the same level of improvement at 53%. By adding a bump at the vicinity of the remaining shock on the upper surface, a further 4% of drag reduction can be obtained.

The streamwise pressure distribution plots of the various cases are analysed in Figure 5.35. Both optimisations have modified the aerofoil shapes to increase the suction peak at the LE, such that a flatter or "roof-top" like pressure distribution can be achieved. Consequently, the strength of the original normal shock is reduced. As for the case of the coupled shape-bump optimisation, the shock is

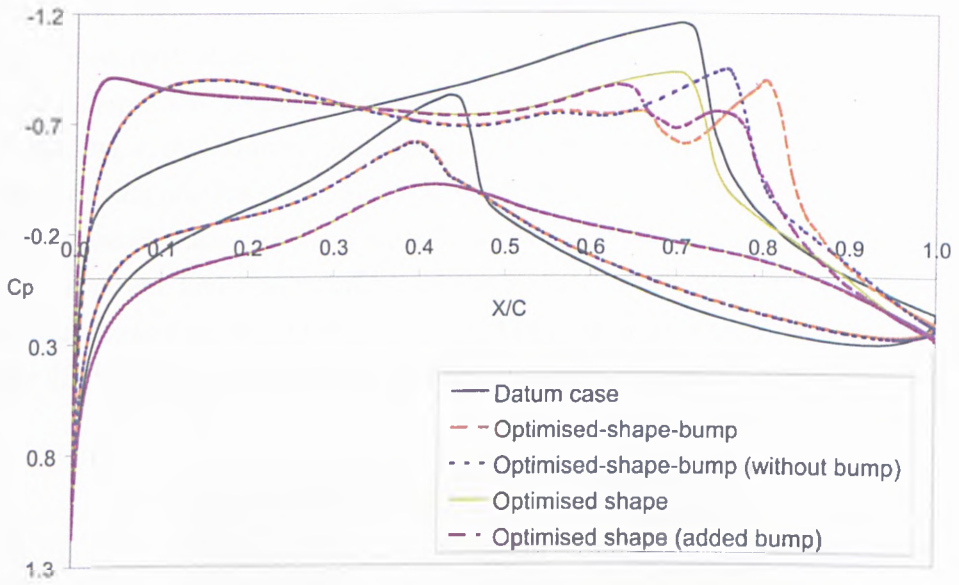


Figure 5.35: Pressure distribution plots for the optimised aerofoil shape and bump, $M_\infty = 0.8$, $C_L = 0.498$.

also weakened and displaced downstream due to the existence of the bump. This is observable in the two calculations of the coupled optimised shape-bump case, where the bump is manually removed. As for the pure aerofoil shape optimisation case, further weakening of the shock can be achieved by manually adding a bump as shown by the purple-line plot. In these freestream conditions, the datum aerofoil shape has a fairly strong shock on the lower surface. Each optimised shape has largely eliminated this lower-surface shock, particularly the pure aerofoil shape optimisation, where there is virtually no remaining shock on the lower surface. The removal of this lower-surface shock also contributes to much of the attained improvement.

The effects of the evolved aerofoil shapes and 2D bumps as discussed in the previous paragraph are also reflected in the Mach number contour plots presented in the series of Figures 5.36, 5.37 and 5.38. The distinct difference of the flowfield from the two optimisation cases is observed from these plots. The beneficial effects of the 2D bumps on the remaining shock is clearly shown here too.

The evolved aerofoil shapes and bump from the optimisation cases are shown in

Figure 5.39. Here, it is observed that both of the cases have reduced the camber at the front part of the aerofoil. As for the downstream part of the aerofoil, the coupled shape-bump case still retains the amount of camber such that the level of rear loading is maintained. In contrast, the pure aerofoil shape case reduces the camber at this portion of the aerofoil. These effects can be seen in the streamwise pressure distribution plots in Figure 5.35. Notice that for the pure aerofoil shape case, the upper and lower surface pressure distribution lines converges close to each other before reaching the TE. In addition, the local contour modification due to the 2D bump on the coupled shape-bump case is observable at the 80%c region.

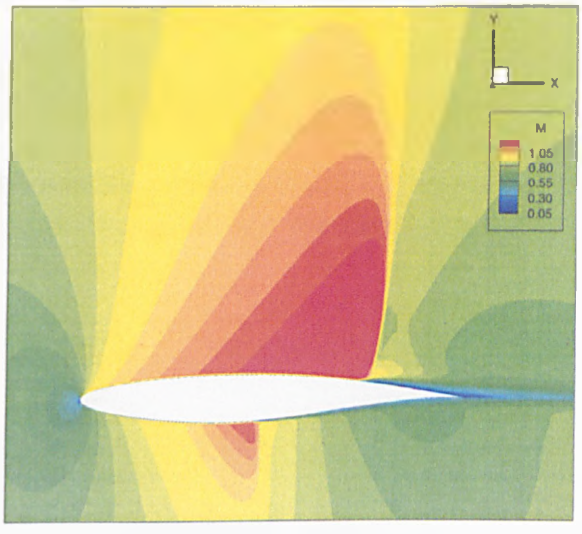


Figure 5.36: Mach number of the datum case for the coupled shape-bump optimisations, $M_\infty = 0.8$, $C_L = 0.498$.

Figure 5.40 presents the *y' vs Cp* plots for the various cases. In this figure, the first obvious changes to the datum case is the huge shrinkage of the upper-right area, which actually corresponds to the strong upper-surface shock as seen in Figure 5.36. It is obviously converted into a much weakened shock as indicated by the remaining small area at the upper-right region. With the presence of 2D bumps, this remaining shock is further weakened through a series of re-compressions and expansions. The rest of the drag and thrust regions also undergo significant changes. The area at the bottom of the plot that corresponds to the lower-surface original normal shock has also been virtually eliminated. The pure aerofoil shape optimisation case has a much lower maximum $y'$ as compared to the others since

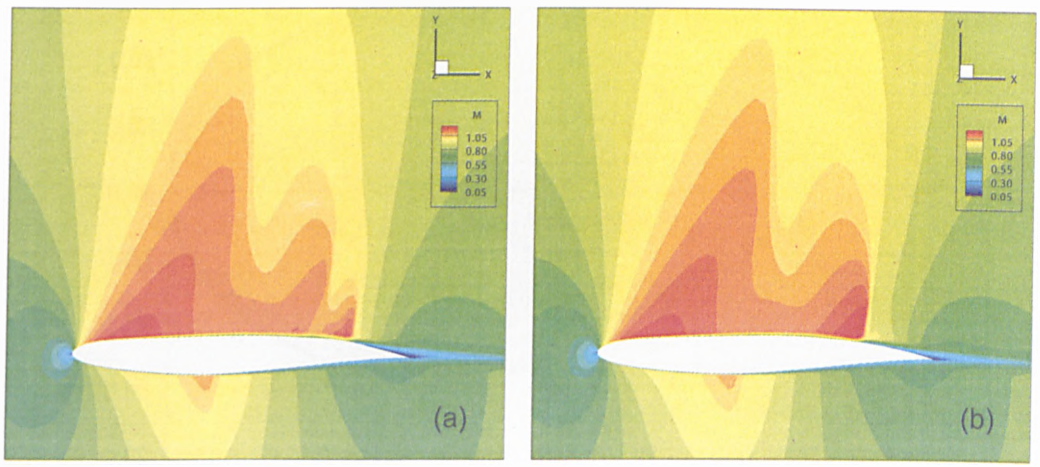


Figure 5.37: Mach number contours of the (a) coupled optimised shape with bump and (b) the optimised shape with the bump manually removed, $M_\infty = 0.8$, $C_L = 0.498$.

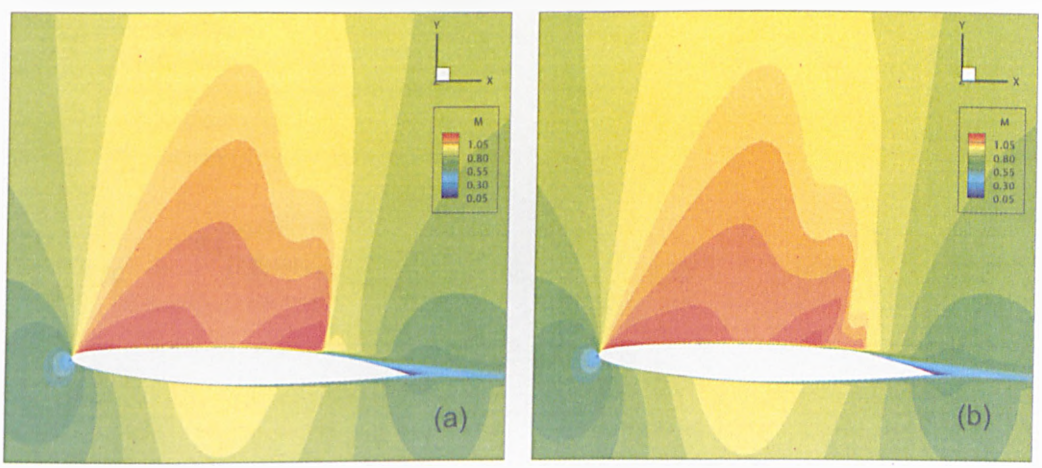


Figure 5.38: Mach number contours of the (a) optimised shape and (b) the optimised shape with a bump manually added, $M_\infty = 0.8$, $C_L = 0.498$.

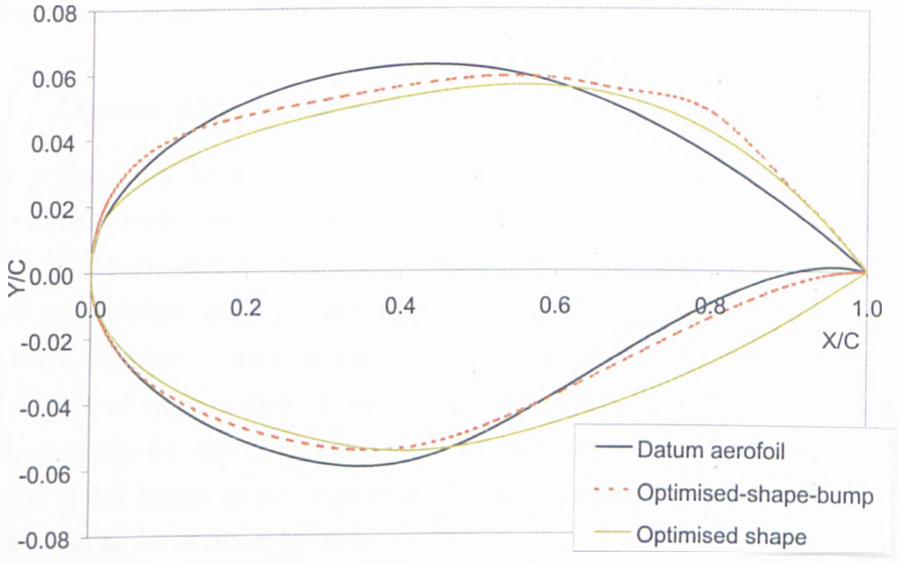


Figure 5.39: Shape changes of the optimised aerofoil shapes and bump, $M_\infty = 0.8$, $C_L = 0.498$.

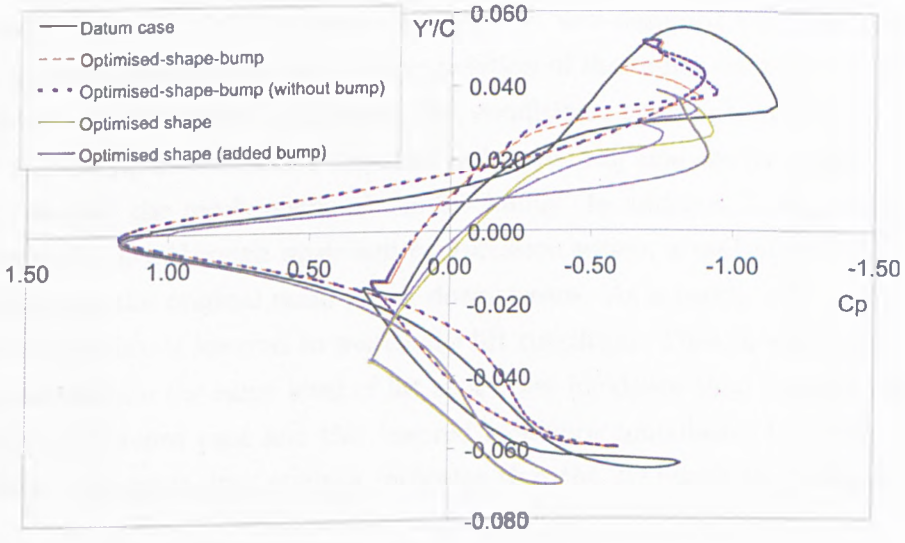


Figure 5.40: *Y' vs Cp* plots of the optimised aerofoil shapes and bump, $M_\infty = 0.8$, $C_L = 0.498$.

it has a much higher incidence than the others, which also contributes to the total elimination of the lower-surface shock.

### 5.6.3 Optimisation Issues

In this preliminary study of combining aerofoil shape of an unswept wing with shock control bump optimisations at a much higher off-design freestream Mach number, it is realised that there are several issues that have to be tackled. The flow for an unswept wing at such high speed (e.g. $M_\infty = 0.8$) has very strong shock wave/boundary layer interaction, which could lead to large separation at the rear part of the aerofoil. Thus, during this study, convergence issues occur quite frequently for the flow solution. The robustness of the adjoint solver for separated flows needs to be improved. Relative scaling of the different design variables has to be studied further.

## 5.7 Concluding Remarks

Various parameters of the 2D bump have been optimised on an unswept wing with two different types of aerofoil section, including a NLF type and a turbulent type. Both efforts have demonstrated the effectiveness of 2D bumps in drag reduction and the important aspects of a well-designed bump in terms of its location on the aerofoil, the relative position of the bump crest and its height. For optimal performance at different flow conditions, the height of the 2D bump needs to be adaptive. Detailed pressure and wave drag analysis have been carried out to analyse the mechanisms of the 2D bump. In addition to the weakening of the shock wave through upstream compression waves, a well-placed 2D bump also displaces the original main shock downstream. As a result, lift is enhanced and the incidence is lowered to match the lift condition. Thus, a wing with a 2D bump can sustain the same level of lift at a lower incidence than the corresponding datum reference case and this lowered incidence contributes to further drag reduction. The wave drag analysis indicates that the 2D bump also reduces form drag.

A preliminary study of a coupled optimisation of the aerofoil shape of an unswept wing with the 2D bump at a high off-design freestream Mach number has been presented at the end of this chapter. It is demonstrated that a fairly strong

shock still remains on the optimised aerofoil shapes. With the 2D bump, further improvement can be obtained. Nonetheless, some optimisation issues have been addressed that could help to improve the optimisations for this problem. The following chapter will then present the results on the performance of a three-dimensional shock control device, 3D bumps on unswept wings.

# Chapter 6

# Mechanisms and Optimisations of 3D Bumps on Unswept Wings

This chapter will present the optimisation results of a 3D bump on unswept wings by employing the same adjoint-based optimisation method. Both pressure and wave drag analysis are carried out along the investigations. The performance of both the 2D and 3D bumps are then compared and analysed. The chosen aerofoil sections for the infinite unswept wing are still the RAE 5243 NLF aerofoil and the RAE 2822 turbulent aerofoil. First, the 2D bump parameterisations are extended to model the 3D bump, which will be presented in the following section.

## 6.1 Initial Parameterisations

The initial design of the 3D bump was proposed by Qin *et al.* [47, 46], and is shown in Figure 6.1. A cutoff area from one of the x-y planes across the 3D bump would resemble the shape of a 2D bump. The area of this shape gradually shrinks from the maximum size at the 3D bump centreline to virtually a sharp end tip. For a structured three-dimensional surface grid, the approach of generating a 3D bump of such design in Figure 6.1 is relatively simple. For an unswept wing with infinite span, only half of the 3D bump is required due to the symmetry plane. Starting from the symmetry plane, which is located at the spanwise centreline of the 3D bump, at each spanwise sections, a 2D bump is generated using Eqn. (5.1) but shrinking them gradually towards the tip. The gradient at the crest is set to zero and the intersection of the base of the bump with the surface of the wing are devised such that the continuity of the slope at the point of the wing

surface is maintained.

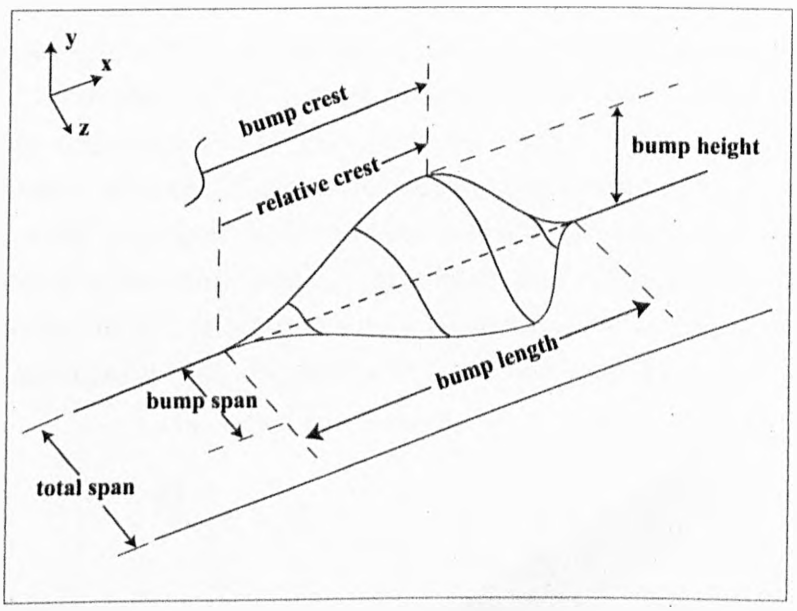


Figure 6.1: Initial design of 3D bump with the six design variables.

As a result of that, in addition to the four design variables that have been defined for the 2D bump, two more design variables are added to define the shape of the 3D bump. Figure 6.1 also illustrates these six design variables on the halved 3D bump. Since the symmetry boundary condition is employed at both spanwise boundaries, the last design variable, $z_{total\_span}/c$, which is actually the total span width of the computational grid, also defines the spanwise spacing between the array of consecutive 3D bumps on the infinite span unswept wing. However, the technical issues revolving the ability to expand and shrink this design variable and hence the whole computational grid appropriately and efficiently; has only been solved at certain stage of this project. Therefore, some of the preliminary optimisation results that are presented later, do not take this design variable into account.

The fifth design variable is the width of the 3D bump, defined as $\frac{z_{bump\_span}}{z_{total\_span}} \times 100\%$, which is in the percentage of the total width ($z_{total\_span}/c$). This strategy has been chosen so that it is guaranteed that the width of the 3D bump will not cross-over with the total width. For example, if the fifth design variable were the absolute

value defining the width of the 3D bump, e.g. $z_{bump\_span}/c$, it is possible that $z_{bump\_span}/c > z_{total\_span}/c$, where the grid generation will then end up with errors.

The designation of a 3D bump example that has a spanwise width covering 60% of the total span width of 1%c, which can also be interpreted as a 2%c distance between the centrelines of the consecutive 3D bumps can be expressed as *l20-cre60-cb50-h0.6-s60-wid1*. Note that the spanwise width of the 3D bump and the total span width correspond to the last two terms in the designation respectively. An example of a fine structured grid generated with a 3D bump of this design is shown in Figure 6.2. In order to save computational time, the actual adopted spanwise resolution for the calculations is less than this example.

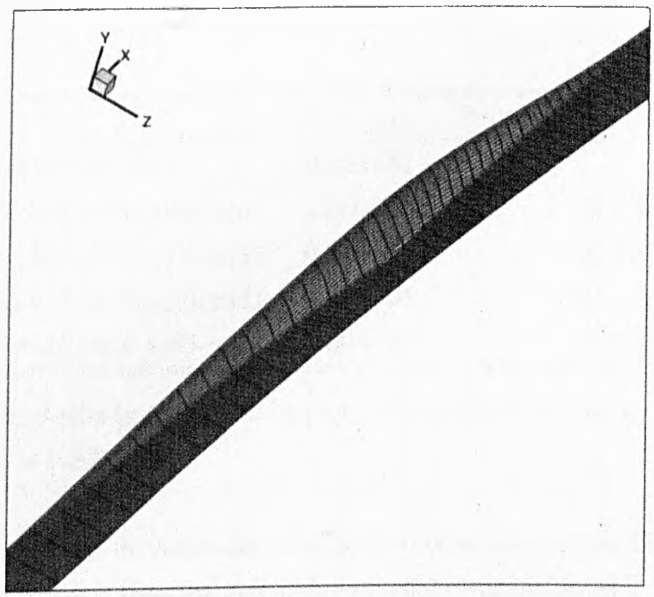


Figure 6.2: Example of a fine surface grid with 3D bump.

## 6.2 Inviscid Effects of 3D Bumps on RAE 5243

### 6.2.1 Effects of the Spanwise Width of the 3D Bump

The initially generated 3D bump has a designation of *l20-cre62-cb50-h0.6-s60-wid1*. For an infinite span wing with half of the 3D bump generated, it can be seen here that the grid spans 1%c, which can also be translated to a 2%c distance between the centrelines of the array of consecutive 3D bumps. The fifth design

variable indicates that the bump spans 60% of the total width.

By adopting the 3D bump *l20-cre62-cb50-h0.6-s60-wid1* and fixing *wid1* and the other parameters, whilst increasing the bump width gradually by an increment of 10% from *s60* to *s90*, the drag reduces gradually too. This is shown in Table 6.1. The results are compared under the same lift condition of $C_L = 0.823$ at $M_\infty = 0.68$. Note that the grid employed here actually bears the same streamwise grid resolutions and distribution strategy as the computational grid employed in the investigations of the 2D bumps. The difference is obviously the additional spanwise resolutions required to resolve the 3D bump shape in the spanwise direction. Here, ten additional grid points are added in the $k$-direction, giving a resolution of $248 \times 31 \times 11$.

| | $C_{Dpressure}$ | **Total Drag Reduction** |
|---|---|---|
| Datum aerofoil | 0.011681 | - |
| *l20-cre62-cb50-h0.6-**s60**-wid1* | 0.009519 | 18.6% |
| *l20-cre62-cb50-h0.6-**s70**-wid1* | 0.009260 | 20.8% |
| *l20-cre62-cb50-h0.6-**s80**-wid1* | 0.008994 | 23.1% |
| *l20-cre62-cb50-h0.6-**s90**-wid1* | 0.008731 | 25.3% |

Table 6.1: Inviscid effects of the 3D bumps with respect to the bump span width, $M_\infty = 0.68$, $C_L = 0.823$.

This is rather expected because the smaller the remaining unmodified flat surface of the wing, the closer is the distance between the adjacent bumps due to the symmetry boundary conditions of the computational grid and hence, providing larger interaction surface with the shock wave. However, since this parameter should have significant effects on the boundary layer, so the optimum characteristic of this parameter has yet to be concluded from this parametric study.

### 6.2.2 Cross-sectional Area Hypothesis

This hypothesis suggests that if the maximum cross-sectional area ($y$-$z$ plane as referred to Figure 6.1) of the 3D bump were about the same as the maximum cross-sectional area of the 2D bump, the 3D bump would be as affective as the 2D bump in reducing drag at a design point. Thus, in three-dimensional sense, consider cutting off a spanwise section of 1%c width from an infinite span wing with

a continuous 2D bump of optimised design stretching across the wing as shown in Figure 6.3 (a) with the blue-dashed line. Therefore, the maximum cross-sectional rectangular area of the 2D bump with a 0.6%c height across this cutoff section is $6 \times 10^{-5}$.

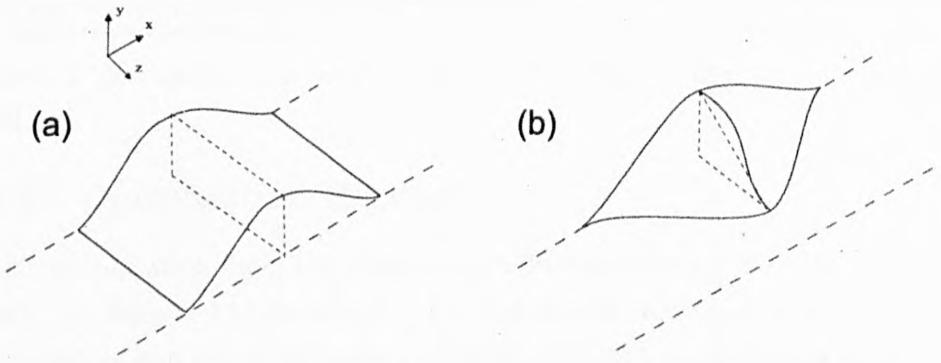


Figure 6.3: Maximum cross-sectional area of (a) a 2D bump and (b) a 3D bump.

Next, consider the cutoff for the maximum cross-sectional area of the 3D bump with similar width of 1%c as shown in Figure 6.3 (b). For simplicity, the maximum cross-sectional area of a halved 3D bump is approximated as a right triangle as indicated by the blue-dashed line. Thus, if the position and the shape of the 3D bump were optimised, for a halved 3D bump with 0.6%c spanwise width, a bump height of 2%c chord would be needed to match the maximum cross-sectional area of the aforementioned effective 2D bump.

Subsequently, the 3D bump *l20-cre62-cb50-h2-s60-wid1* was tested. However the result was disappointing, resulting in a strong double-shock system. Hence, the bump height should be slightly relaxed. However, in order to retain the same level of maximum cross-sectional area with a reduced bump height, the width of the bump itself has to be increased. Therefore, the bump width is increased and fixed at 0.8%c, while the bump height is increased progressively. Consequently, the bump height can now reach up to 1.2%c. The computed drag reduction for this 3D bump design is an encouraging 37%. At the same lift coefficient, $C_L = 0.82$, the data from this brief study is shown in Table 6.2. This study has implied that a relatively higher or larger size would be necessary for the 3D bump to be effective in reducing drag. Results from the latter section on the viscous effects will refer back to this assumptions with more discussions.

| | $C_{Dpressure}$ | Total Drag Reduction |
|---|---|---|
| Datum aerofoil | 0.011681 | - |
| *l20-cre62-cb50-**h0.8**-s60-wid1* | 0.008972 | 23.1% |
| *l20-cre62-cb50-**h0.8**-s80-wid1* | 0.008230 | 29.6% |
| *l20-cre62-cb50-**h0.9**-s80-wid1* | 0.007862 | 32.8% |
| *l20-cre62-cb50-**h1.2**-s80-wid1* | 0.007356 | 37.1% |

Table 6.2: Maximum cross-sectional area hypothesis studies, $M_\infty = 0.68$, $C_L = 0.823$.

### 6.2.3 Optimisation Results

In this optimisation task, the chosen target lift coefficient is still $C_L = 0.823$ as before. As discussed in *Section 6.1*, the last design parameter that is the spanwise width of the grid is actually not included in this optimisation effort. The maximum chordwise bump length is limited to only 20%c and that the bump spanwise width is subjected to a maximum of 90% of the total spanwise width.

The designation of the optimised 3D bump is *l20-cre62.5-cb62.3-h1.07-s90-wid1*. The improvement gained from this design is about 40% reduction in drag, as shown in Table 6.3. Its performance is comparable to that of the optimised 2D bump, which has a designation of *l20-cre63.3-cb66.8-h0.61*. It can be seen here that the optimiser also "favours" a wider 3D bump where the bump span is at the allowable maximum of 90%. The 3D bump has an asymmetrical bump shape that comprises a longer upstream concave. The 3D bump reaches a height of more than 1%c in this case, which is roughly twice the size of the 2D bump. This result fairly agrees with the cross-sectional area hypothesis that an effective 3D bump needs to match the maximum cross-sectional area of the 2D bump.

| | $C_{Dpressure}$ | Total Drag Reduction |
|---|---|---|
| Datum aerofoil | 0.011681 | - |
| *Optimised **3D** bump* | 0.007074 | 39.5% |
| *Optimised **2D** bump* | 0.006582 | 43.1% |

Table 6.3: Comparisons of the inviscid performance for the optimised 3D bump, $M_\infty = 0.68$, $C_L = 0.823$.

In Figure 6.4, the chordwise pressure distribution at three spanwise sections of

the wing with the optimised 3D bump are plotted and compared along with the datum wing. These chosen spanwise sections include the symmetry plane that is situated along the centreline of the bump and the other one that sits on the unmodified surface. In addition, another section that is situated at the mid-span position between the bump crest and tip is also selected. It is noticed here that although the shape of the 3D bump inflicts geometrical variation in the spanwise direction, the variation of the chordwise pressure distribution between these three different spanwise sections is comparatively negligible. This suggests that the inviscid flow field of the 3D bump is largely two-dimensional. The effect of the 3D bump on the shock wave is quite similar to that of the 2D bump, where the upstream maximum Mach number of the shock wave is significantly reduced and hence so is the wave drag.

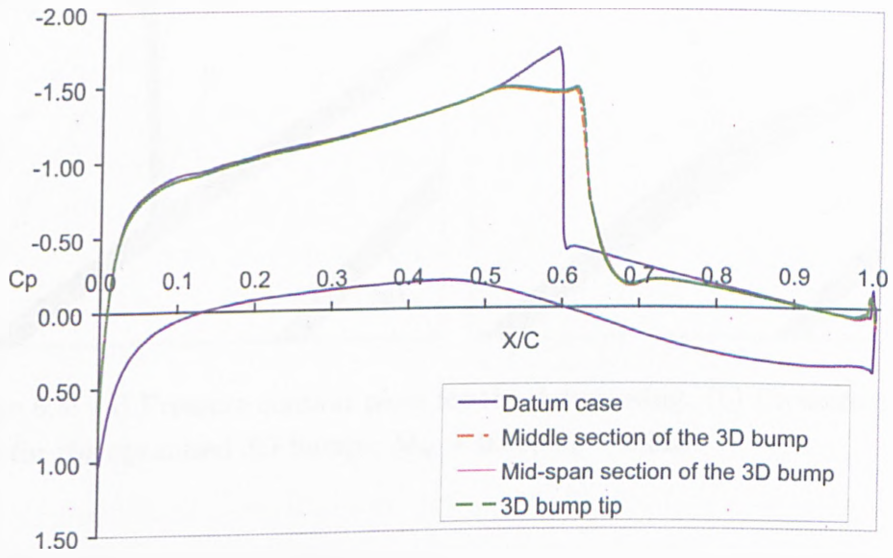


Figure 6.4: Chordwise pressure distributions at various span of the Euler optimised 3D bump, $M_\infty = 0.68$, $C_L = 0.823$.

The pressure contour plots at the vicinity of the shock wave are shown in Figures 6.5 (a) and (b). It is obvious from the comparisons that the strong normal shock wave on the datum wing is significantly weakened by the presence of the 3D bump. Notice that the pressure contour lines are less clustered and spread out in Figure 6.5 (b). In the pressure distribution plots of Figure 6.4, it is shown that the minimum suction peak of the shock wave is lowered and hence so is the

upstream maximum Mach number ahead of the shock wave. The position of the shock has also been displaced slightly downstream. Additionally, one can observe that there are virtually no spanwise variations for the contour lines across the 3D bump surface.

This inviscid optimisation study shows that the 3D bump has the potential to perform as well as the 2D bump. Although the sixth design variable or the total span width has not been included here, it is demonstrated that the modified grid modeller and the adjoint solver for the 3D bump optimisation work reasonably well. The next section will focus on the results of the viscous effects of the 3D bump on the unswept wing with the same aerofoil section.

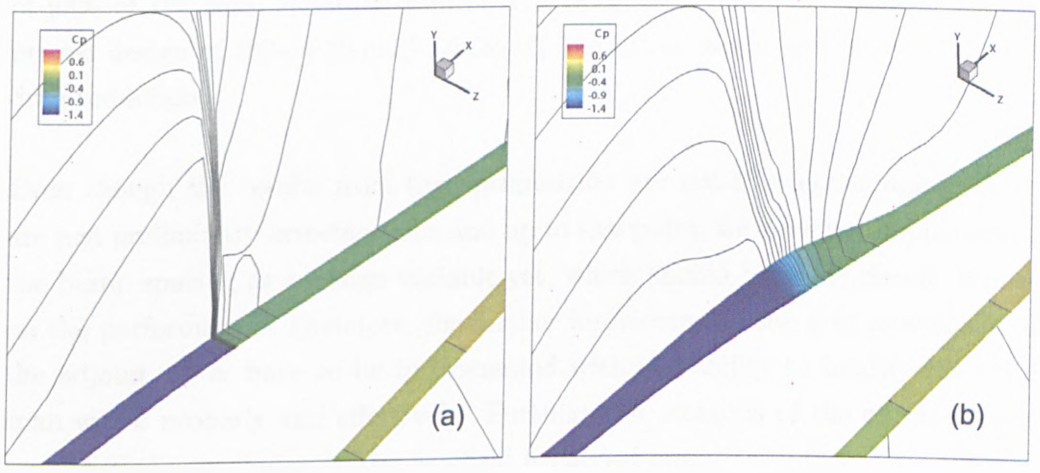


Figure 6.5: (a) Pressure contour plots for the datum wing. (b) Pressure contour plots for the optimised 3D bump , $M_\infty = 0.68$, $C_L = 0.823$.

## 6.3 Viscous Effects of 3D Bump on RAE 5243

### 6.3.1 Preliminary Investigations

A 3D bump design of *l20-cre60-cb57.5-h0.5-s60-wid1* has been investigated by Qin *et al.* [47] at freestream conditions of $M_\infty = 0.68$, $\alpha = 1.5$ and $Re_c = 1.9\times10^6$. The lift coefficient computed at these freestream conditions with the current grid is $C_L = 0.69$. The present computation for this design indicated that around 1.7% improvement in drag reduction has been achieved. The design from the Euler optimisation is also adopted but with the position of the bump shifted

slightly upstream to match the shock wave location in viscous flow and with a lower height (*l20-cre60-cb62.3-h0.5-s90-wid1*) provides a 2.5% reduction in drag. The drag reduction is relatively low, considering that the 2D bump can achieve a drag reduction around 6% for this level of lift coefficient.

An optimisation has then been carried out at this lift coefficient of $C_L = 0.69$ in an attempt to explore whether a much better design could be achieved even without considering the spacing between the 3D bumps as a design parameter. So the optimisation retains only five design variables as investigated in the Euler optimisation presented earlier. Similarly, the maximum chordwise bump length is limited to only 20%c and the bump spanwise width is subjected to a maximum of 98% of the total spanwise width. The optimiser could only uncover an improved design of *l20-cre59-cb63-h0.59-s84-wid1* that would only provide a 2.7% drag reduction.

Even though the results from the optimisation are not that encouraging, these are just preliminary investigations and up to this point, we have not implemented the bump spacing as a design variable yet, which should have significant impact on the performance. Therefore, for further improvement, the grid modeller and the adjoint solver have to be implemented with the ability to modify the total span width properly and effectively. Furthermore, analysis of the effects of this type of 3D bump design in the flowfield is carried out.

### 6.3.2 Flowfield Analysis and Issues

Detailed flowfield analysis of the 3D bump (*l20-cre60-cb57.5-h0.5-s60-wid1*) has revealed some interesting results. Figure 6.6 depicts the surface streamline at the downstream half of the 3D bump. It can be observed from the streamlines that there is streamwise separation along the downstream foot or the base of the bump and with some "swirling" too. This is undesirable from the performance point of view. It is suggested that the separation is largely due to the irregularities along the foot of the bump. These irregularities emerge at the foot of the bump is not defined by the grid lines as shown in the closeup of these areas in Figure 6.7.

These surface geometry anomalies can be resolved by adopting an alternative grid generation strategy that ensures the grid lines be defining the boundary of the

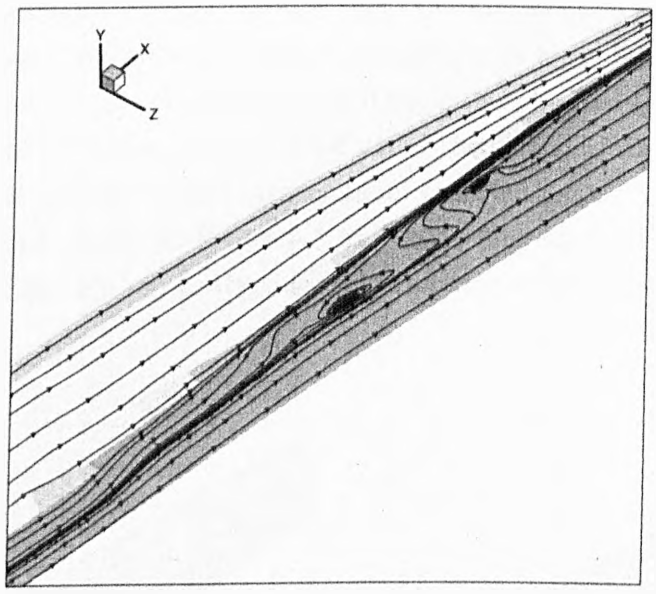


Figure 6.6: Surface streamline on a 3D bump with original design.

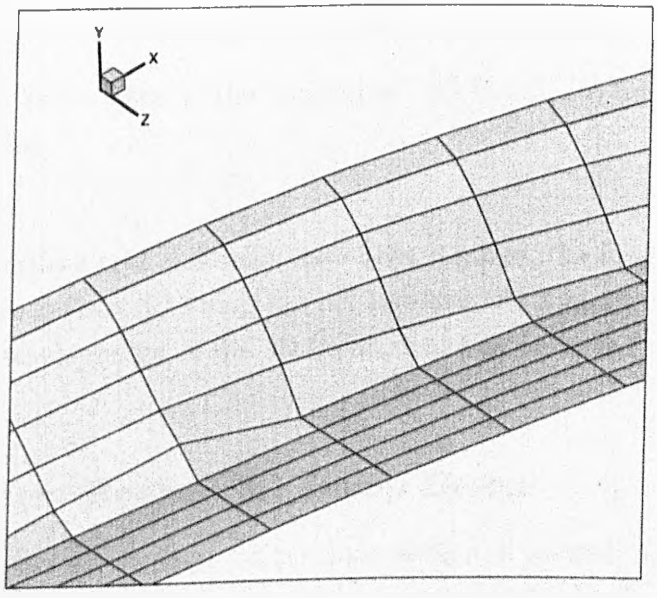


Figure 6.7: Closeup on the surface grid of a 3D bump with original design.

base of the bump. After going through some tests by employing the different grid distribution strategies available in Ref. [96], the re-generated 3D bump of the same designation (*l20-cre60-cb57.5-h0.5-s60-wid1*) with a smooth base is demonstrated in Figure 6.8 (a) and compared with the earlier original grid in Figure 6.8 (b). The revised 3D bump is then tested under the same freestream conditions. Figure 6.9 plots out the surface streamline of this "smoothen" 3D bump. The "swirling" as seen earlier in Figure 6.4 has been eliminated. However, further downstream of the 3D bump, there is still some degree of reverse flow close to the base.

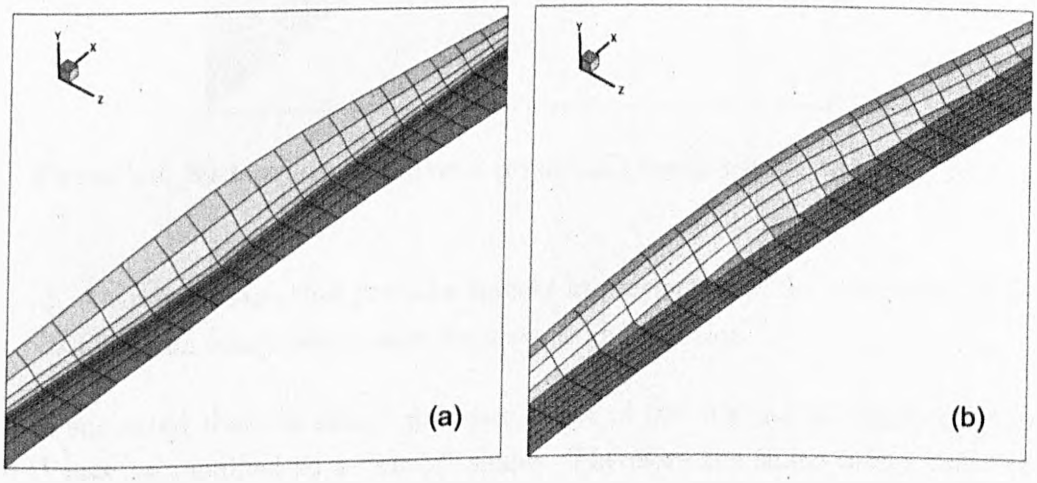


Figure 6.8: (a) Surface grid of the "smoothen" 3D bump. (b) Surface grid of the original 3D bump.

Although the surface grid anomalies have been resolved, the drag reduction performance of this revised 3D bump did not improve. As a result, it is considered to change the whole design of the 3D bump, which is discussed in the following section.

### 6.3.3 Further Revised 3D Bump Design

Following the experiences from the previous section, a revised 3D bump should meet these two requirements:

1. Smooth, continuous base to avoid undesirable viscous effects in the flowfield.

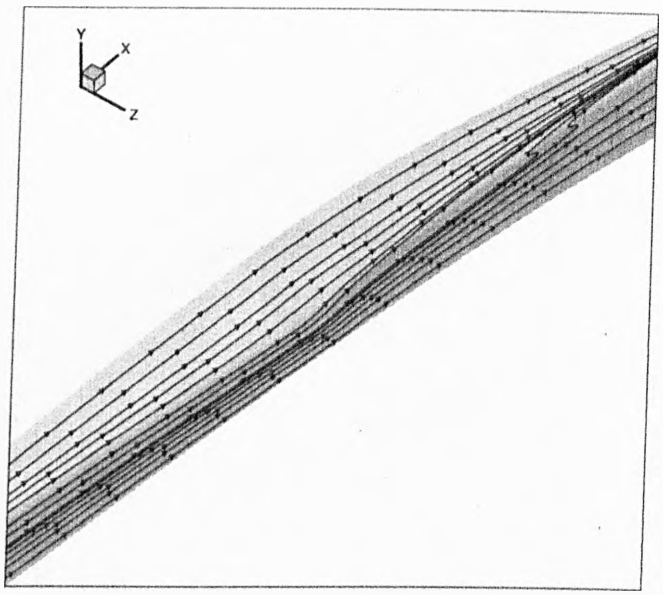


Figure 6.9: Surface streamline on a revised 3D bump with a "smooth" base.

2. A revised shape that provides further improvement in the generation of an upstream compression wave for wave drag reduction.

It is suggested that the sharp upstream shape of the original 3D bump (Figure 6.1) may be modified to a "blunt" shape. Therefore the sharp bump tip is to be removed and the planform of the 3D bump base will represents a rectangular shape instead of a curvilinear one as before. These descriptions are depicted more clearly in Figure 6.10, which illustrates this updated shape. Note that even though the shape has been revised, the original six parameters remain the same. A surface grid showing this revised 3D bump design is shown in Figure 6.11. These modifications will at least satisfy *requirement 1* as stated earlier. This is proven in the visualisation of the surface streamline for this 3D bump in Figure 6.12. As shown in Figure 6.12, the undesirable "swirling" and chordwise flow separation have altogether been removed. The somewhat "blunt" upstream shape could also provide more compression since there are more interacting regions with the flow, which should result in an increase in flow displacement.

A 3D bump with a designation of *l20-cre60-cb57.5-h0.4-s90-wid1* has been generated via both the revised version and original 3D bump. Both of the designs are then computed at the same flow conditions and compared. The results are

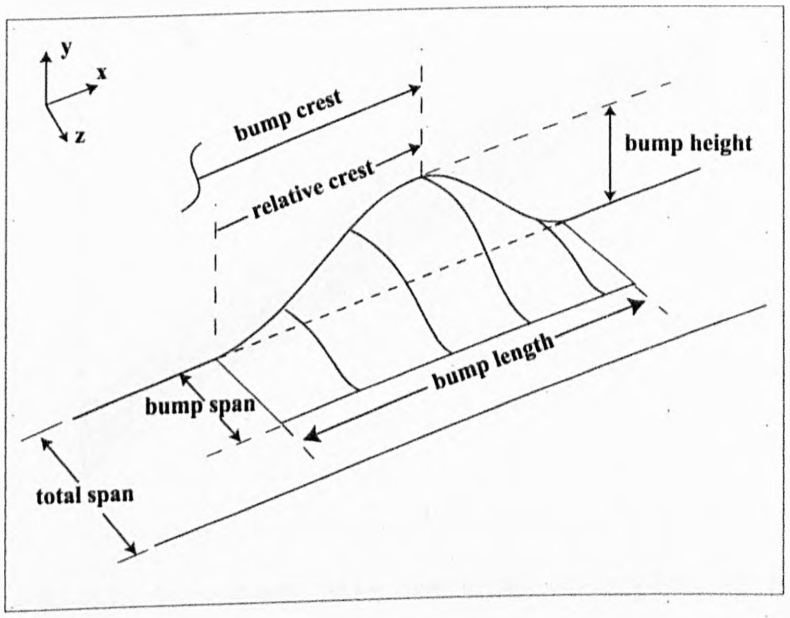


Figure 6.10: Further revised design for the 3D bump.

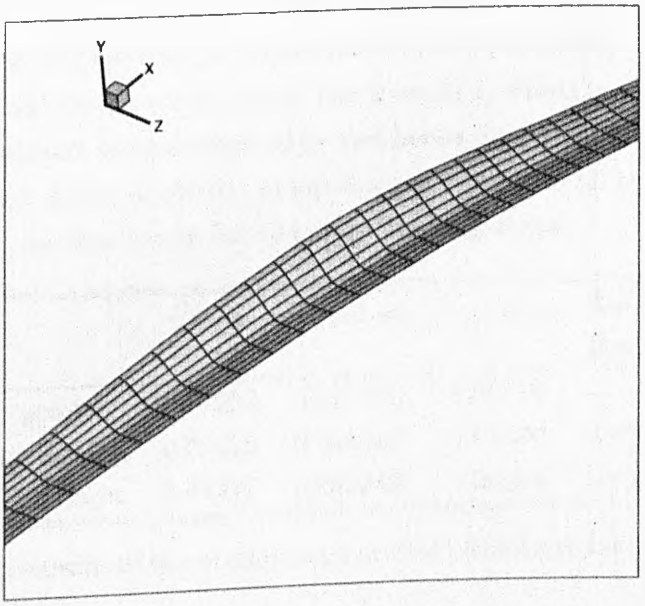


Figure 6.11: Surface grid for the revised design of the 3D bump.

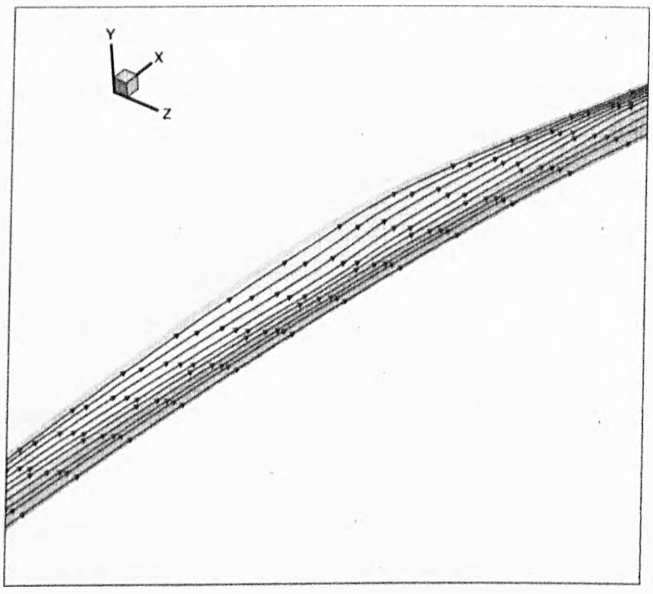


Figure 6.12: Surface streamline for the revised design of the 3D bump.

shown in Table 6.4. It is demonstrated in this table that the present revised design outperforms the original design by 2% in total drag reduction. Although the skin friction drag from both of the designs has slightly increased compared to the datum aerofoil, the revised design induces slightly less skin friction drag penalty than the original design. These results seem promising and suggest that the present revised design could satisfy *requirement 2*, which is to improve generation of the upstream compression wave and hence drag reduction performance. Since this revised design of the 3D bump has fairly satisfied all the requirements, it is decided to use this design for upcoming investigations.

| | $C_{Dtotal}$ | $C_{Dpressure}$ | $C_{Dfriction}$ | **Total Drag Reduction** |
|---|---|---|---|---|
| Datum aerofoil | 0.01282 | 0.007023 | 0.00579 | - |
| ***Original design*** | 0.01238 | 0.006485 | 0.00590 | 3.4% |
| ***Revised design*** | 0.01213 | 0.006249 | 0.00588 | 5.4% |

Table 6.4: Comparisons of the original and revised 3D bump designs, $M_\infty = 0.68$, $C_L = 0.823$.

### 6.3.4 Optimisation Results

At this stage, the sixth design parameter, $z_{total\_span}/c$ has finally been implemented properly into the grid modeller and the adjoint solver. The main obstacle to this implementation is really in the adjoint solver, which has been discussed earlier in *Chapter 4*. Before starting the optimisation, a few design cases that have fully incorporated the design parameter, $z_{total\_span}/c$, have been tested. Their performances are presented in Table 6.5.

| | $C_{Dtotal}$ | $C_{Dpressure}$ | $C_{Dfriction}$ | **Total Drag Reduction** |
|---|---|---|---|---|
| Datum aerofoil | 0.01622 | 0.010634 | 0.005585 | - |
| *l20-cre60-cb57.5-**h0.7**-s90-**wid2*** | 0.01432 | 0.008617 | 0.005698 | 14.4% |
| *l20-cre60-cb57.5-**h0.9**-s90-**wid4*** | 0.01388 | 0.008195 | 0.005688 | 16.8% |

Table 6.5: Comparisons of the test cases that have variable total spanwise width, $M_\infty = 0.68$, $C_L = 0.823$.

It is shown from the above table that by increasing both the bump height and $z_{total\_span}/c$, substantial improvement in performance can be obtained. The drag reduction gained are now in the order of 10%, which is quite encouraging.

For the optimisation task, $C_L = 0.82$ is still preferred as the target lift coefficient for the reason stated in the optimisation of the 2D bump (*Section 5.4.2*). This is an off-design condition for the aerofoil with a strong shock. In addition, it would then be possible to compare the performance of both the optimised 2D and 3D bump at the same lift condition. The maximum allowable chordwise bump length is limited to 40%c and the bump width is allowed to grow up to 98% of the total width.

The acquired optimised 3D bump has a designation of *l32.9-cre62.7-cb54.1-h1.38-s98-wid11.9*. Figure 6.13 presents the full three-dimensional shape of the 3D bump. Note that here the scale in the $y$-direction has been slightly modified in order to enhance the visualisation of the height of the bump. The height of this optimised shape is around twice the size of the optimised 2D bump at 1.38%c. Note that the optimised 2D bump has a designation of *l31.3-cre59.7-cb66.1-h5.9*. Since the bump width has grown to around 98% of the total width, therefore it

indicates that the spanwise tips of the consecutive bumps are very close to each other. Its spanwise total size has reached 12%c, which can be translated into 24%c spacing between the centrelines of the consecutive bumps. The shape of the 3D bump on the upper surface of the aerofoil is shown in Figure 6.14.

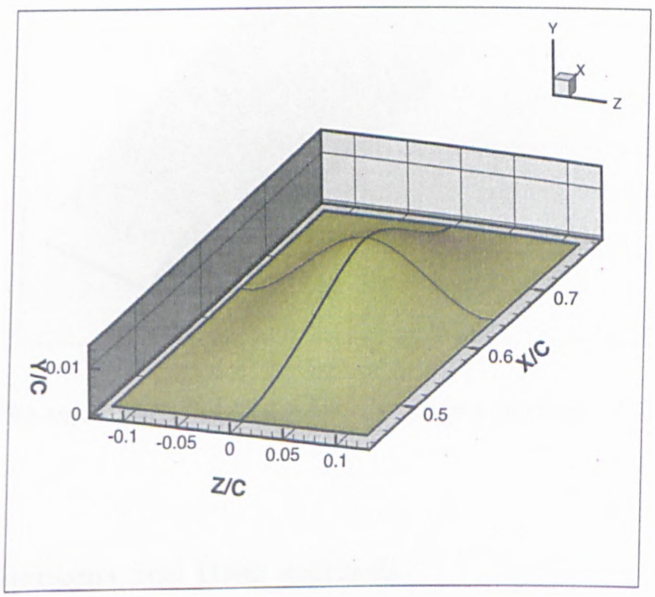


Figure 6.13: The shape of the optimised 3D bump.

| | $C_{Dtotal}$ | $C_{Dpressure}$ | $C_{Dfriction}$ | **Total Drag Reduction** |
|---|---|---|---|---|
| Datum aerofoil | 0.01622 | 0.010634 | 0.005585 | - |
| *Optimised **3D** bump* | 0.01296 | 0.007208 | 0.005755 | 20.1% |
| *Optimised **2D** bump* | 0.01326 | 0.007563 | 0.005699 | 18.2% |

Table 6.6: Comparisons of the optimised 2D and 3D bumps. (RAE 5243, $M_\infty = 0.68$, $C_L = 0.82$)

From the comparisons in Table 6.6, it is shown that the optimised 3D bump reduces drag better than the optimised 2D bump by around 3 drag counts or 2%. Similar to the effects of a 2D bump, there is also a small increase in skin friction drag from the 3D bump. However, compared to the substantial reduction gained in pressure drag, this drag penalty is considered insignificant.

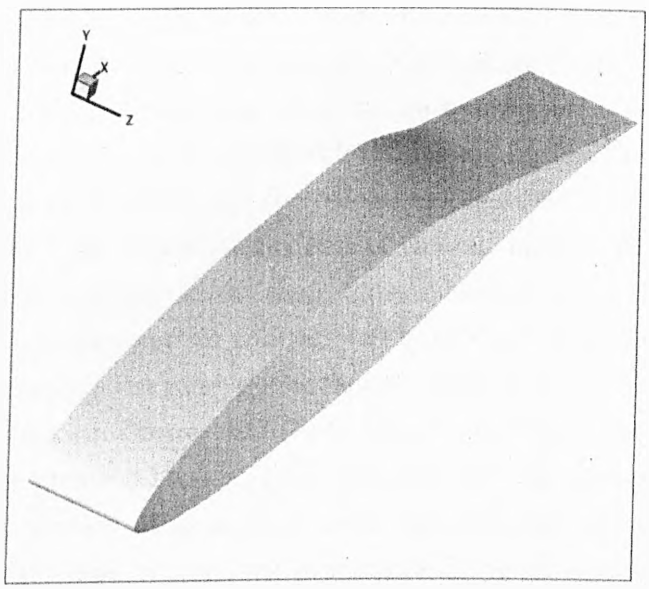


Figure 6.14: The optimised 3D bump on the upper surface of RAE 5243 NLF aerofoil.

#### 6.3.4.1 Mechanisms and Drag Analysis

The effects of the 3D bump on the original normal shock are shown in the sequence in Figures 6.15. Figure 6.15 (a) depicts the 3D bump (red solid-line) superimposed on the surface of the datum wing with the original strong normal shock located about 5%c upstream from the bump crest. Part of the upstream region of the 3D bump lies within the supersonic region of the normal shock, which generates an isentropic compression wave to weaken the normal shock. Concurrently, part of the remaining upstream region of the 3D bump lies between the terminated normal shock and the crest of the 3D bump. In this region, recall that the speed of a subsonic flow will increase when going through a decreasing cross-sectional area; thus, the subsonic flow accelerates to supersonic flow and terminates as a weaker shock at the vicinity of the bump crest. Note that these explanations are rather a repeat of the discussions in *Section 5.4.2.1*.

These descriptions of the bump mechanisms are shown in Figures 6.15 (b) to (d). The figures present the pressure contour lines that are plotted at various spanwise locations, e.g. along the middle or centreline of the bump, the mid-span location between the centreline and the tip and also at the tip of the bump where there

are virtually no shape modifications. It can be observed here that the original normal shock is converted into a weakened "knee"-shape shock. Its position has also displaced slightly downstream close to the bump crest. Variations in the pressure contours at the three spanwise locations are noticeable. Visualisations of the outer inviscid flowfield that correspond to Figure 6.15 (a) to (d) are presented in Figures 6.16. The following sets of contour plots in Figure 6.17 show the Mach number contours at the same three spanwise locations and with the datum case for comparisons. In addition to the obvious variations of the Mach number contours across the span, notice that the contour level at the upstream of the remaining shock (in Figures 6.17 (b) to (d)) is lower than that of the original normal shock in Figure 6.17 (a). This indicates that the maximum upstream Mach number of the remaining shock is lower than the original normal shock. In Figure 6.18, surface skin friction lines around the 3D bump show no indications of flow separations.

These effects are further analysed through the streamwise pressure distribution plots in Figure 6.19. It plots out the streamwise pressure distribution of the 3D bump at the three spanwise locations that correspond to Figures 6.15. The streamwise pressure distribution of the optimised 2D bump (dark solid-line) is added for comparisons. It is shown here that the effects of the 3D bump on the shock wave is similar to that of the 2D bump. Since the shape of the optimised 2D bump has a longer upstream convex, and also due to a slightly varied location of the bump crest, the effects of the optimised 2D bump take place a little earlier than the 3D bump.

The red dashed-line, which denotes the pressure distribution along the centreline of the 3D bump, indicates that the minimum pressure peak of the shock wave has been reduced. Additionally, the shock wave has also been displaced slightly downstream. It can be observed that there are obvious variations of streamwise pressure distributions plotted at the three different spanwise locations of the 3D bump, where the generation of the upstream compression waves seems to be weakening towards the tip. Despite having virtually no geometrical modification at the tip, the effects of the 3D bump have propagated towards the tip. In addition, despite the presence of the bumps, the favourable pressure gradients across most of the upstream part of the upper surface are still maintained.

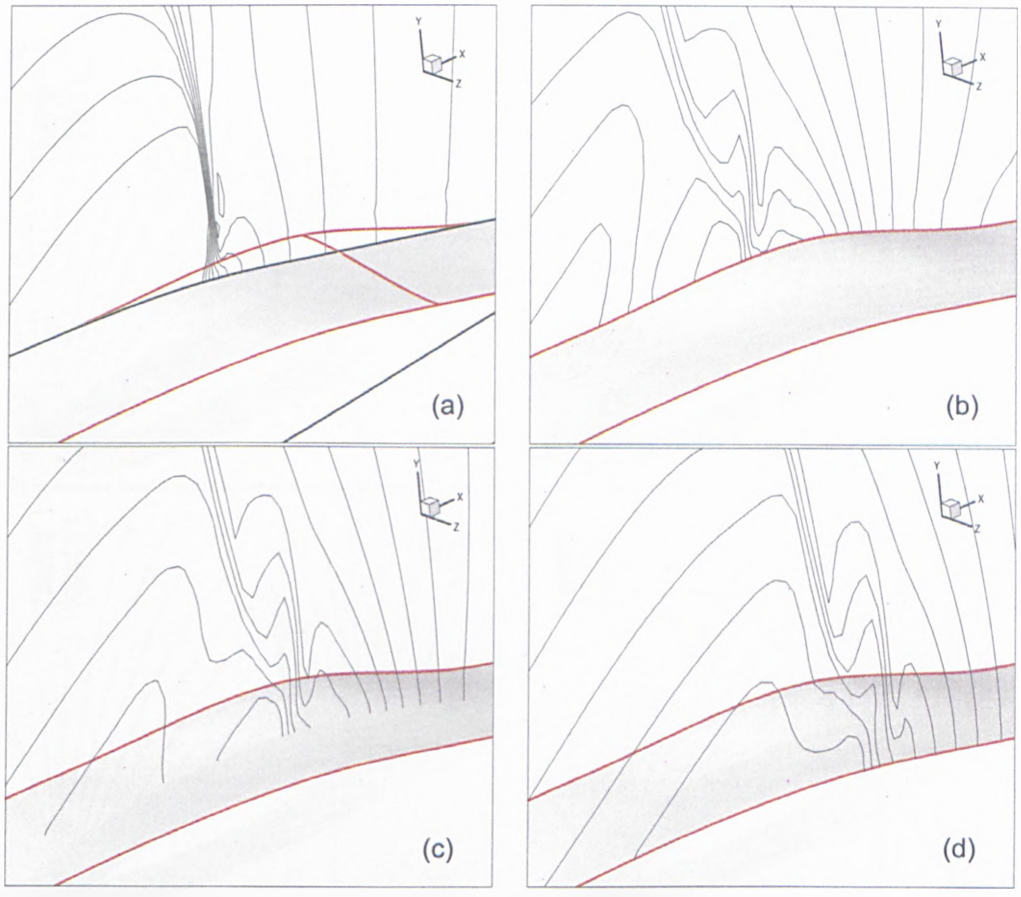


Figure 6.15: (a) Pressure contour lines of the original normal shock wave on the datum aerofoil. (with the shape of the optimised 3D bump superimposed on top of the wing) (b) Pressure contour lines along the centreline of the optimised 3D bump. (c) Pressure contour lines along the mid-span of the optimised 3D bump. (d) Pressure contour lines along the tip of the optimised 3D bump. (RAE 5243, $M_\infty = 0.68$, $C_L = 0.823$)

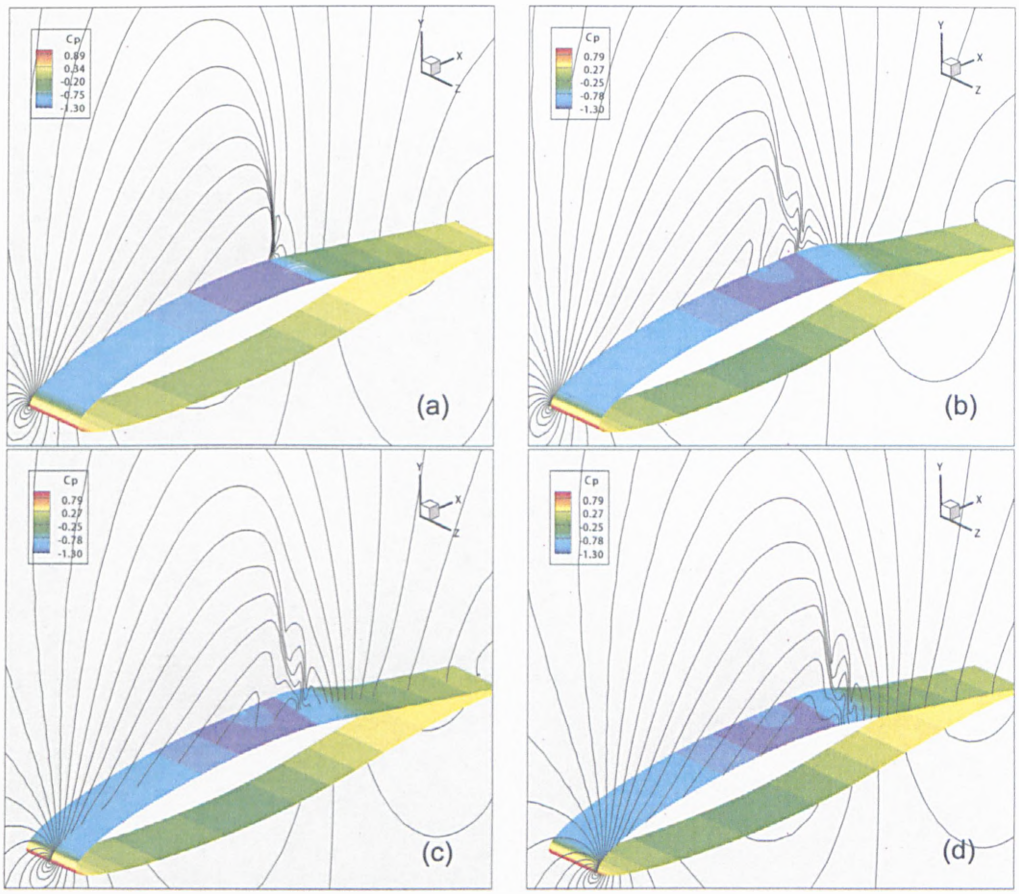


Figure 6.16: (a) Pressure contours of the datum aerofoil. (b) Pressure contours along the centreline of the optimised 3D bump. (c) Pressure contours along the mid-span of the optimised 3D bump. (d) Pressure contours along the tip of the optimised 3D bump. (RAE 5243, $M_\infty = 0.68$, $C_L = 0.823$)

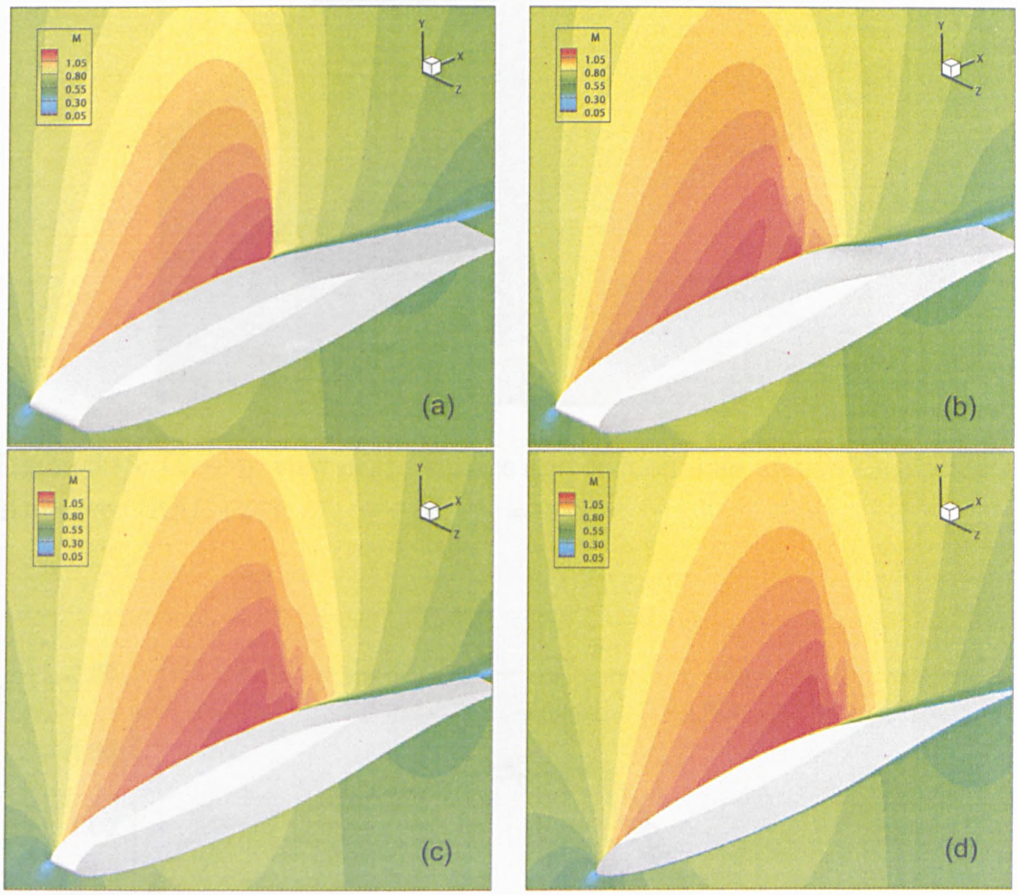


Figure 6.17: (a) Mach number contours of the datum aerofoil. (b) Mach number contours along the centreline of the optimised 3D bump. (c) Mach number contours along the mid-span of the optimised 3D bump. (d) Mach number contours along the tip of the optimised 3D bump. (RAE 5243, $M_\infty = 0.68$, $C_L = 0.823$)

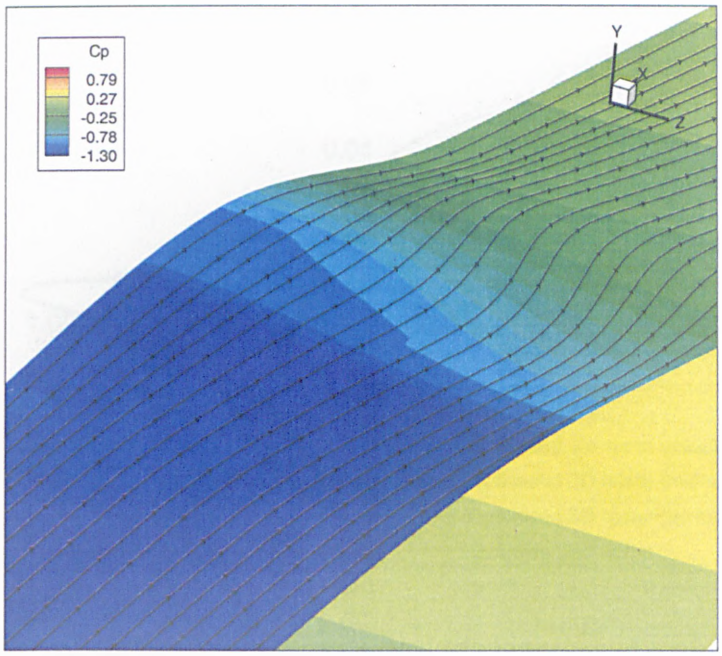


Figure 6.18: Closeup view of the surface skin friction lines around the optimised 3D bump. (RAE 5243, $M_\infty = 0.68$, $C_L = 0.82$)

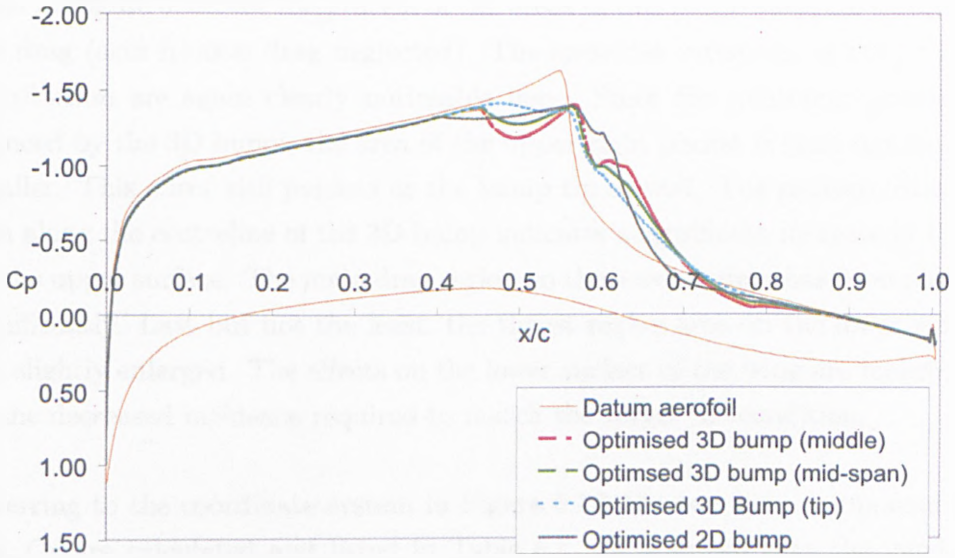


Figure 6.19: The streamwise Cp distribution for the optimised 3D bump on the upper surface of RAE 5243 NLF aerofoil , $M_\infty = 0.68$, $C_L = 0.823$.

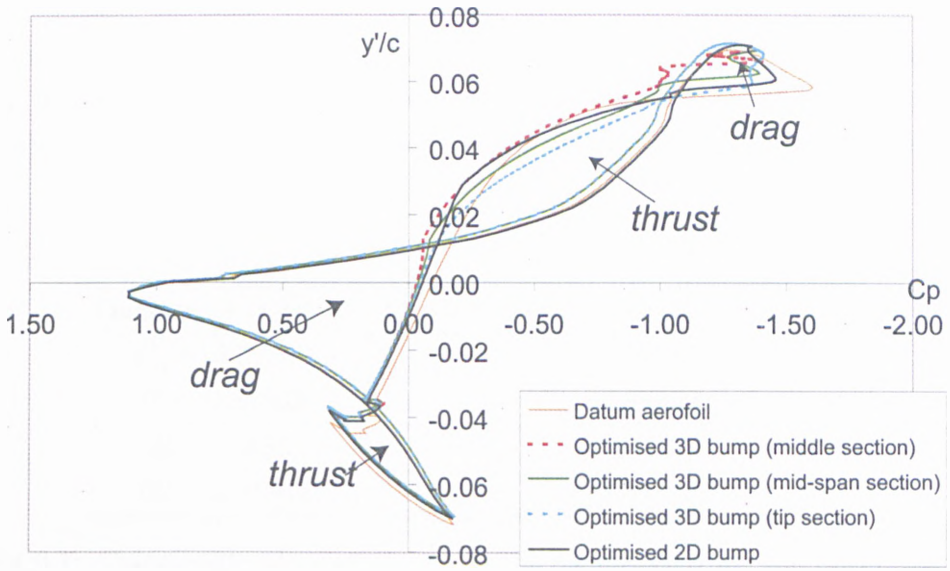


Figure 6.20: $y$' vs $Cp$ plots for the optimised 3D bump on the upper surface of RAE 5243 NLF aerofoil , $M_\infty = 0.68$, $C_L = 0.823$.

Figure 6.20 shows the $y$'-coordinates plotted against $Cp$ at the usual three spanwise locations of the optimised 3D bump. With reference to the coordinate systems in Figure 5.19, the integration of the areas in this plot contribute directly to the drag (skin friction drag neglected). The spanwise variations of the pressure distribution are again clearly noticeable here. Since the minimum pressure is reduced by the 3D bump, the area of the upper right pocket is then significantly smaller. This effect still persists at the bump tip as well. The pressure distribution along the centreline of the 3D bump indicates a significant increase in thrust on the upper surface. The main drag region on the lower surface has been reduced significantly. Last but not the least, the thrust region area on the lower surface has slightly enlarged. The effects on the lower surface of the wing are mainly due to the decreased incidence required to match the target lift condition.

Referring to the coordinate system in Figure 5.19, the two force components $Cy$ and $Cx$ are calculated and listed in Table 6.7. It is shown that the incidence for the 3D bump case is lowered by around 0.27°. The following analysis is very similar to the discussions presented in *Section 5.4.2.1.* The table demonstrated that even though the calculations of the two force components from the two cases

are very close, the same lift condition can be sustained at a lower incidence by the optimised 3D bump. Consequently, drag has been further reduced due to this lower incidence. Although these discussions did not take the skin friction drag contributions into account, nevertheless, its contributions are relatively insignificant.

| **Datum, $\alpha = 2.417°$** | **Optimised 3D Bump, $\alpha = 2.145°$** |
|---|---|
| $C_x$= -0.02393 | $C_x$= -0.02347 |
| $C_y$= 0.81899 | $C_y$= 0.81909 |
| $C_L$= 0.81928 | $C_L$= 0.81939 |
| $C_D$= 0.01064 | $C_D$= 0.007213 |

Table 6.7: Calculated values of the $C_x$ & $C_y$ components for the optimised 3D bump. (RAE 5243, $M_\infty = 0.68$, $C_L = 0.82$)

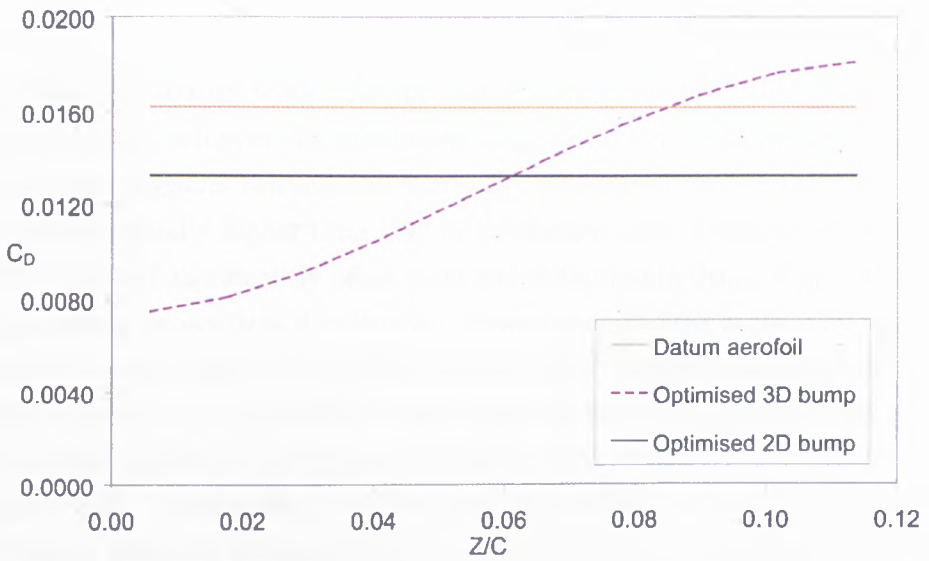


Figure 6.21: Spanwise variations of the total drag for the optimised 3D bump on the upper surface of RAE 5243 NLF aerofoil , $M_\infty = 0.68$, $C_L = 0.823$.

It is interesting to analyse the variations of the drag components across the span. The spanwise changes of the total drag are shown in Figure 6.21. Since there are no spanwise variations for the datum wing and the 2D bump case, the plotted lines for both cases remain straight with the drag level of the 2D bump much

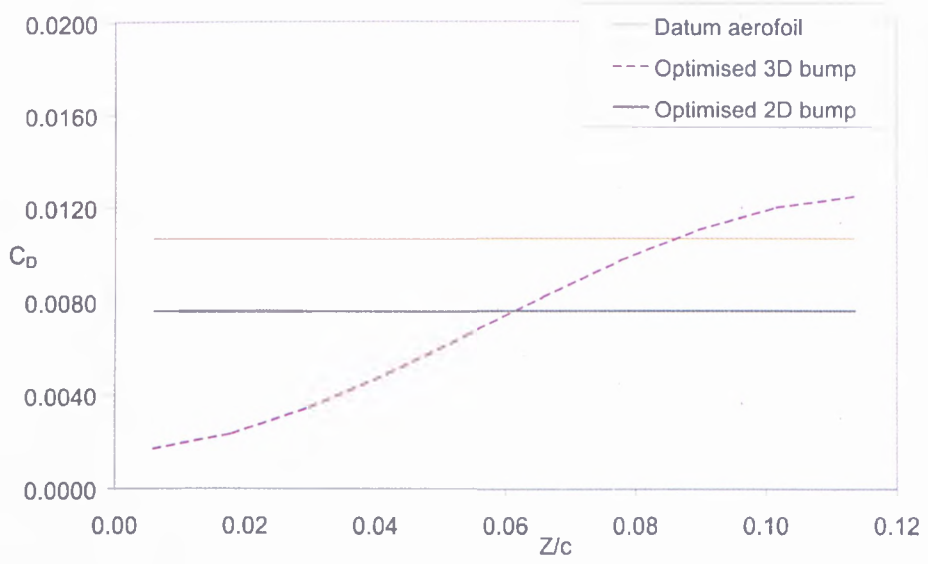


Figure 6.22: Spanwise variations of the pressure drag for the optimised 3D bump on the upper surface of RAE 5243 NLF aerofoil , $M_\infty = 0.68$, $C_L = 0.823$.

lower than the datum wing. As for the 3D bump, it is obvious that the 3D bump centreline achieves the maximum drag reduction. The performance then progressively degrades towards the bump tip. At around z=8%c and beyond, the drag level is actually higher than that of the datum case. Nonetheless, this small penalty does not significantly offset the total reduction in drag. Figure 6.22 plots the spanwise pressure drag distribution. Since pressure drag is the dominant drag component over the skin friction drag, the trend of the plot is very much similar to that of the total drag spanwise distribution in Figure 6.21. At the same scale, the spanwise variations of the skin friction drag are barely noticeable as shown in Figure 6.23. Nonetheless, it is observed that the skin friction penalty from the 3D bump is generally slightly higher than the 2D bump across most of the span.

#### 6.3.4.2 Wave Drag Analysis

The wave drag performance of the 3D bump is assessed by comparing the entropy contour plots with the datum case and by calculating the wave and viscous drag components via the far-field method presented in *Section 2.7*. The wave drag and viscous drag (form drag+skin friction drag) components extracted using the

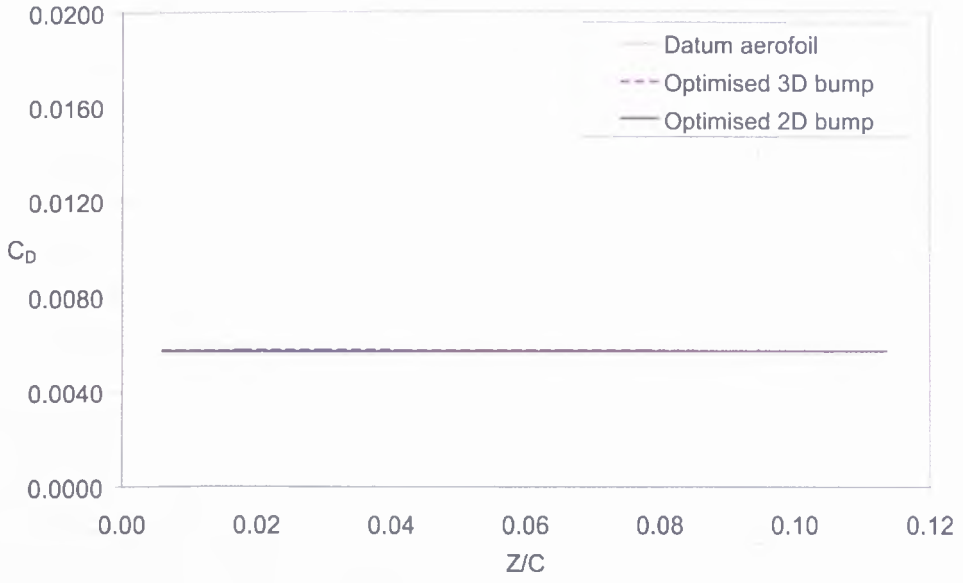


Figure 6.23: Spanwise variations of the skin friction drag for the optimised 3D bump on the upper surface of RAE 5243 NLF aerofoil , $M_\infty = 0.68$, $C_L = 0.823$.

far-field method are presented in the following table:

| | $C_{Dwave}$ | $C_{Dviscous}$ |
|---|---|---|
| Datum aerofoil | 0.0031256 | 0.010264 |
| *Optimised **3D** bump* | 0.0007239 | 0.009696 |
| *Optimised **2D** bump* | 0.0008485 | 0.010107 |

Table 6.8: Comparisons of the wave drag and viscous drag components for the optimised bumps. (RAE 5243, $M_\infty = 0.68$, $C_L = 0.82$)

From Table 6.8, the wave drag reduction performance of both the optimised bumps are at about the same level, each reducing more than 20 drag counts. Additionally, there is also a slight decrease in viscous drag as well, which should come from form drag since the surface integration method suggests that there is a small skin friction drag penalty.

The spanwise variations of both the wave and form drag are shown in Figure 6.24 and Figure 6.25 respectively. The wave drag distribution across the span shows similar trends to that of the pressure drag where the middle or centreline of the

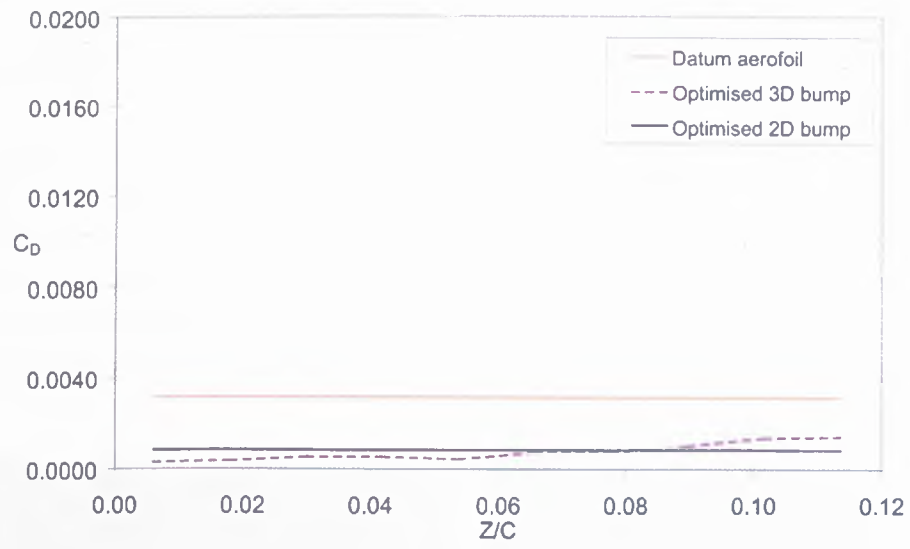


Figure 6.24: Spanwise variations of the wave drag for the optimised 3D bump on the upper surface of RAE 5243 NLF aerofoil , $M_\infty = 0.68$, $C_L = 0.823$.

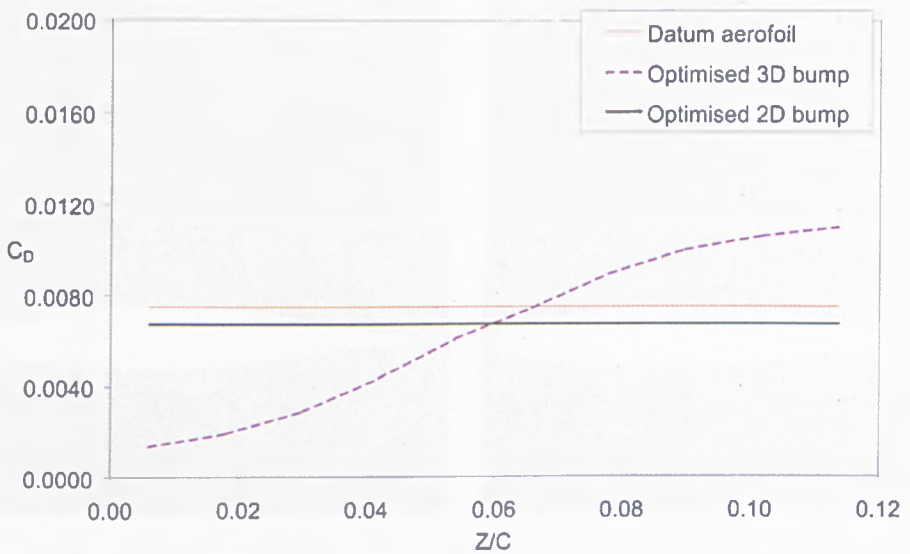


Figure 6.25: Spanwise variations of the form drag for the optimised 3D bump on the upper surface of RAE 5243 NLF aerofoil , $M_\infty = 0.68$, $C_L = 0.823$.

3D bump has the maximum drag reduction. As the reduction progressively drops down towards the bump tip, at z=8%c and beyond, the 3D bumps exerts more wave drag than the 2D bump. Nevertheless, all the level of the spanwise sections remain below the datum case.

In Figure 6.25, it is shown that the level of form drag from the 2D bump case is below the datum case. While the 3D bump has part of the spanwise region below the datum level and the other half above it. Again, it is still the part closer to the centreline that acquires more beneficial effects. Despite that, the overall form drag is reduced by the 3D bump as suggested from the calculations in Table 6.8.

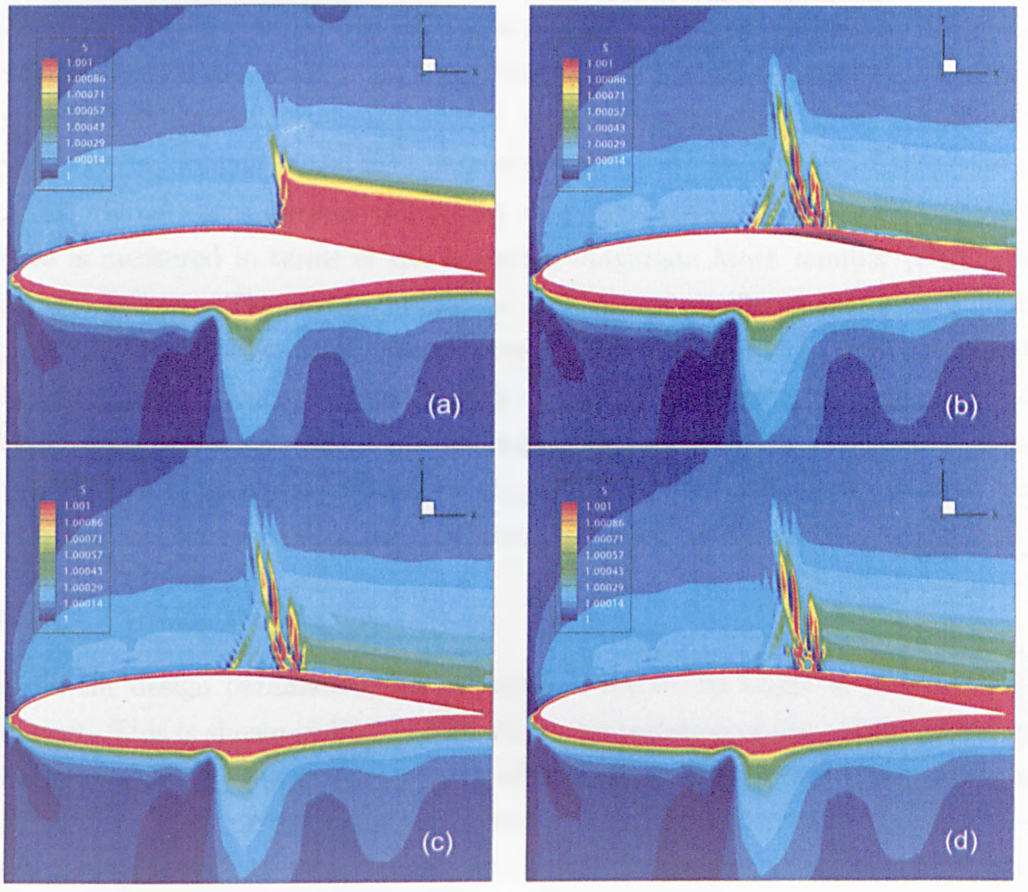


Figure 6.26: (a) Entropy contours of the datum aerofoil. (b) Entropy contours at the spanwise centreline of the optimised 3D bump. (c) Entropy contours at the mid-span of the optimised 3D bump. (d) Entropy contours at the tip of the optimised 3D bump. (RAE 5243, $M_\infty = 0.68$, $C_L = 0.823$)

Figures 6.26 (a)-(d) include the entropy contours plot of the datum case and the three representative spanwise locations of the 3D bump. The extensive rise of entropy across the original strong normal shock (as indicated by the reddish region behind the shock in Figure 6.26 (a)) has been converted into a much weakened shock by the 3D bump. Within the same range of contour levels, the high-red entropy level region behind the remaining shock has almost been eradicated. The variations across the spanwise locations are indicated by the eventual appearance of more green contour level behind the remaining shock at the bump tip.

### 6.3.5 Correlations of 3D Bump Design Parameters

In addition to the optimisation work, it is also useful to derive a low-order model for the 3D bump. This low-order model will be a guidance for the designers or engineers on designing a 3D bump for various operating conditions without carrying out high-fidelity optimisations at each design point. In this study, we correlate the designs of the 3D bump with respect to the strength and position of the original shock wave on the datum wing. The strength of the original shock wave is measured in terms of the upstream maximum Mach number ($M_{max}$) of the shock wave. The investigations are carried out on the unswept wing with the RAE 5243 NLF aerofoil. The freestream Mach number ($M_\infty$) is still fixed at 0.68 and the incidence is varied in order to change the strength of the original shock wave or $M_{max}$. Therefore, a range of angles of attack has been chosen, $\alpha = 0.0 \sim 3.5$, which correspond to $M_{max}$=1.13 $\sim$ 1.37. The designs of the 3D bump are optimised at each lift condition as defined by the range of angles.

#### 6.3.5.1 Bump Height

Of all the design parameters, the variation of the bump height is the most significant. This is shown in Figure 6.27 where the variation of the optimised bump height is plotted against the strength of the original shock wave, $M_{max}$. It is shown here that for optimum performance, the height of the 3D bump varies with respect to $M_{max}$. The stronger the shock wave is, the higher the 3D bump has to be. A smaller bump height is required at low-lift conditions to avoid a severe double-shock system as in the 2D bump cases. Nevertheless, the 3D bump still has some advantage over 2D bump at these conditions as shown in later sections. Additionally, added here are the heights of the 3D bumps that are optimised on the RAE 2822 turbulent aerofoil (*Section 6.4*) and the infinite swept

wing (*Section 7.1*). For the corresponding shock strength at $M_{max} = 1.35$, an optimised 3D bump with greater height is obtained for the RAE 2822 turbulent aerofoil case. On the other hand, the height of the optimised 3D bump at that particular design point for the infinite swept wing lies closer to the trend line of the current correlation study.

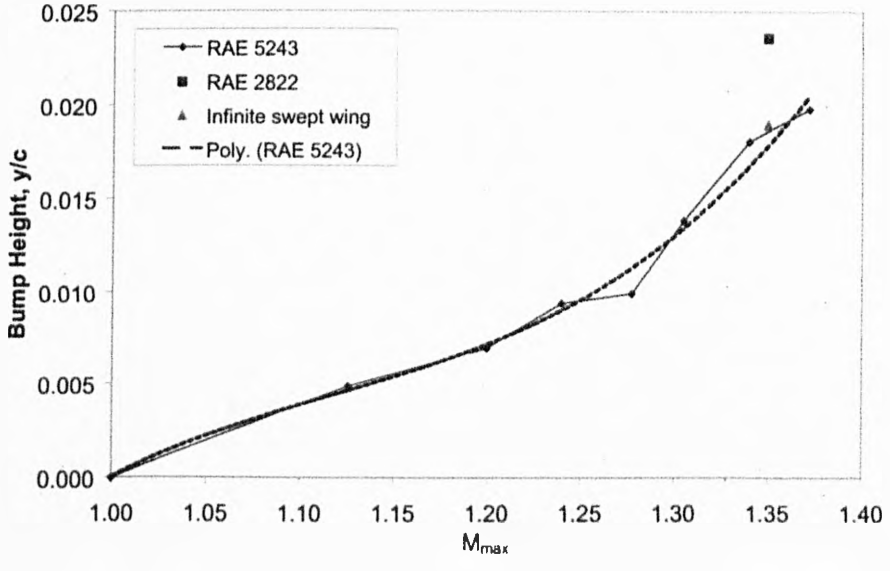


Figure 6.27: Correlations of the bump height for the 3D bump on the RAE 5243 NLF aerofoil.

#### 6.3.5.2 Position of the Bump Crest, $\Delta X_{crest}/c$

The position of the original shock wave is defined according to Figure 6.28. The variation of its position is presented in Figure 6.29. It can be seen here that for this type of NLF aerofoil, the position of the normal shock wave does not vary significantly with the changing incidence. Due to different aerofoil shape designs and freestream conditions, the position of the original shock wave on the RAE 2822 aerofoil and infinite swept wing is relatively further downstream. By referring to Figure 6.28 as well, the relative position of the 3D bump crest, $\Delta X_{crest}/c$ is defined as the distance between the original shock wave and the crest of the 3D bump. In Figure 6.30, the variation of $\Delta X_{crest}/c$ seems to be oscillatory around $\Delta X_{crest}/c = 0.062$ or 6.2%. However, the uncertainty in the definition of the shock position may contribute to this. For the RAE 2822 case,

at that particular design point, the crest of the optimised 3D bump is placed around 9%c downstream of the original shock wave. The crest of the 3D bump is situated around 5% downstream on the infinite swept wing. Nevertheless, these results again indicate that the crest of the 3D bump has to be placed slightly downstream of the original shock wave.

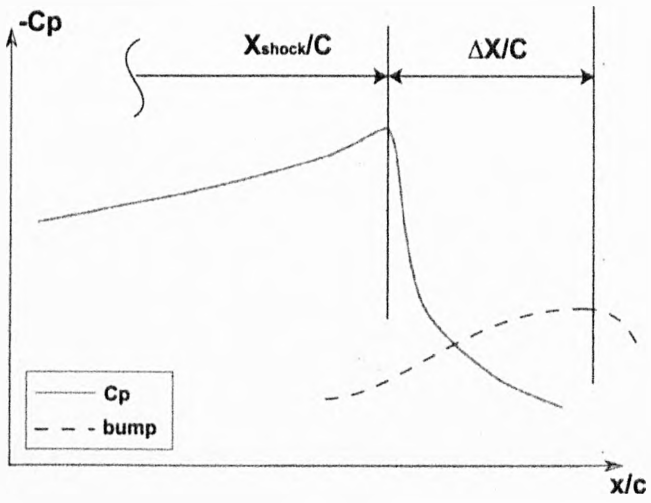


Figure 6.28: Definition of the position of the original shock wave on the RAE 5243 NLF aerofoil.

#### 6.3.5.3 Bump Length

The streamwise length of the 3D bump does not seem to vary much as well, as presented in Figure 6.31. From the black-dashed trend line, the mean value is around 32%c. The sizes of the 3D bumps optimised at a design point on the RAE 2822 aerofoil and the infinite swept wing are slightly larger as compared to the NLF aerofoil cases.

#### 6.3.5.4 Relative Position of the Bump Crest

This design parameter defines the relative position of the bump crest with respect to the streamwise bump length. Its variation in Figure 6.32 is limited as well. The recovered mean value from the trend line is around 54%. The optimised 3D bumps on the RAE 2822 aerofoil and infinite swept wing at a corresponding shock strength again have slightly different shapes.

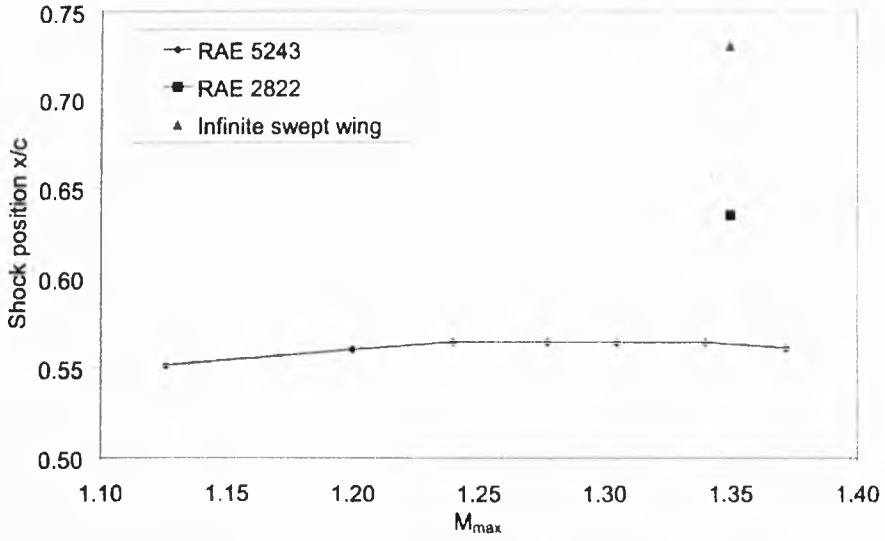


Figure 6.29: Position of the original shock wave on the RAE 5243 NLF aerofoil.

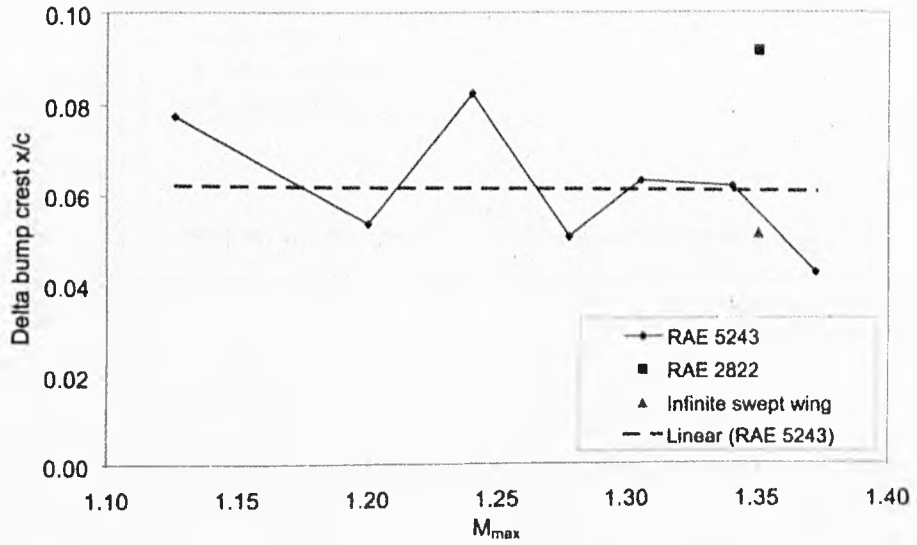


Figure 6.30: Correlation of $\Delta X_{crest}/c$ on the RAE 5243 NLF aerofoil.

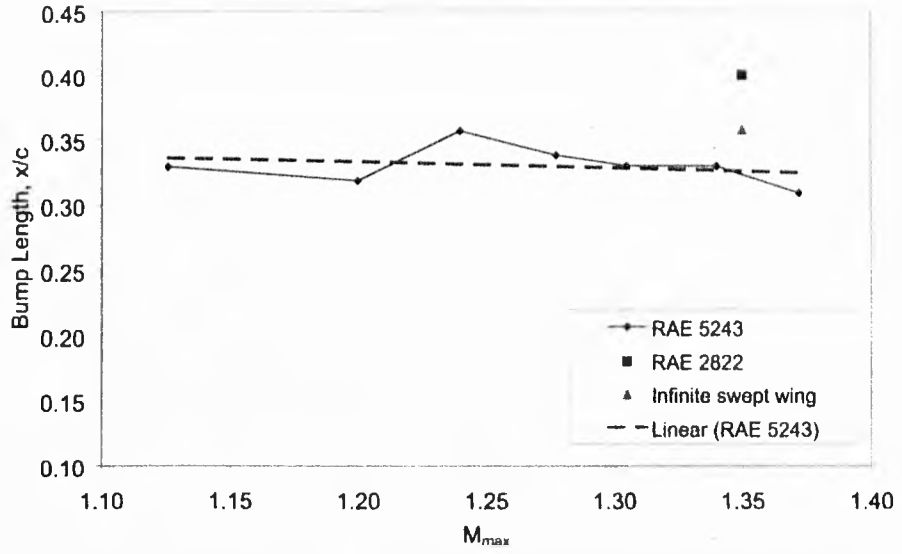


Figure 6.31: Correlations of the bump length of the 3D bump on the RAE 5243 NLF aerofoil.

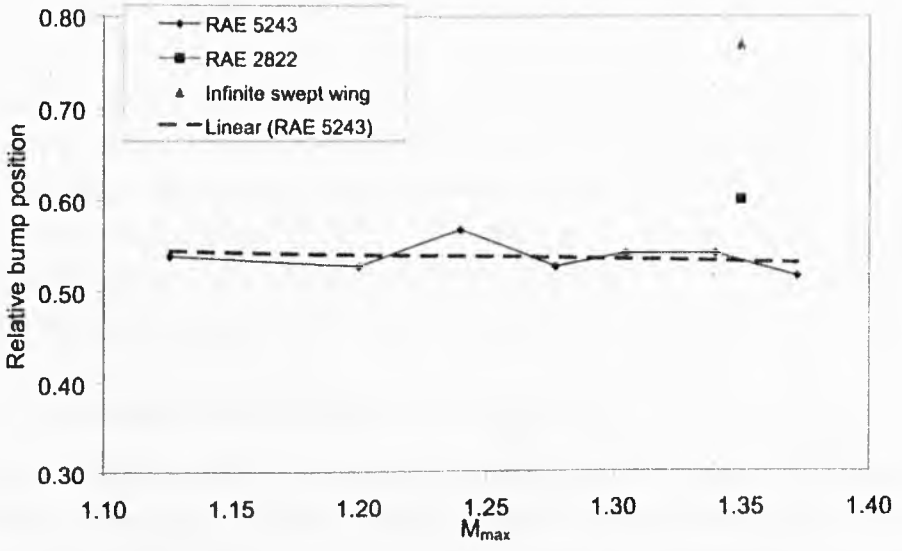


Figure 6.32: Correlations of the relative position of the 3D bump crest on the RAE 5243 NLF aerofoil.

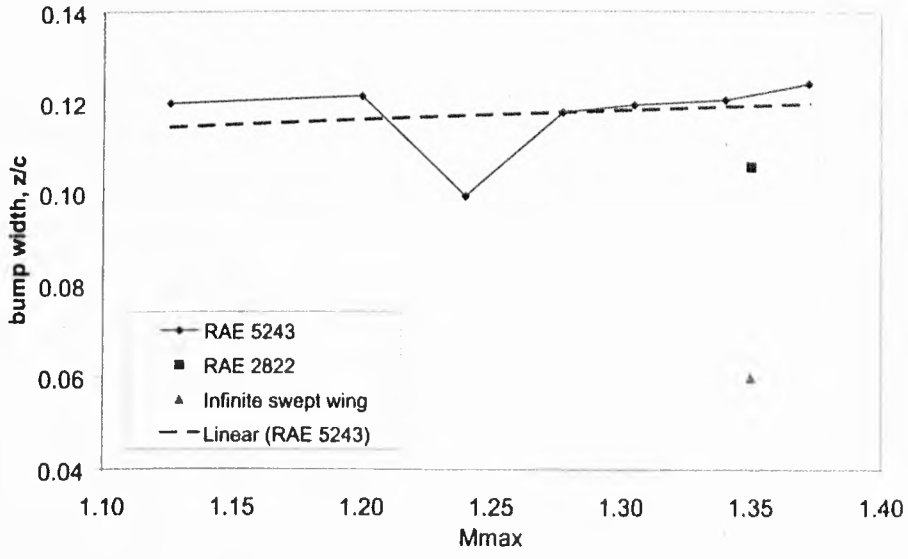


Figure 6.33: Correlations of the 3D bump width/spacing on the RAE 5243 NLF aerofoil.

#### 6.3.5.5 Bump Width/Bump Spacing

These two design parameters are put together here because the consecutive 3D bumps are always favoured to link up close to each other at the bump tips. Thus, the width of the 3D bump is about the same value as that of the spacing width. Note that the values considered here are half of the total bump width or spacing. Their variations are shown in Figure 6.33. Even though there is a dip at one of the design points, the overall variations are limited as well. Again from the trend line, the mean value is about 12%c. The width of the optimised 3D bump on the turbulent aerofoil is in the order of 10%c. However, a narrower 3D bump is actually preferred on the infinite swept wing for that design point.

#### 6.3.5.6 Sensitivities Calculated from Adjoint

The drag sensitivities of the six design parameters can be assessed through the calculated values from the adjoint solver. Two optimisation cases from the correlation study on the NLF aerofoil have been chosen to represent a strong shock case and a relatively weaker one. The strong shock case comprises a $M_{max}$ of 1.372. The sensitivities of the design parameters calculated for the optimised point are shown in Table 6.9. The $M_{max}$ of the weaker shock case is 1.2. The

sensitivities calculated for this case are listed in Table 6.10.

In both cases, the values from the tables demonstrate that the bump height (as highlighted in red) is the most sensitive parameter. The rest of the design parameters are at about the same level of sensitivity. As a result of that, the bump height produces a more significant changes.

| Design variables | Drag Sensitivities |
|---|---|
| *Bump Length* | 1.66e-3 |
| *Bump Crest* | -4.88e-2 |
| *Relative Bump Crest* | 8.98e-3 |
| *Bump Height* | -2.23e-1 |
| *Bump Width* | -6.25e-3 |
| *Bump Spacing* | 6.31e-3 |

Table 6.9: Drag sensitivities calculated from the adjoint for the stronger shock case, $M_{max}$=1.372.

| Design variables | Drag Sensitivities |
|---|---|
| *Bump Length* | 1.30e-4 |
| *Bump Crest* | -7.34e-4 |
| *Relative Bump Crest* | 6.42e-4 |
| *Bump Height* | -9.76e-2 |
| *Bump Width* | -7.42e-4 |
| *Bump Spacing* | 2.93e-5 |

Table 6.10: Drag sensitivities calculated from the adjoint for the weaker shock case, $M_{max}$=1.2.

#### 6.3.5.7 Designing 3D Bumps From The Low-Order Model, Strong Shock

Based on the constructed low-order model, we attempt to design 3D bumps for various conditions of different shock strength on the RAE 5243 NLF aerofoil. The first selected case has the same freestream Mach number at 0.68 as usual and $\alpha = 2.7$ which corresponds to a shock strength of $M_{max} = 1.324$ on the datum wing. By referring to the plots of Figure 6.27 to 6.33, the values of the six design

parameters are derived according to the given $M_{max}$ and listed in Table 6.11. The improvement gained by this low-order model designed 3D bump is compared in the following Table 6.12. This designed 3D bump achieved a 21% reduction of drag as compared to the datum case at the same lift condition.

| Length | $\Delta X/c$ | Relative position | Height | Width\Spacing |
|---|---|---|---|---|
| 32.5%c | 6%c | 54% | 1.55%c | 12%c |

Table 6.11: Designing a 3D bump from the low-order model (strong shock, $M_\infty$ = 0.68, $M_{max}$ = 1.324)

| | $C_L$ | $C_{Dtotal}$ | Total Drag Reduction |
|---|---|---|---|
| Datum aerofoil | 0.8608 | 0.01775 | - |
| ***Designed 3D bump*** | 0.8619 | 0.00139 | 21% |

Table 6.12: Performance of the low-order model designed 3D bump for $M_\infty$ = 0.68, $M_{max}$ = 1.324.

#### 6.3.5.8 Designing 3D Bumps From The Low-Order Model, Weaker Shock

This case concerns a weaker original shock on the datum wing (RAE 5243). The freestream Mach number is retained at the same value as the previous strong shock case. The incidence is lowered to 1.3° which corresponds to a weaker shock strength of $M_{max}$ = 1.226. The derived designs and the acquired performance of the 3D bump are shown in Table 6.13 and 6.14 respectively.

| Length | $\Delta X/c$ | Relative position | Height | Width\ Spacing |
|---|---|---|---|---|
| 32.5%c | 6%c | 54% | 0.9%c | 12%c |

Table 6.13: Designing a 3D bump from the low-order model (weak shock, $M_\infty$ = 0.68, $M_{max}$ = 1.226)

#### 6.3.5.9 Designing 3D Bumps From The Low-Order Model, Strong Shock ($M_\infty = 0.72$)

The previous two design exercises were carried out at $M_\infty$ = 0.68 on the NLF wing, where the position of the original shock wave has minimal displacement

| | $C_L$ | $C_{Dtotal}$ | Total Drag Reduction |
|---|---|---|---|
| Datum aerofoil | 0.6586 | 0.01238 | - |
| *Designed **3D** bump* | 0.6584 | 0.01138 | 8% |

Table 6.14: Performance of the low-order model designed 3D bump for $M_\infty = 0.68$, $M_{max} = 1.226$.

when the incidence is changed. Therefore, the third selected case study has a higher freestream Mach number at 0.72 on the same wing, where the position of the datum shock moves a small distance downstream compared to the $M_\infty = 0.68$ datum case. At an incidence of 2.42, the strength of the original shock wave on the datum wing is measured to be $M_{max} = 1.47$. Even though the original datum shock has moved downstream compared to the $M_\infty = 0.68$ cases, but by placing the bump crest 6%c downstream of the datum shock and the other parameters being derived as usual and listed in Table 6.15, substantial drag reduction can still be obtained as shown in Table 6.16.

| Length | $\Delta X/c$ | Relative position | Height | Width\ Spacing |
|---|---|---|---|---|
| 32.5%c | 6%c | 54% | 2.4%c | 12%c |

Table 6.15: Designing a 3D bump from the low-order model (strong shock, $M_\infty = 0.72$)

| | $C_L$ | $C_{Dtotal}$ | Total Drag Reduction |
|---|---|---|---|
| Datum aerofoil | 0.7391 | 0.03384 | - |
| *Designed **3D** bump* | 0.7404 | 0.02752 | 18% |

Table 6.16: Performance of the low-order model designed 3D bump for $M_\infty = 0.72$, $M_{max} = 1.47$.

#### 6.3.5.10 Performance of the Designed 3D Bumps

The performance of the three 3D bumps designed previously using the low-order model is assessed in comparisons with the optimised 3D bumps. In Figure 6.34, the reduction in drag relative to the datum case at each $M_{max}$ are measured in terms of drag counts. It is obvious from the graph that the stronger the original shock wave is, the more drag reduction can be achieved by the 3D bump. The black-dashed line represents a linear trend line imposed on the sets of optimised

design points. It is demonstrated here that three low-order model-designed 3D bumps perform at the level close to that of the optimised cases. Therefore, this exercise indicates that the low-order model is reasonably good. Figure 6.35 plots out the coefficient of the drag of the various points investigated above. It is shown here that, for shock strength up to 1.30, the drag of the datum wing is significantly lowered by the 3D bump to the level comparable to the weak shock cases ($M_{max} < 1.30$).

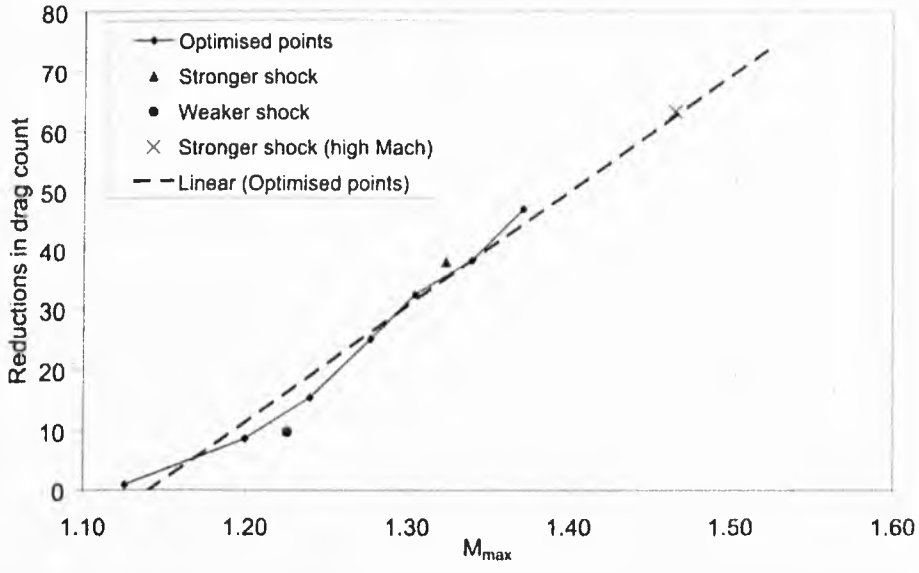


Figure 6.34: Performance of the 3D bumps designed using the low-order model.

### 6.3.6 Performance over a Range of $C_L$

In Figure 6.36, the performance of the 3D bump optimised at the design points of $C_L = 0.76$ and $C_L = 0.82$ over a range of lift conditions are compared with that of the 2D bump optimised at $C_L = 0.82$, as well as the datum case. Note that they are all run at the same freestream Mach number of $M_\infty = 0.68$. The lift-drag ratio plot for these optimised bumps is investigated in Figure 6.37.

Moving away from the design point towards higher lift conditions, where the shock strength increases progressively, all the bumps still provide beneficial effects, e.g. delaying the buffet onset. Of all the three cases, the 3D bump that is optimised at $C_L = 0.76$ slightly under-performs compared to the other two

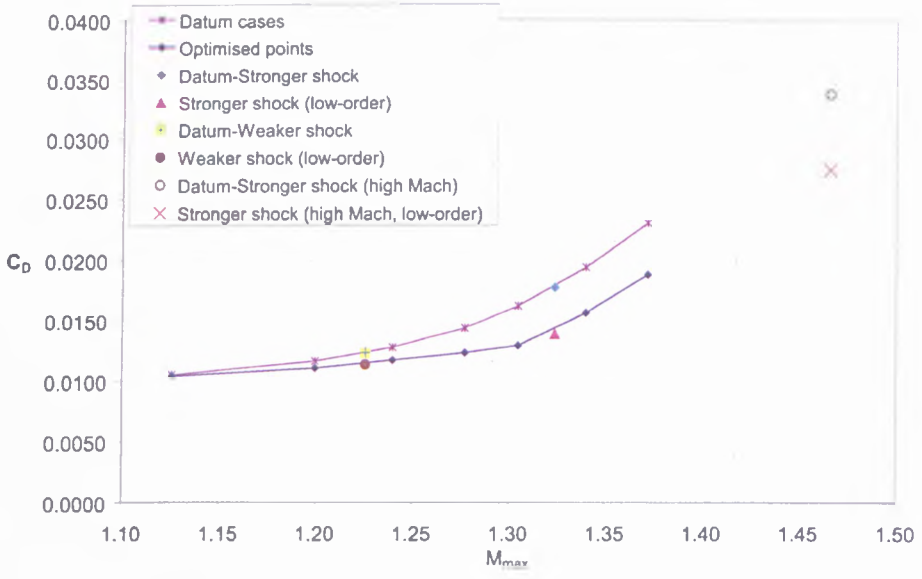


Figure 6.35: Comparisons of the drag level of the 3D bumps designed using the low-order model.

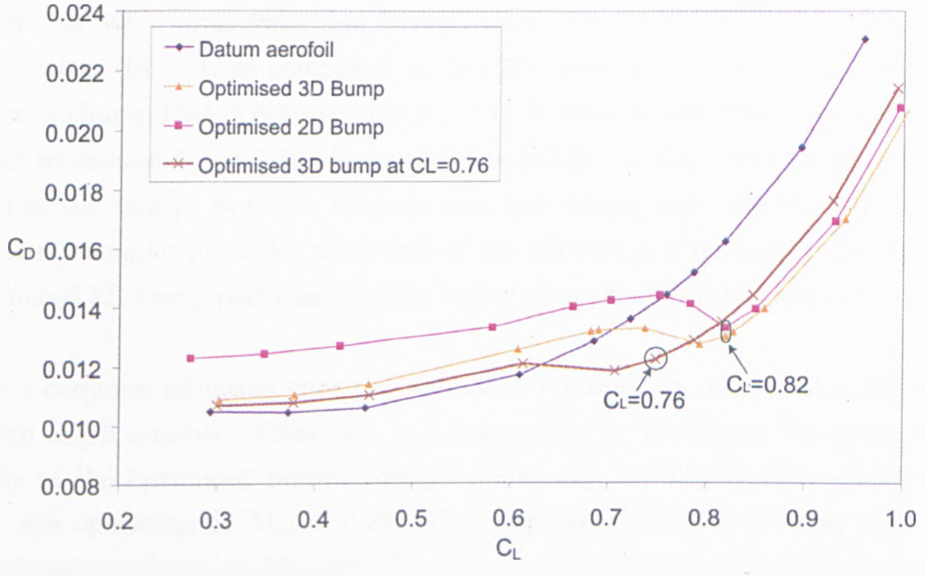


Figure 6.36: Comparisons of the drag polar of 2D and 3D bumps optimised on the RAE 5243 aerofoil, $M_\infty = 0.68$.

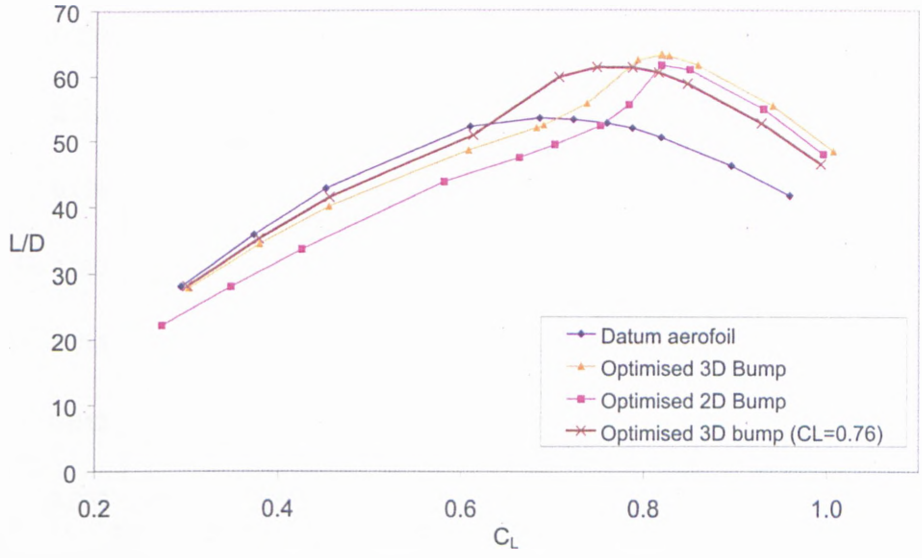


Figure 6.37: Comparisons of the lift-drag ratio *vs* lift plots of 2D & 3D bumps optimised on the RAE 5243 aerofoil, $M_\infty = 0.68$.

at these high-lift conditions. However, in between the region of *0.7∼0.8*, where the lift is slightly lower than the optimised design points, the 3D bumps still maintains some drag reduction benefit while the drag rises rapidly for the 2D bump case. In fact, as compared to the 3D bump optimised at $C_L = 0.82$, the other 3D bump that is optimised at $C_L = 0.76$ extends this effective-range further down to around $C_L = 0.62$. At low-lift conditions ($< 0.6$), even though the drag level of the bumps begin to increase over the datum case, the 3D bumps suffer relatively smaller penalties than that of the 2D bump. Once again, the lower-lift optimised 3D bump performs slightly better than the one optimised at $C_L = 0.82$.

It is a common situation that the aircraft is required to operate at a higher off-design Mach number. Therefore, it is interesting to investigate the performance range of the optimised bumps (design point: $M_\infty = 0.68$ & $C_L = 0.82$) when they are operating at $M_\infty = 0.70$. The drag polar and the lift-drag ratio plots are shown in Figure 6.38 and 6.39 respectively. Overall, the 3D bump seems to perform better than the 2D bump over the entire operating range. The 3D bump is able to sustain effectiveness over a wide $C_L$ range of $0.5 \sim 0.95$, which is somewhat wider than the effective range seen in Figure 6.36. This could be explained by the fact that the original datum shock is fairly strong even at low-

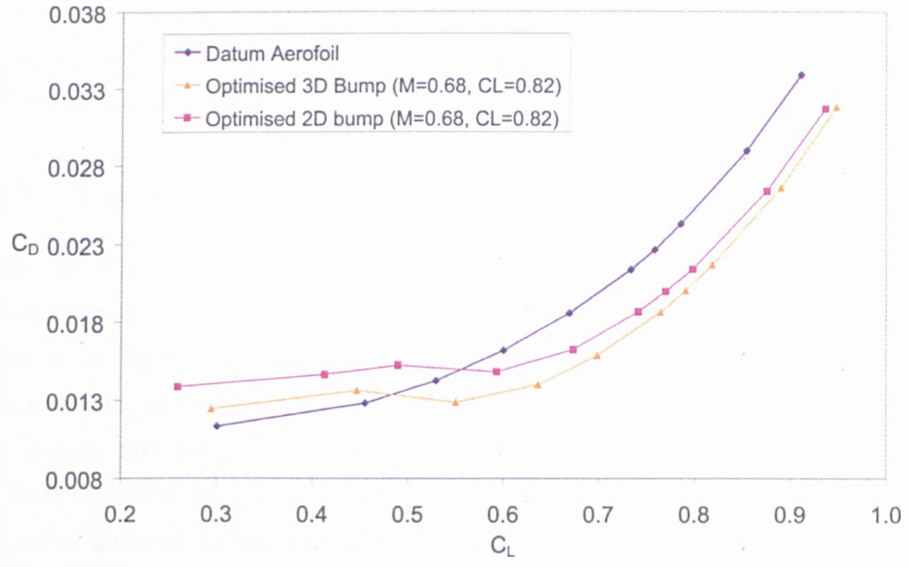


Figure 6.38: The drag polar of the 3D bump optimised on the RAE 5243 aerofoil operating at higher Mach number, $M_\infty = 0.70$.

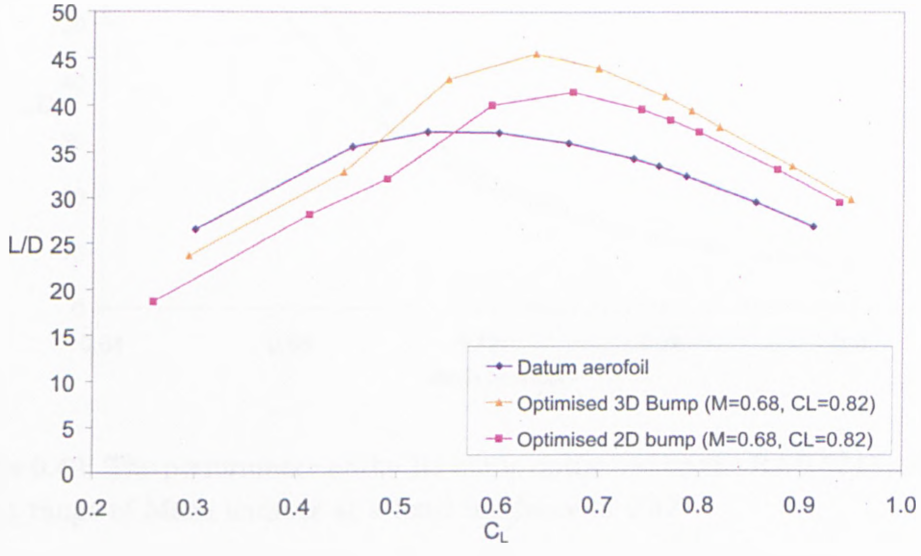


Figure 6.39: The lift-drag ratio *vs* lift plot of the 3D bump optimised on the RAE 5243 aerofoil operating at higher Mach number, $M_\infty = 0.70$.

lift coefficient at this higher Mach number, thus the 3D bump could still remain effective at lower-lift conditions. Nonetheless, it is demonstrated here that the bumps are still able to achieve beneficial effects at a slightly higher off-design freestream Mach number.

### 6.3.7 Performance over a Range of $M_\infty$

In this investigation, the incidence is fixed at 2.42° and the calculations are performed over a range of freestream Mach number from 0.65 to 0.80. Since the incidence is fixed and that the lift coefficient is changing with the respective Mach number, therefore it is more useful to look at lift-drag ratio plot in Figure 6.40. Again, the design point is at $M_\infty = 0.68$. It is shown here that the bumps are effective up to $M_\infty = 0.75$ beyond the design point. However, when the Mach number is lowered below the design point, the effectiveness of the bumps drop back down but the 3D bump can still sustain almost the same level of lift-drag ratio as the datum case.

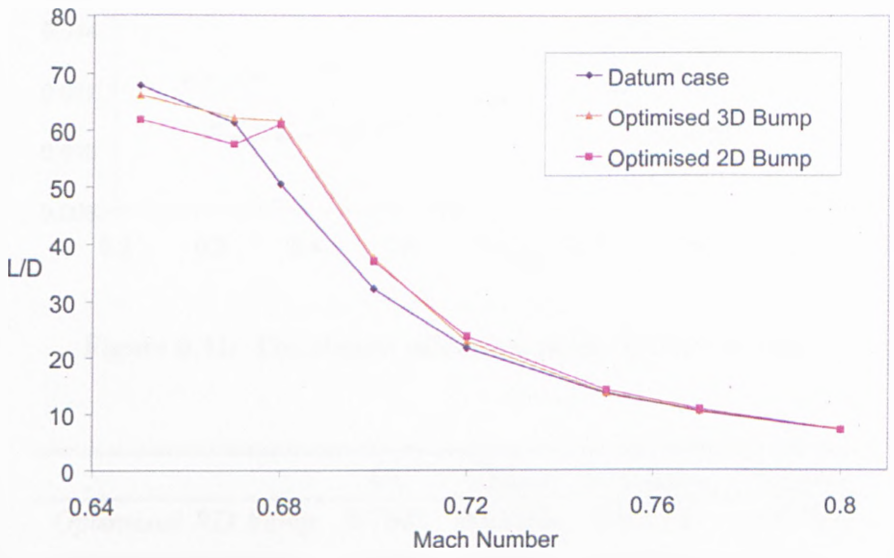


Figure 6.40: The performance of the 3D bump optimised on the RAE 5243 aerofoil over a range of Mach number at a fixed incidence of 2.42°.

### 6.3.8 Analysis at Off-Design Condition

The previous section has already demonstrated the advantage of the optimised 3D bump over the 2D bump in the operational lift range, so this section sets out to investigate the different effects that the optimised bumps deliver at off-design conditions. From Figure 6.41, we selected an off-design point at $C_L = 0.753$, where the 3D bump has an obvious advantage over the 2D bump. Their performances are compared in Table 6.17. At the same level of lift, the 3D bump is about 8 drag counts better than the 2D bump.

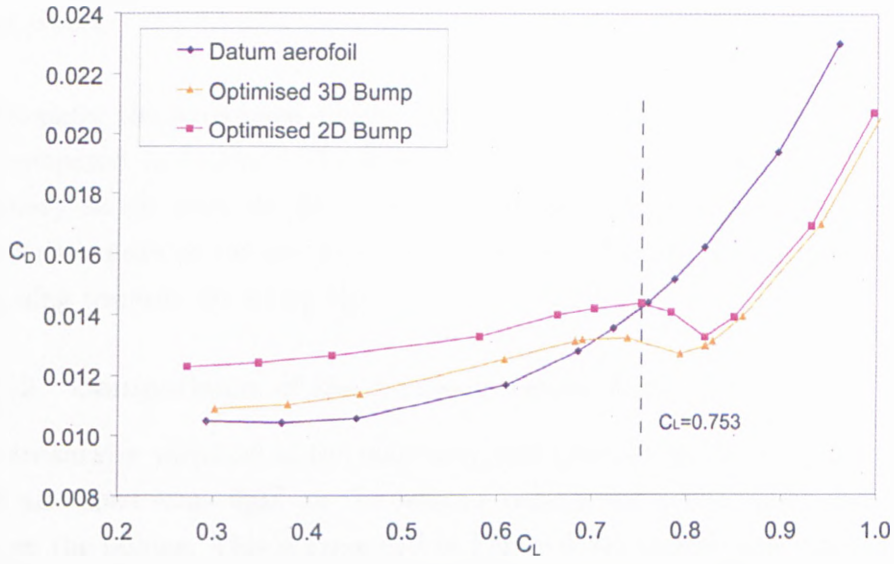


Figure 6.41: The chosen off-design point in the $C_L$ range.

| | $C_L$ | $C_{Dtotal}$ | $C_{Dpressure}$ | $C_{Dfriction}$ |
|---|---|---|---|---|
| *Optimised 3D bump* | 0.7531 | 0.01363 | 0.007721 | 0.005899 |
| *Optimised 2D bump* | 0.7527 | 0.01439 | 0.008729 | 0.005664 |

Table 6.17: Comparisons of the performance of the bumps at a off-design condition (RAE 5243)

#### 6.3.8.1 Comparisons of the Flowfield

A straightforward way to assess this is to plot the Mach number contours for both cases and compare them. They are plotted out in Figures 6.42. Overall,

it is obvious that at this off-design point, both of the bumps are subjected to a double-shock system. However, close examinations of the four figures suggest that the secondary shock on the 2D bump is slightly stronger. This is also supported by calculations of the maximum Mach number upstream of the secondary shock ($M_{max}$) as printed out on each figures. It indicates that the secondary shock on the 2D bump has a strength of $M_{max} = 1.23$. As for the 3D bump, at the centreline, $M_{max}$ is around 1.21. Away from the centreline, the mid-span slice has a $M_{max}$ value of 1.185 and at the tip, $M_{max}$ drops down to 1.181. Therefore, it is demonstrated here that the 3D bump has a weaker secondary shock due to its ability to "relax" the flow such that the re-compression of a secondary shock is less severe.

Additionally, the streamwise pressure distribution plots of these cases are plotted and compared in Figure 6.43. From here, it is clear that the strength of the secondary shock from the 2D bump is generally stronger than the 3D bump. The suction peak of the secondary shock on the 3D bump is again shown to be weakening towards the bump tip.

#### 6.3.8.2 Comparisons of the Cross-sectional Area

The streamwise variation of the cross-sectional area across the wing with bumps could also shed some light on the reasons behind the performance discrepancy between the bumps. This is presented in Figure 6.44. Overall, the smoothness of the change of area, even with the presence of the bumps, is maintained. Excluding the cross-section of the aerofoil shape, the maximum cross-sectional area of both bumps are found to be quite close with just a 6% difference. In this case, the maximum cross-sectional area of the 3D bump is actually slightly larger than the 2D bump. These results support the cross-sectional area hypothesis presented in *Section 6.2.2* that suggest that the maximum cross-sectional area of the 3D bump has to be close to that of the 2D bump, in order to match its performance.

It is also useful to look at the gradient or the rate of change of area across the wing as plotted in Figure 6.45. From the graph, the wing with 2D bump has a steep change in gradient at $x/c = 0.67$, which indicates a high second order derivative. Thus, it is shown here that the difference in area variation contributes to the different behaviour of the two optimised bumps. In addition to the beneficial

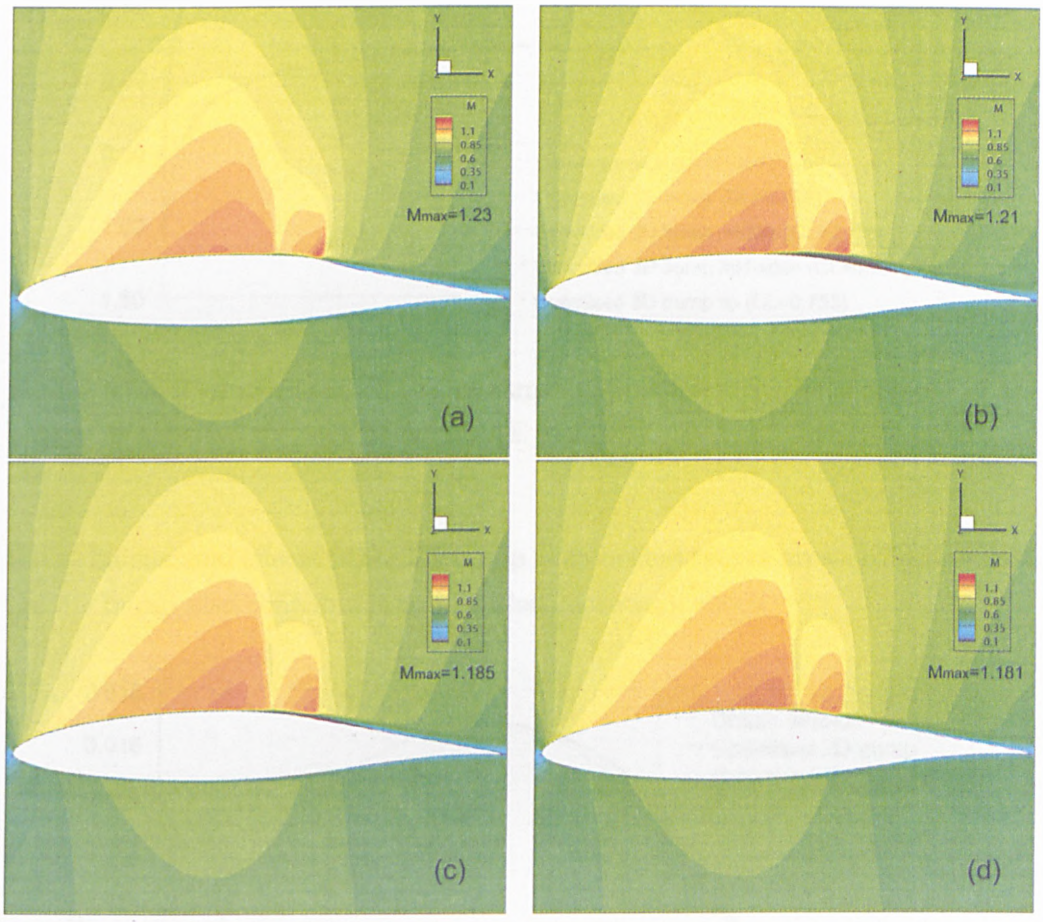


Figure 6.42: (a) Mach number contours of the optimised 2D bump. (b) Mach number contours along the centreline of the optimised 3D bump. (c) Mach number contours along the mid-span of the optimised 3D bump. (d) Mach number contours along the tip of the optimised 3D bump.

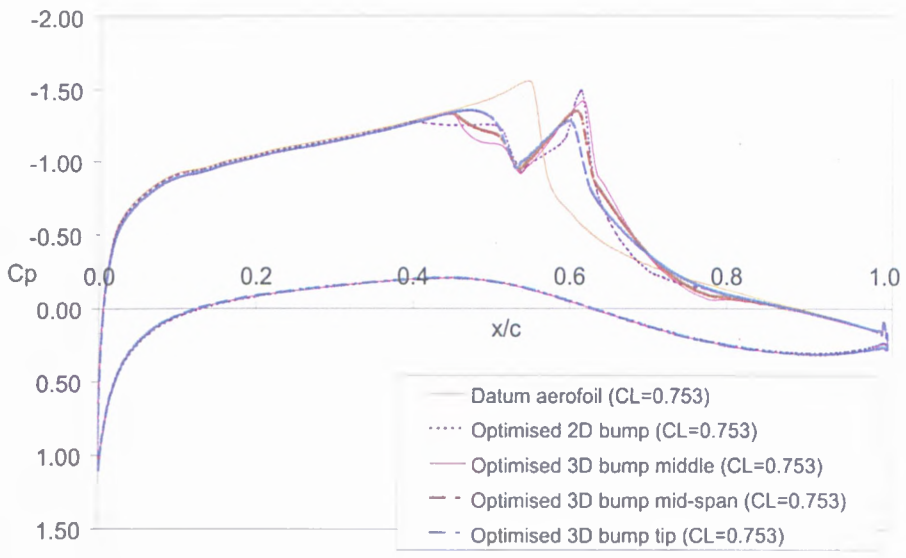


Figure 6.43: Comparisons of the streamwise pressure distribution plots of the bumps at an off-design condition. (RAE 5243)

three-dimensional effects of the 3D bump, a smoother rate of area variation across the 3D bump also contributes to a weaker secondary shock.

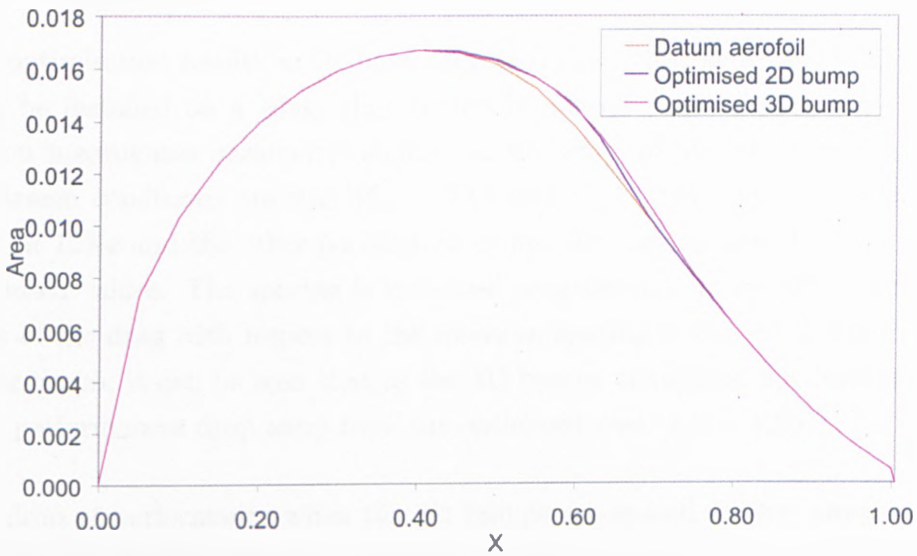


Figure 6.44: The variations of the cross-sectional area of the bumps optimised on the RAE 5243 aerofoil over a range of Mach number.

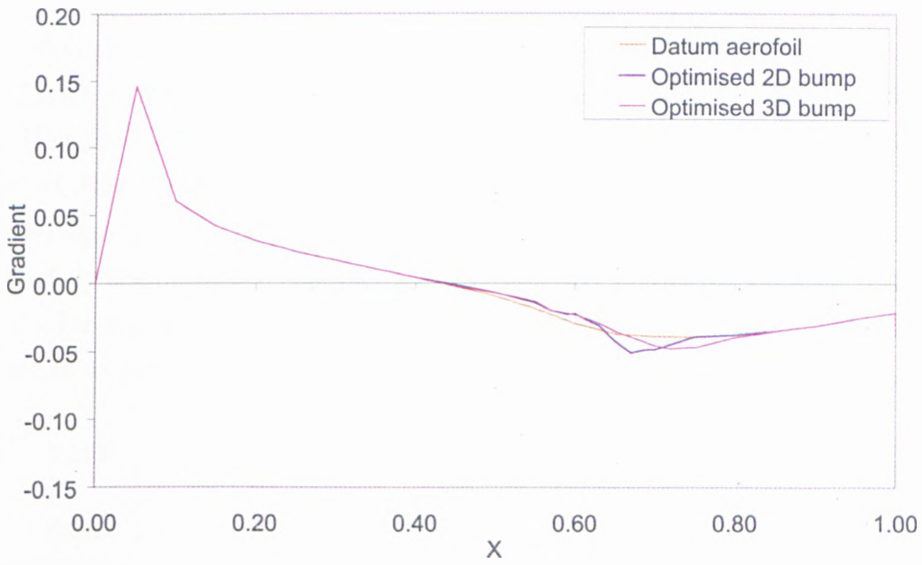


Figure 6.45: The rate of change of the cross-sectional area of the bumps optimised on the RAE 5243 aerofoil over a range of Mach number.

### 6.3.9 Further Parametric Studies of 3D Bump Spanwise Spacing

The optimisation results so far have suggested that when an array of 3D bumps is to be installed on a wing, they should be placed close to each other. This section investigates parametric studies on the effect of 3D bump spacing. The freestream conditions are still $M_\infty = 0.68$ and $C_L = 0.82$. The bump width is fixed at 12%c and the other parameters except the spacing, are also fixed at the optimised values. The spacing is increased progressively up to 50%c. The variation of the drag with respect to the spanwise spacing is plotted in Figure 6.46. In the graph, it can be seen that as the 3D bumps are spaced out further away, their performances drop away from the optimised case ($z/c = 12\%$).

The drop of performance when the 3D bumps are spaced further away is obviously due to the decrease of the maximum cross-sectional area per unit spanwise width. So, if both the 3D bump width and spacing were fixed, the only other parameter available to off-set this loss of area is the bump height. Additionally, instead of fixing the bump width to 12%c, it is reduced to 8.5%c and the

spacing is fixed at 17%c. The results are shown in Figure 6.47. The blue-line shows that the performance can be slightly regained when the height is increased from 1.5%c to 2%c. Its drag level then rises when the height is increased up to 3%c. However, when the spacing is increased to 26%c and with the height maintained at 3%c (the orange-square marker), the level of efficiency can actually be regained significantly. The reason behind this is that with a less "confined" flow provided by the increased spacing, the substantially higher 3D bump is less prone to a double-shock system, or even with a double-shock, the secondary shock is somewhat weaker.

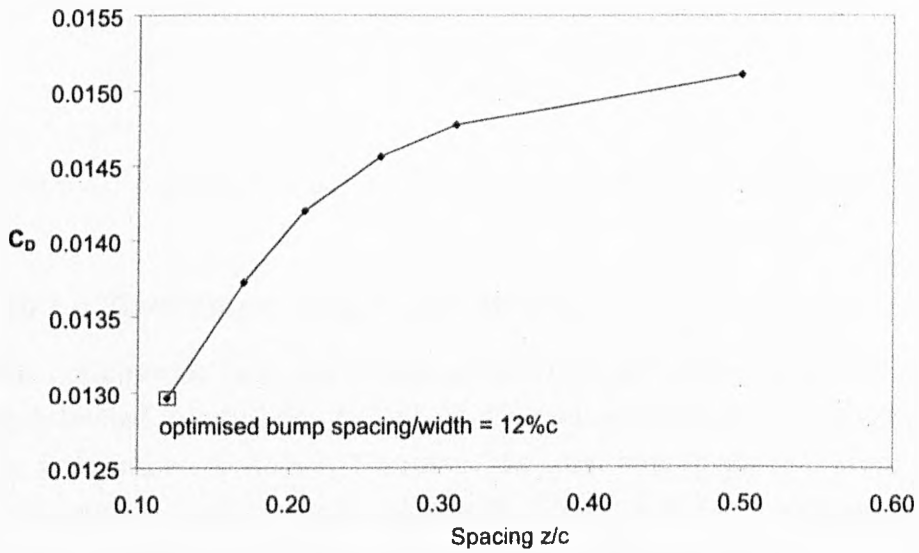


Figure 6.46: Parametric studies of the 3D bump spanwise spacing.

### 6.3.10 Optimisation of a Relatively Small-sized 3D Bump

As shown in the preceding results, it is suggested that an effective 3D bump requires a streamwise length of about 30% and spans around 11% wide. However, when it comes to implementation, a smaller-sized 3D bump is preferred. Therefore, in this section, we present some investigations on the possibility of employing a relatively small-sized 3D bump.

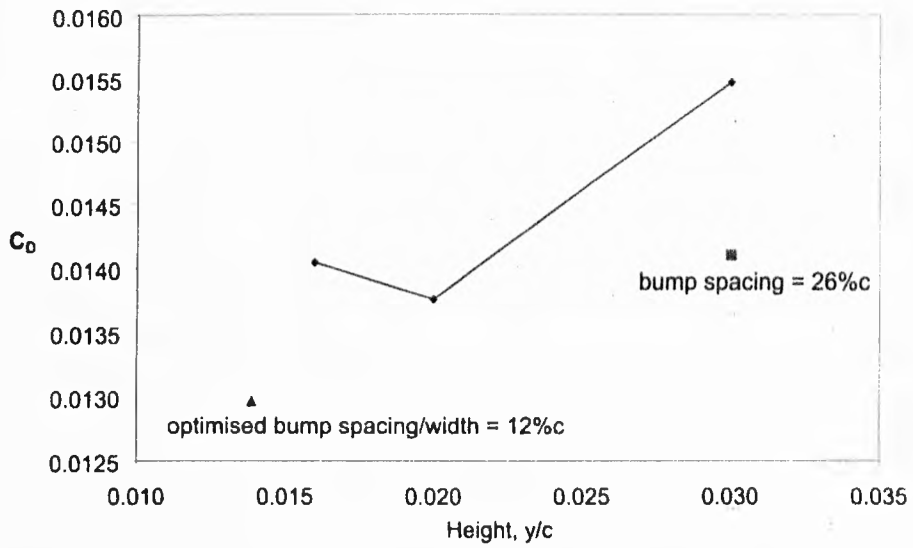


Figure 6.47: Parametric studies of the 3D bump height with different spacing.

#### 6.3.10.1 Fixed Bump Length and Width

In this optimisation task, the maximum allowable streamwise length of the 3D bump is limited to only 5%c. As for half of the bump width, due to the symmetry plane, it is limited to 2.5%c. Therefore, the total bump width is actually 5%c too, the same as that of the bump length. The rest of the design parameters are free to evolve. The freestream Mach number remains at 0.68 and the target lift condition is chosen at 0.82. The optimised 3D bump has a designation of *l5-cre57.6-cb61.7-h0.312-s98-wid5*. From this designation, it can be interpreted that the width of the 3D bump is around the same as the spacing. Notice that due to the reduced maximum allowable chordwise length at just 5%c, the crest of the bump moves upstream closer to the original shock, as compared to the previous optimised 3D bump with 30%c length. This is required because if the 3D bump crest remained at 62%c, with just a streamwise length of 5%c, the 3D bump would not have sufficient region or no region at all to interact with the original shock. As for the bump height, it is around 0.3%c, which is much smaller compared to the previous one. Table 6.18 shows that with this optimised small-sized 3D bump, a 4% or 6 drag counts of drag reduction can still be gained. Nonetheless, the results here imply that a bump of reasonable length is required to generate sufficient upstream compression to weaken the shock wave and also

to generate additional lift.

| | $C_{Dtotal}$ | $C_{Dpressure}$ | $C_{Dfriction}$ | Total Drag Reduction |
|---|---|---|---|---|
| Datum aerofoil | 0.01622 | 0.010634 | 0.005585 | - |
| *Optimised 3D bump (small)* | 0.01562 | 0.009905 | 0.005715 | 4% |
| *Optimised 3D bump (large)* | 0.01296 | 0.007208 | 0.005755 | 20.1% |

Table 6.18: Comparisons of the optimised smaller-sized 3D bumps on RAE 5243 aerofoil. ($M_\infty = 0.68$, $C_L = 0.82$)

#### 6.3.10.2 Fixed Bump Width

From the studies of the previous section, it is shown that limiting the 3D bump to a small bump length and width has significant impact on the performance of the 3D bump. Therefore, the following optimisation will allow the bump length to reach 40%c and leaves the other parameters free as usual. However, we would like to keep the size of the 3D bump small, so the maximum allowable bump width remains at 2.5%c. Consequently, starting initially from 5%c, the chordwise length of the optimised 3D bump has grown to 21%c. Due to this enhanced bump length, the bump crest is then moved back downstream to settle at around 60%c. Interestingly, the obtained optimised spacing is 4.8%c, which is wider than the fixed bump width of 2.5%c. This indicates that there is about 50% of unmodified surface. In addition to all these changes, the bump height reaches up to 1.56%c, which is in fact higher than the previous optimised large 3D bump with all the parameters free. To sum up, the designation of this optimised 3D bump is *l21.4-cre59.7-cb53.7-h1.56-s52.3-wid4.8*. With the longer bump length and an increased bump height. The performance of the 3D bump is shown and compared with other 3D bumps in Table 6.19 below. From the table, although this current 3D bump (small-width) is still 11% shy of the performance of the larger 3D bump, it has still achieved more than 9% or 23 drag counts of drag reduction from the datum case, which is significant.

| | $C_{Dtotal}$ | $C_{Dpressure}$ | $C_{Dfriction}$ | Total Drag Reduction |
|---|---|---|---|---|
| Datum aerofoil | 0.01622 | 0.010634 | 0.005585 | - |
| *Optimised **3D** bump (small-width)* | 0.01394 | 0.008196 | 0.005749 | 9.4% |
| *Optimised **3D** bump (small)* | 0.01562 | 0.009905 | 0.005715 | 4% |
| *Optimised **3D** bump (large)* | 0.01296 | 0.007208 | 0.005755 | 20.1% |

Table 6.19: Comparisons of the optimised fixed-width 3D bumps on RAE 5243 aerofoil. ($M_\infty = 0.68$, $C_L = 0.82$)

## 6.4 Unswept Wing with RAE 2822 Turbulent Aerofoil Section

### 6.4.1 Optimisation Results

The flow conditions chosen for this optimisation task are similar to that in *Section 5.5.2*, where $M_\infty = 0.75$, $Re_c = 6.5 \times 10^6$ and $\alpha = 2.31$. The calculated lift for the datum case at these flow conditions is $C_L = 0.75$, which is set as the target lift condition for the optimisations. The objective function remains as to minimise the total drag.

The maximum chordwise bump length is still limited to 40%c and the bump width is allow to grow up to 98% of the total width. The design of the acquired optimised 3D bump is *l40-cre72.6-cb60.1-h2.36-s98-wid10.6*. From the optimised 3D bump designation, it is noticed that the height of the bump is still roughly twice of that of the optimised 2D bump at 2.4%c. Note that the optimised 2D bump has a designation of *l40-cre70.6-cb57.5-h1.2*. The comparisons of the maximum cross-sectional area will be discussed in more detail later. The width of the 3D bump extends up to 98% of the spacing width, which is about 11%c wide. The shape of the 3D bump is shown in Figure 6.48. The scale in the normal direction has been modified to enhance the visualisation of the bump height. Figure 6.49 depicts the 3D bump generated on the upper surface of the unswept wing.

Table 6.20 above compares the drag components calculated from the optimised 2D and 3D bump with reference to the datum case. Generally, both the optimised bumps have roughly the same level of performance with around 32% of the datum drag being reduced. As for the skin friction drag, there is only a minor 1-2 drag

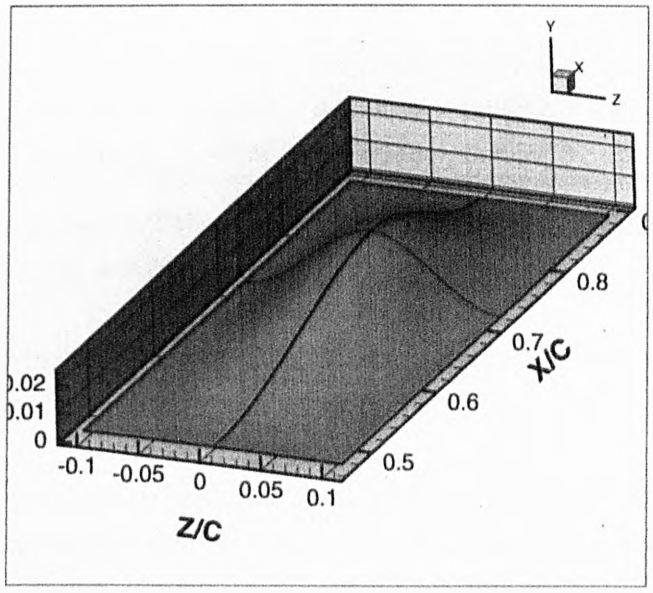


Figure 6.48: The shape of the 3D bump optimised for the RAE 2822 aerofoil.

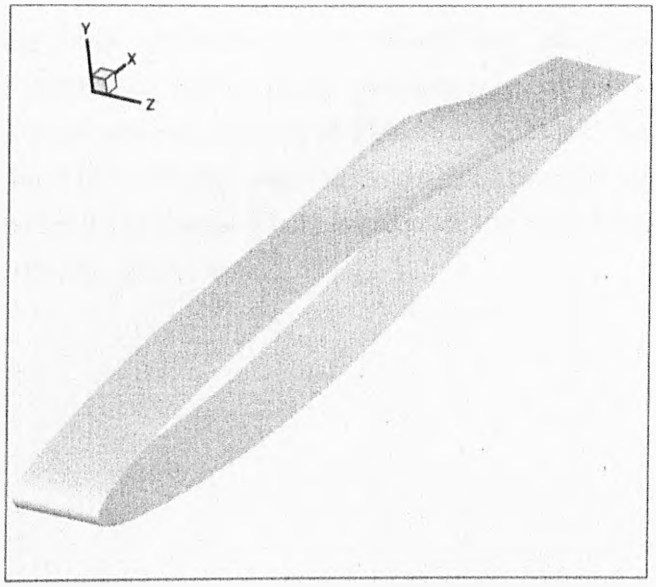


Figure 6.49: Visualisation of the shape of the 3D bump optimised on the RAE 2822 aerofoil.

| | $C_{Dtotal}$ | $C_{Dpressure}$ | $C_{Dfriction}$ | **Total Drag Reduction** |
|---|---|---|---|---|
| Datum aerofoil | 0.02296 | 0.017146 | 0.005813 | - |
| *Optimised **3D** bump* | 0.01559 | 0.009546 | 0.006023 | 32.1% |
| *Optimised **2D** bump* | 0.01555 | 0.009576 | 0.005978 | 32.3% |

Table 6.20: Comparisons of the optimised 2D and 3D bumps on RAE 2822 aerofoil. ($M_\infty = 0.75$, $C_L = 0.75$)

count penalty, which is relatively insignificant compared to the reduction gained in pressure drag.

Figure 6.50 (a) presents a closeup of the original strong normal shock on the upper surface of the datum wing. The red solid-line denotes the optimised 3D bump that is superimposed on the wing. Following it are Figures 6.50 (b) to (d), which show the pressure contours lines plotted across different spanwise locations. The variations of the pressure distribution at these three locations are clearly noticeable here in Figure 6.50 (b) to (d). Part of the original normal shock is converted into a much weakened "knee"-shape shock and being displaced slightly downstream close to the bump crest. However, it is observed that there still remains a reasonably strong shock wave away in the inviscid flow field. Clearer plots of the outer inviscid flowfield are shown in the pressure contour plots of Figures 6.51 and in the Mach number contour plots of Figures 6.52. With the similar range of contour levels, the Mach number plots again demonstrate the significant level of reduction of upstream maximum Mach number of the remaining shock wave on the 3D bump from the datum case.

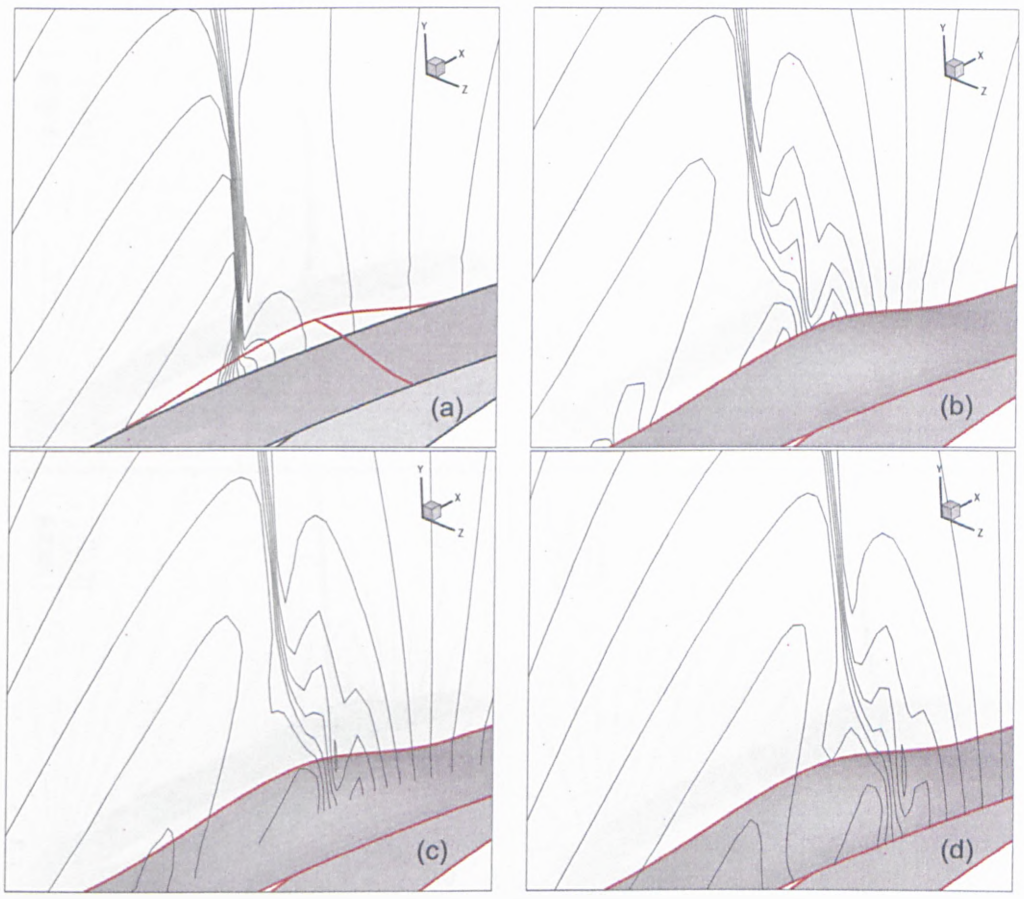


Figure 6.50: (a) Pressure contour lines of the original normal shock wave on the datum aerofoil. (with the shape of the optimised 3D bump superimposed on top of the wing) (b) Pressure contours distribution along the centreline of the optimised 3D bump. (c) Pressure contours distribution along the mid-span of the optimised 3D bump. (d) Pressure contours distribution along the tip of the optimised 3D bump. (RAE 2822, $M_\infty = 0.75$, $C_L = 0.75$)

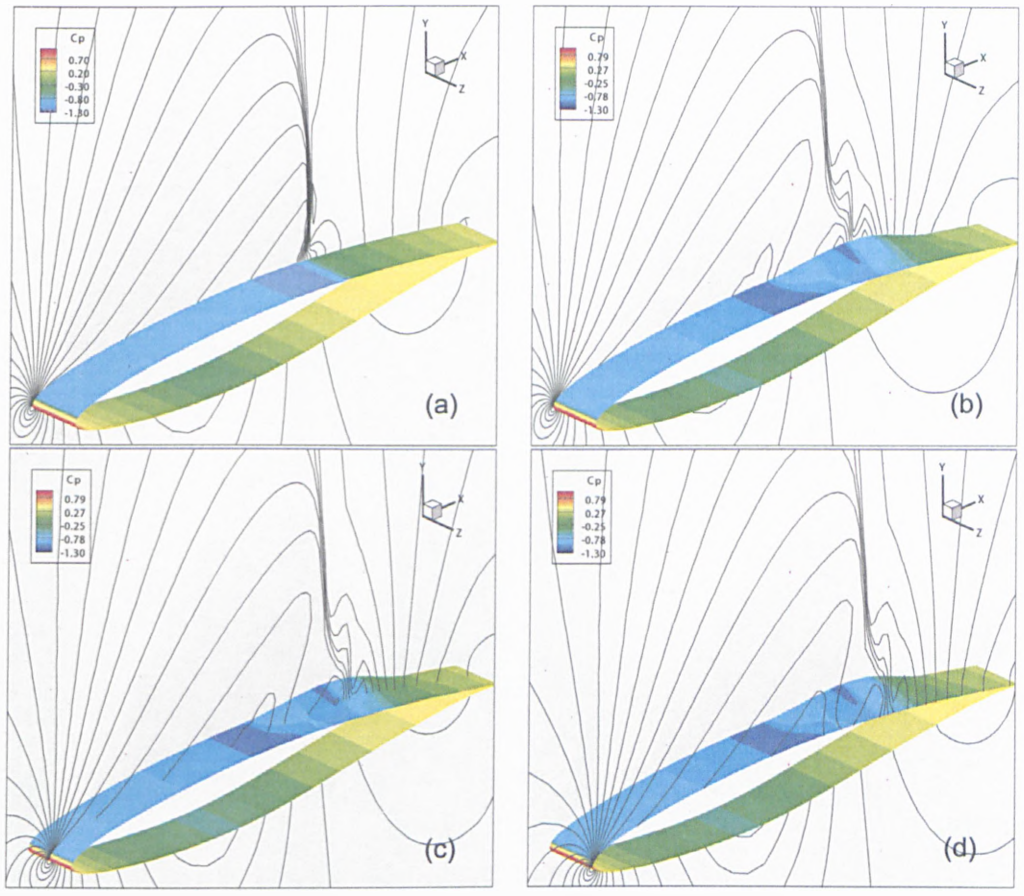


Figure 6.51: (a) Pressure contours of the datum aerofoil. (b) Pressure contours distribution along the centreline of the optimised 3D bump. (c) Pressure contours distribution along the mid-span of the optimised 3D bump. (d) Pressure contours distribution along the tip of the optimised 3D bump. (RAE 2822 aerofoil, $M_\infty = 0.75$, $C_L = 0.75$)

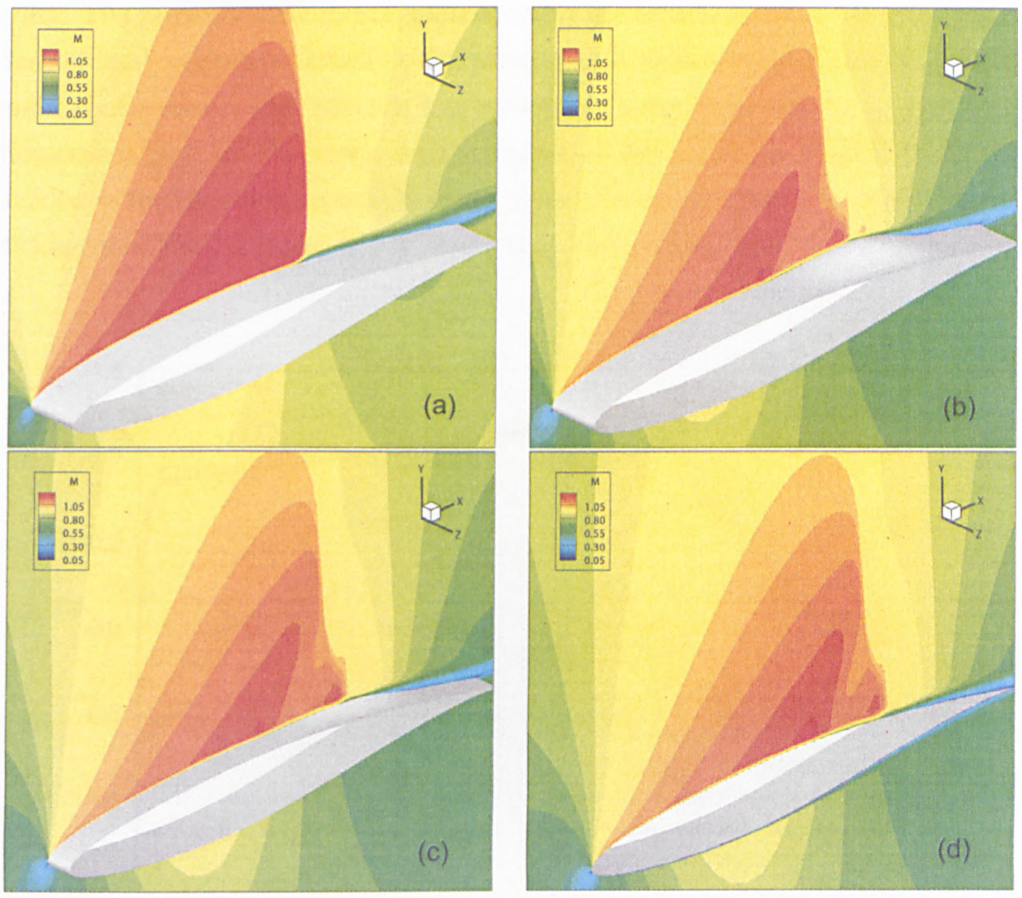


Figure 6.52: (a) Mach number contours of the datum aerofoil. (b) Mach number contours along the centreline of the optimised 3D bump. (c) Mach number contours along the mid-span of the optimised 3D bump. (d) Mach number contours along the tip of the optimised 3D bump. (RAE 2822 aerofoil, $M_\infty = 0.75$, $C_L = 0.75$)

The effects of the 3D bump are also reflected in the streamwise pressure distribution plot as shown in Figure 6.53. It is clear that the upstream compression of the flowfield by the 3D bump has weakened progressively from the centreline section towards the tip. The position of the main shock wave from both the 2D and 3D bump cases have displaced about $3 \sim 5\%$ downstream close to the bump crest. The pressure distribution plotted along the centreline of the 3D bump (red-dashed line) indicates a small re-compression of a weak secondary shock after the main shock wave. This effect is less noticeable away from the bump centreline. Remember that all the cases are computed at the same lift condition and the incidence for the bump cases is lower than the datum case. In this case, the incidence of the 3D bump is 0.4° lower than the datum case.

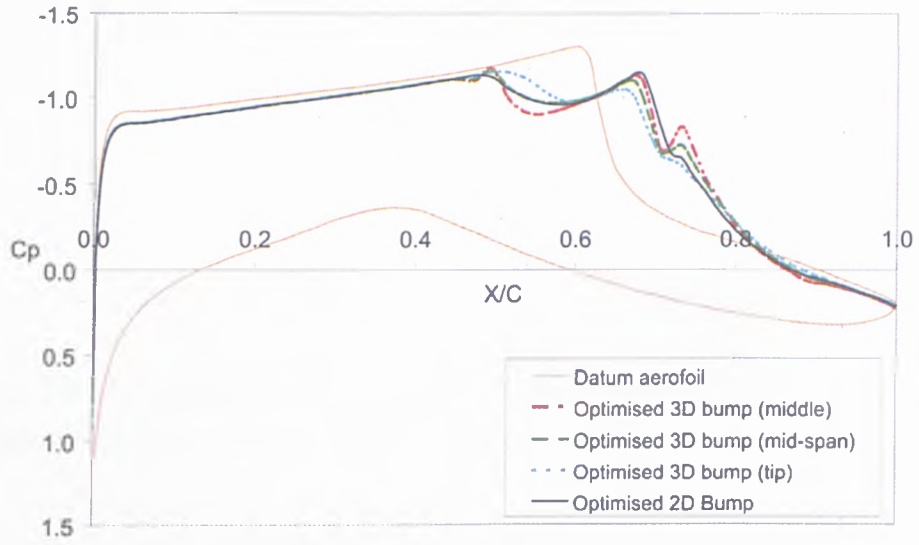


Figure 6.53: The streamwise pressure distribution for the optimised 3D bump on the upper surface of RAE 2822 aerofoil , $M_\infty = 0.75$, $C_L = 0.75$.

Another alternative pressure distribution analysis is via plotting the $y$-coordinates of the wing against $Cp$. In order to provide a straightforward picture of the drag, Figure 6.54 plots $Cp$ with the $y'$-coordinates, which is the coordinate system aligned with the incoming flow direction (with reference to Figure 5.19). The "drag" and "thrust" regions are labeled out in Figure 6.54. The uppermost right drag region of the datum case (orange solid-line) denotes the drag contribution from the original strong normal shock wave. The presence of this normal shock

pushes the minimum pressure peak further down and hence increases the drag. It is observed that this area of the uppermost right drag regions of all three spanwise locations have been reduced. In addition to that, it is noticed that there are a series of re-compressions and re-expansions along the centreline of the 3D bump and also on the 2D bump. However, these phenomena become less apparent at the stations away from the centreline.

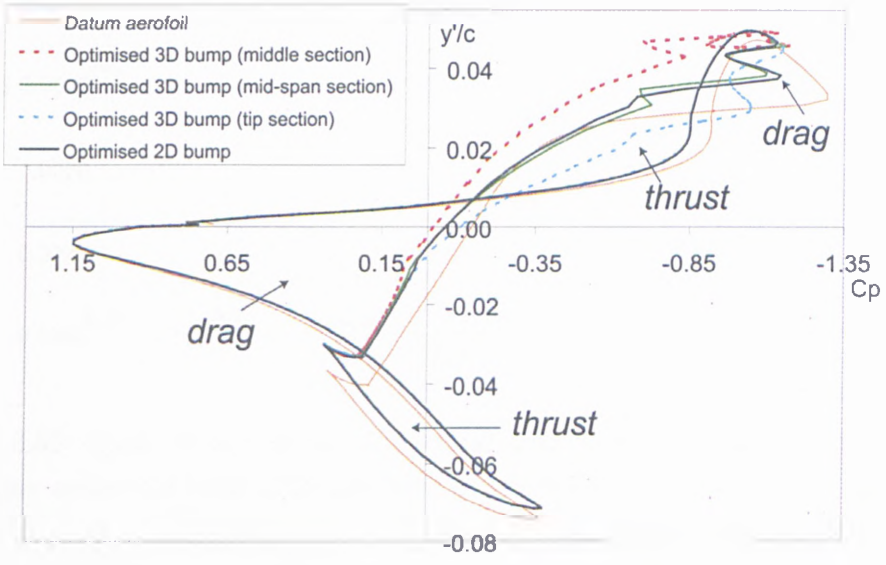


Figure 6.54: $y'$ against $Cp$ distribution for the optimised 3D bump on the upper surface of RAE 2822 aerofoil , $M_\infty = 0.75$, $C_L = 0.75$.

In addition to the weakened shock wave, there are significant variations in the thrust regions of these three spanwise locations. Thrust is substantially increased along the centreline of the 3D bump, while this beneficial effect again progressively diminishes towards the tip. Nonetheless, the overall effect is still beneficial. On the lower surface, the large area of the main drag component is much smaller now for the case with 3D bump. This is mainly due to the lowered attack angle for the bump cases. There is also a minor augmentation of the bottom thrust region.

Once again, from this pressure distribution analysis, it is demonstrated that not only the original normal shock has been weakened, but the 3D bumps deployed on the wing also allow the same lift condition to be sustained as the datum case

at a much lower incidence. As a result of that, its drag reduction ability has been significantly enhanced.

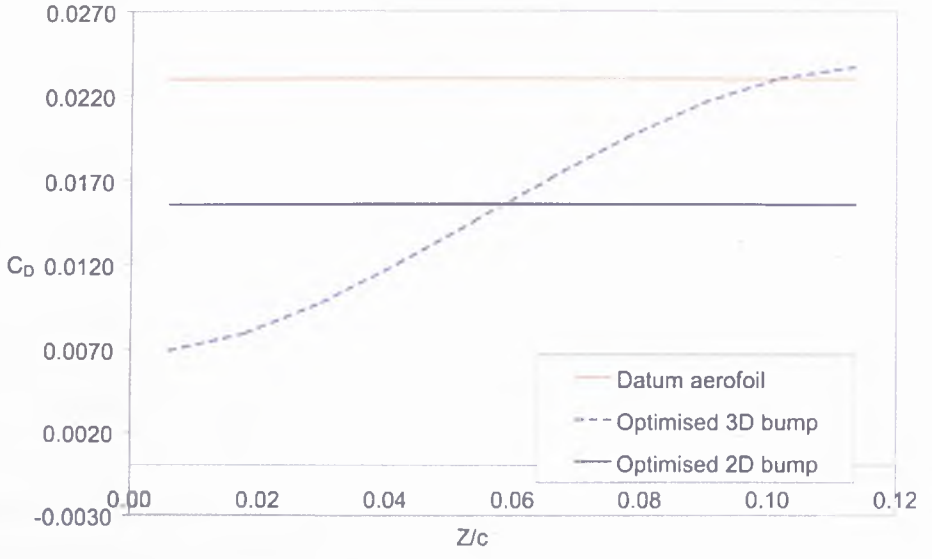


Figure 6.55: Spanwise variations of the total drag of the optimised 3D bump on the upper surface of RAE 2822 aerofoil , $M_\infty = 0.75$, $C_L = 0.75$.

The preceding pressure distribution analysis implies that there are substantial spanwise variations in the drag components on the wing with the optimised 3D bump. This is shown in Figure 6.55 where the spanwise variations of the total drag of each case is plotted. For the 3D bump, despite conceding a minor drag penalty at the tip, most of the plot is well below the drag level of the datum wing. When compared to the 2D bump, it can be observed that the latter half ($z/c > 0.06$) of the 3D bump is above the drag level of the 2D bump, thus off-setting the advantage gained by the other half of the 3D bump. Consequently, they have a similar drag reduction as presented in Table 6.20.

The spanwise variations of the pressure drag are shown in Figure 6.56. One can observe that the trends of the plots in Figure 6.56 bear close resemblance of that in Figure 6.55.

As for the skin friction drag, its spanwise variations are presented in Figure 6.57. Due to the scale, the three dimensionality of this drag component is less apparent

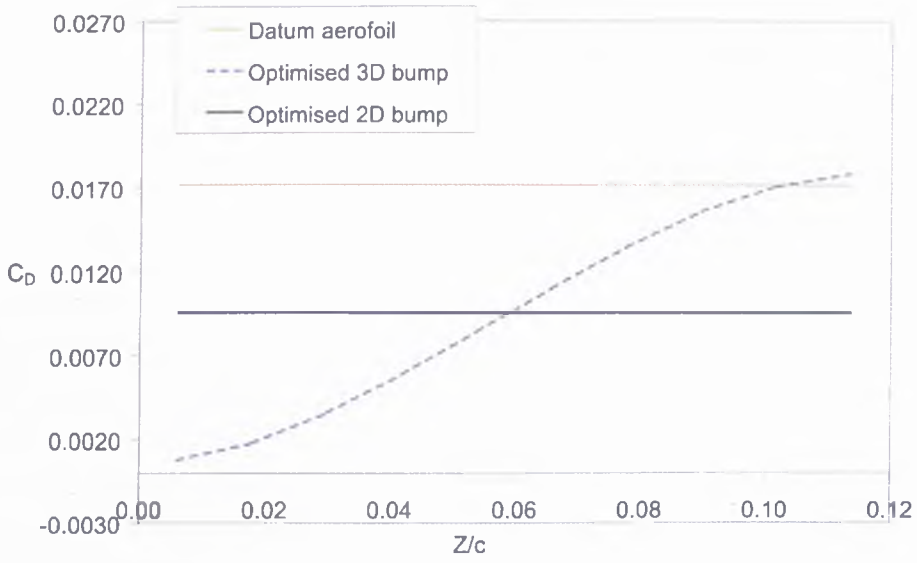


Figure 6.56: Spanwise variations of the pressure drag of the optimised 3D bump on the upper surface of RAE 2822 aerofoil , $M_\infty = 0.75$, $C_L = 0.75$.

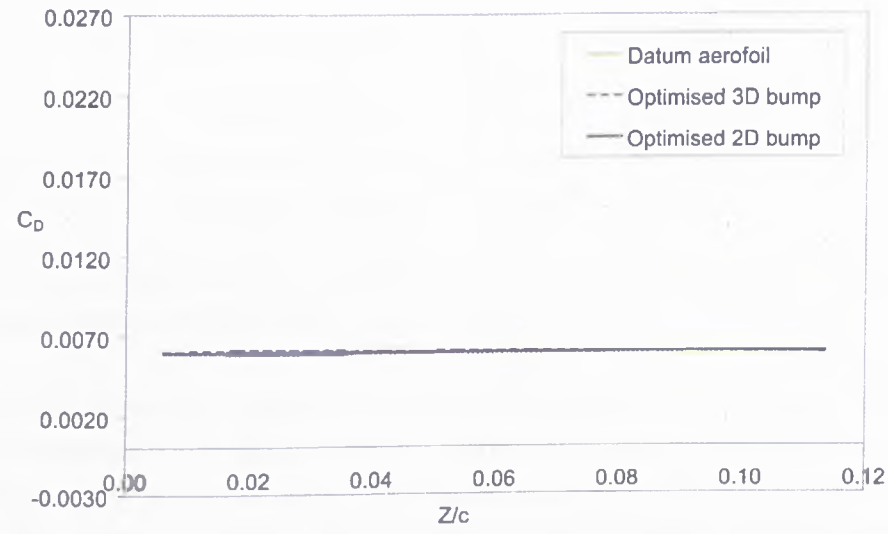


Figure 6.57: Spanwise variations of the skin friction drag of the optimised 3D bump on the upper surface of RAE 2822 aerofoil , $M_\infty = 0.75$, $C_L = 0.75$.

here. Nonetheless, it can still be observed that the drag level is higher closer to the bump centreline. Generally, the drag level of both the bumps is slightly higher than the datum case. A careful closeup examination of the graph suggests that part of the drag level of the 3D bump near the tip is actually below the level of the 2D bump.

#### 6.4.1.1 Wave Drag Analysis

In this section, we will still assess the wave drag reduction performance of the 3D bump optimised on this unswept turbulent wing based on the entropy contour plots and the far-field method. Using the far-field method, the calculated wave drag and viscous drag (form drag + skin friction drag) components shown in Table 6.21 indicate that both bumps that are optimised on the turbulent wing have a similar level of drag reduction performance. In terms of wave drag, the 3D bump slightly edges out the 2D bump, but this advantage has been off-set by the increase of the viscous drag. Nevertheless, both bumps still reduce viscous drag when compared to the datum case. Therefore, it is suggested that the reduction of the viscous drag component is contributed by the reduction of the form drag. This is implied by the increase of skin friction drag as indicated by the surface integration results in Table 6.20.

| | $C_{Dwave}$ | $C_{Dviscous}$ |
|---|---|---|
| Datum aerofoil | 0.0094937 | 0.010972 |
| *Optimised **3D** bump* | 0.0023757 | 0.010701 |
| *Optimised **2D** bump* | 0.0025426 | 0.010313 |

Table 6.21: Comparisons of the wave drag and viscous drag components for the optimised bumps on RAE 2822, $M_\infty = 0.75$, $C_L = 0.75$.

Figure 6.58 shows the variation of the wave drag across the wing span. Surprisingly, there is no major variation in this graph, with just a small dip at $z/c = 0.06$. This is possibly due to the fairly strong remaining shock in the outer inviscid flow-field. Nevertheless, the wave drag level is relatively higher near the bump tip. On the other hand, the spanwise form drag plots in Figure 6.59 present some interesting results. Near the centreline of the 3D bump, some negative drag or thrust is actually generated. However, this benefit is again compensated by the

rise of the drag away from the centreline.

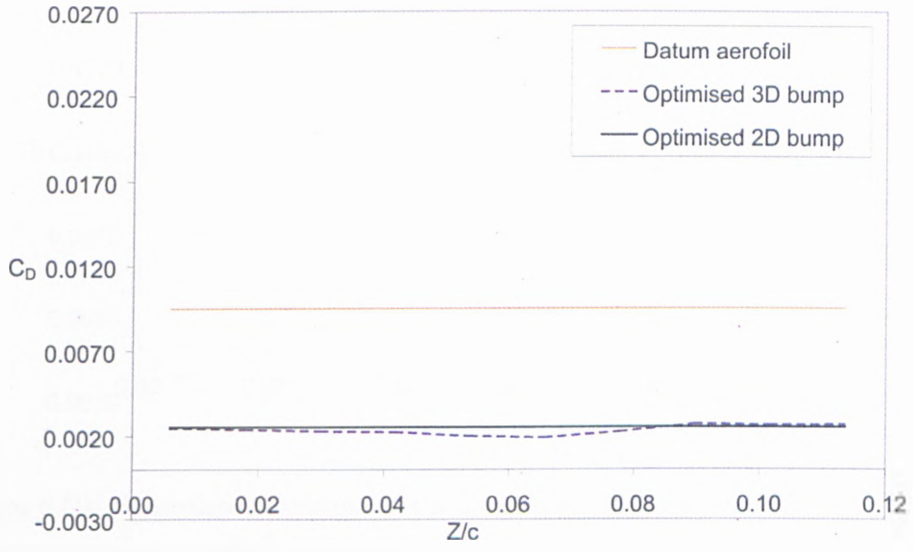


Figure 6.58: Spanwise variations of the wave drag of the optimised 3D bump on the upper surface of RAE 2822 aerofoil , $M_\infty = 0.75$, $C_L = 0.75$.

Entropy contours are plotted at the three corresponding spanwise locations as chosen for Figure 6.52. Starting from the upper-left corner plot of Figure 6.60, which shows the large increase in entropy across the strong original normal shock wave on the datum aerofoil upper surface as indicated by the red contour level behind the normal shock. The following three figures suggest that albeit the substantial reduction of entropy increase of the weakened shock closer to the wing surface, a fairly strong shock still remains in the outer inviscid flowfield. This is consistent with the pressure contour plots presented earlier. Nonetheless, the weakened part is already sufficient to inflict a substantial improvement on the performance of the wing.

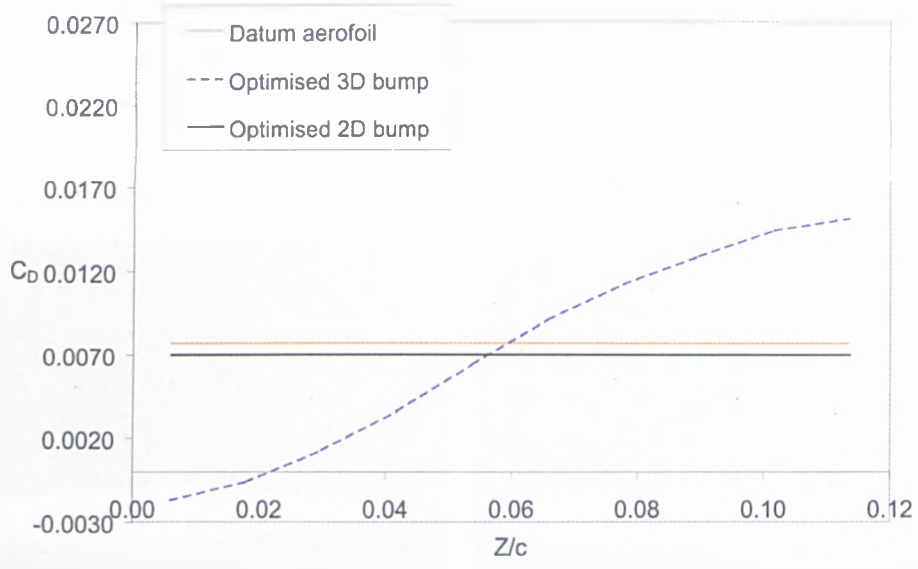


Figure 6.59: Spanwise variations of the form drag of the optimised 3D bump on the upper surface of RAE 2822 aerofoil , $M_\infty = 0.75$, $C_L = 0.75$.

### 6.4.2 Performance over a Range of $C_L$

The off-design performance of the optimised 2D/3D bumps over a range of $C_L$ is plotted in Figure 6.61. Note that the bumps are optimised at $C_L = 0.75$. The freestream Mach number is fixed at 0.75. Overall, both of the bumps perform at a similar level. Despite that, at lower lift coefficients ($C_L < 0.75$), the 3D bump still edges out the 2D bump with 4 or more drag counts reduction. Nonetheless, by looking at the other graph where lift-drag ratio is plotted against incidence in Figure 6.62, the advantage of the 3D bump looks more promising at lower lift conditions over the 2D bump. Again, at higher off design conditions ($C_L > 0.75$), their performance are at similar level.

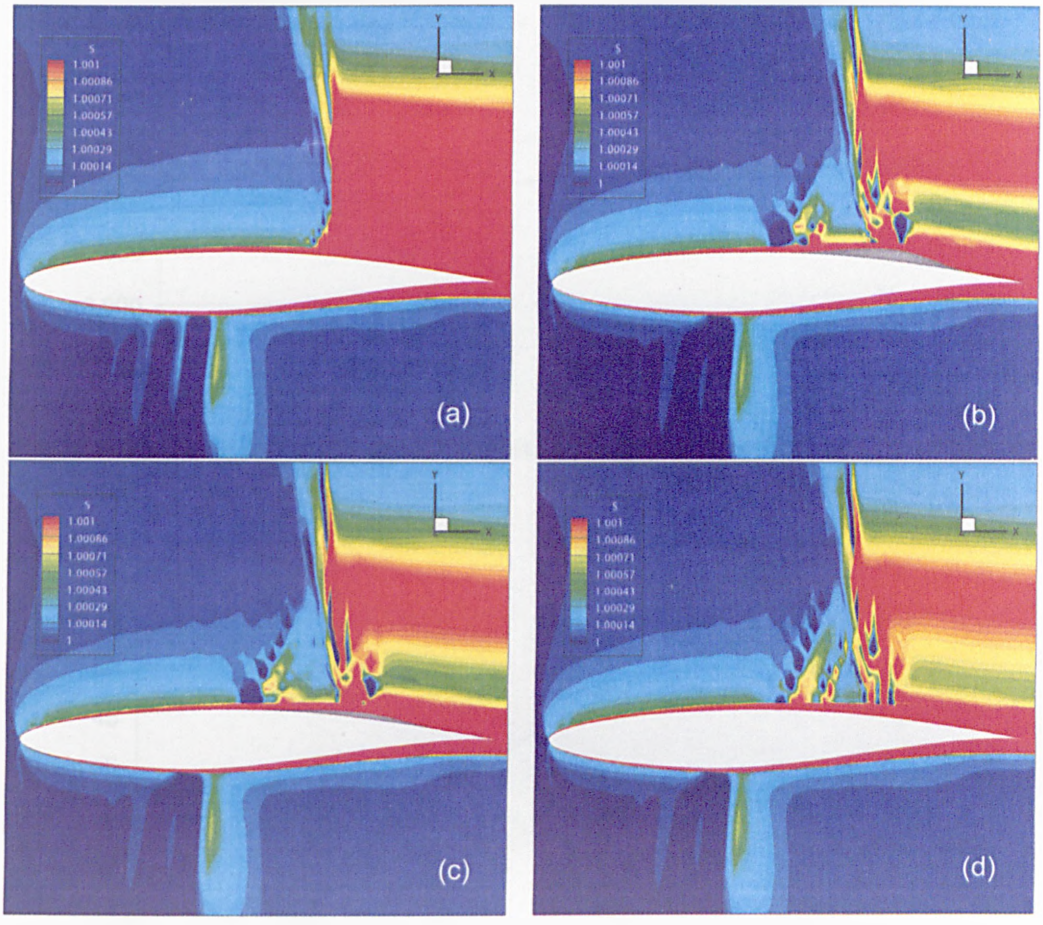


Figure 6.60: (a) Entropy contours of the datum aerofoil. (b) Entropy contours along the centreline of the optimised 3D bump. (c) Entropy contours along the mid-span of the optimised 3D bump. (d) Entropy contours along the tip of the optimised 3D bump. (RAE 2822, $M_\infty = 0.75$, $C_L = 0.75$)

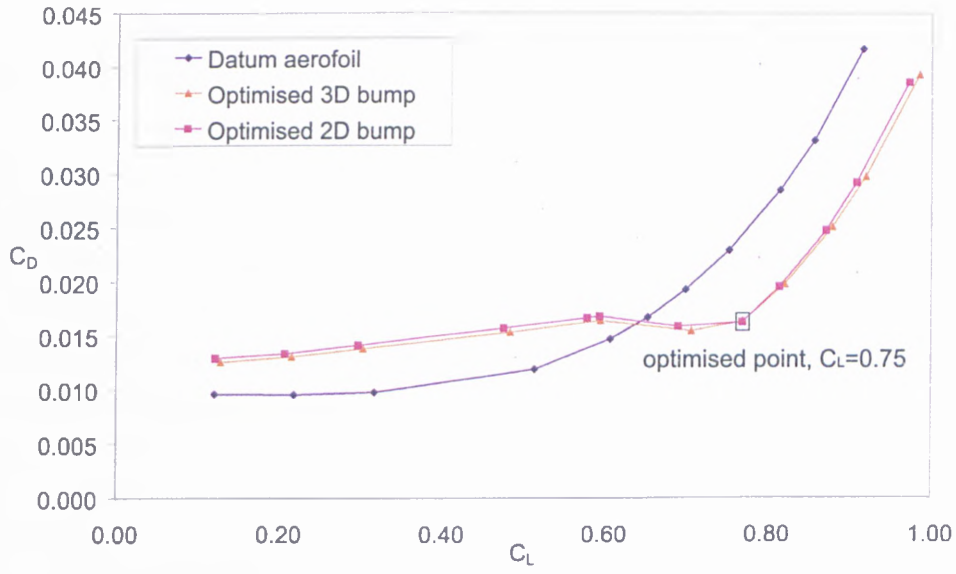


Figure 6.61: Drag polar for the optimised 3D bump on the upper surface of RAE 2822 aerofoil, $M_\infty = 0.75$.

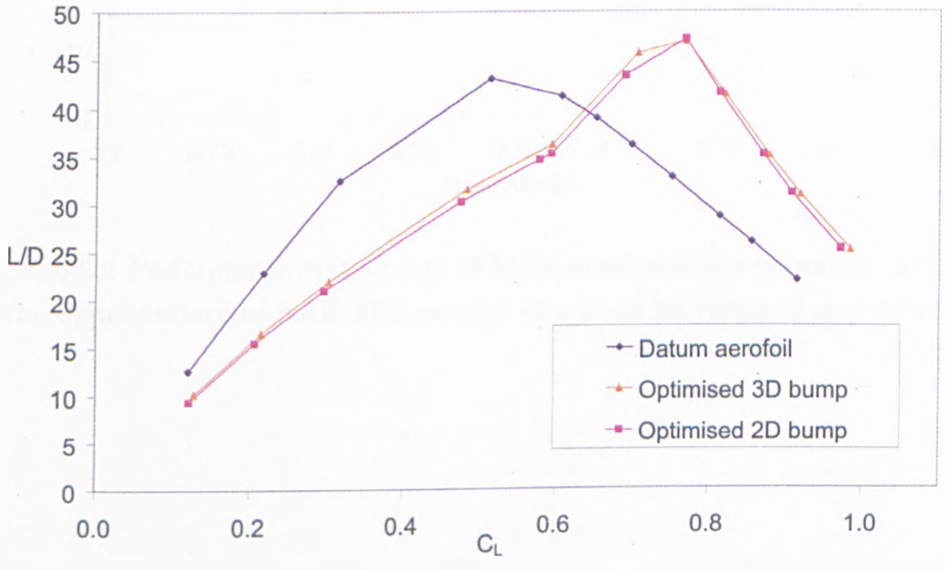


Figure 6.62: Lift-drag ratio polar for the optimised 3D bump on the upper surface of RAE 2822 aerofoil, $M_\infty = 0.75$.

### 6.4.3 Performance Over a Range of $M_\infty$

The effectiveness of the bumps over a range of freestream Mach number is investigated in Figure 6.63. All the calculations are carried out at a fixed incidence of $\alpha = 2.31°$ and that the bumps are optimised at $M_\infty = 0.75$. Once again, since the $C_L$ is not fixed, it is more useful to look at the lift-drag ratio plot. At a slightly lower Mach number at 0.74, the 2D bump is slightly better than the 3D bump. However, at lower Mach numbers, the 3D bump regains the advantage. At higher Mach numbers, their performance is similar until they reach $M_\infty = 0.78$ and 0.80, where again the 2D bump has a slight edge over the 3D bump. Beyond and higher than that, they are more or less equal.

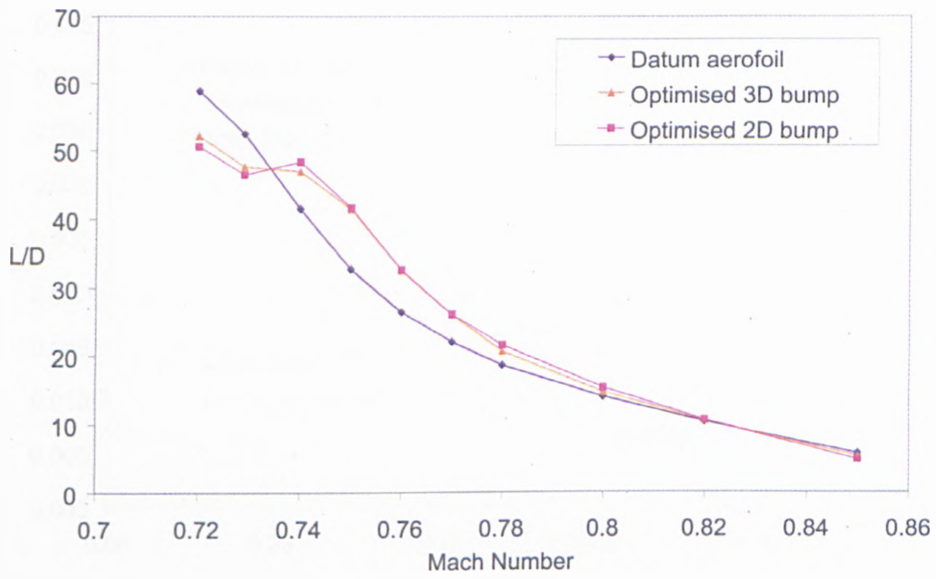


Figure 6.63: Performance over a range of Mach number of the optimised 3D bump on the upper surface of RAE 2822 aerofoil at a fixed incidence of $\alpha = 2.31°$.

### 6.4.4 Analysis at Off-Design Condition

The purpose of this section is similar to that of *Section 6.3.8*, which is to analyse the effects of both optimised bumps at an off-design point. Bear in mind that the design lift condition is 0.75. From the drag polar plot, we have chosen an off-design point at a lower lift condition, $C_L = 0.59$ as marked out in Figure 6.64. At this off-design point, both of the bumps start to have a negative impact on the drag as compared to the datum case. However, the 3D bump still has a slight edge over the 2D bump. This is shown with further details in Table 6.22. At the same level of lift condition, the drag level of the 3D bump is about 4 drag counts less than that of the 2D bump.

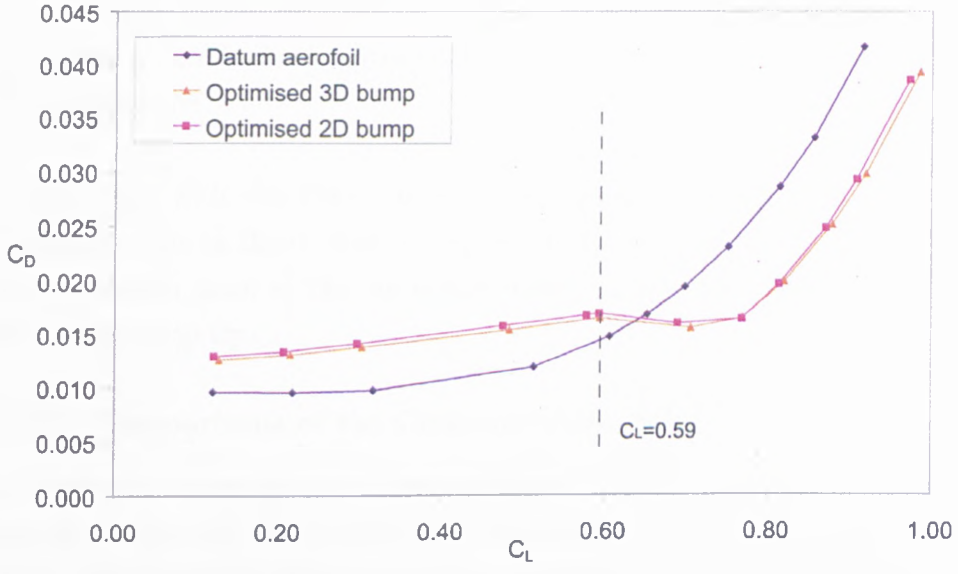


Figure 6.64: The chosen off-design point for the optimised bumps on the upper surface of RAE 2822 aerofoil.

| | $C_L$ | $C_{Dtotal}$ | $C_{Dpressure}$ | $C_{Dfriction}$ |
|---|---|---|---|---|
| Datum aerofoil | 0.5940 | 0.01424 | 0.00822 | 0.006019 |
| *Optimised 3D bump* | 0.5944 | 0.01643 | 0.01049 | 0.005938 |
| *Optimised 2D bump* | 0.5934 | 0.01684 | 0.01097 | 0.005874 |

Table 6.22: Comparisons of the performance of the bumps at an off-design condition. (RAE 2822)

#### 6.4.4.1 Comparisons of the Flowfield

The Mach number contours from both cases are shown in Figures 6.65. Notice that the values of the $M_{max}$ are given for each plot. Figure 6.65 (a) indicates that the strength of the secondary shock generated by the 2D bump is around $M_{max} = 1.235$. Surprisingly, it is shown in Figure 6.65 (b) that the strength of the secondary shock generated at the crest of the 3D bump is actually stronger with a value of 1.264. Nonetheless, as we move towards the tip, this secondary shock drops significantly to 1.221 at the mid-span section. Eventually, it settles down to a value of 1.191 at the bump tip. Therefore, it is demonstrated here that the three dimensionality of the 3D bump does relax the re-compression of the secondary shock generated by the bump crest. As a result of that, the 3D bump performs better than 2D bump at lower lift-coefficient off-design conditions, where a double-shock system is almost inevitable if the bump heights were not adjusted lower.

In conjunction with the Mach number contour plots, the streamwise pressure distribution plots of these cases as plotted in Figure 6.66 clearly demonstrates that the suction peak of the secondary shock on the 3D bump is weakening towards the bump tip.

#### 6.4.4.2 Comparisons of the Cross-sectional Area

The chordwise variations of the cross-sectional area for the wing including the bumps in Figure 6.67 show that the area variations of both cases are generally smooth. The maximum cross-sectional area calculated for both bumps (excluding the aerofoil cross-section) are very close with just less than 1% difference. These calculations again support the cross-sectional area hypothesis suggested earlier. As for the rate of area change as shown in Figure 6.68, it is observed that there is still a steep change of gradient for the 2D bump case at $x/c = 0.75$. In contrast, the change of gradient along the chord for the 3D bump is smooth with no steep variations. Again, the discrepancy of the rate of area change between the bumps could contribute to the performance advantage the 3D bump has over the 2D bump.

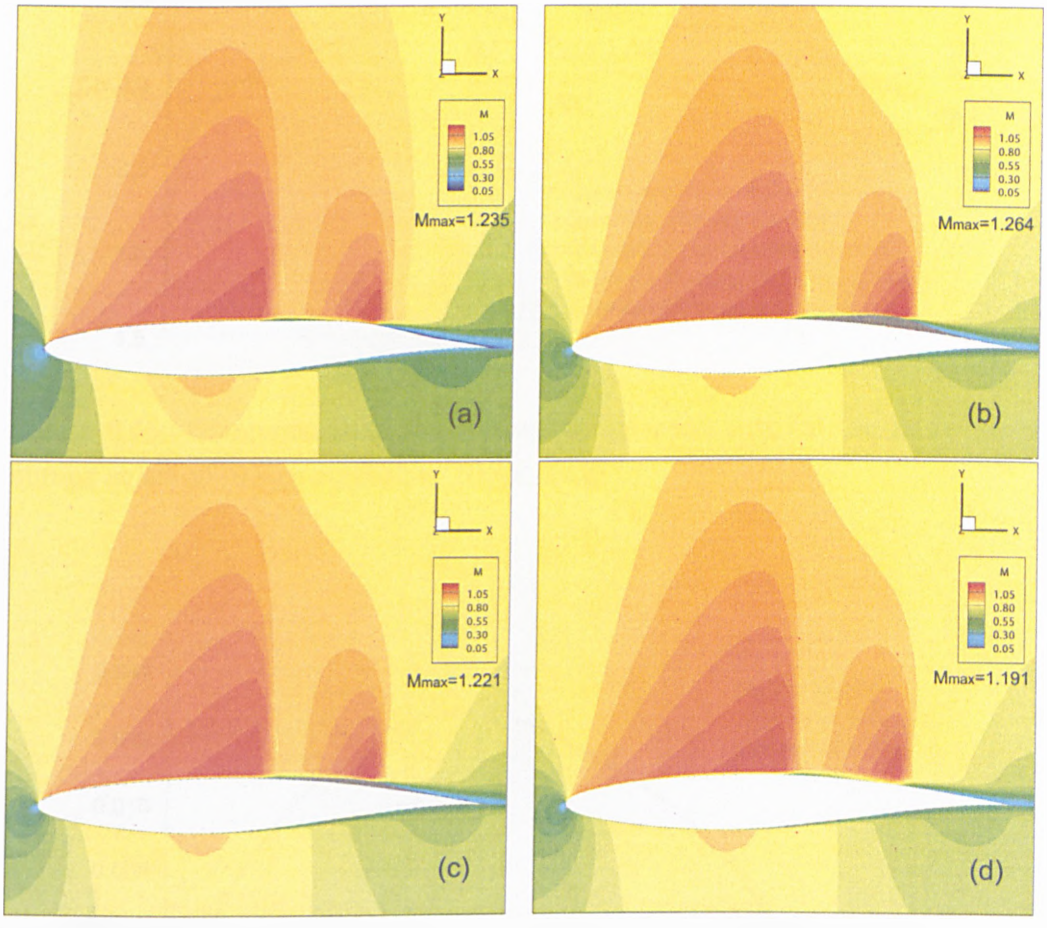


Figure 6.65: (a) Mach number contours of the optimised 2D bump. (b) Mach number contours along the centreline of the optimised 3D bump. (c) Mach number contours along the mid-span of the optimised 3D bump. (d) Mach number contours along the tip of the optimised 3D bump. (RAE 2822 aerofoil)

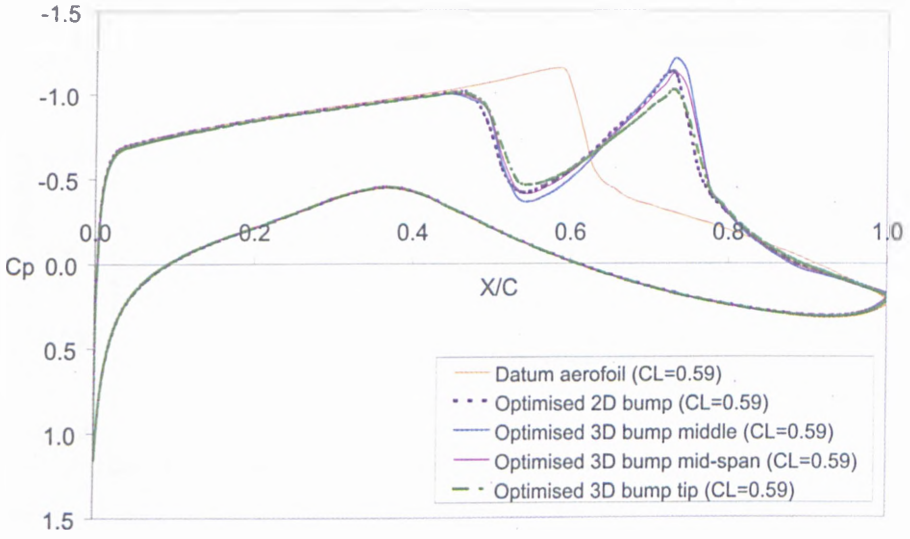


Figure 6.66: Comparisons of the streamwise pressure distribution plots of the bumps at an off-design condition. (RAE 2822)

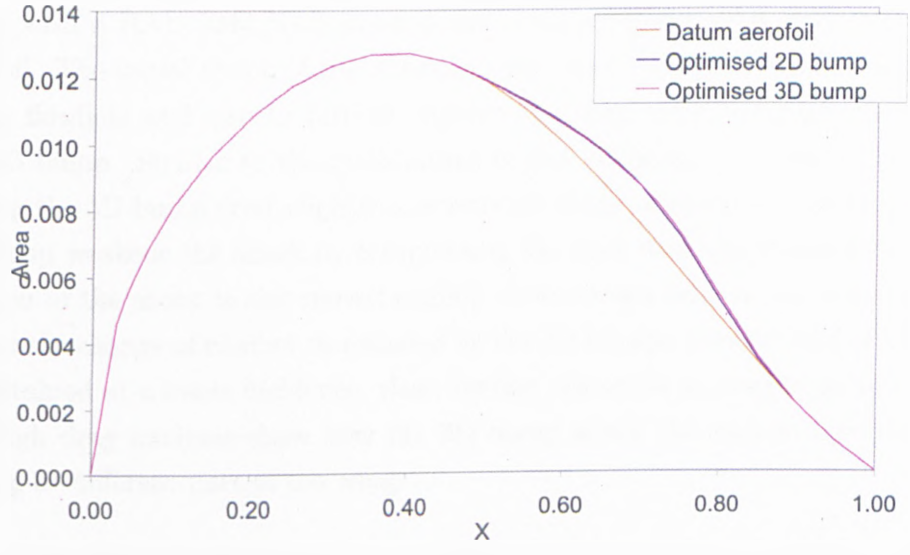


Figure 6.67: Chordwise cross-sectional area variations for the optimised bumps on the upper surface of RAE 2822 aerofoil.

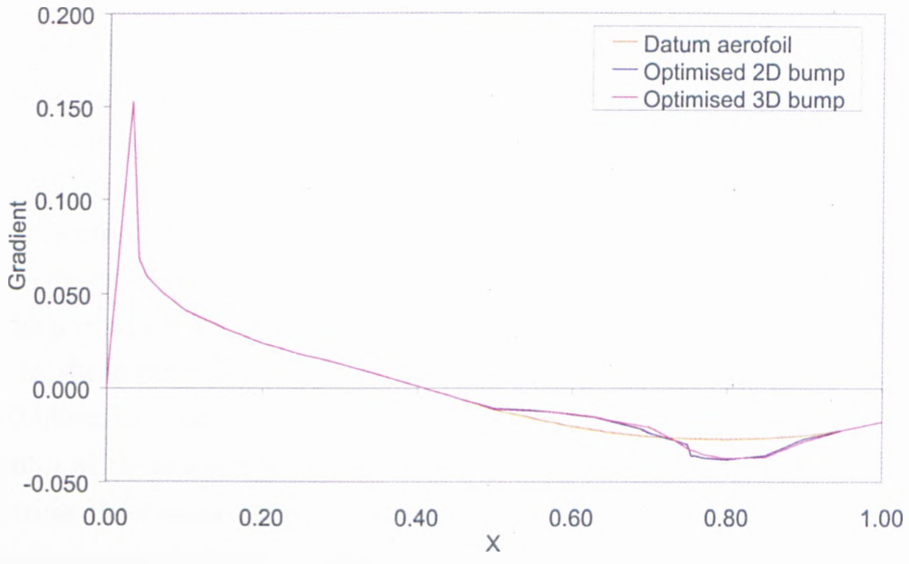


Figure 6.68: Chordwise cross-sectional area rate of change for the optimised bumps on the upper surface of RAE 2822 aerofoil.

## 6.5 Concluding Remarks

This chapter has presented the results for the 3D bumps, optimised on unswept wings with a RAE 5243 NLF aerofoil and a higher-speed RAE 2822 turbulent aerofoil. The initial shape of the 3D bump has been revised to avoid separation in the flowfield and also to further improve the drag reduction performance of the 3D bump. Similar to the mechanisms of the 2D bump, it is shown that by placing the 3D bump crest slightly downstream of the original normal shock, the 3D bump weakens the shock by compressing the upstream supersonic flow. The position of the shock is also moved slightly downstream near to the bump crest. Due to the change of camber introduced by the 3D bumps, a same level of lift can be sustained at a lower incidence, thus, further reduction in drag is gained. The thorough drag analyses show how the 3D bump alters the various contribution to drag at different part of the wing.

A spanwise variation plot of the drag components, including wave drag, show the three-dimensionality of the flowfield imposed by the 3D bump. It is found that the 3D bump reduces both the wave drag and the form drag effectively with just a minor skin friction drag penalty. Comparisons of the drag polars from both the

2D and 3D bumps suggest that at off-design conditions, particularly at lower lift conditions, the performance of the 3D bump is better than the 2D bump. An off-design point at a lower lift condition is chosen for further analysis for each type of aerofoil. The comparisons of the flowfield from both bumps indicate the ability of the 3D bump to relax the re-compression of the secondary shock at the bump crest, thus leading to a weaker double-shock system. Analyses of the rate of change of the chordwise cross-sectional area variations indicate that there is a steep gradient change imposed by the 2D bumps. This observation could assist in the explanation of the performance advantage the 3D bump has over the 2D bump at lower-lift off-design conditions. Based on the optimisation of the 3D bump at several design points, a low-order geometrical model is derived by correlating the design parameters with respect to the position and strength of the original normal shock. The effectiveness of the 3D bumps designed using this low-order geometrical model was then demonstrated.

The parametric studies on the spacing for the 3D bumps show that with a fixed bump size, spacing them further apart reduces their effectiveness. However, the bump height can be adjusted to be higher to regain some efficiency. Optimisation of a relatively small-sized 3D bump suggest that an appropriate bump length is required to generate sufficient upstream compression to weaken the shock wave and also to generate lift. The following chapter extends the investigations of 3D bumps on an infinite swept wing, a three-dimensional transonic swept wing and a Blended-Wing-Body.

# Chapter 7

# 3D Bumps on Swept Wings

This chapter extends the investigations to employing 3D bumps on an infinite swept wing, a three-dimensional transonic swept wing and a Blended-Wing-Body. Based on the experience gained from the preceding investigations and developed numerical tools, we begin with the optimisation of the 3D bump on an infinite/periodical span swept wing. From there, the design of the 3D bump is extracted and placed on a 3D transonic swept wing. Following that, the feasibility of carrying out a coupled-optimisation of the wing shape with an array of 3D bumps is demonstrated on a Blended-Wing-Body.

## 7.1 3D Bumps on an Infinite/Periodical Swept Wing

Instead of moving directly into optimising an array of 3D bumps on a full three-dimensional wing, it is more sensible to first optimise a 3D bump placed on an swept wing with infinite span. If the performance of the three-dimensional bump were to be optimised directly on the three-dimensional transonic wing, it would be expensive in terms of computational resources. Additionally, the selected 3D wing will also be adopted later in the investigations of 3D bumps on a full 3D swept wing. Therefore, the aerofoil profile chosen for this infinite swept wing is extracted from the mid-span section of this transonic swept wing. The planform view of the 3D wing is shown in Figure 7.1. In this figure, a black vertical dashed-line marks the location of the extracted aerofoil profile. Note that the tip of the wing was closed up manually by the author.

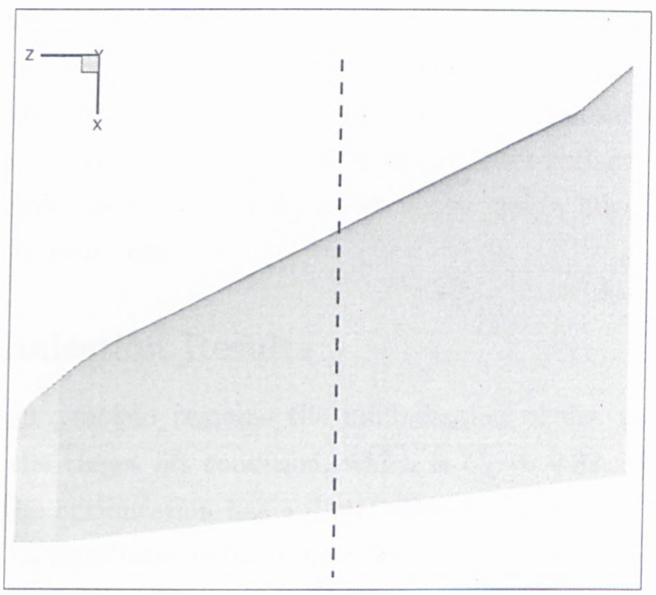


Figure 7.1: The planform view of a Hawk wing.

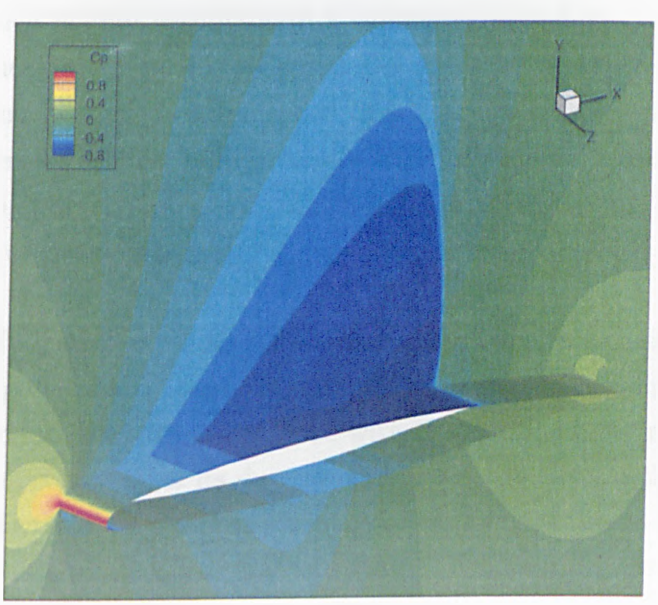


Figure 7.2: Pressure contour plots of the datum infinite swept wing, $M_\infty = 0.85$, $C_L = 0.32$.

The freestream conditions for this 3D swept wing are $M_\infty = 0.85$, $Re_m = 20 \times 10^6$ and $\alpha = 0.0$, which will be employed by the infinite swept wing as well. The pressure contour plots for this clean infinite swept wing are shown in Figure 7.2. In addition to the fairly strong upper-surface shock, it is observed that there is also a small low-pressure region at the L.E. of the lower-surface. The calculated lift at these conditions is $C_L = 0.32$, which is the design lift condition for the following optimisation task.

### 7.1.1 Optimisation Results

The optimisation problem remains the minimisation of the total drag whilst constrained at the target lift condition, which is $C_L = 0.32$. The best design obtained from the optimisation has a designation of *l35.7-cre78.1-cb77.1-h1.95-sp95.5-wid11.6*. A significant point to note here is that the last parameter in the designation above denotes the total width of the spacing between the subsequent bumps instead of half the value as discussed in the unswept wing cases. This is for the reason that for the infinite swept wing problem, the periodical boundary condition is employed at both spanwise boundaries. As a result, a full-size 3D bump has to be generated on the surface of the wing instead of just half of the bump, which is only feasible with a symmetry boundary condition at both spanwise boundaries. Figure 7.3 depicts the shape of the optimised 3D bump with the dimensions scaled by the chord length. The depiction of this optimised 3D bump generated on the infinite wing is shown in Figure 7.4 and a closeup in Figure 7.5. It is clearly shown here that a full-size 3D bump has been generated on the surface of the swept wing.

At the same lift condition, Table 7.1 compares the drag components of the optimised 3D bump with the datum case. The computed results indicate that up to 23% of reduction in drag can be obtained with this 3D bump. It is demonstrated that the 3D bump maintains its drag reduction benefits even with the inclusion of the sweep effects. Similar to the preceding results of 3D bumps on an unswept wing, there is still a minor skin friction penalty, which remains relatively insignificant compared to the reduced pressure drag.

The effects of the 3D bump are further examined in the visualisation of the computed flowfield as shown in the following figures. Figures 7.6 display the pressure

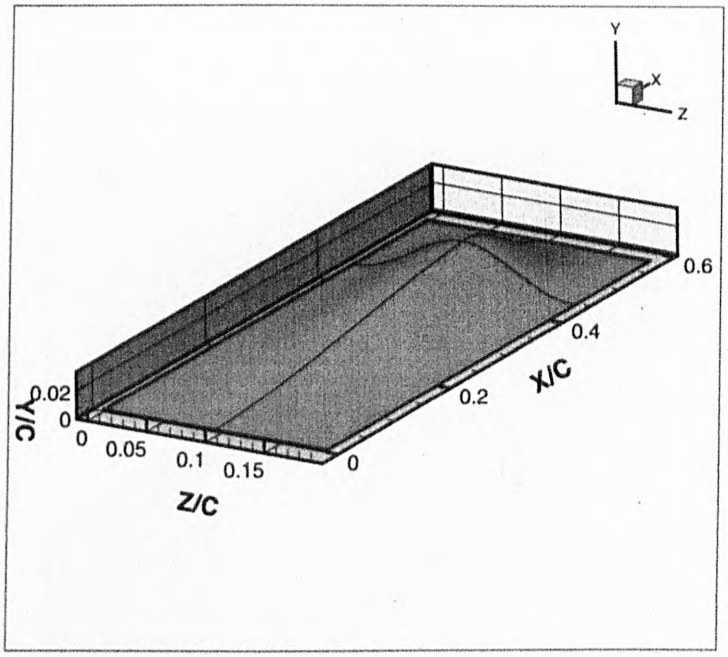


Figure 7.3: Shape of the optimised 3D bump on the infinite swept wing.

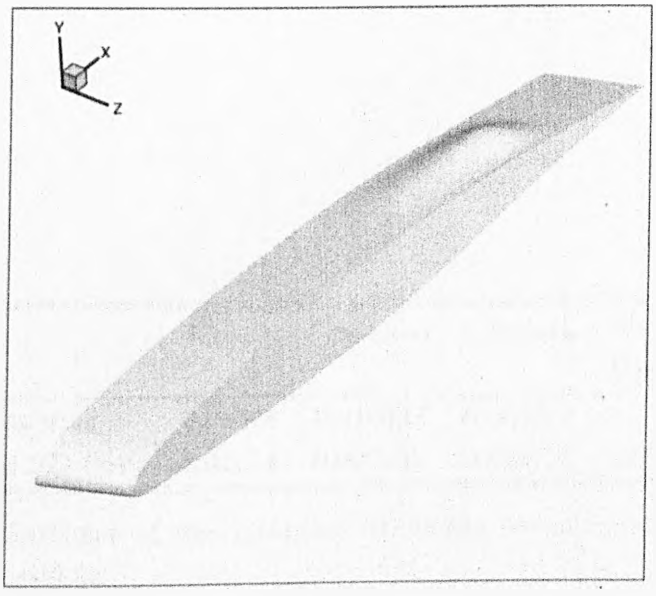


Figure 7.4: The optimised 3D bump generated on the infinite swept wing.

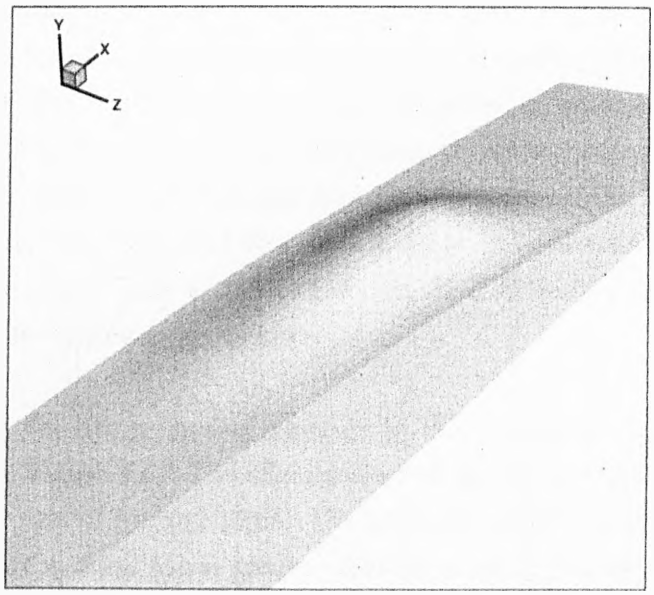


Figure 7.5: Closeup of the optimised 3D bump generated on the infinite swept wing.

| | $C_{Dtotal}$ | $C_{Dpressure}$ | $C_{Dfriction}$ | **Total Drag Reduction** |
|---|---|---|---|---|
| Datum wing | 0.01524 | 0.010633 | 0.004607 | - |
| *Optimised **3D** bump* | 0.01174 | 0.007037 | 0.004706 | 22.9% |

Table 7.1: Performance of the optimised 3D bump on an infinite swept wing, $M_\infty = 0.85$, $C_L = 0.32$.

contours plotted at various spanwise locations across the 3D bump. With reference to the datum wing of Figure 7.6 (a), all the spanwise slices indicate that a relatively weaker shock still remains close to the surface of the wing. Further away from the surface, the pressure contour lines of the remaining shock are much less clustered and spread out, suggesting a much lower wave drag. The position of the shock wave has also displaced downstream. However, in contrast to the earlier results for an unswept wing, at least from these pressure contours, the spanwise variations of the contours are less apparent here. Another thing to notice is that Figure 7.6 (b) and (f) show that the contour plots at both spanwise boundaries are actually the same. This is due to the periodical boundary condition that is employed at these spanwise boundaries.

Figures 7.7 plot the Mach number contours at the corresponding spanwise locations defined in Figure 7.6. The effectiveness of the 3D bump is again demonstrated in these sets of contour plots. The spanwise variations of the flowfield is still less apparent in these Mach number contour plots. It can be seen from these Mach number plots that contour levels at the upstream maximum Mach number of the shock is substantially lower than the datum case.

The streamwise pressure distribution plot of these identified spanwise locations is shown in Figure 7.8. In addition to the strong normal shock wave on the upper surface of the datum wing, there is a fairly strong pressure jump at the L.E. of the pressure side of the wing. The occurrence of this shock is mainly due to the original design shape of the extracted aerofoil. As implied in the pressure contour plots of Figures 7.6, variations of the pressure distribution across different spanwise locations are limited. Displacement of the original shock wave to a slightly downstream position is also shown here. Note that the target lift condition is matched at a lower incidence with the 3D bump. As a result of that, it is noticed that the shock at the L.E. of the lower-surface is slightly strengthened. Nevertheless, this small penalty should have minor effects on the overall drag reduction benefit.

Figure 7.8 is re-plotted in Figure 7.9, where the transformed $y'$-coordinates are plotted against $Cp$. As a recap of some basic concepts, the integration of the areas in this figure directly associated with drag. The drag and thrust areas are labeled in the figure too. Due to the existence of the lower-surface shock wave at the L.E.,

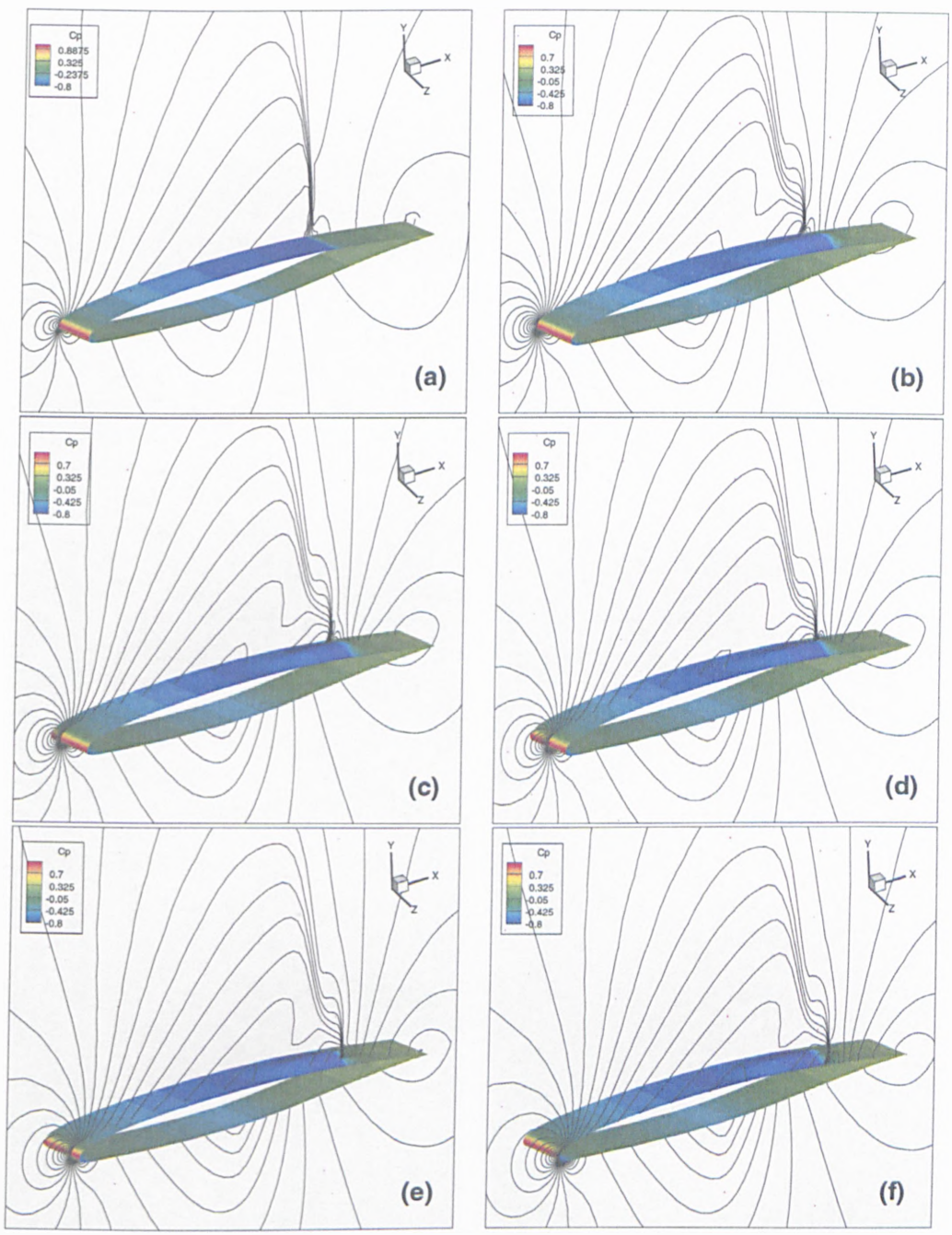


Figure 7.6: (a) Pressure contours of the original normal shock wave. (b) Pressure contours along the tip of the optimised 3D bump. (c) Pressure contours along the mid-span of the optimised 3D bump. (d) Pressure contours along the centreline of the optimised 3D bump. (e) Pressure contours along the mid-span of the optimised 3D bump. (f) Pressure contours along the tip of the optimised 3D bump. (On the infinite swept wing, $M_\infty = 0.85$, $C_L = 0.32$.)

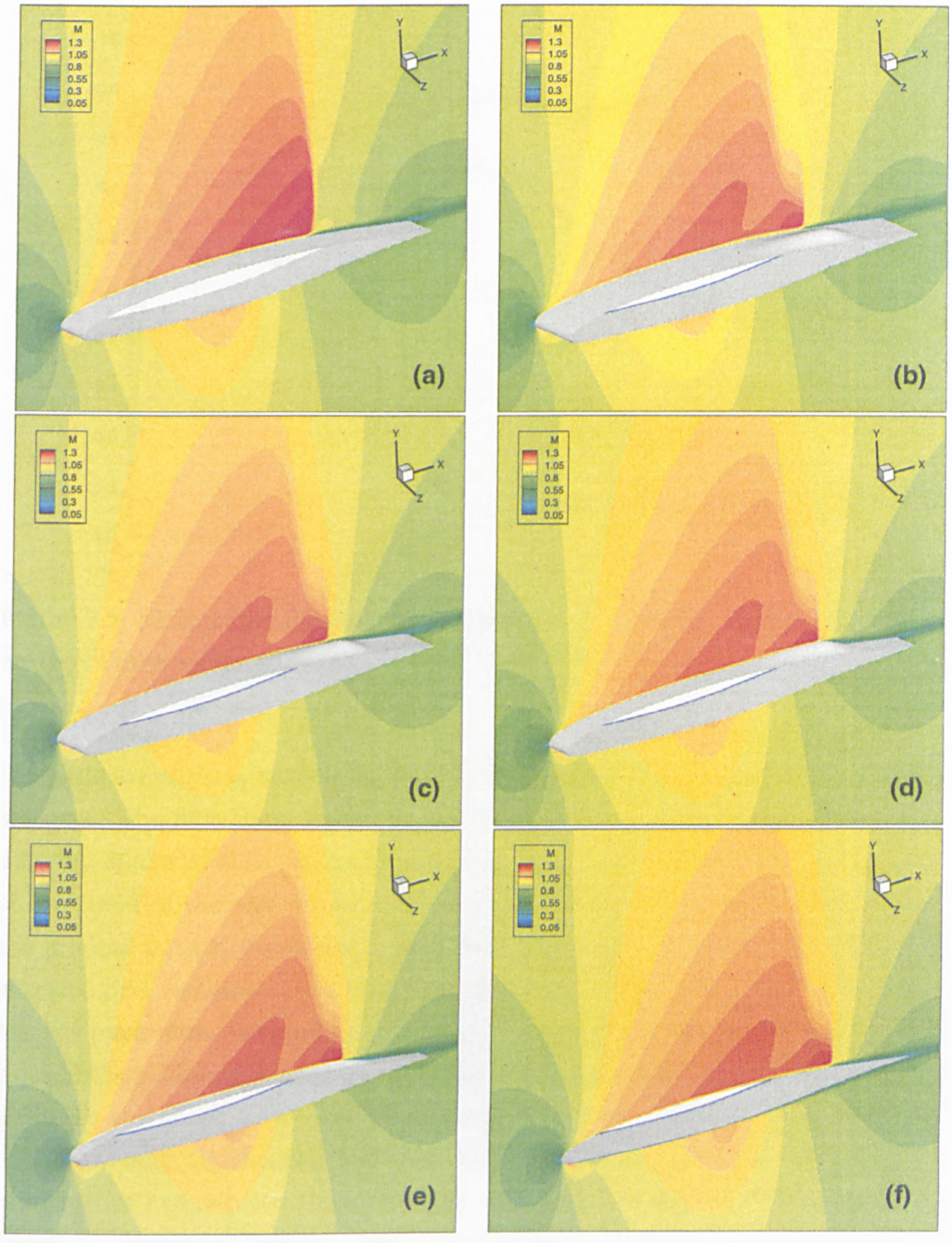


Figure 7.7: (a) Mach number contours of the original normal shock wave. (b) Mach number contours along the tip of the optimised 3D bump. (c) Mach number contours along the mid-span of the optimised 3D bump. (d) Mach number contours along the centreline of the optimised 3D bump. (e) Mach number contours along the mid-span of the optimised 3D bump. (f) Mach number contours along the tip of the optimised 3D bump. (On the infinite swept wing, $M_\infty = 0.85$, $C_L = 0.32$.)

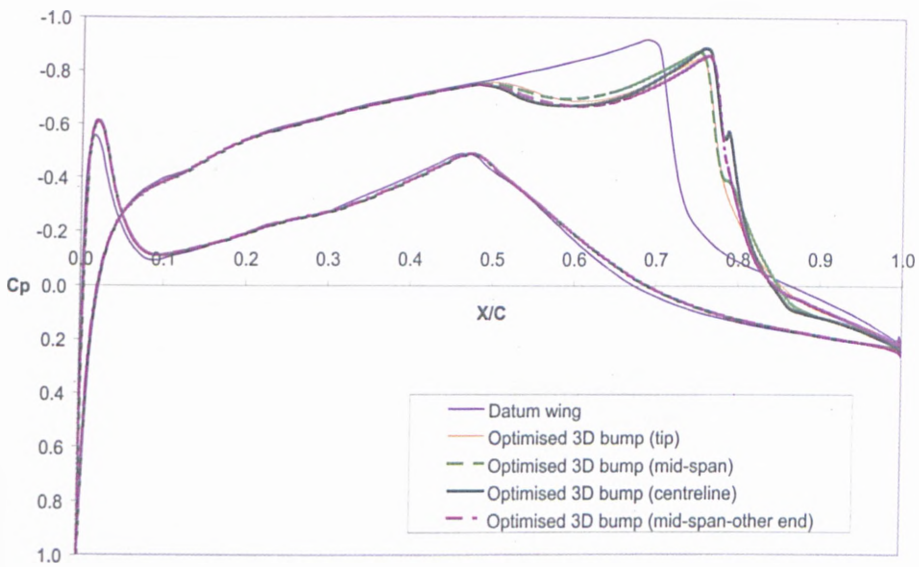


Figure 7.8: Streamwise pressure distribution of the optimised 3D bump generated on the infinite swept wing, $M_\infty = 0.85$, $C_L = 0.32$.

the plots are slightly more complicated than the similar plots shown in previous sections. The first thing to notice is a more pronounced difference between the different spanwise stations, particularly on the upper-surface. Close examination of the trend of the plot shows that the drag pocket (upper-right corner area) of the original normal shock has largely been reduced by the 3D bump. The most effective part remains at the centreline of the 3D bump where flow displacement reaches maximum. It can be pointed out that the two mid-span sections on both sides of the 3D bump bear close similarity with some small differences. At the tip, although the shock wave drag pocket retains a reasonable size here, the thrust region has been significantly increased like the other spanwise stations. A change of incidence has reduced the size of the main drag region and a considerable increase in the thrust region on the lower surface. Nevertheless, as indicated by the flowfield visualisations, the drag area for the lower-surface shock wave has increased slightly. However, this minor increase could be considered as insignificant.

The variation of the breakdown drag components (pressure drag & skin friction drag) across the span are shown in Figure 7.10. Clearly, the maximum reduced pressure drag is achieved at the station where the crest is located. The drag

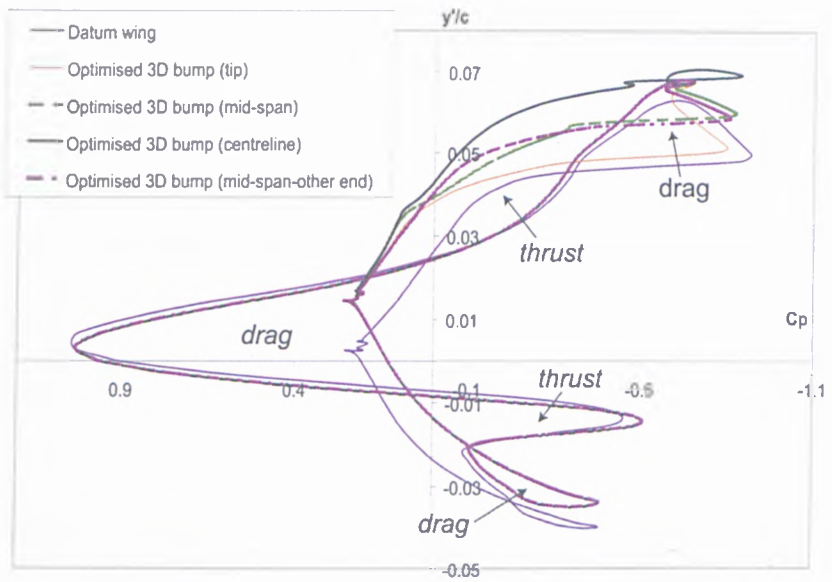


Figure 7.9: $Y'$-coordinates vs streamwise pressure distribution of the optimised 3D bump generated on the infinite swept wing, $M_\infty = 0.85$, $C_L = 0.32$.

then increases progressively towards the bump tip at both ends. Although it is indicated here that there is a slight penalty near to the bump tip, it is still obvious that the overall drag has been reduced significantly. Since pressure drag is the dominant component over skin friction drag, the plot for the total drag will have the same trend as well. As for the skin friction drag, close examination shows that there is a minor drag penalty across the region of the bump crest. This penalty eventually diminishes at the bump tip. The skin friction penalty suggests that the presence of the bump is accompanied by a slightly thickening of the boundary layer momentum thickness. Since flow displacement is minimal at the bump tip, the increase in skin friction drag is then relatively smaller too.

The entropy contour plots shown in Figures 7.11 demonstrate the wave drag reduction capability of the 3D bump, even with the sweep effects being taken into account. It can be seen here that a huge part of the red-region (severe rise in entropy) on the datum wing is converted to green-level (less increase in entropy). Similar to the pressure and Mach number contour plots presented earlier, the observed spanwise variations are quite limited.

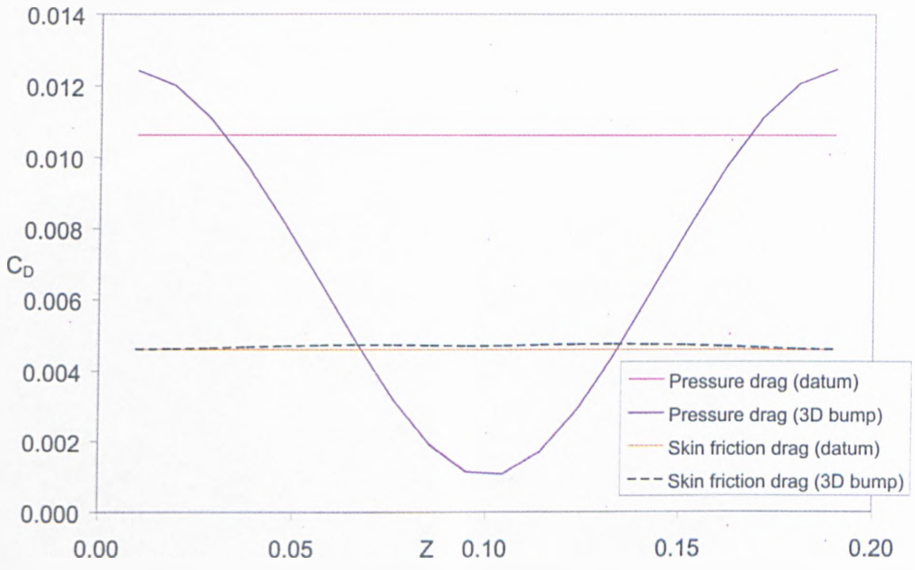


Figure 7.10: Spanwise drag distribution of the optimised 3D bump generated on the infinite swept wing, $M_\infty = 0.85$, $C_L = 0.32$.

| | $C_{Dwave}$ | $C_{Dviscous}$ |
|---|---|---|
| Datum wing | 0.0058093 | 0.006797 |
| *Optimised 3D bump* | 0.0013111 | 0.008104 |

Table 7.2: Comparisons of the wave drag and viscous drag components for the optimised 3D bump on an infinite swept wing, $M_\infty = 0.85$, $C_L = 0.32$.

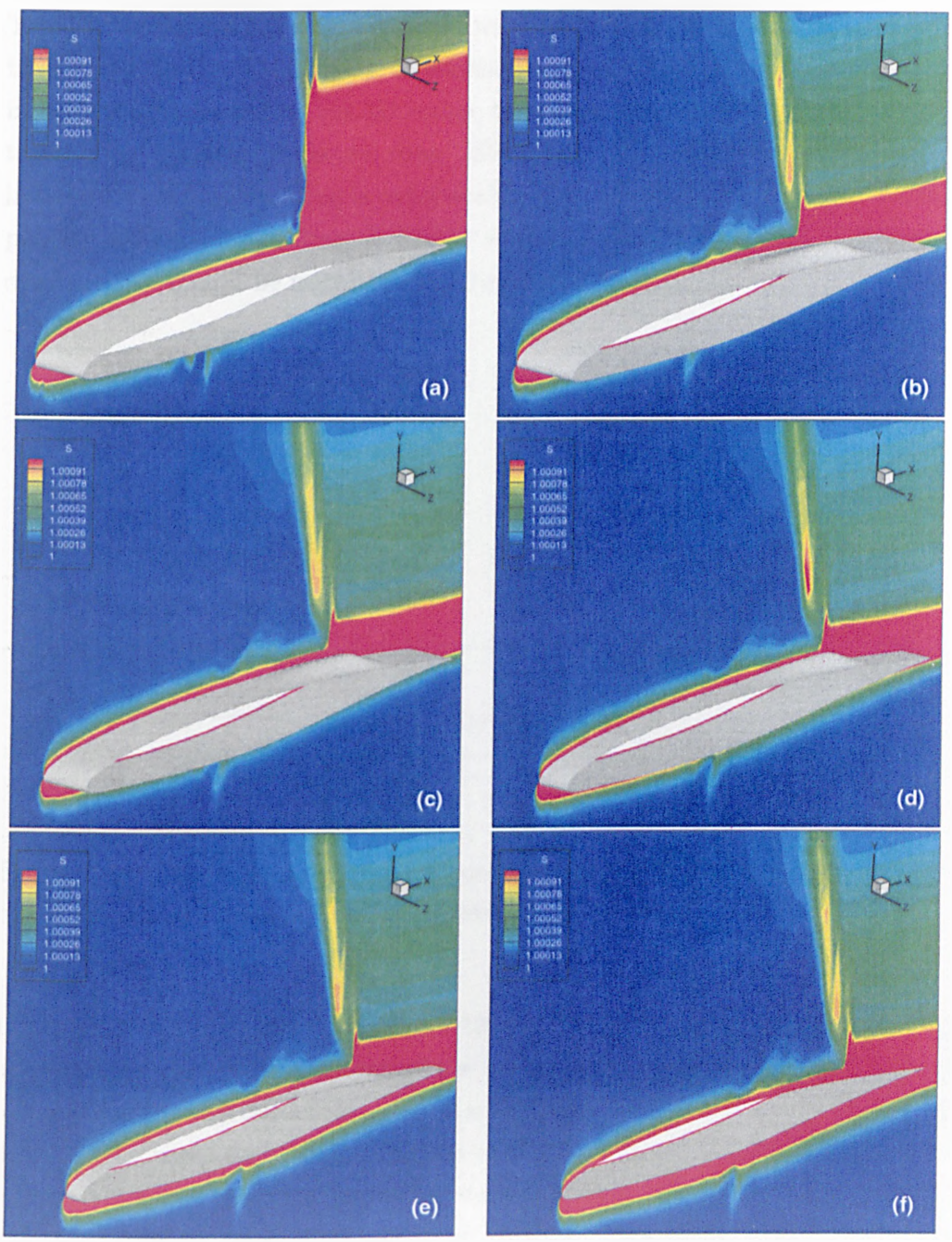


Figure 7.11: (a) Entropy contours of the original normal shock wave. (b) Entropy contours along the tip of the optimised 3D bump. (c) Entropy contours along the mid-span of the optimised 3D bump. (d) Entropy contours along the centreline of the optimised 3D bump. (e) Entropy contours along the mid-span of the optimised 3D bump. (f) Entropy contours along the tip of the optimised 3D bump. (On the infinite swept wing, $M_\infty = 0.85$, $C_L = 0.32$.)

Table 7.2 compares both the extracted wave and viscous drag from the flow solutions using the far-field method. In addition to the predicted significant reduction in wave drag achieved by the 3D bump, the calculations actually suggested that there is an increase in viscous drag. Since the preceding results have already indicated that pressure drag is considerably reduced whilst there is only a minor penalty in skin friction drag; it is thus suggested by Table 7.2 that the viscous drag penalty should be mainly contributed by form drag.

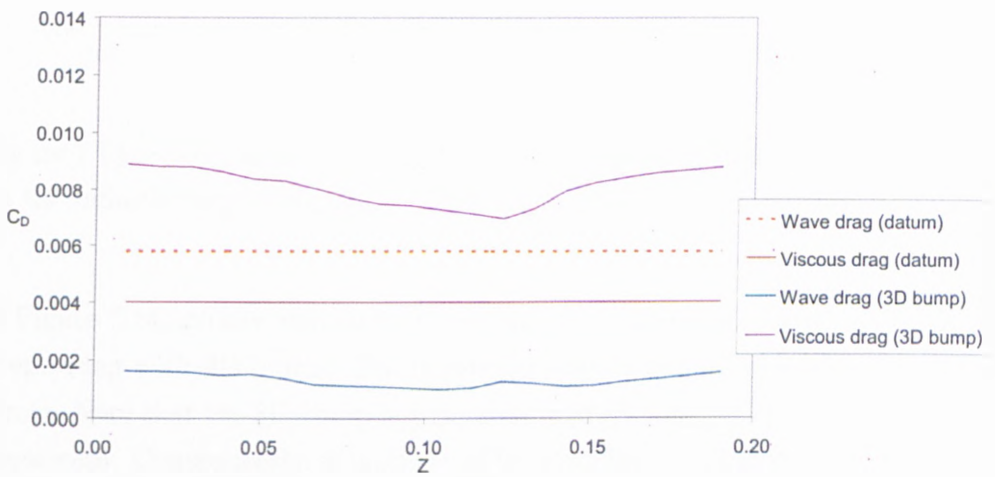


Figure 7.12: Spanwise wave and viscous drag distribution of the optimised 3D bump generated on the infinite swept wing, $M_\infty = 0.85$, $C_L = 0.32$.

In conjunction with Table 7.2, Figure 7.12 presents the variations of the wave drag and viscous drag across the span of the wing. Besides the significant reduction of wave drag across the whole span, it is accompanied by an increase of viscous drag. As discussed early, this should be contributed by the form drag. The other Figure 7.13 shows the variations of the deduced form drag, where the penalty occurs away from the crest of the 3D bump. However, this increase of form drag for this particular case could very much due to the fairly strong lower-surface shock wave. Bear in mind that the spanwise variation of drag components shown here are forces contributed from both the upper and lower surface. The strengthening of this shock due to a lower incidence explains a possible thicker boundary layer at the lower surface. Consequently, the reduction of form drag due to 3D bump is very much offset by the increase of the form drag on the lower surface.

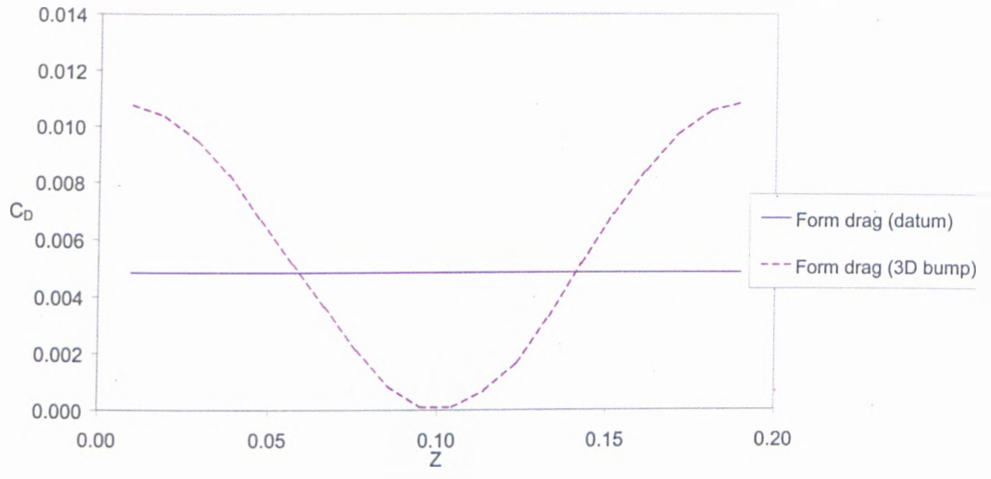


Figure 7.13: Spanwise form drag distribution of the optimised 3D bump generated on the infinite swept wing, $M_\infty = 0.85$, $C_L = 0.32$.

In Figure 7.14, surface skin friction lines are plotted on the surface of the infinite swept wing with 3D bump. The freestream direction is illustrated here with an arrow. Note that the 3D bump is generated in alignment with the direction of the freestream. Consequently, it is observed here in Figure 7.14 that due to the sweep angle, the 3D bump is slightly misaligned with the local surface streamlines. This phenomena also explains the increase of the form drag.

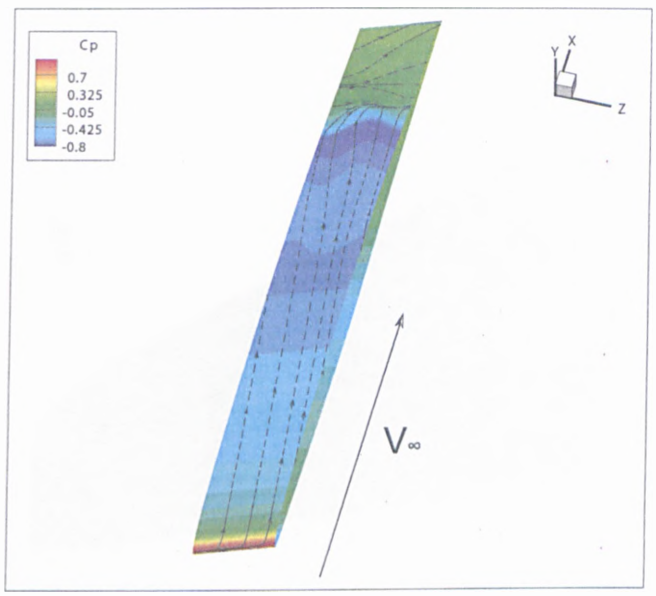


Figure 7.14: Surface skin friction lines of the optimised 3D bump generated on the infinite swept wing, $M_\infty = 0.85$, $C_L = 0.32$.

## 7.2 3D Bumps on a Three-dimensional Transonic Swept Wing

Several options were considered on transforming the optimised 3D bump designs from the previous section to a three-dimensional transonic wing. The first logical approach is to place a finite number of 3D bumps that would cover the regions with strong shock wave. Each individual size, including height and width, are scaled by the chord length of the wing section having the centre of the subsequent bumps. The position of the bump crests are placed linearly along the span and parallel to the trailing edge since the variation of the shock wave locations is minimal for most of the spanwise locations and approximately linear and parallel to the TE as shown in the planform view of the wing surface pressure, Figure 7.15. However, a number of numerical experiments suggest that scaling the bump sizes according to local wing section does not work particularly well in terms of performance. Also note that all the flow solutions for the three-dimensional transonic wing are computed under the same freestream conditions as that of the infinite swept wing described in the previous section.

As a result, the size of all the bumps are instead predetermined and assumed to

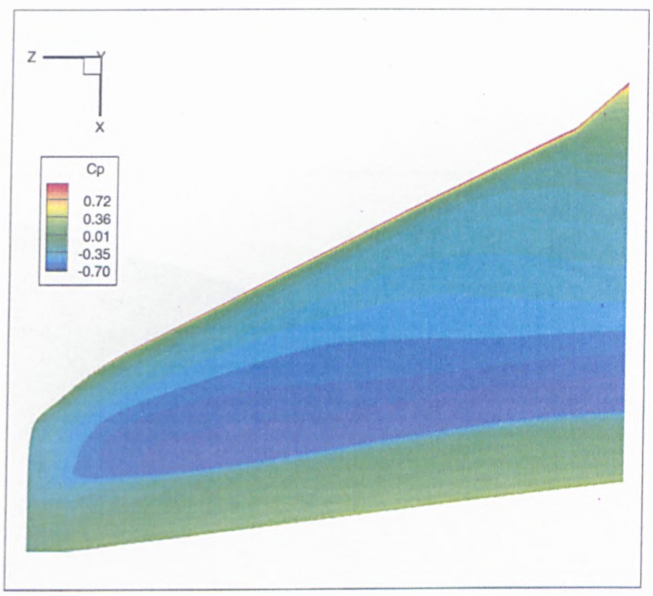


Figure 7.15: Planform view of the surface pressure contours of the 3D swept wing.

be the same and scaled by the chord length of the mid-span wing section, which is the section where the constant aerofoil section for the infinite swept wing has been extracted. The bumps are still positioned parallel to the TE accordingly. A closeup on the array of 3D bumps generated on the wing is shown in Figure 7.16. Numerical calculations have shown that this approach gives a better result than the previous ones.

In addition, it has also been experimented to obtain the minimal total number of three-dimensional bumps that can be placed on the transonic wing that will maintain the same level of performance. This is useful to minimise the spanwise resolution required to resolve the three-dimensional bump shapes on the wing, thus cutting down the computing time and improving the convergence of the flow solution. The end results indicate that a total number of 13 bumps, which will only cover around three quarters of the wingspan, achieve the same improvement as that of 17 bumps that cover almost the whole wingspan. This might be due to the slight misplacement of the bumps near the wing tip. The size of the bump could be a main factor too. Nonetheless, the obtained improvement in lift-drag ratio is around 14%.

In Table 7.3, the breakdown of the drag components from both the datum wing

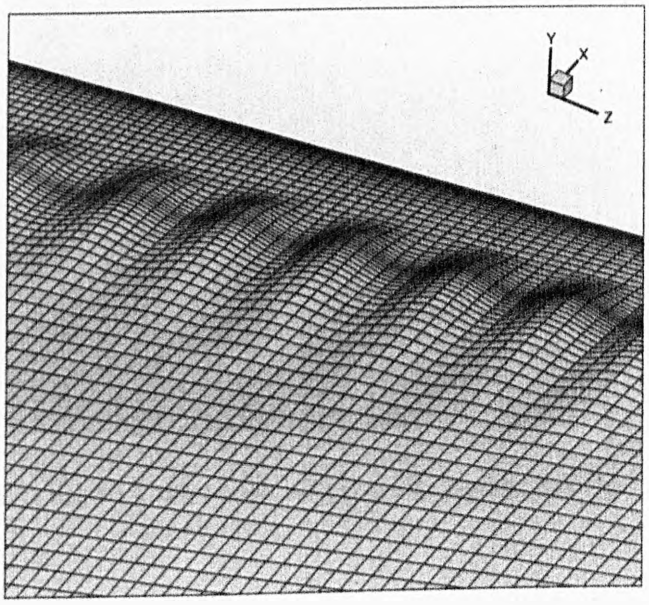


Figure 7.16: Closeup on the array of the 3D bumps generated on the 3D swept wing.

| | $C_L$ | $C_{Dtotal}$ | $C_{Dpressure}$ | $C_{Dfriction}$ | $C_{Dwave}$ |
|---|---|---|---|---|---|
| **Datum wing** | 0.2068 | 0.02068 | 0.01249 | 0.008120 | 0.004302 |
| ***3D bumps*** | *0.2217* | *0.01939* | *0.01110* | *0.008292* | *0.001701* |

Table 7.3: Comparisons of drag components for the wing with and without 3D bumps.

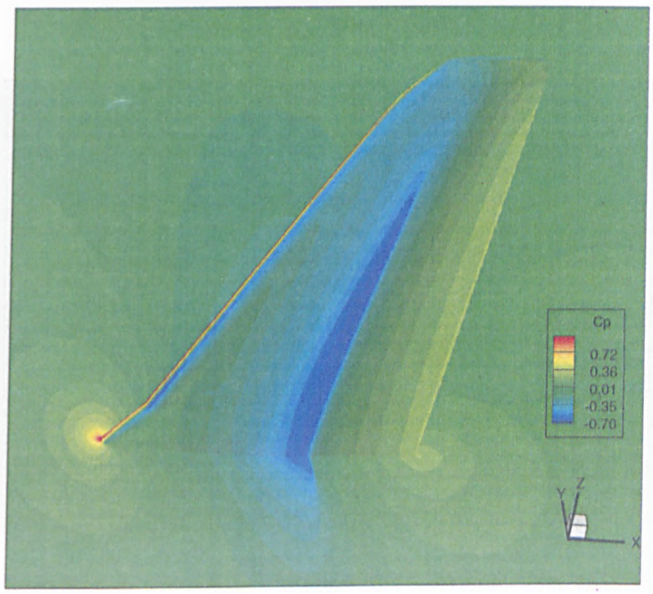


Figure 7.17: View of the shock wave on the pressure side of the wing.

and the wing with three-dimensional bumps are compared. From this table, the lift coefficient is not matched specifically due to the existence of another fairly strong shock wave on the pressure side of the wing, which is shown in Figure 7.17. Decreasing the incidence will then strengthen this shock wave, hence compensating the improvement incurred. There is a slight increase in skin friction drag of 2 drag counts, but the penalty is relatively small compared to the reduction achieved in pressure drag or wave drag.

Figure 7.18 (a) & (b) compare the pressure contours of both the datum wing and the one with bumps. It is observed that the presence of the bumps has smeared the strong normal shock into a $\lambda$-shock structure, thus significantly weakening the shock strength. The effects are reflected in the comparisons of the streamwise pressure distribution plots of Figures 7.19, 7.20 & 7.21, for both cases at three different spanwise stations. A properly placed 3D bump would lead to a pressure distribution plot similar to that of station z = 1.53m (Figure 7.20) that is along the centre of a bump at the mid-span wing section. If plotted slightly away from this bump at z = 1.42m (Figure 7.19), the pressure distribution plot is quite similar to that at the center, which indicates that the effects of the bump on the shock wave have propagated to the region even where local contour changes are minimal. Figure 7.21 depicts the pressure distribution plot near the bump that is

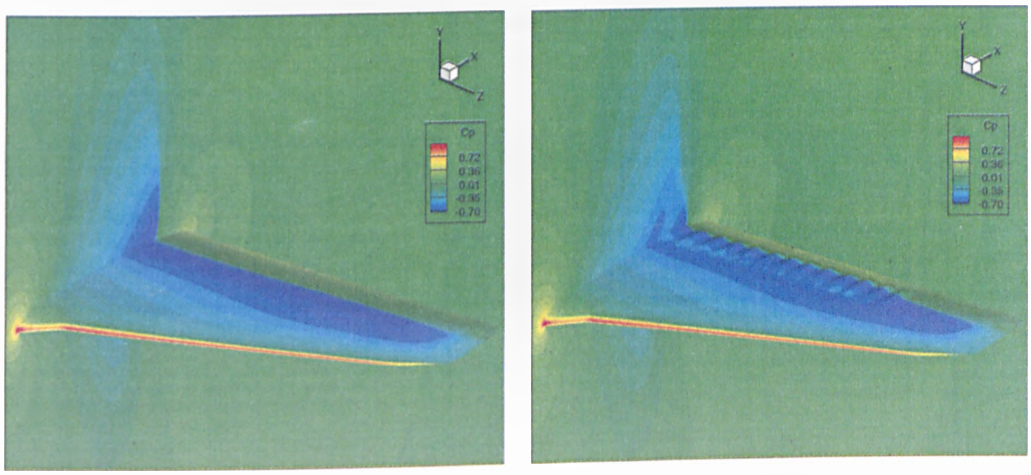


Figure 7.18: (a) Pressure contours of the datum case. (b) Pressure contours of the wing with 3D bumps.

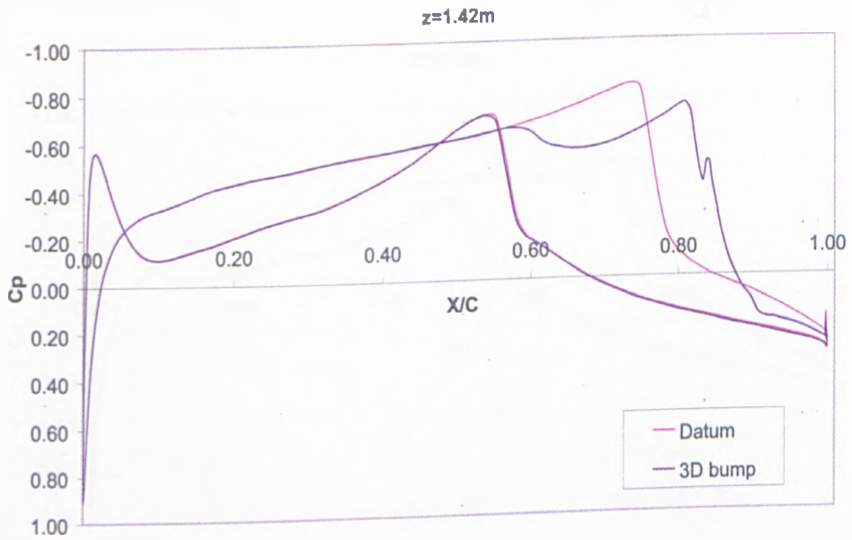


Figure 7.19: Streamwise pressure distribution plot at z = 1.42m on 3D swept wing.

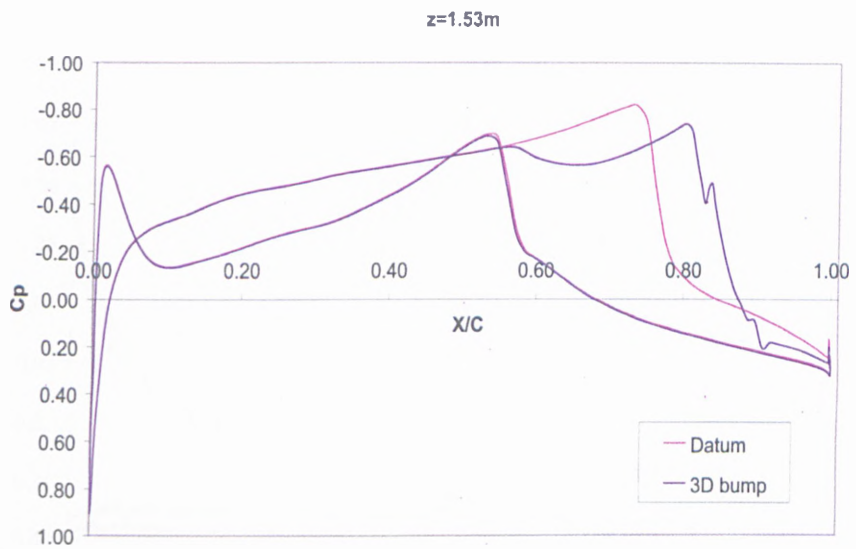


Figure 7.20: Streamwise pressure distribution plot at z = 1.53m on 3D swept wing.

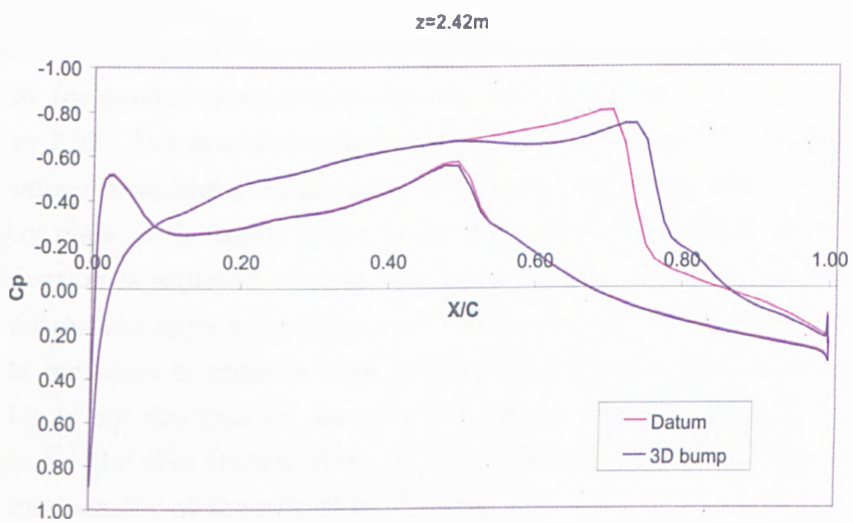


Figure 7.21: Streamwise pressure distribution plot at z = 2.42m on 3D swept wing.

positioned further away from the symmetry plane at z = 2.42m, and suggesting that the bump is still at the right place.

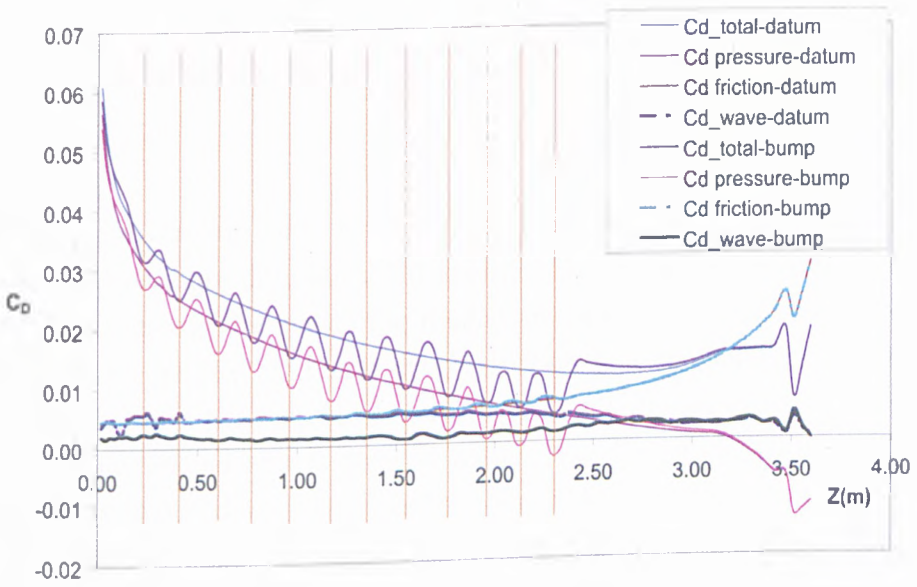


Figure 7.22: Variations of drag components along the wingspan.

Variations of the drag components along the wingspan are extracted from both near-field (or surface integration) method and the far-field method, are shown in Figure 7.22. The orange straight vertical lines represent the position of each bump centres including a halved-size bump at z = 0m, where its centre is at the symmetry plane. It is clearly shown from the total drag plots that the maximum drag reduction is achieved close to the bump centres. However, away from the bump centres and approaching the area without any contour modifications, there are slight increases in pressure drag as compared with the datum line. Interestingly, this is not the case for the two last bumps situated between z = 2 and 2.3m. as for the skin friction drag, a closer examination shows that there is a minor drag penalty at the side of the bumps.

Furthermore, there are slight oscillations or "spikes" on the computed wave drag for the datum wing in the region between z = 0 and 0.4m. This could well be the increase in spurious drag contribution since the skewness of the grid in three-dimensions is more significant than that of a relatively simple two-dimensional

aerofoil grid. Nevertheless, overall, the predicted wave drag for the datum wing is around 20 drag counts higher than that of the wing with bumps. The variation of wave drag with respect to the wingspan in both cases is approximately negligible, again suggesting that the three-dimensional nature of the bumps still impose a largely two-dimensional effect on the inviscid flow field. Beyond z = 2.5m, where there are no bumps deployed, the two wave drag lines eventually intersect with each other, signifying minimal or no wave drag reduction in this region.

An observation one can make from the plot is the oscillatory nature of the total drag and the pressure drag along the span for the bump control case. However the skin friction and the wave drag remain smooth. This is an indication that the mechanism for the 3D bump drag reduction is a combination of the wave drag reduction and the form drag reduction. While the wave drag reduction is more two dimensional and inviscid in nature, the form drag reduction is very three dimensional and viscous in nature. The maximum form drag reduction is achieved near the mid span of the bump but a slight increase in the form drag is implied near the middle between the two bumps. However the span average of the form drag is certainly reduced because of the bump as the overall drag reduction is greater than that provided by the wave drag reduction.

### 7.2.1 Some Practical Implications on Aircraft Performance

This subsection will provide some brief analysis and discussion about the impact of the 3D bumps on aircraft performance and some practical implication from there. If the aircraft were cruising at a constant lift-drag ratio, the Breguet's range equation is written as [97, 98]:

$$r = -\frac{V L/D}{g \quad sfc} \times ln\left(\frac{w_{end}}{w_{start}}\right) \tag{7.1}$$

where $r$ is the range of the aircraft, $g$ is the gravitational acceleration constant, $sfc$ is the specific fuel consumption from the engines and $w_{end}$ and $w_{start}$ are the total aircraft weight at the start and end of the cruise respectively.

From this Eqn. (7.1), it is obvious that the range is directly proportional to the lift-drag ratio of the aircraft. Take the preceding case of a 3D transonic wing with an array of 3D bumps as an example. If the 12% improvement of $L/D$ is

achievable on a full aircraft configuration, it implies a significant extended range for the same $sfc$.

Nonetheless, the effects of the improvement and the additional structural weight with 3D bumps on fuel consumption can also be assessed via Eqn. (7.1). Define $m_{bump}$ as the mass of the added 3D bumps on the aircraft, $(L/D)_{new}$ as the improved lift-drag ratio and $\Delta m_f$ as the change of fuel carried onboard at the start of the cruise. For the same range as the aircraft with 3D bumps cruising at the same speed and that the $sfc$ of the engine remains the same, Eqn. (7.1) can then be re-written as

$$r = -\frac{V(L/D)_{new}}{g \quad sfc} \times ln\left(\frac{m_{end} + m_{bump}}{m_{start} + m_{bump} + \Delta m_f}\right) \tag{7.2}$$

Therefore, by combining Eqn. (7.1) and (7.2), the equation is reduced to

$$\left(\frac{m_{end}}{m_{start}}\right) = \left(\frac{m_{end} + m_{bump}}{m_{start} + m_{bump} + \Delta m_f}\right)^{\varepsilon} \tag{7.3}$$

With further manipulations, Eqn. (7.4) can be expressed as

$$\Delta m_f = -\left[\left(\frac{\xi^{1/\varepsilon} m_{start} - m_{end}}{\xi^{1/\varepsilon}}\right) - \left(\frac{1 - \xi^{1/\varepsilon}}{\xi^{1/\varepsilon}}\right) m_{bump}\right] \tag{7.4}$$

where $\xi$ is defined as the mass ratio $\frac{m_{end}}{m_{start}}$ and $\varepsilon$ is the ratio of the new $(L/D)$ to the old $(L/D)$, e.g. 1.12 or 12% higher than the old setup. Here, the unknowns are $m_{bump}$ and $\Delta m_f$ and note that the negative sign indicates that it is a reduction as long as $m_{bump}$ is not too large. Now let us construct a possible scenario of an aircraft (an A380 without 3D bumps) weighing 560 tonnes at the start of the cruise with 251 tonnes of fuel on board. At the end of the flight, assume there must be at least 38.6 tonnes of fuel held in reserve for emergency. Therefore, $m_{start} = 560$ tonnes and $m_{end} = 347.6$. In addition, assume that the added array of 3D bumps have a rough estimated weight of 2 tonnes and that $\varepsilon = 1.12$ or a 12% improvement in lift-drag ratio, the reduced fuel required onboard is worked out to be about 27 tonnes, which implies a significant increase in payload or a much reduced operation cost.

## 7.3 Combined Optimisation of a BWB Shape with 3D Bumps

### 7.3.1 Introduction

The recent surge in oil prices has stimulated further interest in non-conventional aircraft designs such as the Blended-Wing-Body (BWB) for future air transportation [99, 100, 101]. Conceptually, the main aerodynamic advantages of the new BWB design come from its lower wetted area to volume ratio and lower interference drag as compared to conventional aircraft. Investigations by Qin *et al.* [102] have demonstrated the importance of span loading distribution for BWB performance. By an inverse design method, the mean of an elliptic and a triangular span load distribution was shown to provide better aerodynamic performance than that from an elliptic load distribution for the BWB geometry at Mach 0.85. However, the benefits of a BWB configuration can only be fully explored through further careful and detailed aerodynamic shape design and optimisation including multi-disciplinary interaction with structures and flight dynamics. Aerodynamic optimisation of a BWB shape involves hundreds of design variables and constraints but with a relatively much smaller number of objective functions. Le Moigne and Qin [83, 103] carried out shape optimisation of the BWB for a given planform by employing an efficient adjoint-based optimisation methodology. The obtained optimised shape has resulted in significant drag reduction from the baseline configuration. The optimised shape has also been used within the European MOB project [104] on Multidisciplinary Optimization of a Blended Wing Body aircraft. Nonetheless, it still exhibits relatively strong shock waves on the outer wing and the winglet on the aircraft with their associated wave drag.

Provided with the effectiveness of 3D shock control bumps as presented in the preceding chapters, it is therefore interesting to explore whether a BWB shape incorporating an array of 3D shock control bumps could lead to further improvement in BWB aerodynamic performance. Consequently, we need to include both the BWB shape defined by the aerofoils profiles at a series of *master* sections and an array of 3D bumps on the upper surface of the outer wing in the BWB shape parameterisation for design optimisation. This study also demonstrates that efficient parallelisation of the components of the optimisation chain (Figure 4.1), particularly the parallelisation of the adjoint solver as presented in *Section*

*4.3.5*, is essential to enable the optimisation of such a large-scale problem feasible. Thus, Figure 4.1 is re-drawn as Figure 7.23, which indicates that the flow solver, the adjoint solver and also the grid updater are parallelised. Optimisation results that have been carried out on the national high performance computing facility HPCx are presented and discussed regarding the improvement of the BWB aerodynamic performance.

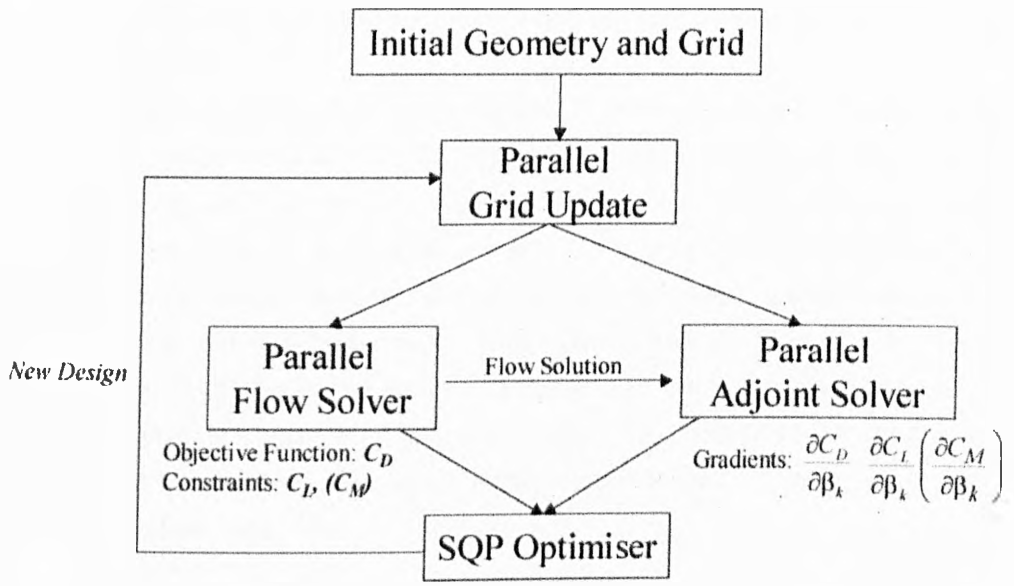


Figure 7.23: Parallelised optimisation chain.

### 7.3.2 BWB Surface Parameterisation

As already presented in *Section 5.6.1*, a Bézier-Bernstein parameterisation is employed to represent the aerofoil shape of the wing master sections. This is then extended to three dimensions to represent a wing or in this study, the BWB shape. The BWB is divided into a series of master sections. Across the fuselage or main body, the master sections are connected via a cubic spline in the spanwise direction for a smooth transition from one master section to the next. As for the master sections throughout the outer wing and the winglet, they are connected linearly as the planform has linear leading and trailing edges. Each of these master sections deforms according to the two-dimensional parameterisation presented earlier. Note that the twist angles of the winglet master sections are also design parameters for optimisation.

### 7.3.3 Optimisation Results

The result presented here is an Euler optimisation of the BWB shape with winglets and a series of 3D bumps installed on the upper surface of the outer wing. The cruise condition is at a freestream Mach number of 0.85. The design $C_L$ is 0.41 based on the trapezoidal reference wing area of 842 $m^2$. The objective of the optimisation task is to minimise the total drag whilst maintaining the lift at the target design condition and also satisfying the volume constraints.

The BWB is divided into 34 master sections, 4 at the fuselage that are connected via a cubic spline expression in the spanwise direction. The rest are located at the outer wing and the winglet, which are connected linearly. Recall that all the master sections are parameterised with 16 active Bézier parameters and a twist-increment design variable, except for the two most outboard sections on the outer wing and winglet junction. These two master sections are only allowed with changes in twist without shape deformation to avoid complexity in the connection between the outer wing and the winglet. As a result, including the design variables for the thirteen 3D bumps, there are a total of 657 design variables for this optimisation task.

In addition to the lift constraint, the internal volumes of the 34 master sections, excluding the presence of the bumps, are constrained. The same strategy discussed in *Section 5.6.3* has been adopted here such that the possible existence of a 3D bump over a master section would not lead to thinning of the internal volume of that section. As a result, the internal volumes constraint stated above will only take the volume defined by the aerofoil section geometry itself into account, excluding the possible additional volume imposed by the 3D bump. In order to resolve the geometry of the 3D bumps in both the chordwise and spanwise directions, a high-fidelity grid that is generated for this problem has a resolution of 236 × 33 × 288 or around 2.2 million points. Consequently, this optimisation task involving a large number of flow and its adjoint solutions can only be run on large high performance computing facilities such as the UK national HPCx in Daresbury. In addition, the grid is decomposed into 128 size-balanced blocks, which is to be run on the 128-processor queue on HPCx. The generated multi-block grid is shown in Figure 7.24. Additionally, Figure 7.25 presents a clearer view of the distribution strategy of the grid resolution on the surface.

Figure 7.26 shows the progression of the objective function, i.e. the drag coefficient with respect to the major design cycles. Due to the limitation of the maximum allowable computing time on a 128-processor queue on HPCx, the 19 design cycles shown in Figure 7.26 were not carried out in one run but in a few runs. The optimisation converges after 19 design cycles when the SQP optimiser has indicated that an optimised solution has been found. Note that each improved design is a feasible design satisfying the constraints as we have adopted a feasible optimisation strategy.

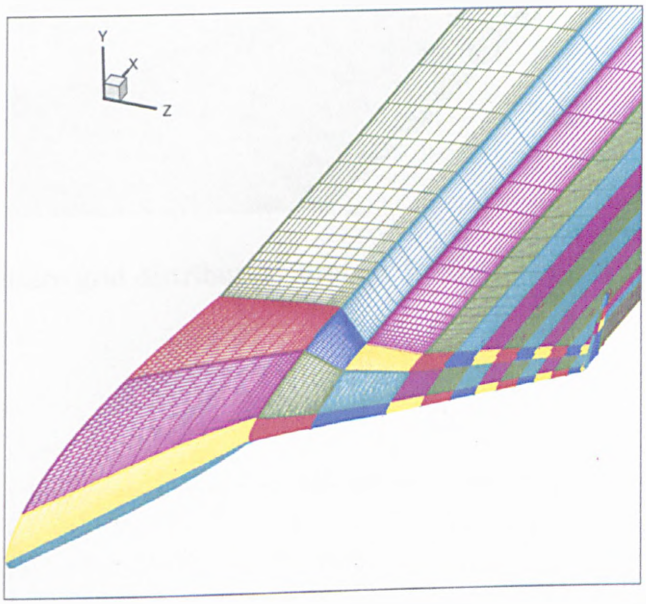


Figure 7.24: The generated 128-block grid for the BWB with 3D bumps case.

Table 7.4 compares the aerodynamic coefficients of the optimised BWB shape with 3D bumps. First of all, it should be noted that in Refs. [103, 105], the calculated drag coefficient for the baseline configuration is different from the present calculations. This discrepancy is due to the fact that the resolution of the high-fidelity Euler grid (around 100 thousands points) employed in Refs. [103, 105] is much lower than the resolution of the current high-fidelity Euler grid, which has over 2 million points. As stated earlier, this level of resolution is required to resolve the shapes of the 3D bumps. As shown in Table 7.4, the optimised design has provided a significant drag reduction of 30% or around 47 drag counts from the baseline configuration. Since in this optimisation problem, the pitching moment is not considered as a constraint, hence it has slightly increased. When

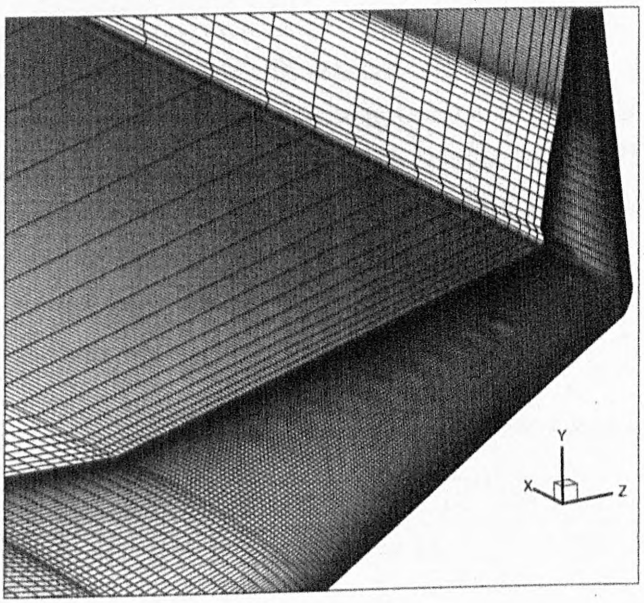


Figure 7.25: Surface grid distribution strategy for the BWB with 3D bumps case.

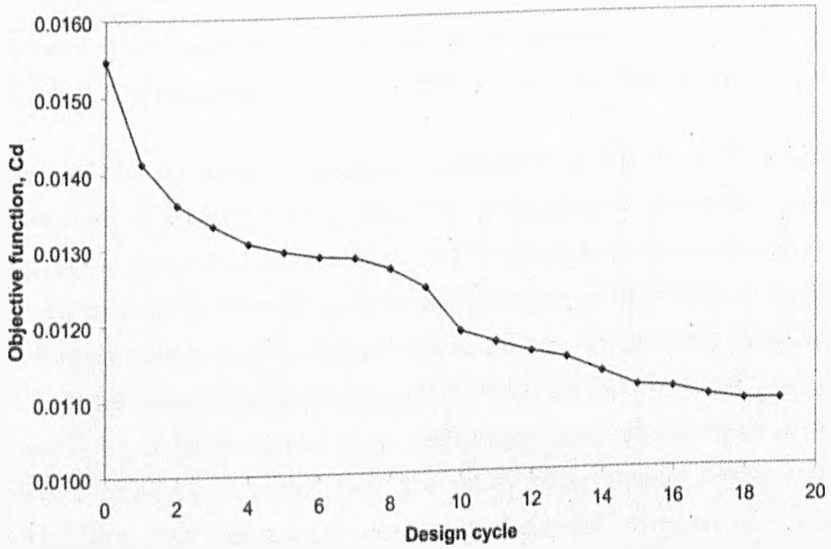


Figure 7.26: Convergence history of the objective function for the BWB+3D bump case.

the 3D bumps are taken away manually from the optimised wing shape, calculations indicate that the drag increases by around 1 drag count. Therefore, the improvement from the 3D bumps still accounts for around 1% of the total drag. This could still be significant for a large wing-body configuration like this BWB. Additionally, it should also be noted that the heights for the 3D bumps at the winglet are limited to a certain height due to possible grid quality degradation when the height is over certain limit. Therefore, this approach should have some impact on the overall performance of the 3D bumps, since the shock remains fairly strong at the winglet.

| | $C_L$ | $C_D$ | L/D | $C_M$ |
|---|---|---|---|---|
| Baseline (present high-fidelity grid) | 0.4112 | 0.01554 | 26.46 | 0.09715 |
| ***Present optimised BWB + 3D bumps*** | *0.4115* | *0.01088* | *37.82* | *0.12301* |
| ***Present optimised BWB* (3D bumps manually removed)** | *0.4111* | *0.01099* | *37.41* | *0.12223* |
| *Optimised BWB with $C_M$ constraint* (Refs. [103, 105]) | *0.4113* | *0.01222* | *33.66* | *0.14330* |
| *Optimised BWB with no $C_M$ constraint* (Refs. [103, 105]) | *0.4114* | *0.01272* | *32.34* | *0.02178* |

Table 7.4: Comparisons of performance for the BWB+3Dbumps.

Comparison of the contours of pressure coefficient in Figure 7.27 indicates that the improvement is largely coming from the reduction of the wave drag. On the outer wing, some beneficial effects from the 3D bumps can be seen. Strong shock waves that formed on the blending area and fuselage of the baseline configuration have been largely eliminated in the optimised design. These effects are highlighted in Figure 7.28 by comparing the computed shock structures from both cases. It can be observed that there is still some remaining weak shock wave on the outer wing, which is more pronounced near the outer wing-winglet intersection. This is due to the fact that the master section at the outer wing-winglet connection is not subjected to shape deformation but just twist increment. In addition, the initial strong normal shock on the winglet has been significantly weakened.

The size of several 3D bumps has decreased due to a weaker shock wave, particularly at places inboard of the wing. On the other hand, the optimiser produces

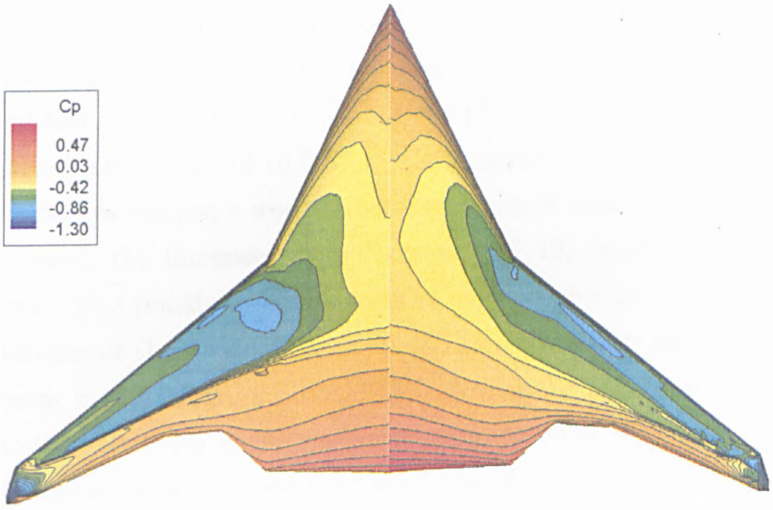


Figure 7.27: Pressure contours. Left–baseline configuration; Right–optimised design.

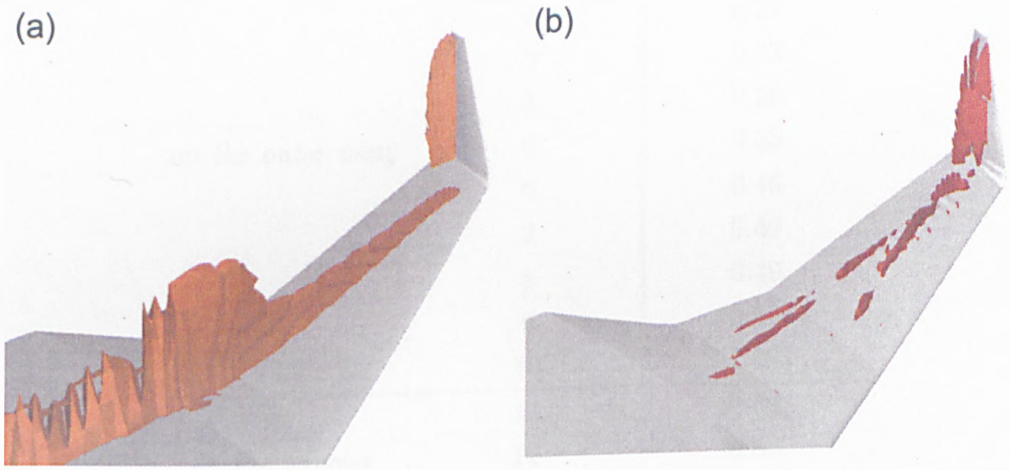


Figure 7.28: Shock structure. (a) baseline configuration; (b) optimised design.

larger-sized 3D bumps that are located towards the outboard of the outer wing and at the winglet, where the remaining shock waves are still relatively strong. The varying heights of the 3D bumps are listed in Table 7.5. Note that the 3D bump numbered 1 is positioned closer to the inboard and the 3D bumps with increasing numbers (up to number 10) are positioned progressively towards the outboard. The last three bumps (11 $\sim$ 13) are placed on the winglet. All the 3D bumps started with a height of 0.6%c. Once again, the reduced heights for most of the 3D bumps suggest a weak remaining shock in that region of the wing. On the other hand, the increased ones (bumps 9 $\sim$ 13) imply a fairly strong remaining shock. The position of the crests of each 3D bump varies between 5 to 7%c downstream of the original shock wave. The chordwise length of the 3D bumps all remain in the range of 35 to 36%c. As for the bump width, changes are not apparent as well, where the values lie close to 15%c with variations less than 0.2%c. It should be noted that the bump tips of the consecutive 3D bumps are very close to each other, therefore, the bump width more or less represents the spacing between the centreline of consecutive 3D bumps as well. Figure 7.29 presents the close-up view of a number of 3D bumps on the surface of the outer wing.

| | **3D bump No.** | **Height, y/c%** |
|---|---|---|
| *on the outer wing* | 1 | 0.33 |
| | 2 | 0.21 |
| | 3 | 0.23 |
| | 4 | 0.26 |
| | 5 | 0.35 |
| | 6 | 0.46 |
| | 7 | 0.49 |
| | 8 | 0.49 |
| | 9 | 0.63 |
| | 10 | 1.09 |
| *on the winglet* | 11 | 0.89 |
| | 12 | 0.89 |
| | 13 | 0.88 |

Table 7.5: List of 3D bump heights on the BWB.

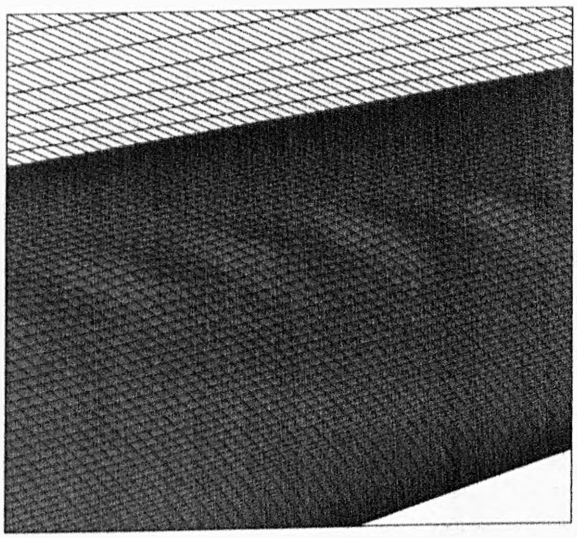

Figure 7.29: Close-up view of the 3D bumps on the BWB.

The preceding discussions are based on inviscid Euler calculations. If the viscous effects were taken into account, the shock strength will be weakened and hence displaced slightly upstream as compared to the inviscid case. Consequently, the position of the 3D bumps can be adjusted upstream with response to the displaced original shock wave such that the relative positions between the original shock wave and bump crests are maintained similar. Additionally, due to the weakened shock wave and viscous effects, it is also necessary to lower the height of the 3D bumps.

The improvements on the winglet are shown more clearly in Figure 7.30. The pressure contour near to the root of the winglet is less clustered than before in the optimised design, implying a much-weakened shock wave. As a result, a weaker shock wave of the winglet is now reflected at the outboard of the outer wing. However, due to the limitation of shape deformation at the winglet tip, the strongest shock wave remains there.

The shape at a section near to the main body and a section close to the outboard of the outer wing with some profound changes are displayed in Figure 7.31. The obtained improvements in aerodynamic performance are significant even though the shape changes are relatively small. Figure 7.32 shows the shape changes at the winglet. In addition to the significant shape changes, it is also indicated that

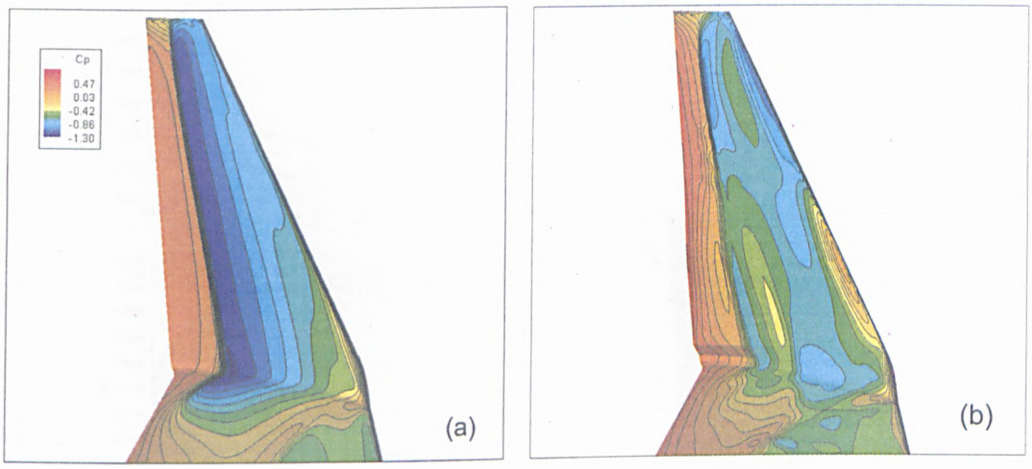


Figure 7.30: Pressure contours on winglet. (a) baseline configuration; (b) optimised design.

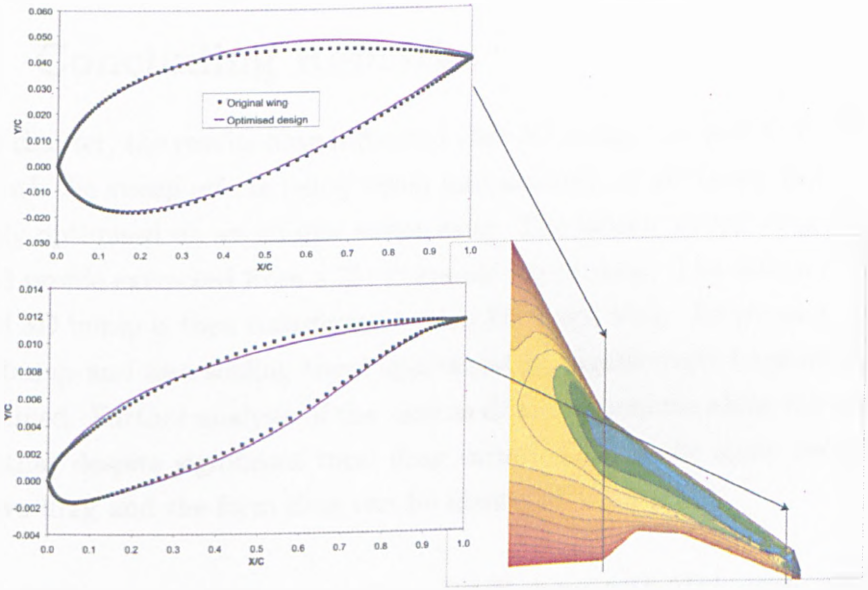


Figure 7.31: Profiles changes on the wing.

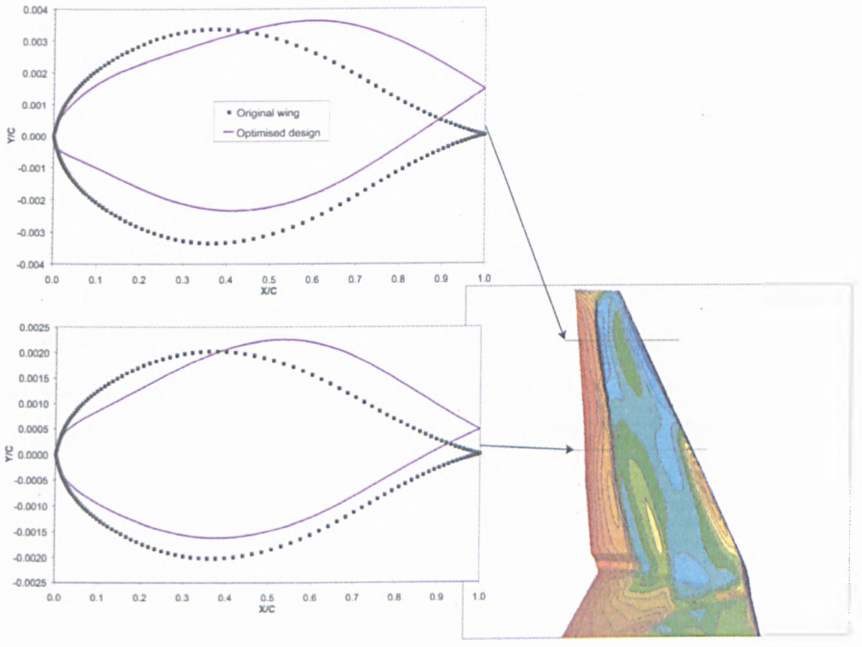


Figure 7.32: Profiles changes on the winglet.

the winglet tip has been twisted slightly outwards.

## 7.4 Concluding Remarks

In this chapter, the results have indicated that 3D bumps can still work efficiently even with the sweep effects being taken into account. A 3D bump has been successfully optimised on an infinite swept wing. The infinite swept wing adopts an aerofoil profile extracted from a 3D transonic swept wing. The design of this optimised 3D bump is then transferred to this 3D swept wing. By placing the array of 3D bump and also scaling them appropriately, significantly improvement can be obtained. Further analysis of the various drag components along the wingspan reveal that despite significant total drag variation along the span, reduction in the wave drag and the form drag can be identified.

The results from the optimisation of the BWB shape with 3D bumps, which also includes optimising the winglet profiles, have demonstrated that the parallelised optimisation setup is able to work on large-scale aerodynamic problems efficiently. The optimised design has shown some interesting improvement on the outer wing

and the winglet with ~30% drag reduction being achieved for the given fixed planform design as compared to the baseline configuration. The designs of the 3D bumps vary across the outer wing and winglet, which indicate the strength of the remaining shock at the region. For example, the 3D bumps placed near the outboard of the outer wing and at the winglet have significantly larger heights since the remaining shock is still strong at these locations. The optimisation has modified the design of the winglet aerofoil sections substantially due to the much lower local mean sweep angle. The tip of the winglet is slightly twisted outwards. However, the strongest shock remains on the inside of the winglet, which can be relieved by introducing some trailing edge sweep for the winglet.

# Chapter 8

# Conclusions

The potential of the 3D bump as an effective wave drag reduction device has been investigated in detail regarding the operational range in comparison with 2D bumps. Before carrying out the numerical investigations and optimisations on 3D bumps, the solutions of the transonic flow over a 3D ramp bump have been validated with experimental data. The comparison between the numerical solutions and the experiments are satisfactory, from which we gain some insight into the flow physics. It shows that careful matching of the simulation with the experiment conditions is crucial.

The flow solver and the adjoint solver have been parallelised using MPI. The calculations of the sensitivity derivatives could be a bottleneck during optimisation when the number of design variables is very large. Therefore, it is important to parallelise both the computation and the data for the sensitivity calculations including grid sensitivity.

Both the 2D and 3D bumps are optimised on unswept wings with an NLF aerofoil section or a transonic turbulent aerofoil section. The performance of the 2D and 3D bumps optimised at one particular design is quite similar. It shows that the maximum cross-sectional area of the 3D bump is close to that of the 2D bump for similar level of optimised performance in drag reduction. By placing the bump crest slightly downstream of the original normal shock, the bump weakens the shock by compressing the upstream supersonic flow. The position of the shock is also moved slightly downstream near to the bump crest and, hence, lift is enhanced. The wing can then achieve the target lift condition at a lowered incidence. Thus, the drag reduction mechanism of the bumps includes both weakening the shock through upstream compression and changing the effective

camber of the wing for lift enhancement.

The drag polars indicate that the performance of the 3D bump is better than the 2D bump at lower lift off-design conditions. In addition to the flowfield visualisations, analyses of the streamwise cross-sectional area across the wing including both the 2D and 3D bumps indicate some relatively steeper gradient change in area variations for the 2D bump, which assist in the explanation of the performance discrepancy between the bumps. The performance advantage the 3D bump has over the 2D bump is however more apparent on the NLF wing as compared to that on the turbulent wing. The implemented far-field drag method allows us to extract wave drag accurately. The wave drag analyses show that the bumps reduce both the wave and the form drag but with only a small skin friction penalty, which is negligible. A number of design points have been tested using the derived low-order geometrical model for the 3D bump. It is demonstrated that the low-order designed 3D bumps have satisfactory performance without further optimisation.

The 3D bumps are also effective in reducing the wave drag when being employed on an infinite swept wing and on a three-dimensional swept wing. The strengthening of the lower-surface shock and a slight misalignment of the 3D bump with the local surface streamlines explain the increase of form drag on the infinite swept wing with the 3D bump. The assessment of the improvement impact of the 3D bumps on an aircraft performance suggests that longer range or increased payload can be obtained provided that the additional weight of the 3D bumps imposed on the aircraft is not too high.

The combined shape with bump optimisation based on the RAE 2822 turbulent aerofoil and on the BWB aircraft shows that at a design point, especially at high transonic Mach number, fairly strong shocks can still remain on the upper-surface of the wing; and by employing 2D or 3D bumps, further drag reduction can be obtained. The combined optimisation of the BWB aircraft with 3D bumps demonstrates the feasibility of carrying out a very large aerodynamic optimisation task with over 600 design variables.

## 8.1 Future Work

The main objectives as presented in *Section 1.5* are then fulfilled with some interesting findings discussed in the previous section. Nonetheless, future work is suggested here to take the investigations further. It is proposed to investigate the effects of placing an array of 3D bumps on the DLR F6 wing. The wing has been widely investigated in the AIAA Drag Prediction Workshop 2 & 3. Thus, grid generation and validation studies should be first carried out based on the large amount of data available from these workshops, which further validate the drag prediction ability of the current numerical tools. From there, we can either manually design the array of 3D bumps or carry out a full Navier-Stokes optimisation of 3D bumps including the wing aerofoil sections and the sweep angle. Multi-disciplinary optimisation, such as fluid-structure interaction, could also be carried out. By taking the structural integrity of the configurations and the wave drag reduction capability of the 3D bumps into account, we might be able to design a wing with low sweep angle.

# Appendix A

# The Flux Vectors from the Navier-Stokes Equations

The convective and diffusive terms from the inviscid and viscous contributions are written as:

$$\mathbf{F}^i = \begin{bmatrix} \rho u \\ \rho u^2 + p \\ \rho uv \\ \rho uw \\ u(\rho E + p) \end{bmatrix} \quad \mathbf{F}^v = \begin{bmatrix} 0 \\ \tau_{xx} \\ \tau_{xy} \\ \tau_{xz} \\ u\tau_{xx} + v\tau_{xy} + w\tau_{xz} - q_x \end{bmatrix}$$

$$\mathbf{G}^i = \begin{bmatrix} \rho v \\ \rho vu \\ \rho v^2 + p \\ \rho vw \\ v(\rho E + p) \end{bmatrix} \quad \mathbf{G}^v = \begin{bmatrix} 0 \\ \tau_{yx} \\ \tau_{yy} \\ \tau_{yz} \\ u\tau_{yx} + v\tau_{yy} + w\tau_{yz} - q_y \end{bmatrix} \tag{A.1}$$

$$\mathbf{H}^i = \begin{bmatrix} \rho w \\ \rho wu \\ \rho wv \\ \rho w^2 + p \\ w(\rho E + p) \end{bmatrix} \quad \mathbf{H}^v = \begin{bmatrix} 0 \\ \tau_{zx} \\ \tau_{zy} \\ \tau_{zz} \\ u\tau_{zx} + v\tau_{zy} + w\tau_{zz} - q_z \end{bmatrix}$$

or with the additional two variables from the turbulence model, they are re-written as:

$$
\mathbf{F}^i = \begin{bmatrix} \rho u \\ \rho u^2 + p \\ \rho uv \\ \rho uw \\ u(\rho E + p) \\ \rho uk \\ \rho u\omega \end{bmatrix} \quad \mathbf{F}^v = \begin{bmatrix} 0 \\ \tau_{xx} \\ \tau_{xy} \\ \tau_{xz} \\ u\tau_{xx} + v\tau_{xy} + w\tau_{xz} - q_x \\ (\mu + \frac{\mu_t}{\sigma_k})\frac{\partial k}{\partial x} \\ (\mu + \frac{\mu_t}{\sigma_\omega})\frac{\partial \omega}{\partial x} \end{bmatrix}
$$

$$
\mathbf{G}^i = \begin{bmatrix} \rho v \\ \rho vu \\ \rho v^2 + p \\ \rho vw \\ v(\rho E + p) \\ \rho vk \\ \rho v\omega \end{bmatrix} \quad \mathbf{G}^v = \begin{bmatrix} 0 \\ \tau_{yx} \\ \tau_{yy} \\ \tau_{yz} \\ u\tau_{yx} + v\tau_{yy} + w\tau_{yz} - q_y \\ (\mu + \frac{\mu_t}{\sigma_k})\frac{\partial k}{\partial y} \\ (\mu + \frac{\mu_t}{\sigma_\omega})\frac{\partial \omega}{\partial y} \end{bmatrix} \tag{A.2}
$$

$$
\mathbf{H}^i = \begin{bmatrix} \rho w \\ \rho wu \\ \rho wv \\ \rho w^2 + p \\ w(\rho E + p) \\ \rho wk \\ \rho w\omega \end{bmatrix} \quad \mathbf{H}^v = \begin{bmatrix} 0 \\ \tau_{zx} \\ \tau_{zy} \\ \tau_{zz} \\ u\tau_{zx} + v\tau_{zy} + w\tau_{zz} - q_z \\ (\mu + \frac{\mu_t}{\sigma_k})\frac{\partial k}{\partial z} \\ (\mu + \frac{\mu_t}{\sigma_\omega})\frac{\partial \omega}{\partial z} \end{bmatrix}
$$

where $\tau$ is the stress tensor, $q$ is the heat flux vector, $\mu$ and $\mu_t$ are the molecular and turbulent (or eddy) viscosities respectively. $\sigma_k$ & $\sigma_\omega$ are constants from the turbulence modelling. The stress tensor $\tau$, is the sum of molecular stress and the Reynolds stress, defined as:

$$
\tau_{ij} = 2(\mu + \mu_t)S_{ij} + \lambda \frac{\partial u_k}{\partial x_k}\delta_{ij} - \frac{2}{3}\rho k \delta_{ij} \tag{A.3}
$$

with the strain-rate

$$
S_{ij} = \frac{1}{2}\left(\frac{\partial u_i}{\partial x_j} + \frac{\partial u_j}{\partial x_i}\right),
$$

$\lambda$ as the second coefficient of viscosity

$$
\lambda = -\frac{2}{3}\mu
$$

and the Kronecker symbol $\delta_{ij}$.

# Appendix B

# Osher's Flux Formulae

| Conditions | $u_0 - a_0 \geq 0$<br>$u_0 + a_0 \geq 0$ | $u_0 - a_0 \geq 0$<br>$u_0 + a_0 \leq 0$ | $u_0 - a_0 \leq 0$<br>$u_0 - a_0 \leq 0$ | $u_0 - a_0 \leq 0$<br>$u_0 - a_0 \leq 0$ |
|---|---|---|---|---|
| $u^* \geq 0$<br>$u^* - a_{1/3} \geq 0$ | $\mathbf{F}(\mathbf{Q}_0)$ | $\mathbf{F}(\mathbf{Q}_0) - \mathbf{F}(\mathbf{Q}_{S1})$<br>$-\mathbf{F}(\mathbf{Q}_{S1})$ | $\mathbf{F}(\mathbf{Q}_{S0})$ | $\mathbf{F}(\mathbf{Q}_{S0}) - \mathbf{F}(\mathbf{Q}_{S1})$<br>$+\mathbf{F}(\mathbf{Q}_1)$ |
| $u^* \geq 0$<br>$u^* - a_{1/3} \leq 0$ | $\mathbf{F}(\mathbf{Q}_0) - \mathbf{F}(\mathbf{Q}_{S0})$<br>$+\mathbf{F}(\mathbf{Q}_{1/3})$ | $\mathbf{F}(\mathbf{Q}_0) - \mathbf{F}(\mathbf{Q}_{S0})$<br>$+\mathbf{F}(\mathbf{Q}_{1/3}) - \mathbf{F}(\mathbf{Q}_{S1})$<br>$+\mathbf{F}(\mathbf{Q}_1)$ | $\mathbf{F}(\mathbf{Q}_{1/3})$ | $\mathbf{F}(\mathbf{Q}_1) + \mathbf{F}(\mathbf{Q}_{1/3})$<br>$-\mathbf{F}(\mathbf{Q}_{S1})$ |
| $u^* \leq 0$<br>$u^* - a_{2/3} \geq 0$ | $\mathbf{F}(\mathbf{Q}_0) - \mathbf{F}(\mathbf{Q}_{S0})$<br>$+\mathbf{F}(\mathbf{Q}_{2/3})$ | $\mathbf{F}(\mathbf{Q}_0) - \mathbf{F}(\mathbf{Q}_{S0})$<br>$+\mathbf{F}(\mathbf{Q}_{2/3}) - \mathbf{F}(\mathbf{Q}_{S1})$<br>$+\mathbf{F}(\mathbf{Q}_1)$ | $\mathbf{F}(\mathbf{Q}_{2/3})$ | $\mathbf{F}(\mathbf{Q}_{2/3}) + \mathbf{F}(\mathbf{Q}_{S1})$<br>$-\mathbf{F}(\mathbf{Q}_1)$ |
| $u^* \leq 0$<br>$u^* + a_{2/3} \leq 0$ | $\mathbf{F}(\mathbf{Q}_0) - \mathbf{F}(\mathbf{Q}_{S0})$<br>$+\mathbf{F}(\mathbf{Q}_{S1})$ | $\mathbf{F}(\mathbf{Q}_0) - \mathbf{F}(\mathbf{Q}_{S0})$<br>$+\mathbf{F}(\mathbf{Q}_1)$ | $\mathbf{F}(\mathbf{Q}_{S1})$ | $\mathbf{F}(\mathbf{Q}_1)$ |

Table B.1: Osher's flux formulae for $\mathbf{F}(\mathbf{Q}_L, \mathbf{Q}_R)$. Note: $\mathbf{Q}_L \equiv \mathbf{Q}_0$ & $\mathbf{Q}_R \equiv \mathbf{Q}_1$.

# Appendix C

# Boundary Conditions

## C.1 Inviscid Wall

When the viscous effects are excluded and hence the inviscid Euler equations are solved, the slip boundary condition is to be applied at the boundary of a physical solid surface or a wall. For example, let $\overline{U}$ denotes the velocity component normal to the wall and $\overline{V}$ & $\overline{W}$ denote the other two velocity components parallel to the wall. It should be noted that these are just referential velocity components to the wall and should not be mixed up with the conserved velocity components, $u$, $v$ & $w$. Therefore, in the halo cells, where the subscript numbers denote the respective halo cells numbering as shown in Figure 2.4,

$$\begin{aligned} \rho_1 &= \rho_2, \quad & \rho_0 &= \rho_3 \\ \overline{U}_1 &= -\overline{U}_2, \quad & \overline{U}_0 &= -\overline{U}_3 \\ \overline{V}_1 &= \overline{V}_2, \quad & \overline{V}_0 &= \overline{V}_3 \\ \overline{W}_1 &= \overline{W}_2, \quad & \overline{W}_0 &= \overline{W}_3 \\ p_1 &= p_2, \quad & p_0 &= p_3 \end{aligned} \tag{C.1}$$

Since the flow properties are stored at the cell centres, the above treatment will ensure that the normal velocity component is canceled out and hence zero at the wall. The two velocity components parallel to the wall are not canceled out, hence making it a slip boundary condition.

## C.2 Viscous Wall

In contrast to the inviscid wall boundary condition, with the viscous effects of the flow taken into account, a no-slip boundary condition has to be applied at the wall. Thus, the flow properties in the halo cells are treated as follow:

$$\begin{aligned} \rho_1 &= \rho_2, \quad \rho_0 = \rho_3 \\ u_1 &= -u_2, \quad u_0 = -u_3 \\ v_1 &= -v_2, \quad v_0 = -v_3 \\ w_1 &= -w_2, \quad w_0 = -w_3 \\ p_1 &= p_2, \quad p_0 = p_3 \end{aligned} \tag{C.2}$$

Hence, the total velocity at the wall is zero and that the conditions are directly applied to the Cartesian velocity components, $u$, $v$ & $w$. Furthermore, if the flow is turbulent, for the zero-equation algebraic models, the turbulent viscosity is just needed in one halo cell, so

$$(\mu_t)_1 = -(\mu_t)_2$$

or for the two-equation $k$-$\omega$ turbulence model, the turbulence kinetic energy is treated as below,

$$k_1 = -k_2, \quad k_0 = -k_3$$

and a Menters formula is employed to fix the specific dissipation rate $\omega$ at the wall,

$$\omega_1 = \frac{60\mu_1}{\rho_1 C_{\omega 2} \delta y^2}, \quad \omega_0 = \frac{60\mu_3}{\rho_3 C_{\omega 2} \delta y^2}$$

where $C_{\omega 2}$ is a specified constant and $\delta y$ is the distance of the first cell from the wall.

## C.3 Pole or Singularity

There are cases where one of the faces of a cell actually collapses to a singularity point or line. Although there are no halo cells created at this boundary, the values at the singularity are still updated using a linear extrapolation from the adjacent cells.

However, more precisely, the convective fluxes "through" the wall or the singularity are actually specified explicitly and hence do not rely on the halo cells values. This is done in order to obtain an accurate flux value that is independent of the accuracy of the application of the above three boundary conditions in the halo cells and also due to the fact that it is possible to get an explicit formulation for the wall or singularity flux. Especially for the singularity case, where there are no "faces" at this boundary, all the fluxes are then zero.

## C.4 Symmetry

This boundary condition has been exploited in a lot of aerodynamic problems, for example, a full 3D blended wing that can be halved into two symmetrical domains. It is then assumed that the flow properties in these two domains are also symmetric. Consequently, the symmetry boundary condition is applied at this boundary splitting the domains and hence only half of the problem is then needed to be solved, which as a result, halving the computational time as well.

The boundary condition treatment of the flow variables in the halo cells is essentially the same as that of the inviscid boundary condition (Eqn. (C.1)) but the physics is slightly different. This is achieved by extrapolating the geometric information of the halo cells at this boundary as the mirror image of that inside the domain. Unlike the inviscid wall case, where the halo cells geometries are extrapolated linearly. As for the turbulent viscosity, in order to maintain continuity of $\mu_t$ across the boundary,

$$(\mu_t)_1 = (\mu_t)_2$$

as well as for the two turbulence variables, they are given by,

$$k_1 = k_2, \; k_0 = k_3$$
$$\omega_1 = \omega_2, \; \omega_0 = \omega_3$$

## C.5 Interface

In MERLIN, each blocks are dealt with separately, at the block boundaries where it is adjacent to other blocks, the flow properties at the boundaries updated during each iteration needed to be exchanged between the adjacent blocks. The schematic diagram in Figure C.1 illustrates an example of this information exchange process between the blocks. As shown from this figure, the values in halo cells $kn + 1$ & $kn + 2$ from block 1 simply copy the information from cells 2 & 3 inside the domain of block 2 respectively and vice versa, as if they are inside a single domain. Note that the same treatment is applied to all the flow variables including the turbulence variables $\mu_t$, $k$ & $\omega$.

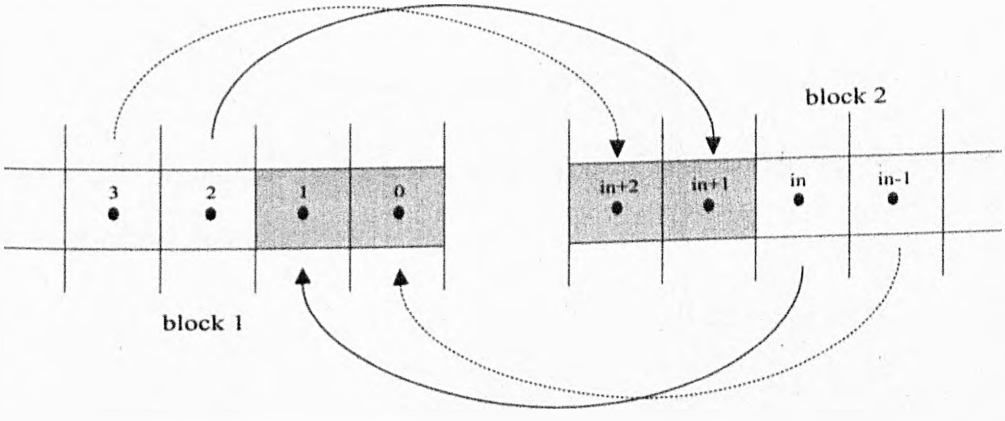


Figure C.1: Schematic diagram of the exchange of information between the blocks at an interface boundary.

## C.6 Periodical

This boundary treatment is applied when, say in a block with two boundaries at both ends in the $\zeta$-direction, the information going out at the boundary ad-

jacent to cell 2 actually goes back into the domain through the boundary at the other end that is adjacent to cell *kn* and vice versa. Therefore, the implementation of the periodical boundary condition is somewhat similar to that of the interface boundary condition. The treatment can be clarified further with another schematic diagram of this boundary condition in Figure C.2. So, it can be seen from the figure that the exchange of information between the corresponding boundaries are treated in a way as if they are actually adjacent to each other like the block interfaces.

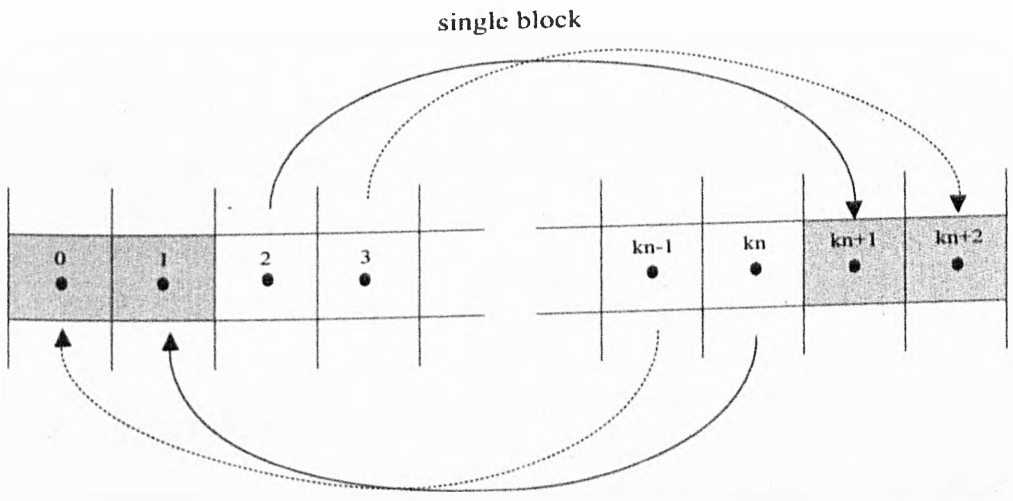


Figure C.2: Schematic diagram of the exchange of information for the halo cells at a periodical boundary.

## C.7 Supersonic Inflow

All the inflow and outflow boundary conditions are based on one-dimensional wave propagation theory. For the supersonic inflow case, all the information is coming into the domain from its exterior. Since the flow properties outside the domain are initialized with the freestream conditions, so the flow properties in the halo cells are set to the freestream values,

$$\rho_1 = \rho_\infty, \quad \rho_0 = \rho_\infty$$
$$u_1 = u_\infty, \quad u_0 = u_\infty$$
$$v_1 = v_\infty, \quad v_0 = v_\infty$$
$$w_1 = w_\infty, \quad w_0 = w_\infty$$
$$p_1 = p_\infty, \quad p_0 = p_\infty$$
$$k_1 = k_\infty, \quad k_0 = k_\infty$$
$$\omega_1 = \omega_\infty, \quad \omega_0 = \omega_\infty$$

The freestream flow is assumed to be turbulence free, thus, the turbulence viscosity needed for the algebraic turbulence models should be zero,

$$(\mu_t)_1 = 0$$

## C.8 Supersonic Outflow

As for the supersonic outflow case, all the information is instead leaving the domain into the exterior. In this work, the halo cells just copy the information from cell 2 that is inside the domain:

$$\rho_1 = \rho_2, \quad \rho_0 = \rho_2$$
$$u_1 = u_2, \quad u_0 = u_2$$
$$v_1 = v_2, \quad v_0 = v_2$$
$$w_1 = w_2, \quad w_0 = w_2$$
$$p_1 = p_2, \quad p_0 = p_2$$
$$k_1 = k_2, \quad k_0 = k_2$$
$$\omega_1 = \omega_2, \quad \omega_0 = \omega_2$$
$$(\mu_t)_1 = (\mu_t)_2$$

## C.9 Subsonic Outflow

The subsonic outflow conditions require that one of the conserved variables to be specified, while the rest of variables are linearly extrapolated at the outlet. In the results that will be presented in later chapter, pressure is chosen to be constant across the outlet and that a constant pressure is also assumed within the boundary layer. Therefore, the halo cells treatments are as follow:

$$\begin{aligned}
\rho_1 &= 2\rho_2 - \rho_3, \quad \rho_0 = 2\rho_1 - \rho_2 \\
u_1 &= 2u_2 - u_3, \quad u_0 = 2u_1 - u_2 \\
v_1 &= 2v_2 - v_3, \quad v_0 = 2v_1 - v_2 \\
w_1 &= 2w_2 - w_3, \quad w_0 = 2w_1 - w_2 \\
p_1 &= p_0 = \text{a specified value} \\
k_1 &= 2k_2 - \rho_3, \quad k_0 = 2k_1 - k_2 \\
\omega_1 &= 2\omega_2 - \omega_3, \quad \omega_0 = 2\omega_1 - \omega_2 \\
(\mu_t)_1 &= 2(\mu_t)_2 - (\mu_t)_3
\end{aligned}$$

## C.10 Far-field

This boundary condition is applied when it is not known in advance whether the flow state at the boundary is either inflow supersonic/subsonic or outflow supersonic/subsonic. This is achieved by using the Riemann invariants to determine the normal velocity $\overline{U}$, the speed of sound $a$ and the various flow properties at the boundary, which is denoted by the subscript $b$. Thus, the following criteria determine the appropriate boundary condition to apply,

If $|\overline{U}_b| \leq a_b$, the boundary is subsonic, else if $|\overline{U}_b| > a_b$, the boundary is then supersonic and,

- if $\overline{U}_b \geq 0$, then it is an outflow boundary,
- else if $\overline{U}_b < 0$, it is an inflow boundary.

# Appendix D

# Calculation of the Exact RHS Jacobian for the Adjoint Solver

Extensive details in this part of the adjoint solver, i.e. different cases at the boundaries that have to be dealt with in the calculation of the viscous laminar components and et cetera, are considered to be beyond the scope of this thesis and the details could be found in Ref. [74]. Thus, the author has taken the calculations of the exact RHS Jacobian at the periodical boundary as an example, since this is the one that the author has added into the solver.

## D.1 Higher-order Inviscid Components

The treatment of the RHS Jacobian at the periodical boundary is exactly the same as that of the interface boundary case. Therefore, the periodical boundaries which they are exchanging data with, are considered to be connected to each other like a typical interface boundary. The philosophy here is that everything should be as if inside the domain. Hence, in order to simplify the explanations, consider a one-dimensional problem as shown in Figure D.1.

The residual at cell $i$ is, in a more generalised form,

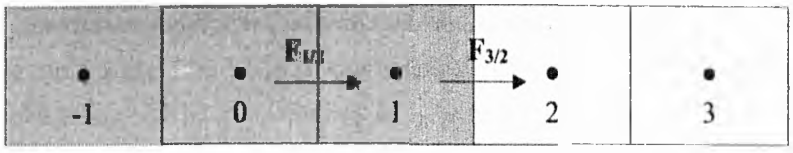


Figure D.1: One-dimensional problem at a periodical boundary.

$$\mathbf{R}_i = \mathbf{F}_{i+1/2} - \mathbf{F}_{i-1/2}$$

where $\mathbf{F}$ are the convective fluxes $\mathbf{F}^i$ from Eqn. (A.1). Hence, with the higher-order scheme, the Jacobians based on the residual are given as

$$\mathbf{C}_i \equiv \frac{\partial \mathbf{R}_i}{\partial \mathbf{P}_i} = \frac{\partial \mathbf{F}_{i+1/2}}{\partial \mathbf{P}_i} - \frac{\partial \mathbf{F}_{i-1/2}}{\partial \mathbf{P}_i} \tag{D.1}$$

$$\mathbf{S}_i \equiv \frac{\partial \mathbf{R}_i}{\partial \mathbf{P}_{i-1}} = \frac{\partial \mathbf{F}_{i+1/2}}{\partial \mathbf{P}_{i-1}} - \frac{\partial \mathbf{F}_{i-1/2}}{\partial \mathbf{P}_{i-1}} \tag{D.2}$$

$$\mathbf{SS}_i \equiv \frac{\partial \mathbf{R}_i}{\partial \mathbf{P}_{i-2}} = -\frac{\partial \mathbf{F}_{i-1/2}}{\partial \mathbf{P}_{i-2}} \tag{D.3}$$

$$\mathbf{N}_i \equiv \frac{\partial \mathbf{R}_i}{\partial \mathbf{P}_{i+1}} = \frac{\partial \mathbf{F}_{i+1/2}}{\partial \mathbf{P}_{i+1}} - \frac{\partial \mathbf{F}_{i-1/2}}{\partial \mathbf{P}_{i+1}} \tag{D.4}$$

$$\mathbf{NN}_i \equiv \frac{\partial \mathbf{R}_i}{\partial \mathbf{P}_{i+2}} = \frac{\partial \mathbf{F}_{i+1/2}}{\partial \mathbf{P}_{i+2}} \tag{D.5}$$

Since the higher-order MUSCL scheme has been used, a term such as that of $\frac{\partial \mathbf{F}_{i+1/2}}{\partial \mathbf{P}_i}$ shall involve the linearisation of both the Osher's Riemann solver and the MUSCL scheme. After all the Jacobians have been calculated, they can now be multiplied with the adjoint vector to form the term $\left[\frac{\partial \mathbf{R}(\mathbf{Q}^*)}{\partial \mathbf{P}}\right]^t \boldsymbol{\lambda}^n$ in Eqn. (4.11) with the following calculations, again, considering just the one-dimensional problem in Figure D.1:

$$\left[\frac{\partial \mathbf{R}(\mathbf{Q}^*)}{\partial \mathbf{P}}\right]^t \cdot \boldsymbol{\lambda}^n = \mathbf{rhs}_i$$
$$= \mathbf{C}_i^t \cdot \boldsymbol{\lambda}_i + \mathbf{N}_{i-1}^t \cdot \boldsymbol{\lambda}_{i-1} + \mathbf{NN}_{i-2}^t \cdot \boldsymbol{\lambda}_{i-2} + \mathbf{S}_{i+1}^t \cdot \boldsymbol{\lambda}_{i+1} + \mathbf{SS}_{i+2}^t \cdot \boldsymbol{\lambda}_{i+2} \tag{D.6}$$

Note that this RHS term has also been renamed as **rhs** for conveniences during future discussions. In the calculation of $\mathbf{rhs}_2$ as well as $\mathbf{rhs}_3$, since the Jacobian

terms are calculated as if they are inside the domain using Eqn. (D.1) to D.3, Figure D.1 then indicates that the calculation of the flux $\mathbf{F}_{1/2}$, which is inside the halo cells will require the value of $\mathbf{P}_{-1}$ which is outside the normal two halo cells. Thus, an additional third layer of halo cells has to be implemented in the adjoint solver for both interface and periodical boundaries. Nevertheless, in three-dimensions, Eqn. (D.6) will have to be expanded to include the contributions from other cells.

## D.2 Viscous Laminar Components

The periodical boundary is still taken as an example here and since the treatment is the same as the interface boundary, thus, the following details are also suitable for calculations inside the domain. The calculation of the diffusive fluxes contribution to the total residual at one cell actually depend upon the values of 19 cells surrounding it. Once again, for the ease of understanding, only the fluxes in the $i$ direction will be considered. Therefore, the residual now depends on 15 cells with 9 of them depicted in two dimensions in Figure D.2, and 6 others perpendicular to the plane.

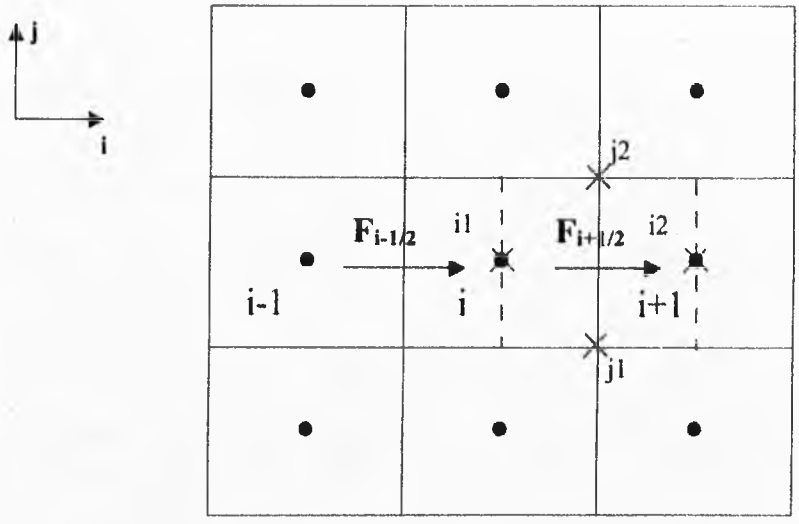


Figure D.2: One-dimensional problem at a periodical boundary for viscous laminar fluxes calculation.

Nevertheless, it should still be viewed in three dimensions since the evaluation of the values at the dual volume faces would require values from all three dimensions as shown earlier in Figure 2.3. If only the fluxes in the $i$-direction are considered, then the residual at cell $i$ is still

$$\mathbf{R}_i = \mathbf{F}_{i+1/2} - \mathbf{F}_{i-1/2}$$

Here, $\mathbf{F}_{i+1/2}$ and $\mathbf{F}_{i-1/2}$ are now the diffusive fluxes $\mathbf{F}^v$. The evaluation of the terms $\dfrac{\partial \mathbf{F}}{\partial \mathbf{P}}$ involves the linearisation of the dual volume method as presented in *Section 2.3.3.* Take the calculation of one of the terms, $\dfrac{\partial \mathbf{F}_{i+1/2}}{\partial \mathbf{P}_{i,j,k}}$ as an example,

$$\begin{aligned}
\frac{\partial \mathbf{F}_{i+1/2}}{\partial \mathbf{P}_{i,j,k}} &= \frac{\partial \mathbf{F}_{i+1/2}}{\partial \mathbf{P}_0}\frac{\partial \mathbf{P}_0}{\partial \mathbf{P}_{i,j,k}} + \frac{\partial \mathbf{F}_{i+1/2}}{\partial \mathbf{P}_{j1}}\frac{\partial \mathbf{P}_{j1}}{\partial \mathbf{P}_{i,j,k}} + \frac{\partial \mathbf{F}_{i+1/2}}{\partial \mathbf{P}_{j2}}\frac{\partial \mathbf{P}_{j2}}{\partial \mathbf{P}_{i,j,k}} + \frac{\partial \mathbf{F}_{i+1/2}}{\partial \mathbf{P}_{k1}}\frac{\partial \mathbf{P}_{k1}}{\partial \mathbf{P}_{i,j,k}} \\
&\quad + \frac{\partial \mathbf{F}_{i+1/2}}{\partial \mathbf{P}_{k2}}\frac{\partial \mathbf{P}_{k2}}{\partial \mathbf{P}_{i,j,k}} + \frac{\partial \mathbf{F}_{i+1/2}}{\partial \mathbf{P}_{i1}}\frac{\partial \mathbf{P}_{i1}}{\partial \mathbf{P}_{i,j,k}} \\
&= \frac{1}{2}\frac{\partial \mathbf{F}_{i+1/2}}{\partial \mathbf{P}_0} + \frac{1}{4}\left(\frac{\partial \mathbf{F}_{i+1/2}}{\partial \mathbf{P}_{j1}} + \frac{\partial \mathbf{F}_{i+1/2}}{\partial \mathbf{P}_{j2}} + \frac{\partial \mathbf{F}_{i+1/2}}{\partial \mathbf{P}_{k1}} + \frac{\partial \mathbf{F}_{i+1/2}}{\partial \mathbf{P}_{k2}}\right) + \frac{\partial \mathbf{F}_{i+1/2}}{\partial \mathbf{P}_{i1}}
\end{aligned}$$

The RHS vector are then calculated with the following expression, again, in just one direction,

$$\begin{aligned}
\mathbf{rhs}_{i,j,k} &= \frac{\partial \mathbf{R}_{i,j,k}}{\partial \mathbf{P}_{i,j,k}}^t \cdot \boldsymbol{\lambda}_{i,j,k} + \frac{\partial \mathbf{R}_{i-1,j,k}}{\partial \mathbf{P}_{i,j,k}}^t \cdot \boldsymbol{\lambda}_{i-1,j,k} + \frac{\partial \mathbf{R}_{i+1,j,k}}{\partial \mathbf{P}_{i,j,k}}^t \cdot \boldsymbol{\lambda}_{i+1,j,k} \\
&\quad + \frac{\partial \mathbf{R}_{i,j+1,k}}{\partial \mathbf{P}_{i,j,k}}^t \cdot \boldsymbol{\lambda}_{i,j+1,k} + \frac{\partial \mathbf{R}_{i-1,j+1,k}}{\partial \mathbf{P}_{i,j,k}}^t \cdot \boldsymbol{\lambda}_{i-1,j+1,k} + \frac{\partial \mathbf{R}_{i+1,j+1,k}}{\partial \mathbf{P}_{i,j,k}}^t \cdot \boldsymbol{\lambda}_{i+1,j+1,k} \\
&= \frac{\partial \mathbf{R}_{i,j-1,k}}{\partial \mathbf{P}_{i,j,k}}^t \cdot \boldsymbol{\lambda}_{i,j-1,k} + \frac{\partial \mathbf{R}_{i-1,j-1,k}}{\partial \mathbf{P}_{i,j,k}}^t \cdot \boldsymbol{\lambda}_{i-1,j-1,k} + \frac{\partial \mathbf{R}_{i+1,j-1,k}}{\partial \mathbf{P}_{i,j,k}}^t \cdot \boldsymbol{\lambda}_{i+1,j-1,k} \\
&\quad + \frac{\partial \mathbf{R}_{i,j,k+1}}{\partial \mathbf{P}_{i,j,k}}^t \cdot \boldsymbol{\lambda}_{i,j,k+1} + \frac{\partial \mathbf{R}_{i-1,j,k+1}}{\partial \mathbf{P}_{i,j,k}}^t \cdot \boldsymbol{\lambda}_{i-1,j,k+1} + \frac{\partial \mathbf{R}_{i+1,j,k+1}}{\partial \mathbf{P}_{i,j,k}}^t \cdot \boldsymbol{\lambda}_{i+1,j,k+1} \\
&\quad + \frac{\partial \mathbf{R}_{i,j,k-1}}{\partial \mathbf{P}_{i,j,k}}^t \cdot \boldsymbol{\lambda}_{i,j,k-1} + \frac{\partial \mathbf{R}_{i-1,j,k-1}}{\partial \mathbf{P}_{i,j,k}}^t \cdot \boldsymbol{\lambda}_{i-1,j,k-1} + \frac{\partial \mathbf{R}_{i+1,j,k-1}}{\partial \mathbf{P}_{i,j,k}}^t \cdot \boldsymbol{\lambda}_{i+1,j,k-1}
\end{aligned}$$

## D.3 Turbulent Components

Since the Baldwin-Lomax algebraic turbulence model is the only model that has been implemented in the adjoint solver, hence this subsection will only concern

the linearisation of the turbulent viscosity in this algebraic turbulence model.

As described in *Section 2.6.1*, the turbulent viscosity $\mu_t$ is calculated along rays and that the location of $F_{max}$ or $y_{max}$, which is required to determine the inner and outer turbulent viscosity regions, is not known in advance. Thus, when these positions are known, it is then possible to linearise $\mu_t$. By analysing the the description of the Baldwin-Lomax model, it can be shown that the turbulent viscosity potentially depends on 17 cells. As a result, 17 terms of $\frac{\partial(\mu_t)_{i,j,k}}{\partial \mathbf{P}_l}$ have to be calculated for each cells. This is just a straightforward differentiation of the way the turbulent viscosity is calculated in *Section 2.6.1*. However, in the calculation of the outer turbulent viscosity, maximum and minimum functions have been used and they are non-differentiable. Therefore, several approximations have to be made.

If the maximum function is smooth, hence the derivative of the maximum is assumed to be equal to the derivative of the function at the maximum point,

$$\frac{\partial F_{max}}{\partial \mathbf{P}_l} \approx \left.\frac{\partial F}{\partial \mathbf{P}_l}\right|_{j=j_{maxF}}$$

However, this assumption did not work particularly well on the minimum function used in the calculation of $F_{wake}$ (Eqn. (2.32)). The solution proposed was to always calculate $F_{wake}$ as follows

$$F_{wake} = y_{max} F_{max}$$

It was found that this assumption provided better accuracy in the calculation of the sensitivity derivatives than the minimum function did. For consistency, this modification was also included into the flow solver MERLIN.

The details presented above are what have been done inside the domain. At the periodical and interface boundary, since the value of turbulent viscosity $\mu_t$ in the halo cells is taken from the neighbouring blocks where it was calculated. Thus, it can still be taken as if $\mu_t$ was calculated along $j$ rays inside the halo cells. This will be always be the case at least within the investigations in this project, where the $j$-boundary will never be a periodical or interface boundary.

# Appendix E

# Descriptions of the SQP Optimiser

In the SQP optimisation method, the search direction $\mathbf{S}^q$ is found by solving an optimisation subproblem with from the neighbouring blocks where it was calculated. Thus, it can and a linear approximation of the constraints. Defining $\widetilde{F}$ as the approximated objective function, the subproblem that needs to be solved is

$$\begin{array}{lll} \text{Minimise} & \widetilde{F}(\mathbf{S}) = F(\boldsymbol{\beta}^q) + \nabla F(\boldsymbol{\beta}^q)^t \cdot \mathbf{S} + \frac{1}{2}\mathbf{S}^t\mathbf{H}^q\mathbf{S} & \\ \mathbf{s} & & \\ \text{Subject to:} & \nabla g_i(\boldsymbol{\beta}^q)^t \cdot \mathbf{S} + \delta_i g_i(\boldsymbol{\beta}^q) \leq 0 & i = 1, l \\ & \nabla h_j(\boldsymbol{\beta}^q)^t \cdot \mathbf{S} + \bar{\delta}_i h_j(\boldsymbol{\beta}^q) = 0 & j = 1, m \end{array} \tag{E.1}$$

with further reference to the original optimisation problem 4.14. Here, the design variables are now the components of $\mathbf{S}$ and the optimum found is the required search direction $\mathbf{S}^q$. The matrix $\mathbf{H}^q$ is a positive definite matrix that is initially the identity matrix. It is updated during the optimisation to approximate the Hessian matrix of the Lagrangian function of problem 4.14. The other parameters $\delta_i$ and $\bar{\delta}_i$ are within the interval $[0, 1]$, are used to prevent the linearisation of the constraints to create an inconsistent problem.

Once the search direction $\mathbf{S}^q$ has been found, a one-dimensional search for $\alpha^q$ needs to be conducted, which is also often referred as a line search. A simple quadratic polynomial interpolation is usually used to find the optimal $\alpha^q$. In

order to ensure the satisfaction of the constraints, the one-dimensional search employed a penalty function as defined below:

$$\Phi(\boldsymbol{\beta}^q) = F(\boldsymbol{\beta}^q) + \sum_{i=1}^{l} \mu_i max[0, g_i(\boldsymbol{\beta}^q)] + \sum_{j=1}^{m} \mu_{l+j} |h_j(\boldsymbol{\beta}^q)|$$

where the $\mu_i$ are based on the value of the Lagrange multipliers obtained during the resolution of the approximate quadratic problem for the search direction.

Once the optimal $\alpha^q$ has been acquired, the design is updated as usual using Eqn. (4.15). However, before starting a new iteration, the approximate of the Hessian matrix $\mathbf{H}^q$ has to be updated as well. One of the formulae widely employed in this case is the Broydon-Fletcher-Goldfarb-Shanno (BFGS) update formula modified by Powell:

$$\mathbf{H}^{q+1} = \mathbf{H}^q - \frac{\mathbf{H}^q \mathbf{p} \mathbf{p} \mathbf{H}^q}{\mathbf{p}^t \mathbf{H}^q \mathbf{p}} + \frac{\boldsymbol{\eta} \boldsymbol{\eta}^t}{\boldsymbol{\eta}^t \mathbf{p}} \tag{E.2}$$

where

$$\begin{aligned} \mathbf{p} &= \boldsymbol{\beta}^{q+1} - \boldsymbol{\beta}^q \\ \boldsymbol{\eta} &= \theta \mathbf{y} + (1-\theta)\mathbf{H}^q \mathbf{p} \\ \mathbf{y} &= \nabla_{\boldsymbol{\beta}} L(\boldsymbol{\beta}^{q+1}, \boldsymbol{\lambda}^q) - \nabla_{\boldsymbol{\beta}} L(\boldsymbol{\beta}^q, \boldsymbol{\lambda}^q) \end{aligned}$$

with the Lagrangian function

$$L(\boldsymbol{\beta}, \boldsymbol{\lambda}) = F(\boldsymbol{\beta}) + \sum_{i=1}^{l} \lambda_i g_i(\boldsymbol{\beta}) + \sum_{j=1}^{m} \lambda_{l+j} h_j(\boldsymbol{\beta})$$

and

$$\theta = \begin{cases} 1, & \text{if } \mathbf{p}^t \cdot \mathbf{y} \geq 0.2 \mathbf{p}^t \mathbf{H}^q \mathbf{p}; \\ \dfrac{0.8 \mathbf{p}^t \mathbf{H}^q \mathbf{p}}{\mathbf{p}^t \mathbf{H}^q \mathbf{p} - \mathbf{p}^t \cdot \mathbf{y}}, & \text{if } \mathbf{p}^t \cdot \mathbf{y} < 0.2 \mathbf{p}^t \mathbf{H}^q \mathbf{p}. \end{cases}$$

As a result, the positive definiteness of $\mathbf{H}^q$ is maintained.

# Bibliography


[1] European aeronautics: A vision for 2020, January 2001. Last accessed URL-http://ec.europa.eu/research/growth/aeronautics2020/pdf/aeronautics2020_en.pdf.

[2] G. Schrauf. Status and perspectives of laminar flow. CEAS/KATnet Aerospace Conference, Bremen, June 2005.

[3] J. Reneaux. Overview on drag reduction technologies for civil transport aircraft. European Congress on Computational Methods in Applied Sciences And Engineering, ECCOMAS, July 2004.

[4] R. Henke. A320 HLF fin flight tests completed. *Air & Space Europe*, 2:76–79, 1999.

[5] J. Maestrati and Ch. Bulgubure. Laminar flow for business jets : Falcon 900 HLFC demonstrator. $2^{nd}$ European Forum on Laminar Flow Technology, Bordeaux, France, June 1996.

[6] K. H. Horstmann, G. Schrauf, D. M. Sawyers, and H. Sturm. A simplified suction system for an HLFC leading edge box of an A320 fin. CEAS Aerospace Aerodynamics Research Conference, London, June 2003.

[7] G. Schrauf and K. H. Horstmann. Simplified hybrid laminar flow control. European Congress on Computational Methods in Applied Sciences and Engineering, ECCOMAS, July 2004.

[8] D. Arnal. Boundary layer transition : Prediction, application to drag reduction. Special Course on Skin Friction Drag Reduction, AGARD Report 786, 1992.

[9] J. Reneaux and A. Blanchard. The design and testing of an airfoil with hybrid laminar flow control. First European Forum on Laminar Flow Technology, Hamburg, Germany, March 1992.

[10] D. M. Bushnell. Aircraft drag reduction–a review. *Journal of Aerospace Engineering*, 217, 2002.

[11] E. Stanewsky. Adaptive wing and flow control. *Progress in Aerospace Sciences*, 37:583–667, 2001.

[12] J.N. Hefner and D.M. Bushnell. Viscous drag reduction via surface mass injection. *Progress in Astronautics and Aeronautics*, 123, 1990.

[13] J. Kim. Active control of turbulent boundary layers for drag reduction. IUTAM Symposium on Mechanics of Passive and Active Control, Göttingen, Kluwer Academic Publishers, September 1999.

[14] M. Walsh and J. Riblets. Viscous drag reduction in boundary layers. *Progress in Astronautics and Aeronautics*, 123, 1990.

[15] E. Coustols and V. Schmitt. Synthesis of experimental riblet studies in transonic conditions. Kluwer Academic Publishers, 1990.

[16] J. P. Robert. Drag reduction : An industrial challenge. AGARD Report 786, 1992.

[17] J. D. Anderson Jr. *Fundamentals of Aerodynamics.* McGraw-Hill International Editions, $2^{nd}$ edition, 1991.

[18] D. Destarac. Far-field / near field drag balance and applications of drag extraction in cfd. VKI Lecture Series 2003, CFD-based aircraft drag prediction and reduction, 2003.

[19] R. Grenon and P. Bourdin. Numerical study of unconventional wing tip devices for lift-induced drag reduction. Cambridge, 2002. CEAS Aerospace Aerodynamics Research Conference.

[20] *M-DAW, Modelling and Design of Advanced Wing Tip Devices.* European 5th Framework G4RD-CT-2002-00837, October 2002.

[21] A. Mann. The M-DAW project, modelling and design of advanced wing tip devices. Bremen, June 2005. CEAS/KATnet Aerospace Conference.

[22] S. Barakat and Eberhard Elsholz. CFD analysis on different wing-tip devices. Bremen, June 2005. CEAS/KATnet Aerospace Conference.

[23] D. M. Bushnell. Shock wave drag reduction. *Annual Review Of Fluid Mechanics*, 36:81–96, 2004.

[24] R. H. Barnard and D. R. Philpott. *Aircraft flight : A description of the physical principles of aircraft flight.* Harlow : Prentice Hall, $3^{nd}$ edition, 2004.

[25] E. Stanewsky, J. Delery, J. Fulker, and P. deMatteis. Drag reduction by shock and boundary layer control, results of the project EUROSHOCK II. *Notes on Numerical Fluid Mechanics and Multidisciplinary Design*, 80, 2001.

[26] S. T. Shaw, D. A. Perigo, and N. Qin. A computational study of shock control using spoilers; contract report for DERA. *Technical report.* Cranfield University, 2001.

[27] J. L. Fulker and M. J. Simmons. An experimental study of shock control methods DRA/AS/HWA/TR94007/1. *Technical report.* DERA, February 1994.

[28] E. Stanewsky, J. Delery, J. Fulker, and W. Geissler. EUROSHOCK-drag reduction by passive shock control. *Notes on Numerical Fluid Mechanics*, 56, 1997.

[29] R. Bur, R. Benay, B. Corbel, and J. Délery. Physical study of shock-wave/boundary-layer interaction control in transonic flow. AIAA-2000-0933. $38^{th}$ Aerospace Sciences Meeting & Exhibit, Reno, Nevada, 2000.

[30] Y. P. Zhu. *Computational Study of Shock Control at Transonic Speed.* PhD thesis, Cranfield University, Cranfield College of Aeronautics, 2000.

[31] N. Qin, Y. Zhu, and S. T. Shaw. Numerical study of active shock control for transonic aerodynamics. *International Journal of Numerical Methods for Heat and Fluid Flow*, 14:444–466, 2004.

[32] J. S. Couldrick, S. L.Gai, J. F. Milthorpe, and K. Shankar. Swept shock wave/turbulent boundary layer interaction control with "smart" flap actuators. AIAA-2002-973. $38^{th}$ Aerospace Sciences Meeting & Exhibit, Reno, Nevada, January 2002.

[33] J. S. Couldrick, S. L. Gai, H. A. Holden, H. Babinsky, J. F. Milthorpe, and K. Shankar. Active control of normal shock wave/turbulent boundary layer interaction using "smart" piezoelectric flap actuators. AIAA-2004-2701. $42^{nd}$ Aerospace Sciences Meeting & Exhibit, Portland, Oregon, June 2004.

[34] C. Dima and P. deMatteis. Effects of shock and boundary-layer control techniques on transonic flows about airfoils. AIAA-2000-0517. $38^{th}$ Aerospace Sciences Meeting & Exhibit, Reno, Nevada, January 2000.

[35] J. L. Fulker, P. R. Ashill, and M. J. Simmons. Study of simulated active control of shock waves on an aerofoil TR 93025. *Technical report.* DERA, May 1993.

[36] J. Birkemeyer, H. Rosemann, and E. Stanewsky. Shock control on a swept wing. *Journal of Aerospace Science and Technology*, pages 147-156, 2000.

[37] Th. Lutz, M. Kutzbach, and S. Wagner. Investigations on shock control bumps for infinite swept wings. AIAA-2004-2702. $2^{nd}$ AIAA Flow Control Conference, Portland, Oregon, 2004.

[38] A. Sommerer, T. Lutz, and S. Wagner. Numerical optimization of adaptive transonic airfoils with variable camber. ICAS CONGRESS, Harrogate, UK, 2000.

[39] Th. Lutz, A. Sommerer, and S. Wagner. Parallel numerical optimization of adaptive transonic airfoils. 2001.

[40] A. Sommerer, Th. Lutz, S. Wagner, W. Wadehn, D. Fokin, and G. Pritschow. Structural concepts and aerodynamic design of shock control bump. ICAS CONGRESS, Toronto, Canada, 2002.

[41] Synaps Inc. http://www.synaps-inc.com/products/pointer/optimize/index.html, 2000.

[42] E. Coustols, G. Pailhas, and P. Sauvage. Scrutinizing flow field pattern around thick cambered trailing edges: Experiments and computations. *International Journal of Heat and Fluid Flow*, 21:264–270, 2000.

[43] Th. Bein, H. Hanselka, and E. Breitbach. An adaptive spoiler to control the transonic shock. *Smart Material Structures*, 9:141–148, 2000.

[44] A. V. Srinivasan and D. M. McFaraland. *Smart Structures, Analysis and Design.* Cambridge University Press, 2001.

[45] Y. Takahashi. Investigation of the aerodynamic effect of a 3d ramp on a 2d transonic wing. Master's thesis, Cranfield University, 2000.

[46] D. Monet. Mechanism and control of transonic shock by 3d bumps on aircraft wings. Master's thesis, Cranfield University, 2001.

[47] N. Qin, D. Monet, and S. T. Shaw. 3D bumps for transonic wing shock control and drag reduction. CEAS Aerospace Aerodynamics Research Conference, June 2002.

[48] H. A. Holden, A. N. Smith, and H. Babinsky. Shock/boundary layer interaction control using 3D bumps. CEAS Aerospace Aerodynamics Research Conference, June 2003.

[49] H. A. Holden and H. Babinsky. Shock/boundary layer interaction control using 3D devices. AIAA-2003-447. $41^{st}$ Aerospace Sciences Meeting & Exhibit, Reno, Nevada, 2003.

[50] D. Perigo. A numerical investigations of the flows in and around clustered module plug nozzles, 2000. EngD thesis.

[51] A. Le Moigne and N. Qin. Large eddy simulation of aircraft wake vortices on unstructured grid. Bremen, Germany, June 2005. CEAS/KATnet Aerospace Conference.

[52] C. E. Manglano. ONERA M6 wing case & computational efficiency study. Unpublished work. College of Aeronautics, Cranfield University, 2002.

[53] S. R. Chakravarthy and S. Osher. Numerical experiments with the osher upwind scheme for the euler equations. *AIAA Journal*, 21:1241–1248, 1983.

[54] B. Van Leer. Towards the ultimate conservative difference scheme. v - a second order sequel to godunovs method (for ideal compressible flow). *Journal of Computational Physics*, 32:101–136, 1979.

[55] B. S. Baldwin and H. Lomax. Thin layer approximation and algebraic model for separated turbulent flows. AIAA-78-0257. $16^{th}$ Aerospace Sciences Meeting & Exhibit, Reno, Nevada, 1978.

[56] D. C. Wilcox. *Turbulence Modelling for CFD, DCW Industries, Inc.* La Canada, 1994.

[57] N. Qin and C. Jayatunga. Algebraic turbulence modelling for vortical flows around slender bodies. Sorrento, Italy, May 1998. NATO/RTO Symposium of the Applied Vehicle Technology Panel on Missile Aerodynamics. Paper 20.

[58] J. D. Anderson Jr. *Computational Fluid Dynamics* The Basics with Applications. McGraw-Hill, 1995.

[59] Dr. A. Tourlidakis. Introduction to CFD: Derivation of fluid flow governing equations. Lecture Notes, Cranfield University, 2003.

[60] Dr. S. Shaw. Governing equations for fluid dynamics. Lecture Notes, Cranfield University, 2002.

[61] Pointwise Inc. *Gridgen User Manual*, 2005.

[62] Prof. N. Qin. Computation of high speed flows. Lecture Notes, Cranfield University, 2002.

[63] S. K. Godunov. A finite difference method for the computation of discontinuous solutions of the equations of fluid mechanics. *Mat.Sb*, 47:357–393, 1959.

[64] S. K. Godunov. *Difference schemes : an introduction to the underlying theory.* Oxford ; New York : North-Holland, $2^{nd}$ edition, 1987.

[65] B. Van Leer. Towards the ultimate conservative difference scheme. iii - upstreamcentered finite-difference schemes for ideal compressible flow. iv -a new approach to numerical convection. *Journal of Computational Physics*, 27:263–299, 1979.

[66] D. Degani and L. B. Schiff. Computation of turbulent supersonic flows around pointed bodies having cross-flow separation. *Journal of Computational Physics*, 66:173–196, 1986.

[67] D. Degani, B. Schiff, and Y. Levy. Physical considerations governing computation of turbulent flows over bodies at large incidence. AIAA-90-0096. $28^{th}$ Aerospace Sciences Meeting & Exhibit, Reno, Nevada, 1990.

[68] A. G. Panaras and J. L. Steger. A thin-layer solution of the flow about a prolate spheroid. *Z. Flugwiss*, 12:173–180, 1988.

[69] M. B. Giles and R. M. Cummings. Wake integration for three-dimensional flowfield computations: theoretical development. *Journal of Aircraft*, 36:357–365, 1999.

[70] D. L. Hunt, M. B. Giles, and R. M. Cummings. Wake integration for three-dimensional flowfield computations: applications. *Journal of Aircraft*, 36:366-373, 1999.

[71] L. Paparone and R. Tognaccini. Computation fluid dynamics-based drag prediction and decomposition. *AIAA Journal*, 41:1647–1657, 2003.

[72] W. J. McCroskey. A critical assessment of wind tunnel test results for the naca 0012 airfoil. agard fluid dynamics panel symposium on aerodynamic data accuracy and quality: Requirements and capabilities in wind tunnel testing. *Technical report.* AGARD Paper 1, 1987.

[73] Top 500 Supercomputer Sites. http://clusters.top500.org/lists/2005/06/, 2005.

[74] A. Le Moigne. *A Discrete Navier-Stokes Adjoint Method for Aerodynamic Optimization of Blended Wing-Body Configurations.* PhD thesis, Cranfield University, Cranfield College of Aeronautics, 2002.

[75] http://www.llnl.gov/computing/tutorials/openMP. *Introduction to OpenMP*, 2000.

[76] B. Booth. *Sheffield High Performance Computer Grid, Titania.* User Manual. The University of Sheffield, 2004.

[77] The White Rose Grid. http://www.shef.ac.uk/wrgrid/, 2003.

[78] B. Booth. *Sheffield High Performance Computer Grid, Iceberg.* User Manual. The University of Sheffield, 2005.

[79] Dr. A. N. Real. *Leeds University High Performance Computer Grid, Snowdon.* User Manual. University of Leeds, 2004.

[80] Compusys Plc. *High Performance Beowulf Cluster User Manual, Bluegrid,* 2003.

[81] D. Lecomber. *Introduction to MPI.* Streamline Computing, 2003.

[82] Dr. P. S. Pacheco and C. M. Woo. *Introduction to Message Passing Programming. MPI User's Guide in Fortran,* 2003.

[83] A. Le Moigne and N. Qin. Variable-fidelity aerodynamic optimization for turbulent flows using a discrete adjoint formulation. *AIAA Journal,* 42(7):1281–1292, 2004.

[84] A. N. Smith, H. Babinsky, P. C. Dhanasekaran, A. M. Savill, and W. N. Dawes. Computational investigation of groove controlled shock wave/boundary layer interaction. AIAA-2003-446. $41^{th}$ Aerospace Sciences Meeting & Exhibit, Reno, Nevada, 2003.

[85] T. Schumacher. Mechanism and control of transonic shock by 3d slots on aircraft wings. Master's thesis, Cranfield University, 2002.

[86] W. C. Engelund, D. O. Stanley, R. A. Lepsch, M. M. McMillin, and R. Unal. Aerodynamic configuration design using response surface methodology analysis. $31^{st}$ Aerospace Sciences Meeting & Exhibit, Reno, Nevada, 1993.

[87] M. Mitchell. *An Introduction to Genetic Algorithms.* Cambridge, Mass : MIT Press, 1996.

[88] A. Oyama. Multidisplinary optimization of transonic wing design based on evolutionary algorithms coupled with CFD solver. ECCOMAS, European Congress on Computational Methods in Applied Sciences and Engineering, 2000.

[89] A. Jameson and L. Martinelli. Optimum aerodynamic design using the navier-stokes equations. *Theoretical Computational Fluid Dynamics,* 10:213–237, 1998.

[90] P. E. Gill, W. Murray, and M. Wright. *Practical Optimization.* London:Academic Press, 1981.

[91] Numerical Algorithm Group. *E04UCF-NAG Fortran library routine document. NAG's Library*, 1999.

[92] J. L. Zhou, A. L. Tits, and C. T. Lawrence. *A FORTRAN code for solving constrained nonlinear (minimax) optimization problems, generating iterates satisfying all inequality and linear constraints. User's guide for FFSQP version 3.7*, 1996.

[93] E. L. Houghton and P. W. Carpenter. *Aerodynamics for Engineering Students.* Elsevier Butterworth Heinemann, 2003.

[94] NPARC Alliance Validation Archive. http://www.grc.nasa.gov/www/wind/valid/, 2005.

[95] M. Nemec and D. W. Zingg. Towards efficient aerodynamic shape optimization based on navier-stokes equations. AIAA-2001-2532. $15^{th}$ AIAA Computational Fluid Dynamics Conference, Anaheim, CA, June 2001.

[96] Dr. A. Tourlidakis. Grid generation in computational fluid dynamics. Lecture Notes. Cranfied University, 1998.

[97] N. Cumpsty. *Jet Propulsion.* Cambridge University Press, $2^{nd}$ edition, 2003.

[98] M. Asselin. *An Introduction to Aircraft Performance.* AIAA Eduction Series, 1997.

[99] M. A. Portsdam, M. A. Page, and R. H. Liebeck. Blended wing body analysis and design. AIAA-97-2317. $35^{th}$ Aerospace Sciences Meeting & Exhibit, Reno, Nevada, 1997.

[100] H. Smith. College of aeronautics blended wing body development programme. ICAS paper 1.1.4. International Council of the Aeronautical Sciences, 2000.

[101] A. L. Biksynovskym, N. O. Buzoverya, B. I. Gurevich, V. E. Denisov, A. I. Dunaevsky, L. M. Shkadov, O. V. Sorin, A. J. Udzhuzhu, and J. P. Zhurihin. Flying-wing problems and decisions. *Aircraft Design*, 4:193–219, 2001.

[102] N. Qin, A. Vavalle, and A. Le Moigne. Spanwise lift distribution for blended wing body aircraft. *Journal of Aircraft*, 42:356–365, 2005.

[103] N. Qin, A. Vavalle, A. Le Moigne, M. Laban, K. Hackett, and P. Weinerfelt. Aerodynamic considerations of blended wing body aircraft. *Progress in Aerospace Sciences*, 40:321–343, 2004.

[104] A. Morris. MOB, an European disributed multi-disciplinary design and optimisation project. AIAA-2002-5444. AIAA/ISSMO Symposium on Multidisciplinary Analysis and Optimization, Atlanta, Georgia, 2002.

[105] A. Le Moigne and N. Qin. Aerofoil profile and sweep optimisation for a blended wing-body aircraft using a discrete adjoint method. *To appear in the Aeronautical Journal*, 2006.

[106] W. S. Wong, N. Qin, and N. Sellars. A numerical study of transonic flow in a wind tunnel over 3D bumps. AIAA-2005-1057. $43^{rd}$ Aerospace Sciences Meeting & Exhibit, Reno, Nevada, 2005.

[107] W. S. Wong, N. Qin, and N. Sellars. Validation and optimisation of 3D bumps for transonic wing drag reduction. CEAS/KATnet Conference on Key Aerodynamic Technologies, Bremen, Germany, June 2005.

[108] W. S. Wong, N. Qin, N. Sellars, H. Holden, and H. Babinsky. Transonic vortical flow structures over three-dimensional shock control bumps at sub-boundary layer scales. *Submitted to Progress of Aerospace and Sciences*, 2006.

[109] W. S. Wong and N. Qin. Drag analysis of three-dimensional shock control bumps on a transonic wing. *Technical report to Airbus*. The University of Sheffield, December 2005.

[110] W. S. Wong, A. Le Moigne, and N. Qin. Parallel adjoint-based optimisation of a blended wing body aircraft with shock control bumps. *To appear in The Aeronautical Journal*, 2006.

[111] W. S. Wong and N. Qin. Mechanisms and correlations of 3D shock control bumps. *Contract report to Airbus*. The University of Sheffield, October 2006.